Physics with Muons
from Atomic Physics to Condensed Matter Physics

Elvezio Morenzoni

Lecture course PHY 432 (Univ. Zürich)
Lecture course 402-0770-00L (ETH-Zürich)

Script on: http://www.psi.ch/lmu/lectures

Address:
Paul Scherrer Institut
WLGA/112
5232 Villigen PSI
Tel: 056 310 3670
elvezio.morenzoni@psi.ch

Physik-Institut
Universität Zürich
Y36/J34
Winterthurerstrasse 190
8057 Zürich
Tel: 044 635 57 50

Version 22.5.2017

Table of contents

Literature

Books

- A. Yaouanc, P. Dalmas de Réotier
  MUON SPIN ROTATION, RELAXATION and RESONANCE (Oxford University Press, 2011)

- E. Karlsson
  SOLID STATE PHENOMENA, As Seen by Muons, Protons, and Excited Nuclei, (Clarendon, Oxford 1995)

- S.L. Lee, S.H. Kilcoyne, R. Cywinski eds.
  MUON SCIENCE: MUONS IN PHYSICS; CHEMISTRY AND MATERIALS, (IOP Publishing, Bristol and Philadelphia, 1999)

- A. Schenck
  MUON SPIN ROTATION SPECTROSCOPY, (Adam Hilger, Bristol 1985)

Introductory articles

- S.J. Blundell
  SPIN-POLARIZED MUONS IN CONDENSED MATTER PHYSICS, Contemporary Physics **40**, 175-192 (1999)

- P. Bakule, E. Morenzoni
  GENERATION AND APPLICATIONN OF SLOW POLARIZED MUONS, Contemporary Physics **45**, 203-225 (2004)

Reviews articles: applications

- P. Dalmas de Réotier and A. Yaouanc
  MUON SPIN ROTATION AND RELAXATION IN MAGNETIC MATERIALS, J. Phys. Condens. Matter **9**, 9113-9166 (1997)

- A. Schenck and F.N. Gygax
  MAGNETIC MATERIALS STUDIED BY MUON SPIN ROTATION SPECTROSCOPY, In: Handbook of Magnetic Materials, edited by K.H.J. Buschow, Vol. 9 (Elsevier, Amsterdam) 57-302, (1995)

- B.D. Patterson
  MUONIUM STATES IN SEMICONDUCTORS, Rev. Mod. Phys. **60**, 69-159 (1988)

- A. Amato
  HEAVY-FERMION SYSTEMS STUDIED BY μSR TECHNIQUES, Rev. Mod. Phys., **69**, 1119-1179 (1997)

- V. Storchak, N. Prokovev
  QUANTUM DIFFUSION OF MUONS AND MUONIUM ATOMS IN SOLIDS, Rev. Mod. Physics, **70**, 929 (1998)

- J. Sonier, J. Brewer, R. Kiefl
  μSR STUDIES OF VORTEX STATE IN TYPE-II SUPERCONDUCTORS, Rev. Mod. Physics, **72**, 769 (2000)

- E. Roduner
  THE POSITIVE MUON AS A PROBE IN FREE RADICAL CHEMISTRY, Lecture Notes in Chemistry No. 49 (Springer Verlag, Berlin 1988)

1. Introduction

The muon is an elementary particle and one of the fundamental fermions of the standard model.

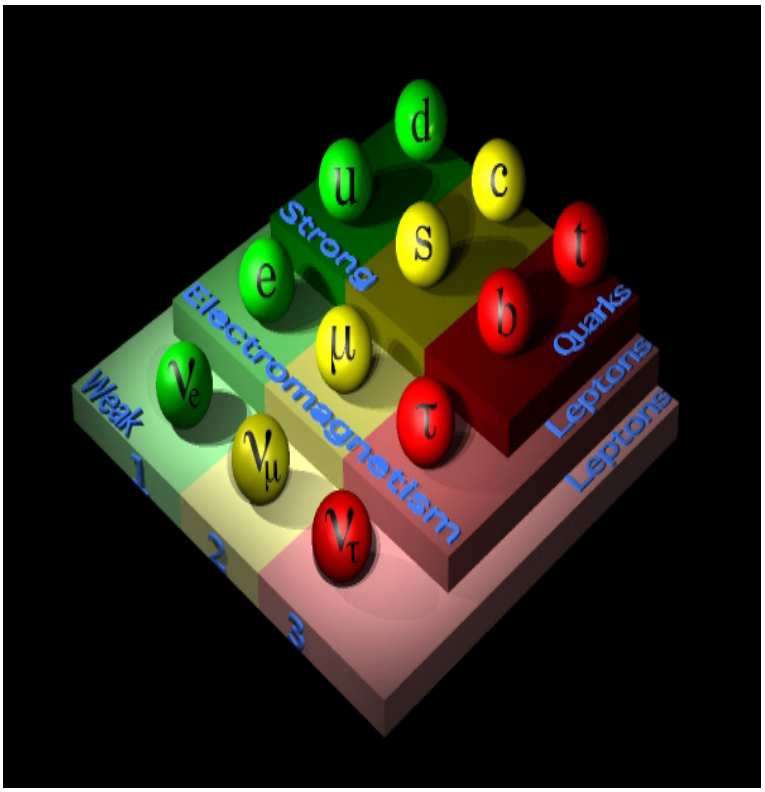

Leptons and Quarks

Leptons (Spin ½)			Quarks (Spin ½)		
Flavor	Mass [MeV/c^2]	Electric charge [e]	Flavor	Approx Mass [GeV/c^2]	Electric charge [e]
ν_e electron neutrino	$< 2 \cdot 10^{-6}$	0	u up	0.0023	2/3
e electron	0.511	-1	d down	0.0048	-1/3
ν_μ muon neutrino	< 0.2	0	c charm	1.275	2/3
μ muon	106	-1	s strange	0.095	-1/3
ν_τ tau neutrino	<18.2	0	t top	173	2/3
τ tauon	1776.82	-1	b bottom	4.7	-1/3

Fundamental fermions (including antiparticles) of the standard model.

1.1 Muon properties

Rest mass, m_μ	105.658 MeV/c^2 206.768 m_e 0.1124 m_p
Charge, e	+1, -1 elementary charges
Spin, I	½
Magnetic Moment, μ_μ	$4.836 \cdot 10^{-3}\ \mu_B,\ \mu_B = \frac{e\hbar}{2m_e} = 0.927 \cdot 10^{-23} Am^2$
Gyromagnetic ratio, γ_μ	$2\pi \cdot 135.538817$ MHz/T $\mu_\mu = g_\mu \frac{e\hbar}{2m_\mu} I = \gamma_\mu \hbar I \quad (g_\mu = 2.002\ 331\ 8414)$
Lifetime, τ	2.197 μs
Decay,	$\mu^+ \rightarrow e^+ + \nu_e + \bar{\nu}_\mu$ ≈ 100% $\mu^+ \rightarrow e^+ + \nu_e + \bar{\nu}_\mu + \gamma$ $1.4 \pm 0.4\ 10^{-2}$ $\mu^+ \rightarrow e^+ + \nu_e + \bar{\nu}_\mu + e^+ + e^-$ $3.4 \pm 0.4\ 10^{-5}$ $\mu^- \rightarrow e^- + \bar{\nu}_e + \nu_\mu$

Properties of the positive muon and muonium compared with those of proton and hydrogen

	Muon	Proton
Mass (m_e)	206.768	1836.15
Spin	½	½
Gyromagnetic ratio, γ ($T^{-1}s^{-1}$)	$8.516155\ 10^8$	$2.675221\ 10^8$
Lifetime (s)	$2.19709\ 10^{-6}$	stable
	Muonium	**Hydrogen**
Reduced electron mass (m_e)	0.995187	0.999456
Radius ground state (nm)	0.0531736	0.0529465
Energy ground state (eV)	-13.5403	-13.5984
Hyperfine frequency (GHz)	4.46330	1.42041

1.2 Discovery of the muon

1910 Theodor Wulf performs experiments with electrometers. He detects more radiation at the top of the Eiffel tower than on ground.

1911-1912 Viktor Hess makes measurements from balloons. He measures increasing charge with increasing altitude.

Millikan uses unmanned balloons to perform experiments at even higher altitude. He creates the expression cosmic radiation.

1933 First muon picture (but not correctly identified) in a Wilson cloud chamber by Kunze (P. Kunze, Z. Phys. **83**, 1 (1933)).

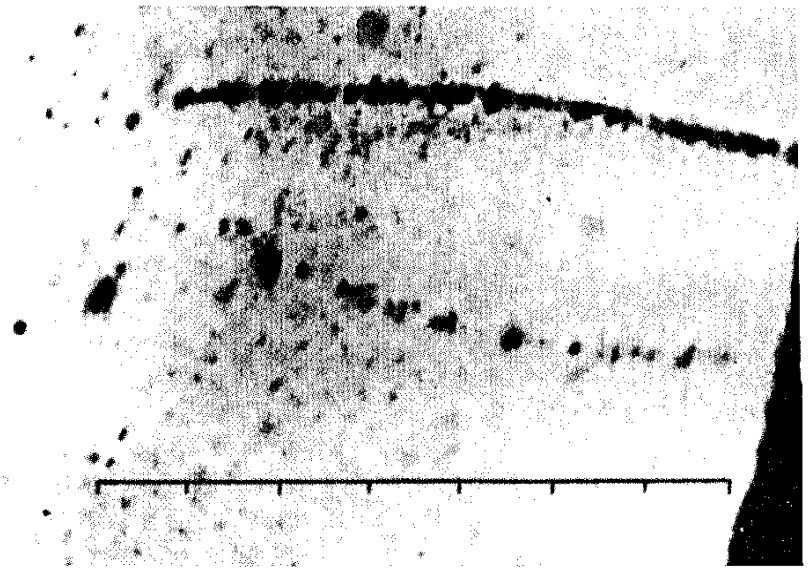

(figure 5) shows closely together the thin trace of an electron of 37 MeV, and a much more strongly ionizing positive particle whith a much larger bending radius. The nature of this particle is unknown; for a proton it does not ionize enough and for a positive electron the ionization is too strong. The present double trace is probably a segment from a "shower" of particles as they have been observed by Blackett and Occhialini, i.e. the result of a nuclear explosion".

Kunze, P., Z. Phys. 83, (1933) 1

1936 V. Hess receives the Nobel Prize for the discovery of cosmic radiation.

Muons are the main component of cosmic radiation at sea level. Identified from Andersen and Neddermayer (1936), however first misinterpreted as so-called Yukawa particles.

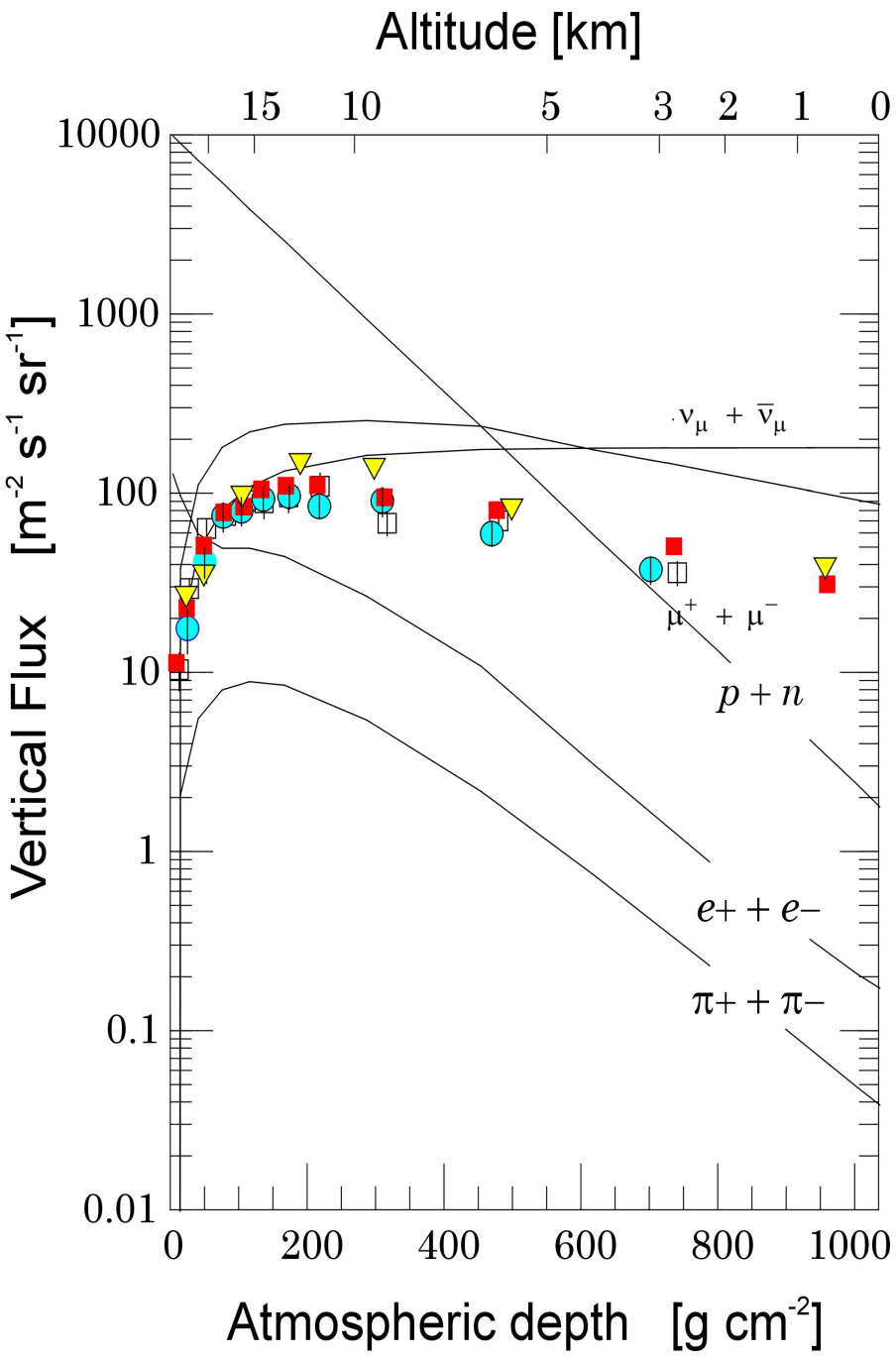

Fig. 1-1: Cosmic rays flux.

Muons are generated at about 15 km height. They reach earth level as a consequence of relativistic time dilatation. They have a broad spectrum of energies.

Flux at sea level: ~ 1 Muon/Min/cm^2

$E_{typical}$ ~ 2 GeV

Time dilatation: $\gamma = \frac{E_{typical}}{m_\mu c^2} \approx 20$ Flight path : $L = v\gamma\tau_\mu \cong c\gamma\tau_\mu$

1945-47 Conversi et al. measure lifetime of positive and negative muons. Lifetime is too long for strongly interacting particles. It turns out that the Yukawa particle is actually the pion.

1957 Garwin et al. and Friedman et al. measure parity violation of μ-decay. Prototype of a muon spin rotation experiment.

1.3 Pion properties and decay

	π^+	π^-	π^0
Lifetime (s)	$26.04\ 10^{-9}$	$26.04\ 10^{-9}$	$0.89\ 10^{-16}$
Spin	0	0	0
Mass (MeV/c^2)	139.5679	139.5679	134.97
Decay	$\pi^+ \rightarrow \mu^+ + \nu_\mu$	$\pi^- \rightarrow \mu^- + \bar{\nu}_\mu$	$\pi^0 \rightarrow \gamma + \gamma$

$\pi^+ \rightarrow \mu^+ + \nu_\mu$

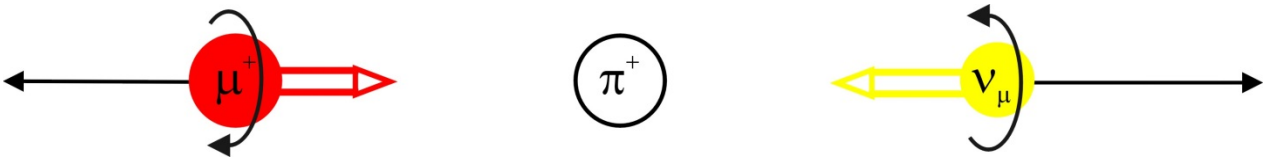

26 ns

Mass	139.6 MeV/c^2	105.66 MeV/c^2	<0.19 MeV/c^2
Spin	0	½	½
Charge	1	1	0
Lepton number	0	-1	1

Decay kinematics:

$p_\mu = 29.79$ MeV/c

$T_\mu = 4.12$ MeV [1-1]

$\beta_\mu = 0.28$

Parity violation in the pion decay

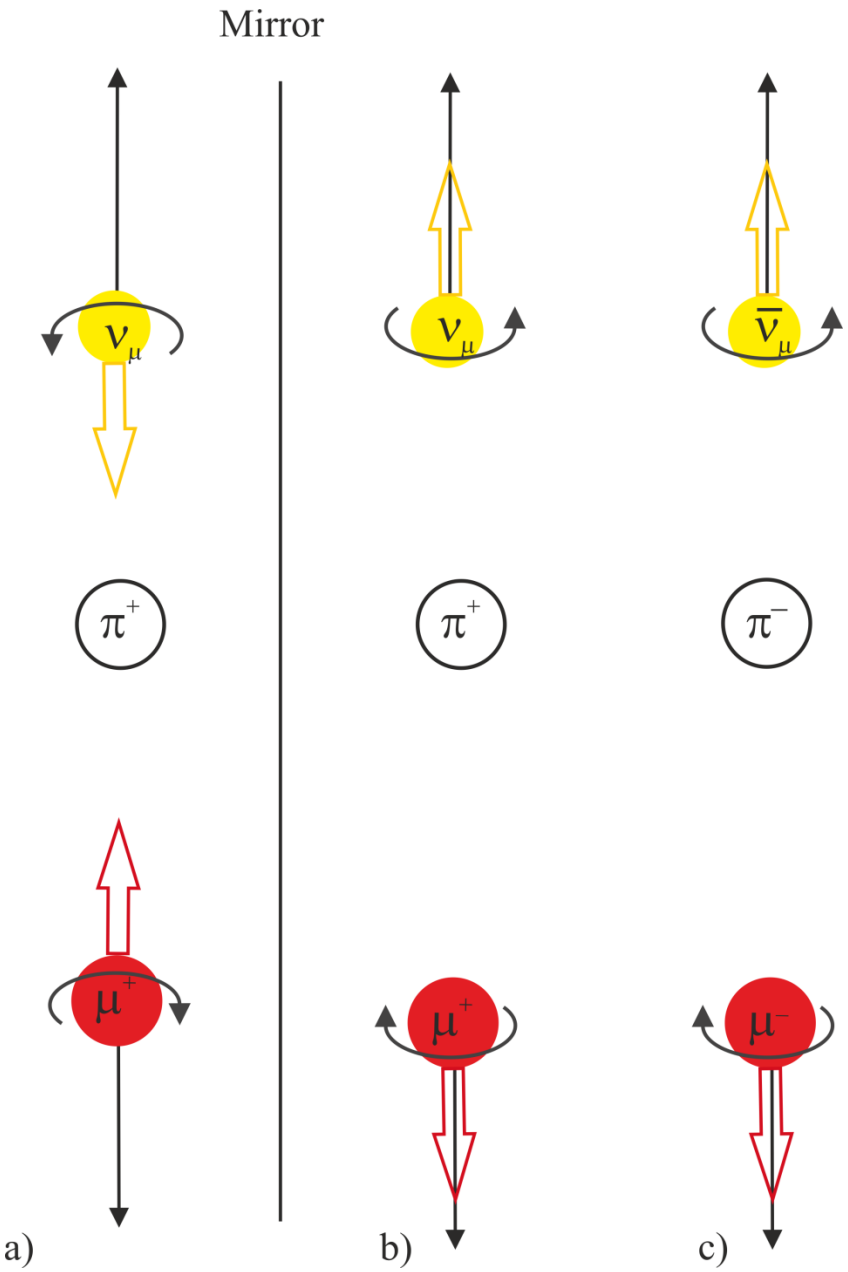

a) Original decay, b) Mirrored decay (corresponding to parity operation on a)), c) Charge conjugated process b).

Process b) does not exist (only left handed ν_μ exist, i.e. direction of spin opposite to direction of momentum, helicity = -1). The parity violation in π-decay allows the production of polarized muons (with up to ~ 100% polarization).

1.4 Muon decay

$$\mu^+ \rightarrow e^+ + \nu_e + \bar{\nu}_\mu$$

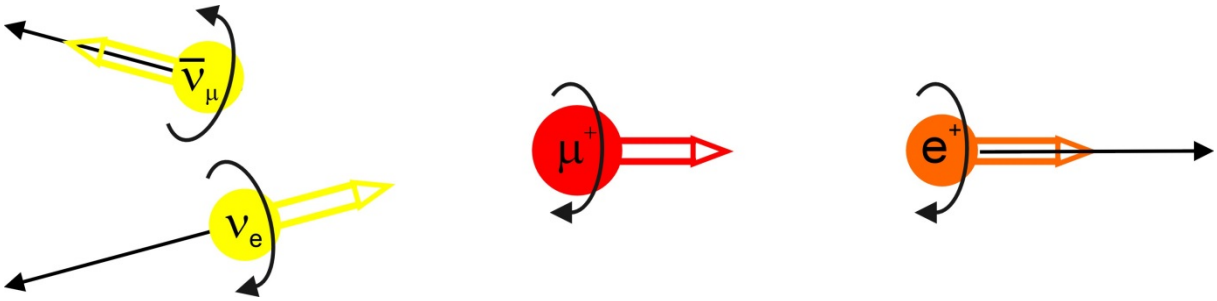

2.2 µs

Neutrinos have negative helicity. Antineutrinos positive. An ultra-relativistic positron behaves like an antineutrino. Thus the positron tends to be emitted along the muon spin direction when ν_e and $\bar{\nu}_\mu$ go off together (highest positron energy).

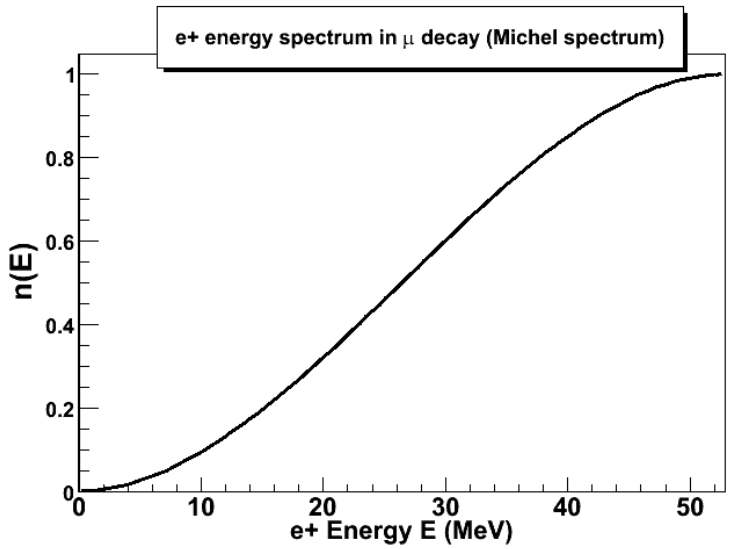

Fig. 1-2: Muon decay and energy spectrum of the positron (Michel spectrum).

Differential positron emission probability:

$$W(x)\,dx = \frac{1}{\tau_\mu} 2x^2(3-2x)\,dx \qquad [1\text{-}2]$$

$$0 \le x \le 1, \qquad x = \frac{2E_{e^+}}{m_\mu c^2} \;,\; \frac{m_\mu c^2}{2} \cong E_{max} = 52.83 \text{ MeV} \;,\; \text{Mean Energy: } \bar{E}_{e^+} = 36 \text{ MeV}$$

Asymmetric decay

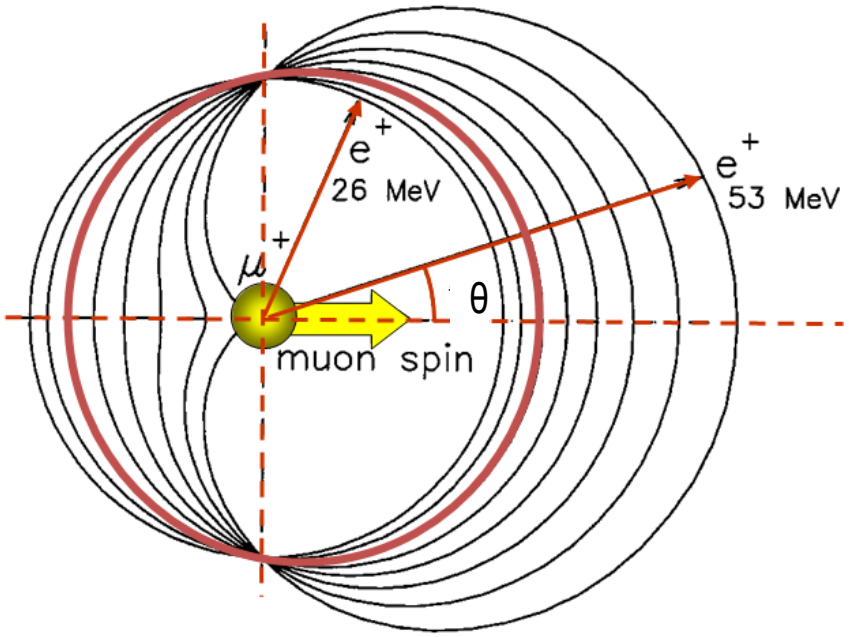

Fig. 1-3: Angular distribution of the e^+ from the muon decay: The asymmetry (anisotropy) of the distribution is 100% for the highest $e^{\pm}$ energy, E_{max} = 52.83 MeV and zero (i.e. an isotropic distribution) for $E_{e+} = E_{max}/2$; for smaller E_{e+} (not shown) the asymmetry is negative. The red curve is the angular distribution averaged over the positron energy.

$$W(x,\cos\theta)dxd(\cos\theta) = \frac{1}{\tau_\mu}x^2(3-2x)\left[1+\frac{(2x-1)}{(3-2x)}\cos\theta\right] = \frac{1}{\tau_\mu}\frac{E(x)}{2}\left[1+a(x)\cos\theta\right]dxd(\cos\theta) \qquad [1\text{-}3]$$

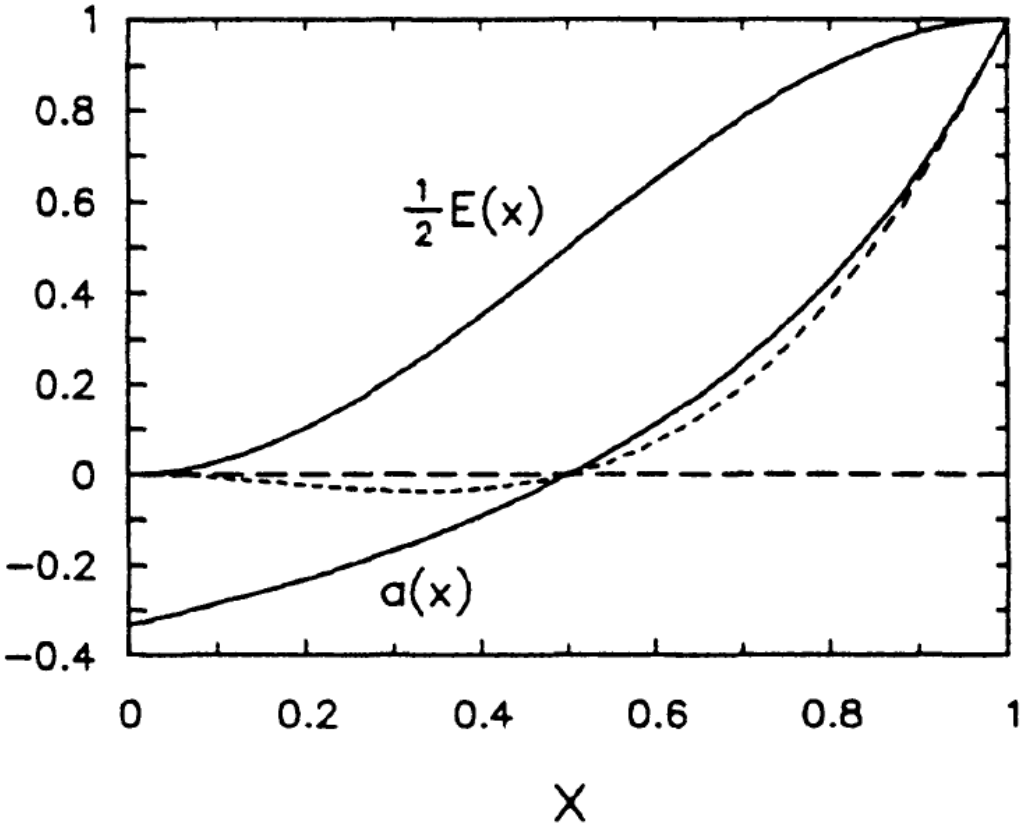

Fig. 1-4: Solid lines: E(x)/2: energy spectrum (Michel spectrum). Positron/electron energy from the normal $\mu^{\pm}$ decay: $E_e = 52.83 \cdot x$ MeV. a(x): $e^{\pm}$ energy dependence of the $\mu^{\pm}$ decay asymmetry (degree of correlation between $e^{\pm}$ momentum and $\mu^{\pm}$ spin direction). For the μ^- decay a(x) has the opposite sign. Dashed line: weighted μ^+ decay asymmetry spectrum, the product of E(x)/2 and a(x).

Average asymmetry:

$$A = \frac{\int_0^1 a(x)E(x)dx}{\int_0^1 E(x)dx} = \frac{1}{3} \qquad [1\text{-}4]$$

Angular distribution:

$$\frac{dW(\theta)}{d(\cos\theta)} \propto (1 + A\cos\theta) = (1 + \frac{1}{3}\cos\theta) \qquad [1\text{-}5]$$

1.5 Pion production reactions

To produce pions, nucleons are bombarded with other nucleons of sufficient energy so that the available energy in the center of mass system exceeds the pion mass of 140 MeV/c^2.

Typical reactions:

$$p + p \rightarrow p + n + \pi^+ \qquad p + p \rightarrow d + \pi^+$$
$$\rightarrow p + p + \pi^0$$
$$p + n \rightarrow p + n + \pi^0$$
$$\rightarrow p + p + \pi^-$$
$$\rightarrow n + n + \pi^+$$

These reactions („single pion production“) have a threshold energy in the laboratory system of ~280 MeV. The cross section increases rapidly with energy. Optimum energy for pion and muon production is between 500 and 1000 MeV. This defines the energy of the accelerator needed for the production of muon and pion beams.

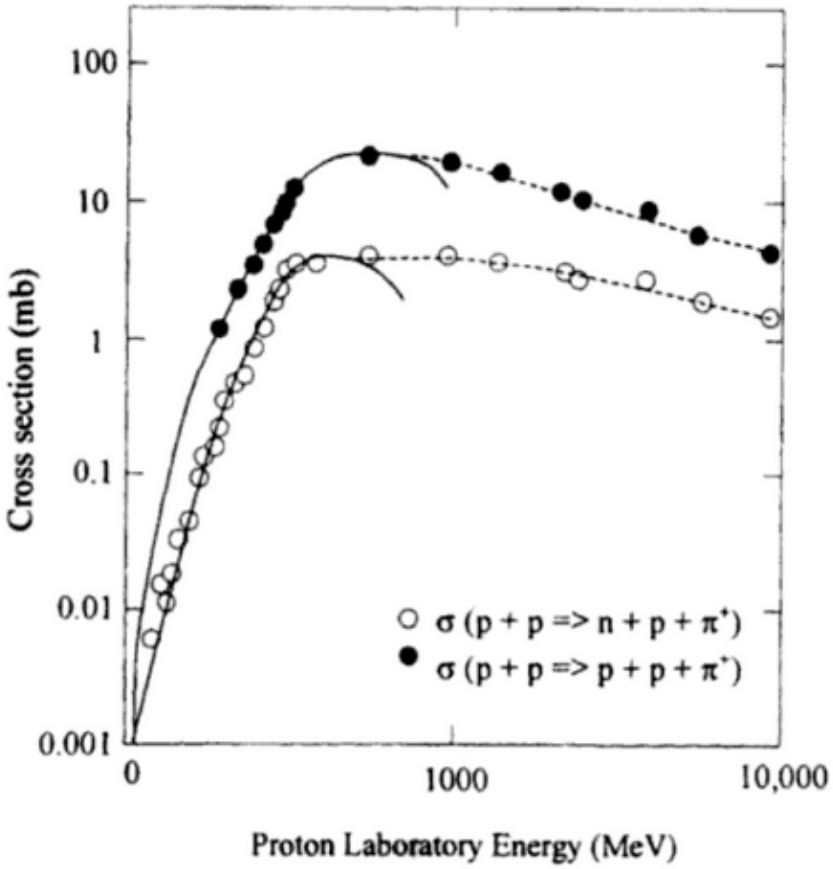

Fig. 1-5: Cross sections for single pion production (From G. Eaton, S. Kilcoyne, in Muon Science: Muons in Physics, Chemistry and Materials, S.L Lee, R Cywinski, S.H Kilcoyne eds., 1999).

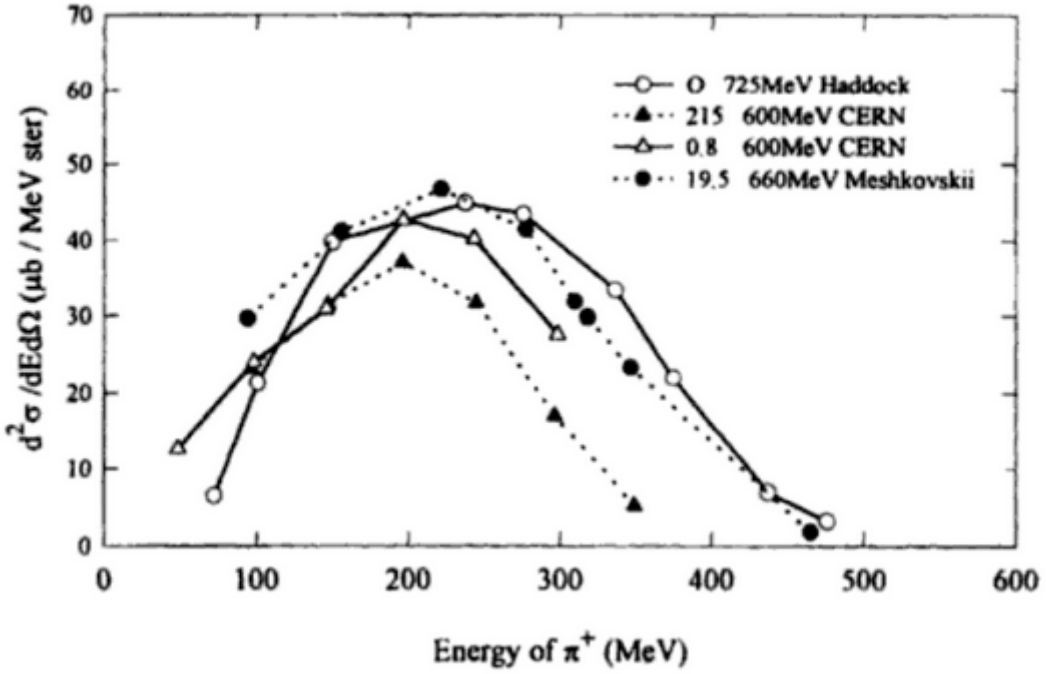

Fig. 1-6: Energy spectra of π^+ produced at different angles in proton-carbon collisions.

The above mentioned reactions produce 3 particles. For incoming protons of 600 MeV, pions have a broad spectrum of energies around a maximum of 200 MeV.

With more energetic accelerators one can make use of double pion reactions:

$$
\begin{aligned}
p + p &\rightarrow p + p + \pi^+ + \pi^- \\
&\rightarrow p + p + \pi^0 + \pi^0 \\
&\rightarrow n + \pi^0 + \pi^+ + \pi^+ \\
&\rightarrow n + p + \pi^+ + \pi^0 \\
&\rightarrow d + \pi^+ + \pi^0 \\
p + n &\rightarrow p + n + \pi^+ + \pi^- \\
&\rightarrow p + n + \pi^0 + \pi^0 \\
&\rightarrow n + n + \pi^+ + \pi^0 \\
&\rightarrow p + p + \pi^- + \pi^0 \\
&\rightarrow d + \pi^+ + \pi^- \\
&\rightarrow d + \pi^0 + \pi^0
\end{aligned}
$$

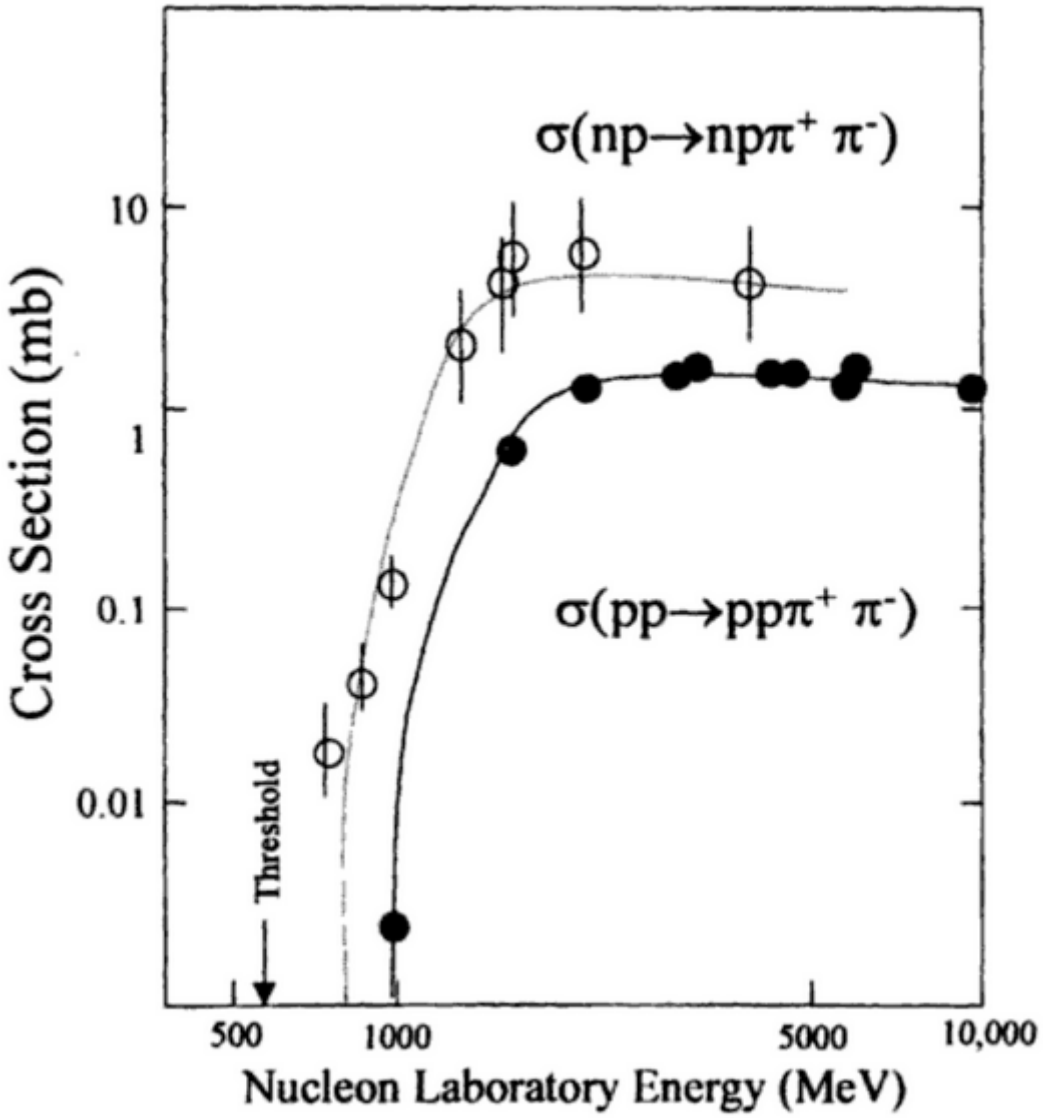

Fig. 1-7: Examples of cross-sections for double pion production.

Pion/Muon production target at PSI (target E)

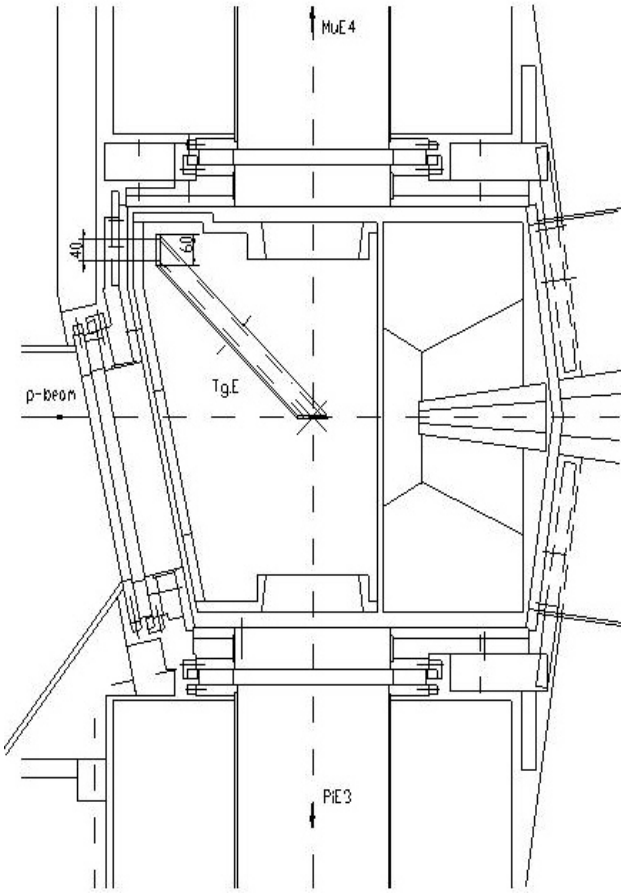

Pion production:

$I_p = 2200\ \mu A \cong 1.37\ \cdot\ 10^{16} p/\sec$

$\sigma_\pi \approx 20\ \text{mbarn} = 2.10^{-26} cm^2$

Target E thickness : 4 cm Graphite = d :

$N = \rho \frac{L}{A} = 2.26 g/cm^3 * 6.10^{23} / 12 g = 1.13 \cdot 10^{23}$ Atoms/cm^3

$N\sigma d = 0.91 * 10^{-2}$

$I_p * N\sigma d = 1.22 * 10^{14} \pi/\sec$ (on 4π solid angle)

1.6 Muon beams

- Decay muon beam (μ^+ or μ^-)

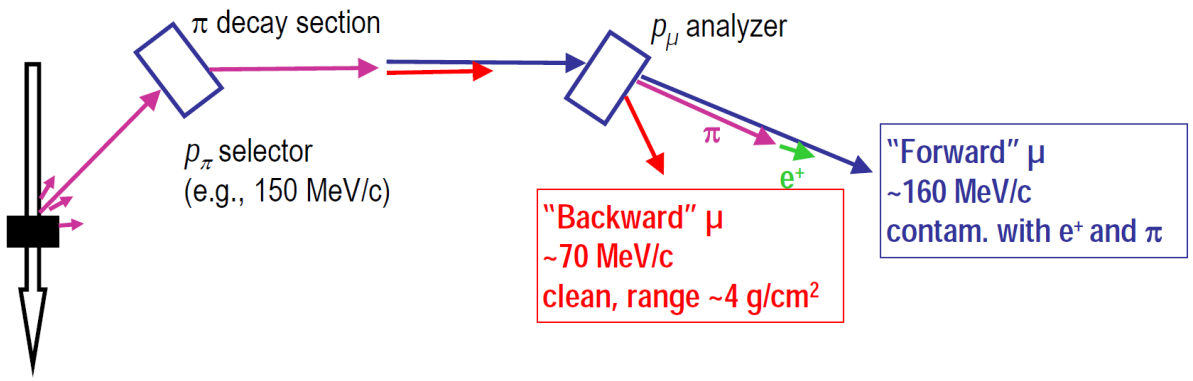

Decay length :

$$\lambda_\pi[\mathrm{m}] = v\gamma\tau_\pi = \frac{p_\pi[\mathrm{MeV/c}]}{m_\pi[\mathrm{MeV/c^2}]} 26\cdot 10^{-9}\,\mathrm{s}\cdot c = 0.055 p_\pi[\mathrm{MeV/c}]$$

- Surface muon beam (μ^+ only)
  (from the pion decay at rest at the surface of the production target)

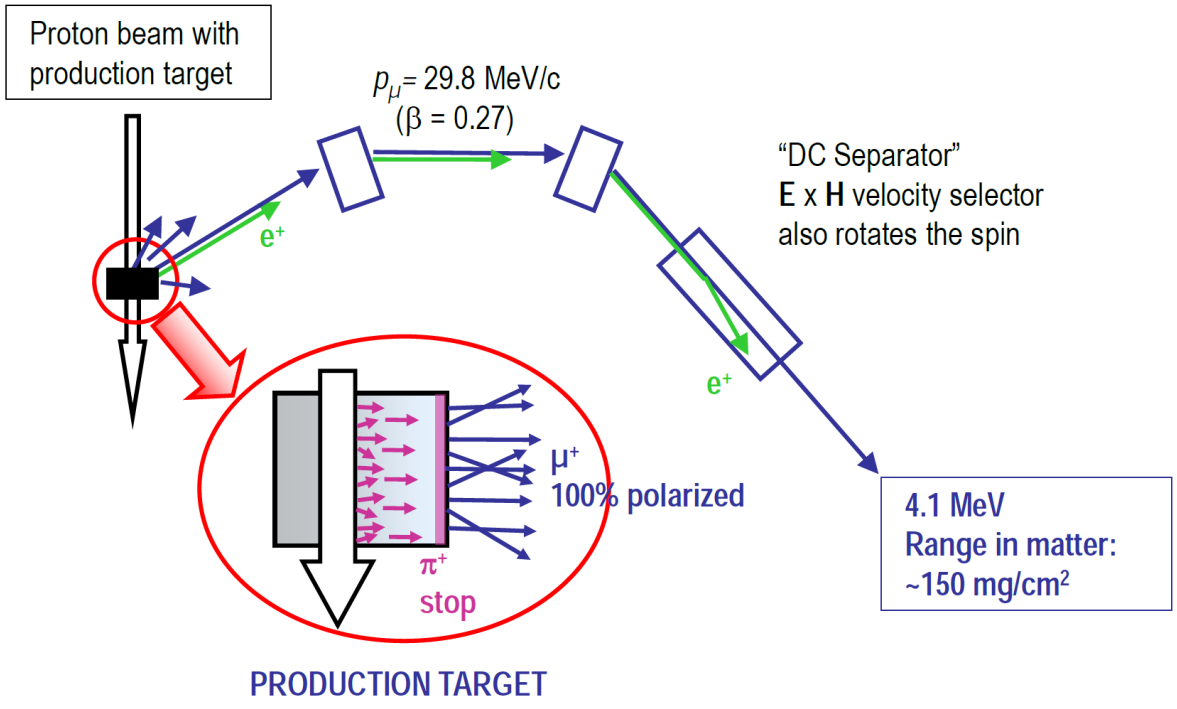

Range of "surface muons" in matter :

$$R = L\rho \cong 150\ \frac{\mathrm{mg}}{\mathrm{cm}^2} \approx \text{ only weakly depending on material}$$

L: Range in [cm]

ρ: Density

Pion decay in flight

A decay muon channel delivers muons with different spin direction (with respect to the momentum). Two useful extreme cases:

1) The muon is emitted in the direction of pion propagation. The momenta p_μ^0 and p_π of both particles are additive. The muon is emitted in the "forward" direction, i.e. the total momentum p_μ is greater that that of the pion from which it originated and has a spin antiparallel to p_π .

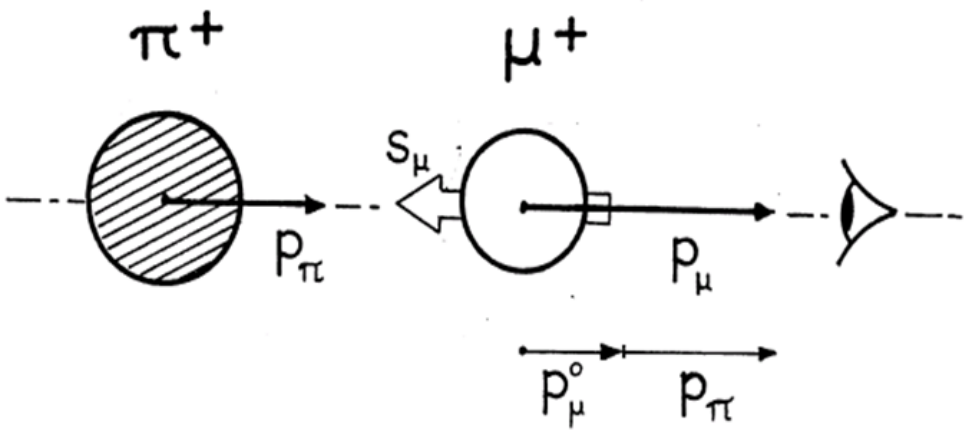

2) on the other hand, a muon emitted in the opposite direction of pion propagation will carry a resultant momentum p_μ smaller than p_π . Such a "backward" muon will have its spin pointing in the direction of propagation.

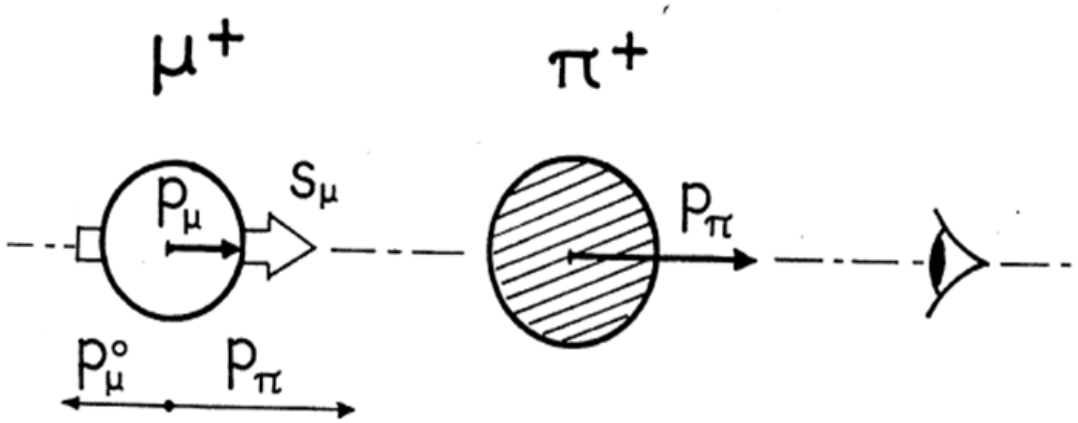

Decay kinematics of the pion decay in flight

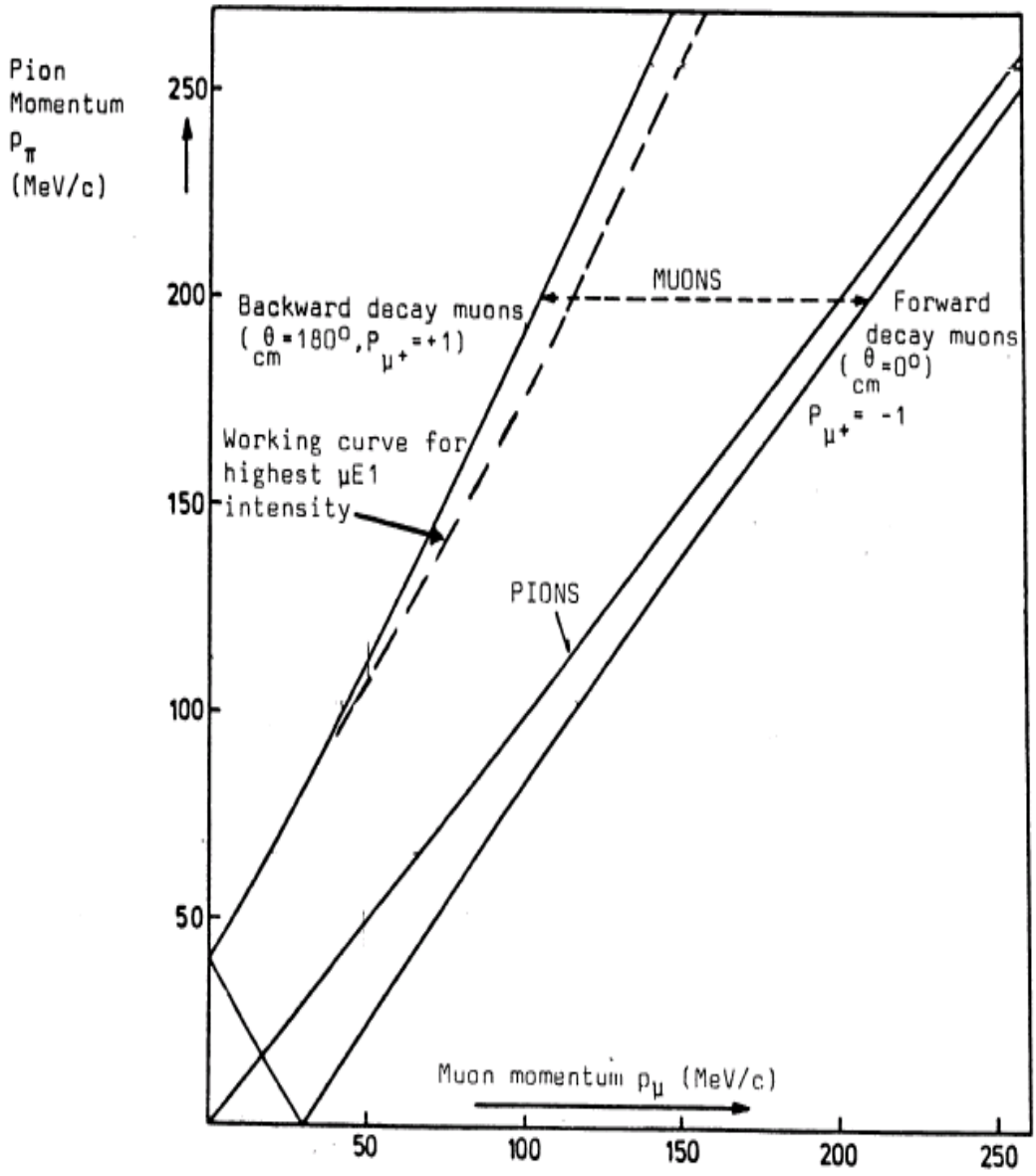

Fig. 1-8: Decay kinematics of the pion decay, showing the kinematically allowed region.

Momentum dependence of beam intensities (πE5 beam line at PSI)

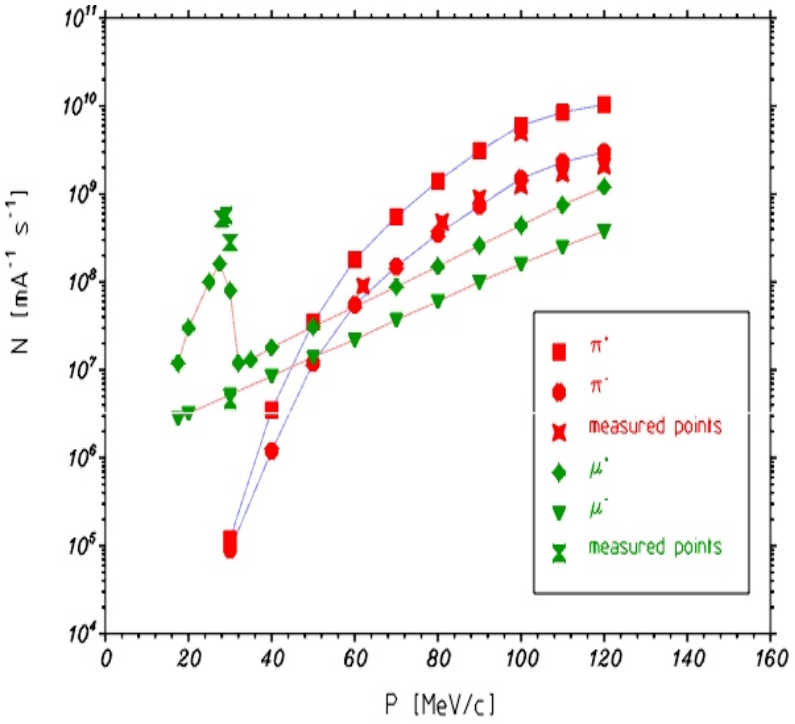

1.7 The PSI HIPA accelerator

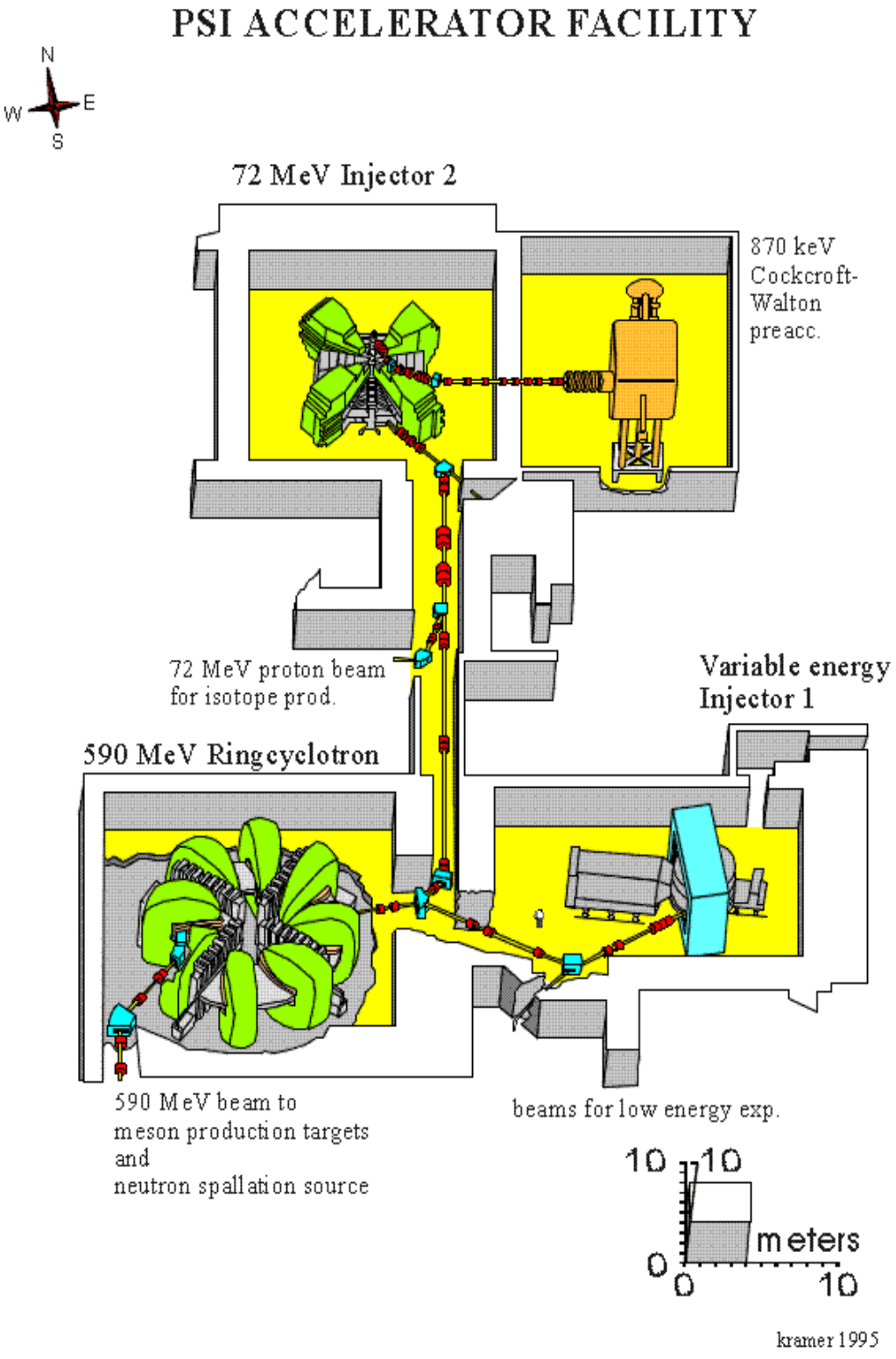

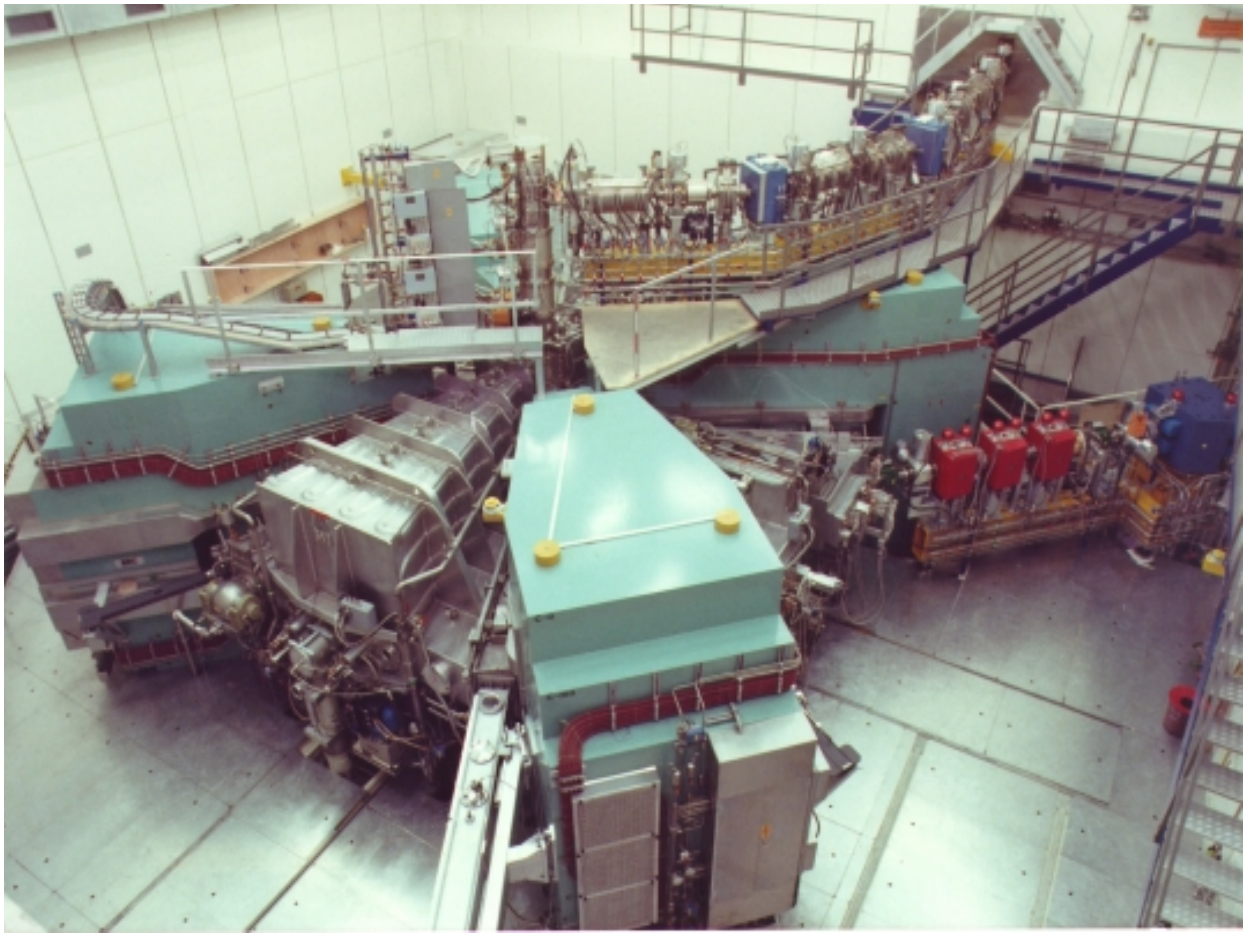

Fig. 1-9: The PSI 72 MeV injector.

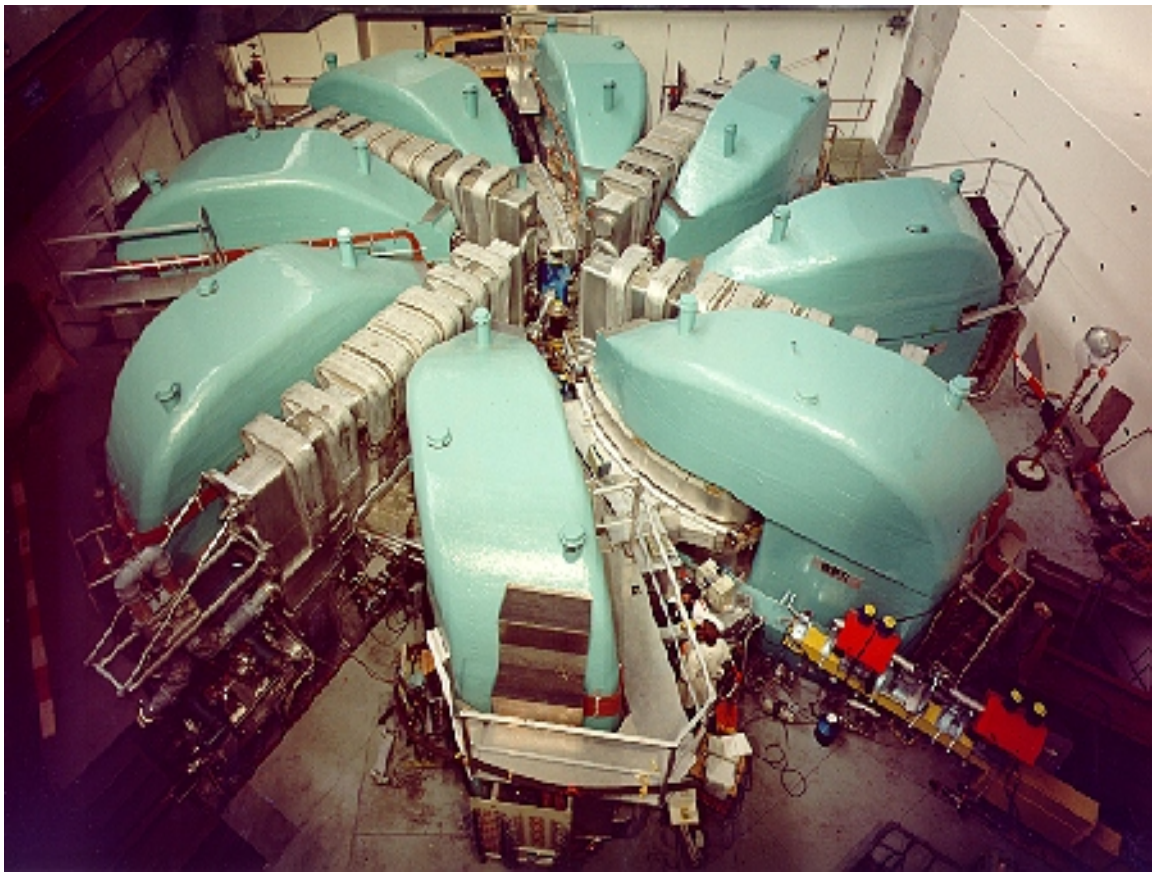

Fig. 1-10: The PSI Ring accelerator.

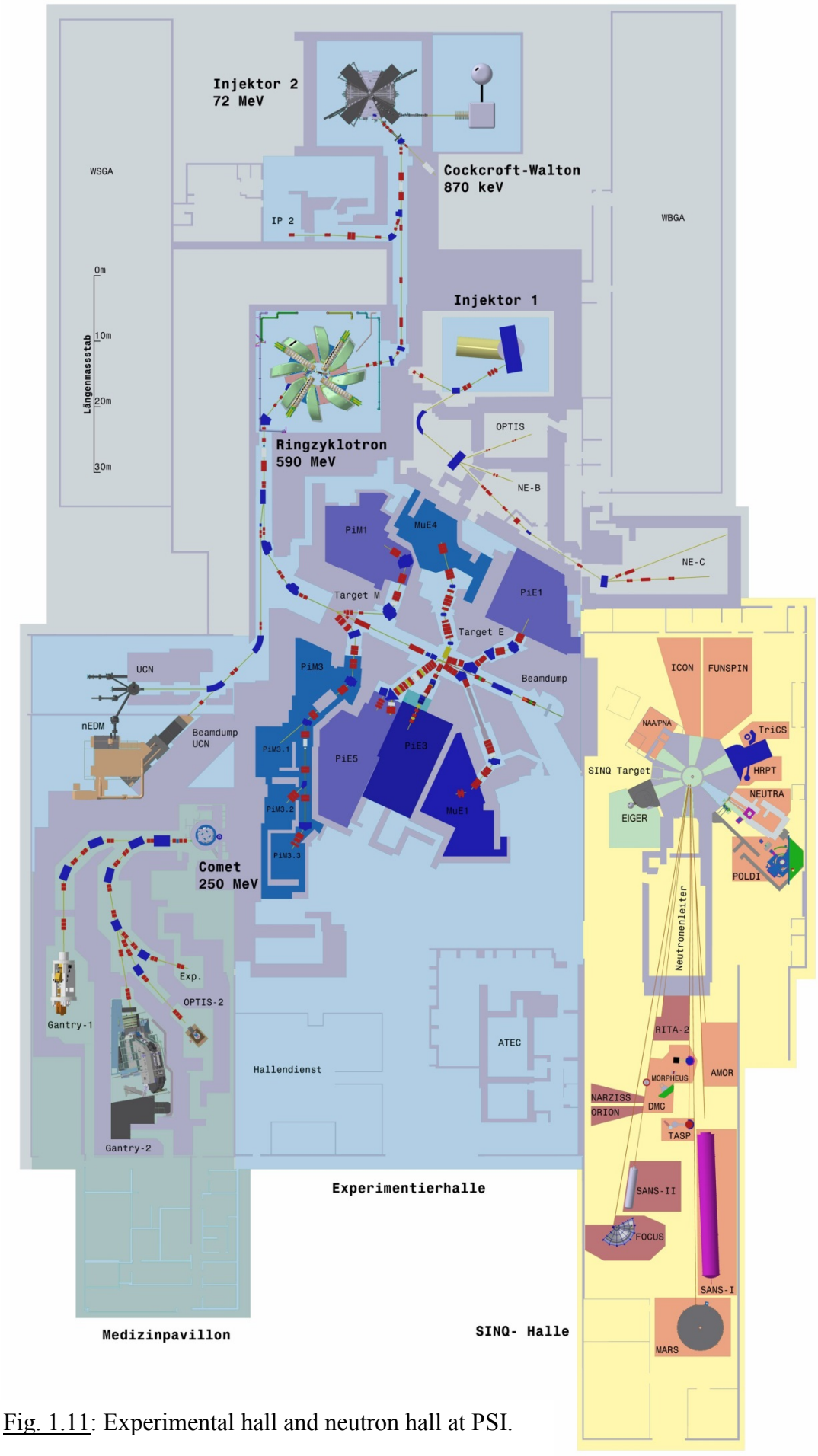

Fig. 1.11: Experimental hall and neutron hall at PSI.

Transport of muons to the experiment (beam line)

A beam line is an arrangement of magnetic (and electric) fields that transport and focus charged particles.
Deflection and transport in magnetic and electric fields:

In magnetic fields[1]:

$$\Delta\varphi \propto \frac{B}{p} \quad (B \perp p) \qquad p[\mathrm{GeV}/c] = 0.299793\ e\ B[\mathrm{T}]r[\mathrm{m}] \qquad [1\text{-}6]$$

In electric fields:

$$\Delta\varphi \propto \frac{|\vec{E}|}{p\beta} \propto \frac{1}{E_{kin}} \quad \leftarrow \text{ non relativistically} \qquad [1\text{-}7]$$

Background suppression (e.g. positrons) with **E** x **B** fields (mass filter or Wien filter).
Total deflection (e=1):

$$\Delta\varphi = \frac{L[\mathrm{m}]}{p[\mathrm{MeV}/c]}\left(\frac{|\vec{E}|[\mathrm{MV}/\mathrm{m}]}{\beta} - 300B[\mathrm{T}]\right) \qquad [1\text{-}8]$$

[1] Kinematics of circular motion (relativistic):

$$\vec{p} = m\gamma\vec{v} \qquad \vec{F} = \frac{d}{dt}\vec{p} = m\frac{d}{dt}(\gamma\vec{v})$$

$$F = \frac{d}{dt}p = m\frac{d}{dt}(\gamma v) \sim m\gamma\frac{d}{dt}v \quad \left(\left(\frac{d}{dt}\gamma\right)v << \gamma\frac{d}{dt}v\right)$$

(longitudinal acceleration much smaller than transverse acceleration)

$$F = m\gamma\left|\frac{d\vec{v}}{dt}\right| = m\gamma\frac{v^2}{r}$$

Lorentz force :

$$\vec{F} = e\vec{v}\times\vec{B}$$

$$F = evB$$

$$qB = m\gamma\frac{v}{r} = \frac{p}{r}$$

$$p = eBr$$

Focusing with magnetic lenses: quadrupole lens

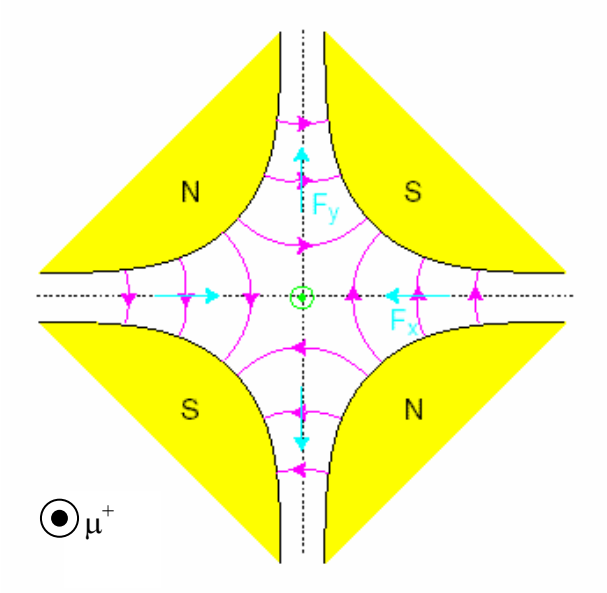

The pole shoes have the shape of hyperbolas, which define equipotential lines: $\Phi(x,y) = -gxy$.

The static magnetic field $\vec{B}(x,y)$ can be written as gradient of the scalar potential $\Phi(x,y)$.

$\vec{B}(x,y) = -\,\mathrm{grad}\Phi(x,y)$ (from $\mathrm{rot}\vec{B}=0$ in the region between the pole shoes)

g is the field gradient $g=\frac{\partial B_y}{\partial x}=\frac{\partial B_x}{\partial y}$

$\mathrm{div}\vec{B} = 0 \rightarrow \Delta\Phi(x,y) = 0 \rightarrow$ Multipole solution

Multipole n-th order → 2(n+1)Pole:

$\Phi_n = -\frac{B_0 r^{n+1}}{(n+1)a^n}(\sin(n+1)\theta)$, B_0 : Field at pole center, a: radial distance from pole center

Special case: Quadrupole n=1 , $x = r\cos\theta$, $y = r\sin\theta$

$\Phi_1 = -\frac{B_0}{a}xy$, $B_x = gy$, $B_y = gx$ $(g = B_0/a)$

A quadrupole creates a field, which is proportional to the lateral deviation of the trajectory and acts as a spring, (for y=0, Lorentz force $F_x \propto B_y = gx$) :

It is focusing in one direction (e.g. x) and defocusing in the other (y). For a total focusing effect one uses so called quadrupole doublets (or triplets).

B-Field:

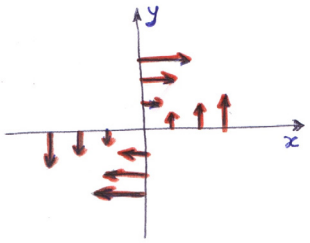

A dipole corresponds to the n=0 term.

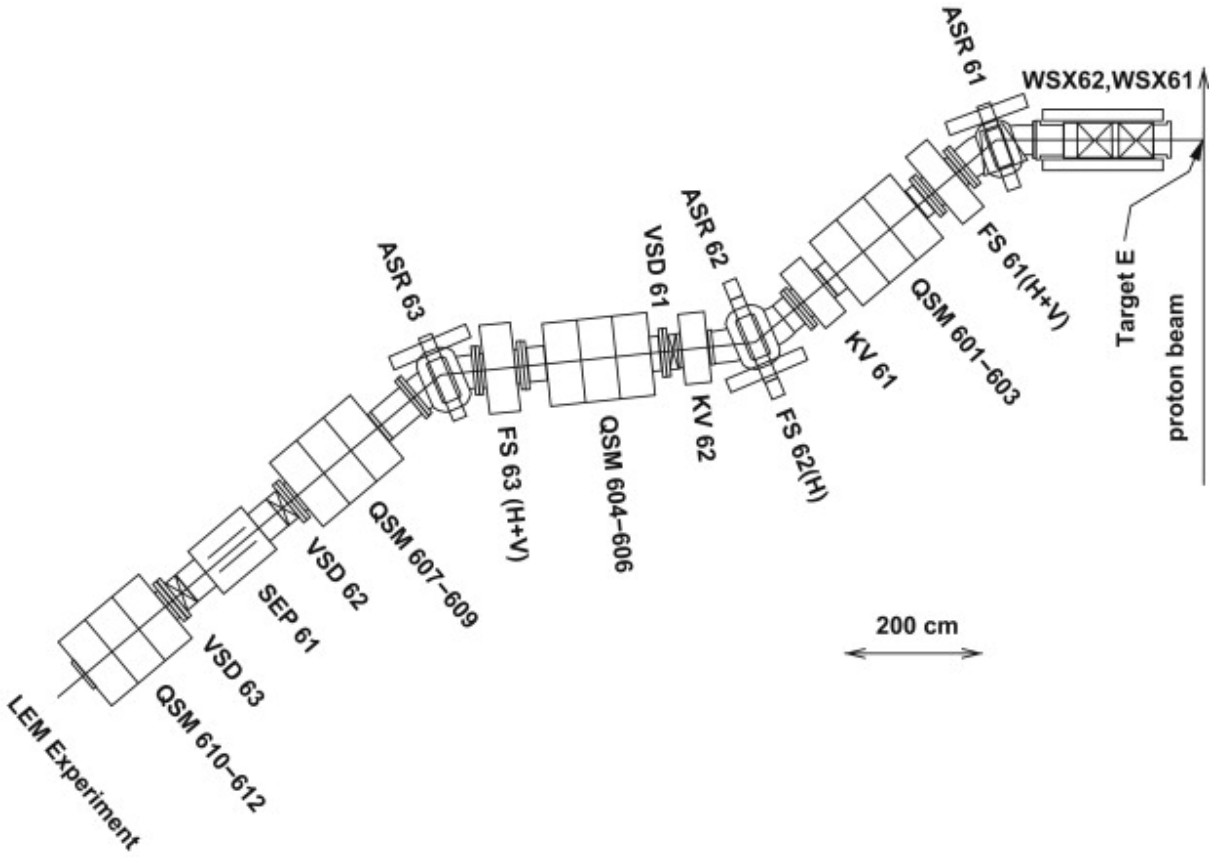

Fig. 1-12: Muon beam μE4 for the Low Energy Muon setup at PSI consisting of a solenoid, magnetic quadrupoles, dipoles, a **E** x **B** filter (separator) and various slits.

2. Particle physics aspects

2.1 Theory of the muon decay

$\mu^+ \rightarrow e^+ + \nu_e + \overline{\nu}_\mu$

$\mu^- \rightarrow e^- + \overline{\nu}_e + \nu_\mu$

The decay reflects the separate conservation of muon and electron lepton number (additive rule).

	L_μ	L_e	L_τ
μ^-, ν_μ	+1	0	0
$\mu^+, \overline{\nu}_\mu$	-1	0	0
e^-, ν_e	0	+1	0
$e^+, \overline{\nu}_e$	0	-1	0
τ^-, ν_τ	0	0	+1
$\tau^+, \overline{\nu}_\tau$	0	0	-1

Evidence for separate conservation of lepton number:

$\mu^+ \rightarrow e^+ + \gamma$ Branching Ratio $< 5.7\ 10^{-13}$
last PSI result, Phys. Rev. Lett. 110, 201801 (2013)
(data set with $3.6\ 10^{14}$ stopped muons)

$\mu^- \rightarrow e^- + e^+ + e^-$ Branching Ratio $< 1.0\ 10^{-12}$

The additive conservation of lepton numbers forbids for instance the process

$\mu^+ + e^- \rightarrow \mu^- + e^+$

A multiplicative conservation rule would allow it.

Recent observations of neutrino oscillations (Super-Kamiokande, Japan: disappearance of muon neutrino and Sudbury Neutrino Observatory, Canada: conversion of electron neutrino in muon and tau neutrino, Nobel Prize 2015) indicate that lepton family conservation is only approximate.

Some useful relations of relativistic quantum mechanics

Four-momentum: $p^{\mu} = \begin{pmatrix} E/c \\ \vec{p} \end{pmatrix} \qquad \mu = 0,1,2,3$

Metrics: $g^{\mu\nu} = g_{\mu\nu} = \begin{pmatrix} 1 & 0 & 0 & 0 \\ 0 & -1 & 0 & 0 \\ 0 & 0 & -1 & 0 \\ 0 & 0 & 0 & -1 \end{pmatrix}$

Covariant vector $p_{\mu} = g_{\mu\nu} p^{\nu}$, (p^{ν} contravariant vector. Sum is over pair of upper and lower indices).

Four-vector product: $p_{\mu} p^{\mu} = \frac{E^2}{c^2} - p^2 = m_0^2 c^2$ (Energy-momentum relation)

(in analogy with $x^{\mu} = \begin{pmatrix} ct \\ \vec{x} \end{pmatrix}$ and $x_{\mu} = \begin{pmatrix} ct \\ -\vec{x} \end{pmatrix}$ $\mu = 0,1,2,3$ $x_{\mu} x^{\mu} = (c^2 t^2 - x^2)$).

Often in particle physics one sets $c = \hbar = 1$ (natural units).

The four-vector operator is given by:

$$p^{\mu} \rightarrow i \frac{\partial}{\partial x_{\mu}} = \begin{pmatrix} i \frac{\partial}{\partial t} \\ -i\vec{\nabla} \end{pmatrix} \qquad \mu = 0,1,2,3 \qquad [2\text{-}1]$$

$$p_{\mu} \rightarrow i \frac{\partial}{\partial x^{\mu}} = \begin{pmatrix} i \frac{\partial}{\partial t} \\ i\vec{\nabla} \end{pmatrix} \qquad \mu = 0,1,2,3$$

The Dirac equation for a spin ½ particle with mass m without external field corresponds formally to the relativistic energy – momentum relation for the operators:

$$i\gamma^{\mu} \frac{\partial \Psi}{\partial x^{\mu}} - m\Psi = 0 \qquad (\text{or } i\gamma^{\mu} \partial_{\mu} \Psi - m\Psi = 0 \ ) \qquad [2\text{-}2]$$

$$\Psi(\vec{x},t)=\begin{pmatrix}\Psi_0(\vec{x},t)\\ \Psi_1(\vec{x},t)\\ \Psi_2(\vec{x},t)\\ \Psi_3(\vec{x},t)\end{pmatrix} \qquad 4\text{ - component spinor,} \qquad [2\text{-}3]\ ^{2}$$

the corresponding conjugated spinor

$$\overline{\Psi}(\vec{x},t)=\Psi^{+}(\vec{x},t)\gamma_0 \qquad \Psi^{+}(\vec{x},t)=\left(\Psi_0^{*},\Psi_1^{*},\Psi_2^{*},\Psi_3^{*}\right)$$

fulfills equation

$$i\gamma^{\mu}\frac{\partial\overline{\Psi}}{\partial x^{\mu}}+m\overline{\Psi}=0$$

γ_μ , $\mu=0,1,2,3$ are 4 x 4 γ-Matrices

<u>γ–Matrices and their characteristics</u>

The γ–Matrices can be written in term of 2 x 2 Pauli matrices $\vec{\sigma}=(\sigma_x,\sigma_y,\sigma_z)$:

$$\sigma_x=\begin{pmatrix}0 & 1\\ 1 & 0\end{pmatrix} \qquad \sigma_y=\begin{pmatrix}0 & -i\\ i & 0\end{pmatrix} \qquad \sigma_z=\begin{pmatrix}1 & 0\\ 0 & -1\end{pmatrix} \qquad [2\text{-}4]$$

$$\gamma_0=\begin{pmatrix}I & 0\\ 0 & -I\end{pmatrix} \qquad \vec{\gamma}=\begin{pmatrix}0 & \vec{\sigma}\\ -\vec{\sigma} & 0\end{pmatrix} \qquad [2\text{-}5]$$

$$\gamma_5\equiv i\gamma_0\gamma_1\gamma_2\gamma_3=\begin{pmatrix}0 & I\\ I & 0\end{pmatrix} \qquad \text{where} \quad I=\begin{pmatrix}1 & 0\\ 0 & 1\end{pmatrix} \quad \text{and } 0=\begin{pmatrix}0 & 0\\ 0 & 0\end{pmatrix}$$

γ_0 is hermitian $(\gamma_0)^{+}=\gamma_0$ and γ_μ are anti-hermitian $(\gamma_\mu)^{+}=\gamma_0\gamma_\mu\gamma_0$

Commutation relations:

$$\gamma_\mu\gamma_\nu+\gamma_\nu\gamma_\mu=2g_{\mu\nu}I_{4x4} \qquad \mu=0,1,2,3$$
$$\gamma_\mu\gamma_5+\gamma_5\gamma_\mu=0 \qquad [2\text{-}6]$$

---

[2] $(K^{+})_{ij}=(K_{ji})^{*}$

Following relations are valid for the traces of products of γ-matrices :

$$\mathrm{Sp}(\gamma_\mu\gamma_\nu) = 4\delta_{\mu\nu}$$
$$\mathrm{Sp}(\gamma_\mu\gamma_\nu\gamma_\rho\gamma_\sigma) = \delta_{\mu\nu}\delta_{\rho\sigma} + \delta_{\nu\rho}\delta_{\mu\sigma} - \delta_{\mu\sigma}\delta_{\nu\sigma} \qquad [2\text{-}7]$$

Solutions of Dirac equation

For a particle at rest ($\vec{p} = 0$)

$$\Psi = e^{-iEt}u \qquad u = \begin{pmatrix} u_o \\ u_1 \\ u_2 \\ u_3 \end{pmatrix} \qquad [2\text{-}8]$$

If we insert Ψ in the Dirac equation, we get four solutions:
2 with positive energies E=+m and 2 with negative energies E= -m.
Particles with negative energy and spin –s correspond to anti-particles with positive energies and spin +s. The corresponding spinors are

$$\Psi^{\updownarrow\pm} = e^{\pm iEt}u^{\updownarrow\pm} \qquad u^{\uparrow+} = \begin{pmatrix} 1 \\ 0 \\ 0 \\ 0 \end{pmatrix} \qquad u^{\downarrow+} = \begin{pmatrix} 0 \\ 1 \\ 0 \\ 0 \end{pmatrix} \qquad u^{\downarrow-} = \begin{pmatrix} 0 \\ 0 \\ 1 \\ 0 \end{pmatrix} \qquad u^{\uparrow-} = \begin{pmatrix} 0 \\ 0 \\ 0 \\ 1 \end{pmatrix}$$

For moving particles we obtain the solutions from a Lorentz transformation (here c=1):

$$u_{\vec{p}\uparrow} = \sqrt{\frac{E+m}{2m}} \begin{pmatrix} 1 \\ 0 \\ \dfrac{p_z}{E+m} \\ \dfrac{p_x + ip_y}{E+m} \end{pmatrix} \qquad u_{\vec{p}\downarrow} = \sqrt{\frac{E+m}{2m}} \begin{pmatrix} 0 \\ 1 \\ \dfrac{p_x - ip_y}{E+m} \\ \dfrac{-p_z}{E+m} \end{pmatrix} \qquad \text{Particle}$$

$$v_{\vec{p}\downarrow} = \sqrt{\frac{E+m}{2m}} \begin{pmatrix} \dfrac{p_z}{E+m} \\ \dfrac{p_x + ip_y}{E+m} \\ 1 \\ 0 \end{pmatrix} \qquad v_{\vec{p}\uparrow} = \sqrt{\frac{E+m}{2m}} \begin{pmatrix} \dfrac{p_x - ip_y}{E+m} \\ \dfrac{-p_z}{E+m} \\ 0 \\ 1 \end{pmatrix} \qquad \text{Antiparticle} \qquad [2\text{-}9]$$

A fermion (e.g. e^-, μ^-) with momentum $\vec{p}$, energy $E = \sqrt{p^2 + m^2}$ and spin up (in particle rest frame) is represented by a plane wave:

$$\Psi(\vec{x},t) = \frac{1}{\sqrt{V}} u_{\vec{p}\uparrow} e^{i\vec{p}\vec{x}} e^{-iEt} \qquad [2\text{-}10]$$

u four-vector spinor from [2-9], fulfilling equation:

$$(p_\mu \gamma^\mu - m)u = 0$$

(for $\bar{u}$ $\qquad \bar{u}(p_\mu \gamma^\mu - m) = 0$)

The wave function for a spin-up anti-fermion (e^+, μ^+) is then

$$\Psi(\vec{x},t) = \frac{1}{\sqrt{V}} v_{\vec{p}\uparrow} e^{-i\vec{p}\vec{x}} e^{+iEt} \qquad [2\text{-}11]$$

Field operators for fermions and anti-fermions

To describe the decay we quantize the fields. Classical fields and particle wave functions → field operators.

From [2-10] and [2-11] we build Dirac field operators (momentum basis)

$$\Psi(\vec{x},t) = \frac{1}{\sqrt{V}} \sum_{p,s} \sqrt{\frac{m}{E}} \left[b(p,s)u(p,s)e^{-ip_\mu x^\mu} + d^+(p,s)v(p,s)e^{+ip_\mu x^\mu} \right]$$

b and d are annihiliation operators for fermions and antifermions [2-12]

b^+ and d^+ corresponding creation operators

u(p,s) and v(p,s) are spinors as given in Eq. [2-9].
p Momentum four-vector
s Spin

$\bar{\Psi}$ is expressed in a similar way.

Lagrange density of the weak interaction

We need a Lagrange density, which describes the weak interaction.

In general, use principle of smallest action:

$$S = \int d^4x\, L(\phi, \partial_\mu \phi)$$

Lagrange density L:
-Polynomial in φ and $\partial_\mu \varphi(x)$
-Lorentz invariance ←→ L is a scalar field
-Locality ←→ L only function of x (fourfold time-space vector)

From S extremal, Euler equation follows:

$$\delta S = 0 \rightarrow \frac{\partial L}{\partial \phi} - \partial_\mu \frac{\partial L}{\partial_\mu \phi} = 0 \qquad [2\text{-}13]$$

For instance in classical field theory the Lagrange density for electromagnetic fields and currents is:

$$L(A_\mu, \partial_\mu A) = L_{\text{fields}} + L_{\text{interaction}}$$

with

$$L_{\text{interaction}} = -j_\mu A^\mu$$

$$j^\mu = \begin{pmatrix} \rho c \\ \vec{j} \end{pmatrix} \text{ 4-current} \qquad A^\mu = \begin{pmatrix} \phi / c \\ \vec{A} \end{pmatrix} \text{ 4-vector potential}$$

Field quantization leads to the Lagrange density of quantum electrodynamics:

$$L_{QED} = -j_\mu A^\mu \qquad [2\text{-}14]$$

Where here

$j_\mu = e\overline{\Psi}\gamma_\mu\psi$ (electro-magnetic current density associated to field ψ).

In analogy, apply Fermi ansatz to describe β–decay ($n \rightarrow p + e^- + \overline{\nu}_e$) to μ^--decay ($\mu^- \rightarrow e^- + \overline{\nu}_e + \nu_\mu$):

$$L_W = -\frac{G_F}{\sqrt{2}} \underbrace{(\overline{\Psi}_\mu \gamma_\alpha \psi_{\nu_\mu})}_{\text{Polar Vector V}} \underbrace{(\overline{\Psi}_e \gamma^\alpha \psi_{\nu_e})}_{\text{Polar Vector V}} \qquad [2\text{-}15]$$

[2-15] is invariant under Lorentz transformation (and also parity transformation).

The Fermi ansatz describes well the transition probability in the β-decay (to first order).
In principle L could contain other terms e.g.:

$$\underbrace{(\overline{\Psi}_{\mu}\gamma_{\alpha}\gamma_5\psi_{\nu_{\mu}})}_{\text{Axial Vector A}}\underbrace{(\overline{\Psi}_{e}\gamma^{\alpha}\gamma_5\psi_{\nu_{e}})}_{\text{Axial Vector A}}$$

This term conserves also parity. We know that parity is not conserved by weak interaction.
Solution: L must contain not only products of the form V·V or A.A but also mixed terms V·A
→ V-A interaction (Feynman, Gell-Mann)

$$L_W = \frac{G_F}{\sqrt{2}}(j_\lambda j^{\lambda+} + j_\lambda{}^{+} j^{\lambda}) + \text{other terms} \quad \text{for } \tau-\text{decay}$$

$$\uparrow \qquad \uparrow \qquad [2\text{-}16]$$

$$\mu^- \qquad \mu^+ \quad \text{-decay}$$

$$j_\lambda = \overline{\Psi}_{\mu}\gamma_\lambda(1-\gamma_5)\psi_{\nu_{\mu}} + \overline{\Psi}_{e}\gamma_\lambda(1-\gamma_5)\psi_{\nu_{e}}$$

$$j_\lambda{}^{+} = \overline{\Psi}_{\nu_{e}}\gamma_\lambda(1-\gamma_5)\psi_{e} + \overline{\Psi}_{\nu_{\mu}}\gamma_\lambda(1-\gamma_5)\psi_{\mu}$$

For the μ^-–decay it is:

$$L_W = \frac{G_F}{\sqrt{2}}\left[\overline{\Psi}_{\mu}\gamma_\lambda(1-\gamma_5)\psi_{\nu_{\mu}}\overline{\Psi}_{e}\gamma^{\lambda}(1-\gamma_5)\psi_{\nu_{e}}\right] \qquad [2\text{-}17]$$

Which can also be written as follow

$$L_W = \frac{G_F}{\sqrt{2}}\left[\overline{\Psi}_{e}\gamma_\lambda(1-\gamma_5)\psi_{\mu}\overline{\Psi}_{\nu_{\mu}}\gamma^{\lambda}(1-\gamma_5)\psi_{\nu_{e}}\right]$$

$$\uparrow \qquad \uparrow \qquad [2\text{-}18]$$

creation e^- annihilation μ^-

annihilation e^+ creation μ^+

Equation [2-16] describes the coupling of weak currents $j_\lambda, j_\lambda{}^{+}$ at a time-space point (contact coupling) and can be represented by following graph:

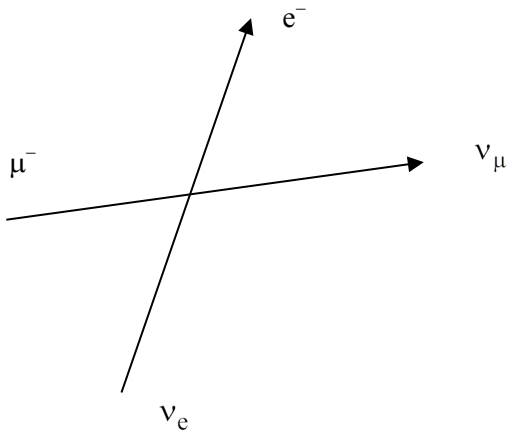

The contact interaction leads to singularities in the calculation of second order corrections. More precisely the weak interaction can be described by the exchange of a heavy boson (W^+, W^- , Z). The corresponding graph is then:

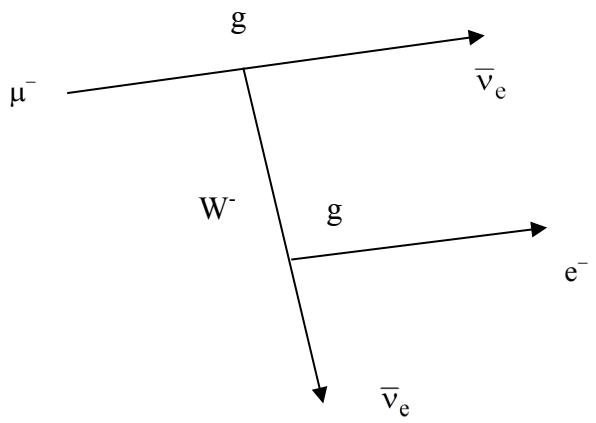

Coupling

$$\frac{g^2}{8m_W{}^2} = \frac{G_F}{\sqrt{2}}$$

g: „weak coupling constant“

However, also here there are problems with singularities: the „naive“ intermediate-boson theory cannot be normalized.

Note about parity operation

How do polar V_α and axial vectors A_α transform under parity operation P ?:

$$\vec{x} \to -\vec{x} \qquad t \to t \qquad x \equiv \begin{pmatrix} t \\ \vec{x} \end{pmatrix} \to \tilde{x} \equiv \begin{pmatrix} t \\ -\vec{x} \end{pmatrix}$$

Transformation for spinors:

$$u(\tilde{x}) = \gamma_0 u(x)$$
$$u \to \gamma_0 u$$
$$\bar{u} \to \bar{u}\gamma_0$$

$$V_\alpha = \bar{u}_1 \gamma_\alpha u_2 \to \bar{u}_1 \gamma_0 \gamma_\alpha \gamma_0 u_2 = \begin{pmatrix} V_\alpha & \text{for } \alpha = 0 \\ -V_\alpha & \text{for } \alpha = 1,2,3 \end{pmatrix}$$

behaves as a polar vector

$$A_\alpha = \bar{u}_1 \gamma_5 \gamma_\alpha u_2 \to \bar{u}_1 \gamma_0 \gamma_5 \gamma_\alpha \gamma_0 u_2 = \begin{pmatrix} -A_\alpha & \text{for } \alpha = 0 \\ A_\alpha & \text{for } \alpha = 1,2,3 \end{pmatrix}$$

behaves as an axial vector

$$L_W \propto j_\lambda j^{\lambda+} \propto V_\alpha V^{\alpha+} + A_\alpha A^{\alpha+} \quad \text{parity invariant}$$
$$+ \; V_\alpha A^{\alpha+} + A_\alpha V^{\alpha+} \quad \text{parity violating}$$

For example the Lagrange density ([2-17] and [2-18]) is not invariant under parity violation.

Calculation of the muon decay rate ($\mu^- \rightarrow e^- + \bar{\nu}_e + \nu_\mu$)

The differential decay probability dΓ (decay probability per time) follows from the the Fermi „golden rule" (first order perturbation theory).

„Golden rule“ non relativistic:

$$W_{i\rightarrow f} = \frac{2\pi}{\hbar} |< f | V | i >|^2 \rho_f \delta(E_f - E_i)$$

↑ ↑

Dynamics phase space

In analogy, relativistically:

$$d\Gamma = (2\pi)^4 \frac{|M|^2}{2E_\mu} \frac{d\vec{k}}{(2\pi)^3 2E_e} \frac{d\vec{q}_1}{(2\pi)^3 2w_1} \frac{d\vec{q}_2}{(2\pi)^3 2w_2} \delta^4(k + q_1 + q_2 - p) \qquad [2\text{-}19]$$

k = Electron four-momentum ($E_e, \vec{k}$)

q_1 = Electron antineutrino four-momentum ($\bar{\nu}_e$) ($w_1, \vec{q}_1$)

q_2 = Muon neutrino four-momentum (ν_μ) ($w_2, \vec{q}_2$)

p = Muon four-momentum ($E_\mu, \vec{p}$)

$|M|$: Matrix element calculated from L_w (Eq. [2-18]).

For the explicit calculation we need the field operators, commutation relation of γ matrices, trace calculations etc.

Neutrinos are not measured in the muon decay measurement. Therefore, we can integrate over dq_1 and dq_2.

Moreover, we sum over all possible neutrinos spin directions. Also if the electron polarization is not observed and its mass is neglected, one finds for the differential decay probability dΓ

$$d\Gamma = W(x, \cos\theta) dx d(\cos\theta) =$$
$$= \frac{G_F{}^2 m_\mu{}^5}{192\pi^3} \left[(3 - 2x) - (2x - 1)\cos\theta\right] x^2 dx d(\cos\theta) \qquad [2\text{-}20]$$

(see [1-3]).

Here $x = \frac{2E_e}{m_\mu}$ and θ angle between muon spin and direction of electron emission.

For the μ^+– decay the angular dependent part has a positive sign.

$$d\Gamma = W(x, \cos\theta) dx d(\cos\theta) =$$
$$= \frac{G_F{}^2 m_\mu{}^5}{192\pi^3} \left[(3 - 2x) + (2x - 1)\cos\theta\right] x^2 dx d(\cos\theta) \qquad [2\text{-}21]$$

Equation [2-21] gives the differential emission probability as a function of energy of the emitted positrons and of the emission angle with respect to the muon spin direction.
If we have a muon ensemble, which is less than 100% polarized ($P \leq 1$), the distribution becomes:

$$d\Gamma = \frac{G_F{}^2 m_\mu{}^5}{192\pi^3}(3-2x)\left[1+\frac{(2x-1)}{(3-2x)}P\cos\theta\right]x^2 dx d(\cos\theta)$$
$$a(x) = P\frac{(2x-1)}{(3-2x)} \quad , \text{ asymmetry parameter} \qquad [2\text{-}22]$$

This equation is the basis for the use of polarized muons in the Muon Spin Rotation/Relaxation method (μSR).

Total muon decay rate

$$\Gamma = \int_{-1}^{1}\int_{0}^{1} d(\cos\theta)dx W(x,\cos\theta) = \frac{G_F{}^2 m_\mu{}^5}{192\pi^3} = \frac{1}{\tau_\mu}$$

τ_μ : muon lifetime

With corrections (electro-weak interaction)

$$\frac{1}{\tau_\mu} = \frac{G_F{}^2 m_\mu{}^5}{192\pi^3}\left[1-\frac{8m_e{}^2}{m_\mu{}^2}\right]\left[1+\frac{3m_e{}^2}{5m_W{}^2}-\frac{\alpha}{2\pi}(\pi^2-\frac{25}{4})\right] \qquad [2\text{-}23]$$

Energy spectrum of the decay positron (or electron)

After integration of [2-22] over $\cos\theta$ we obtain:

$$W(x)dx = \int_{-1}^{1} d\cos\theta\ W(x,\cos\theta) = \frac{G_F{}^2 m_\mu{}^5}{192\pi^3}2(3-2x)x^2 dx \qquad [2\text{-}24]$$

(Michel spectrum, see Eq. [1-2]).

2.2 Measurement of the muon lifetime (μ^+)

Various experiments have been performed in the last 30 years (see Review of Particle Physics, K.A. Olive *et al.* (Particle Data Group), Chin. Phys. C, **38**, 090001 (2014) and http://pdg.lbl.gov/)
Experiments are based on the observation of the decay of an ensemble of N_0 muons, which are prepared at time t = 0.

$$N(t) = N_0 e^{-\frac{t}{\tau_\mu}} \qquad [2\text{-}25]$$

The number of positrons $N_e(t)$, which are emitted at time t is given by the number of muons decaying in the interval dt at time t:

$$N_e(t) = -\frac{dN}{dt} = \frac{1}{\tau_\mu} N(t) = \frac{1}{\tau_\mu} N_0 e^{-\frac{t}{\tau_\mu}} \qquad [2\text{-}26]$$

In the experiment one measures the decrease of positron rate as a function of time. To do this it is necessary to measure the lifetime of each individual muon. Various effects can modify Eq. [2-26]:

- Time dependent background B(t):

$$N_e(t) = \frac{1}{\tau_\mu} N(t) + B(t) \qquad [2\text{-}27]$$

- Time dependent polarization $\vec{P}(t)$ of the muon (see Eq. [2-22])

$$N_e(t) = N(t)d\Gamma + B(t) = \left\{ \frac{N(t)}{\tau_\mu} \left[(3-2x) + (1-2x) P(t) \cos\theta(t) \right] x^2 dx + B(t) \right\} \frac{d\Omega}{2\pi} \qquad [2\text{-}28]$$

We have a time dependence of θ, if the muon spin polarization $\vec{P}(t)$ shows Larmor precession, which is the case in the presence of a magnetic field (e.g. earth magnetic field). Depolarization processes (see Chapt. 5. Principles of Muon Spin Rotation/Relaxation/Resonance) lead also to a time dependence of $\left|\vec{P}(t)\right|$. In the lifetime experiment one tries therefore to use unpolarized muons and to shield the earth magnetic field and other stray fields as much as possible. Moreover, it helps to have the largest possible solid angle for the positron detection (since $\int_{-1}^{1} d(\cos\theta)\cos\theta = 0$). Finally muons should be stopped in a material, which either depolarizes them very quickly or not at all.

The mean value of τ_μ obtained from various different measurements (2014) is:

$\tau_\mu = 2.1969811(22)\ \mu s$ $\qquad\qquad$ $\frac{\Delta\tau_\mu}{\tau_\mu} = 1\ \text{ppm}$

(From K.A. Olive *et al.* (Particle Data Group), Chin. Phys. C **38**, 090001 (2014)).

A recent experiment at PSI (Phys. Rev. D **87**, 052003 (2013) is the most precise and measured τ_μ with an accuracy of 1 ppm.

$\tau_\mu = 2.\ 196\ 9803(21)(07)\ \mu s$

From this value the Fermi constant (an important parameter of the Standard model) can be derived; uncertainty in G_F is completely determined by the uncertainty in τ_μ.

$$\frac{G_F}{(\hbar c)^3} = 1.1663787(6) \cdot 10^{-5}\ \text{GeV}^{-2} (0.5\ \text{ppm}).$$

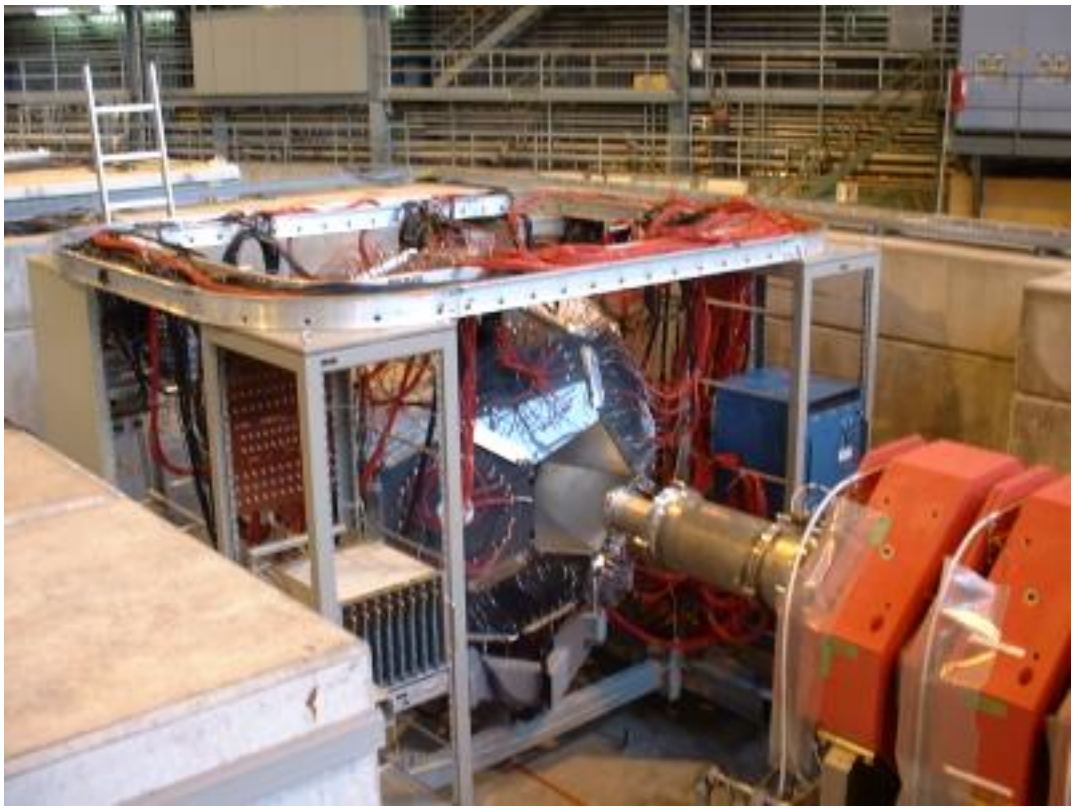

Fig. 2-1: Apparatus to measure the muon life time at PSI.

2.3 Measurement of the muon magnetic anomaly: g – 2

The muon magnetic moment with g=2 follows from the Dirac equation

$$\vec{\mu}_\mu = g\frac{e\hbar}{2m_\mu}\vec{s} = \gamma_\mu \hbar \vec{s} \qquad \gamma_\mu: \text{ gyromagnetic ratio} \qquad [2\text{-}29]$$

e: charge (with sign)

$$\mu_\mu = g\frac{e\hbar}{2m_\mu}\frac{1}{2} \cong \frac{m_e}{m_\mu}|\mu_B| \qquad (\mu_B = \frac{e\hbar}{2m_e}, \text{ Bohr magneton}) \qquad [2\text{-}30]$$

Quantum electrodynamics effects, as well as corrections based on weak and strong interaction lead to a g-factor, which is a larger than 2. The deviation g-2 is therefore very interesting as a test of the standard model of elementary particles.

g -2 has been measured for the electron as well as for the muon.
The deviation from 2 is expressed as:

$g = 2\ (1 + a)$

$$a = \frac{g-2}{2} \qquad \text{(g-factor anomaly)} \qquad [2\text{-}31]$$

The measurement principle is based on the difference between cyclotron frequency ω_c and Larmor frequency ω_L in a magnetic field B.
Non relativistically:

$$\omega_c = -\frac{e}{m_\mu}B \qquad [2\text{-}32]$$

$$\omega_L = -\gamma_\mu B = -g\frac{e}{m_\mu}\frac{1}{2}B \quad |^3 \qquad [2\text{-}33]$$

The difference of the two frequencies gives:

---

[3] From the moment $\vec{M} = \vec{\mu}\times\vec{B} = \frac{d\vec{L}}{dt}$, with $\vec{\mu} = \gamma_\mu \vec{L}$, $\vec{L}$ angular momentum, we get $\frac{d\vec{\mu}}{dt} = \gamma_\mu(\vec{\mu}\times\vec{B})$

which has solutions of the form ($\vec{n} = \frac{\vec{B}}{|\vec{B}|}$):

$$\vec{\mu}(t) = \vec{a} + \vec{b}\cos(\omega_L t) + \vec{c}\sin(\omega_L t) = (\vec{\mu}(0)\cdot\vec{n})\vec{n} + \vec{n}\times(\vec{\mu}(0)\times\vec{n})\cos(\omega_L t) + (\vec{\mu}(0)\times\vec{n})\sin(\omega_L t)$$

$$\Delta\omega = |\omega_L - \omega_c| = \left|(g-2)\frac{e}{2m_\mu}B\right| = \left|a\frac{e}{m_\mu}B\right| \qquad [2\text{-}34]$$

This formula is also valid relativistically[4].

A g – 2 experiment has been recently performed at Brookhaven National Laboratory (BNL). Previously, three experiments have been completed at CERN.

Magnetic moment of point-like and structured particles

$$\mu = g_s \frac{e\hbar}{2m} s$$

Point-like particle (Electron, Muon): g_e=2.0023193, g_μ=2.0023318
Structured particle (Proton, Neutron): g_p=2 ·2.79, g_n=2 · (-1.91)

The g-factor anomaly is due to virtual particles and fields surrounding the particle.

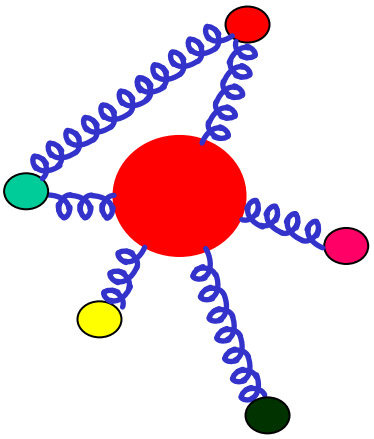

a is therefore sensitive to „new physics“.

a_{Exp} - a_{Theory}= a_{NEW}

$a_{Theorie}$ is determined by QED, weak interaction and hadronic interaction (Standard model)

[4] Relativistically $\omega_c = -\frac{e}{m_\mu \gamma}B$, $\omega_L = -(g\frac{e}{2m_\mu}B + (1-\gamma)\frac{e}{m_\mu\gamma}B)$

Standard Model contributions to g-factor anomaly:
QED + hadronic + weak

Interaction	Field	Particles
QED	photons	$e^+\ e^-\ \mu^+\ \mu^-\ etc$
strong	gluons	$\pi^+\ \pi^-\ \pi^o\ \ quarks\ etc$
weak	$W^+\ W^-\ Z$	$e^+\ e^-\ \mu^+\ \mu^-\ etc$
		$\nu_e\ \bar{\nu}_e\ \nu_\mu\ \bar{\nu}_\mu$

The muon is more sensitive to new physics than the electron since coupling to a virtual particle X $\propto (\frac{m_\ell}{m_X})^2$ l=e, μ. i.e. muon anomaly is 40000 more sensitive than e- anomaly.

QED- contributions to a

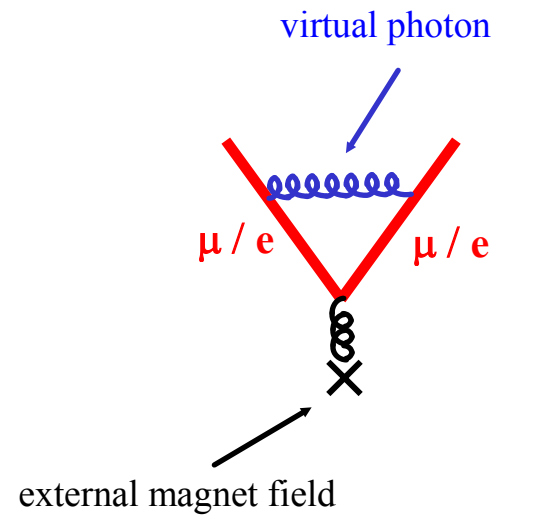

Feynman graph
Lowest order contribution (Schwinger 1947)

$$a = \frac{1}{2\pi}\frac{e^2}{\hbar c} \approx \frac{1}{800}$$

$\alpha \equiv \frac{e^2}{\hbar c}$ Fine structure constant

(S.I: $\alpha \equiv \frac{e^2}{4\pi\varepsilon_0 \hbar c}$)

The QED contribution to the anomaly a is well known and understood. It is the main term and amounts to 99.9930% of the anomaly.

a(QED)= 116 584 718.95(0.08)$\times 10^{-11}$ (error 0.00068 ppm) ($\sim 1.16 \cdot 10^{-3}$)

Some representative graphs: there are hundreds more!

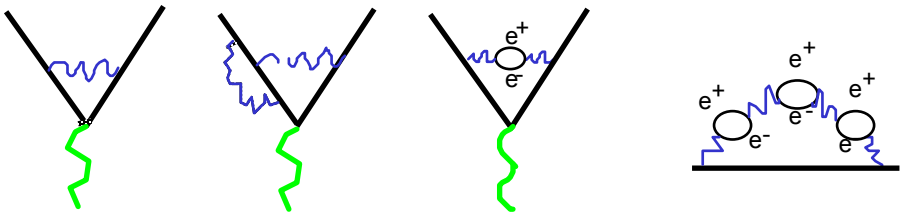

Weak interaction contribution to a

Also well known and understood. Contribution: 1.3 ppm

a(electroweak)= 153.6(1.0) × 10^{-11} (error contribution 0.02 ppm)

Some representative graphs: there are hundreds more!

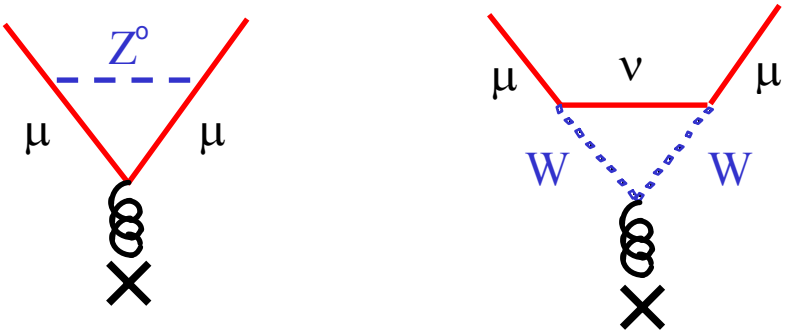

Hadronic contributions to a

Cannot yet be calculated by QCD (Quantum Chromodynamics).

Main term:

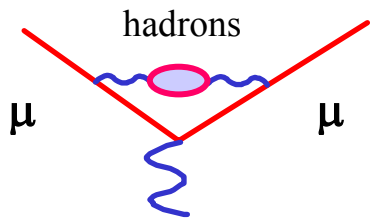

Theory needs:

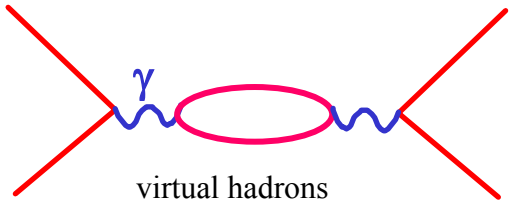

From experiments we can determine:

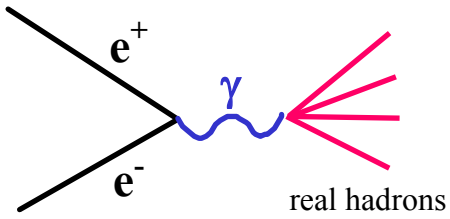

At the moment, the cross section $\sigma(e+e- \rightarrow$ hadrons) gives the "leading order" [LO] contribution

a_{Had} [LO] = 6 923(42)(3) × 10^{-11}

In addition other terms give:

a_{Had} [NLO] = -7(26) × 10^{-11}

(but exact value of hadronic contribution still in discussion).

g-2 experiment at Brookhaven National Laboratory

The main component is a storage ring.

- Muons from forward decay of pions with almost 100 % polarization circulate on a stable trajectory in the storage ring.

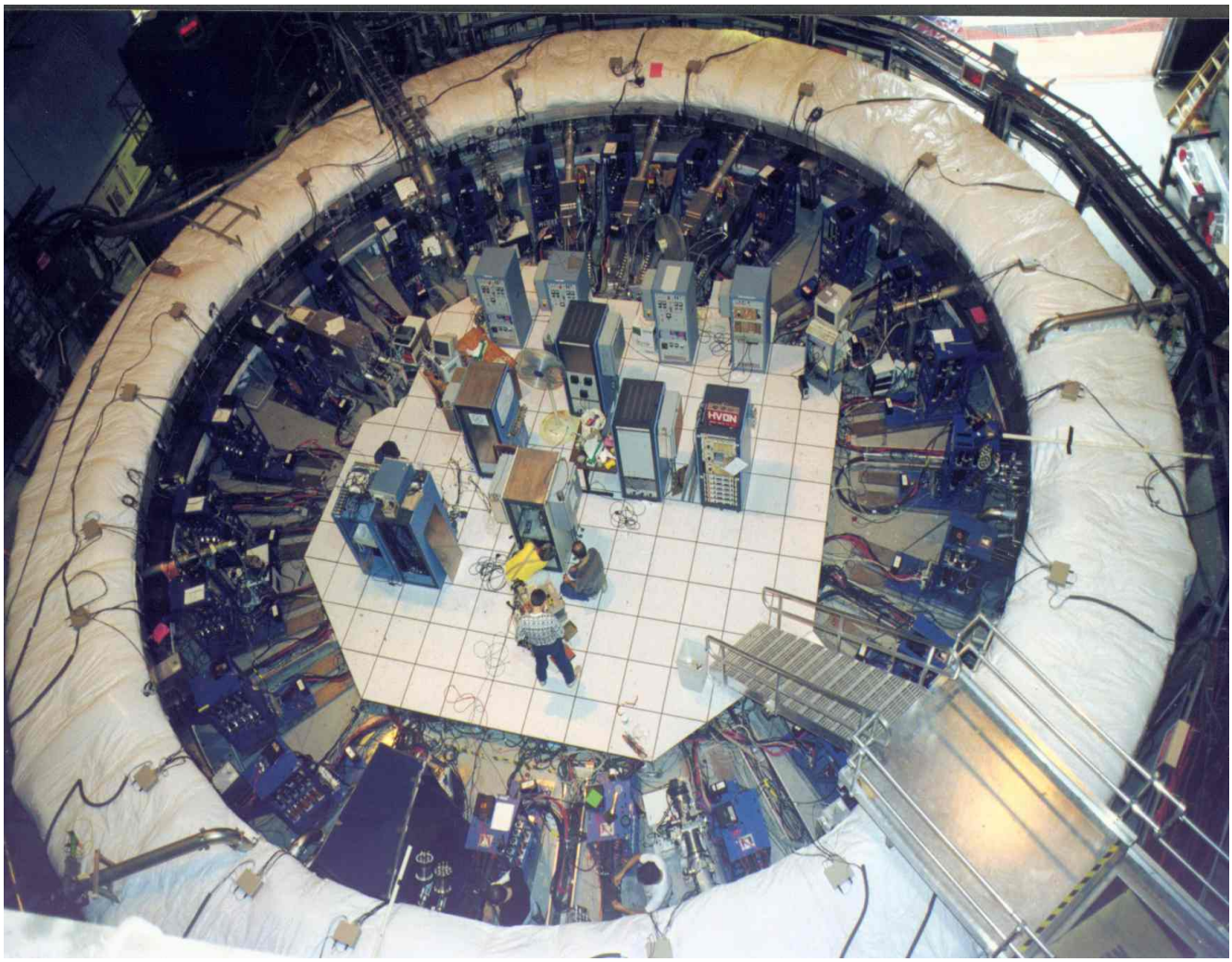

Fig. 2.2: Storage ring / Kicker (Brookhaven, BNL)

Radius :	7112 mm
Aperture :	90 mm
Field :	1.45 T
p_m	3.094 GeV/*c*

- The positrons from muon decay are measured by several detectors placed around the ring

- In the storage ring the muon spin precesses with respect to the momentum with frequency $\propto g-2$

- The parity violating muon decay gives the muon spin direction and allows to measure the precession

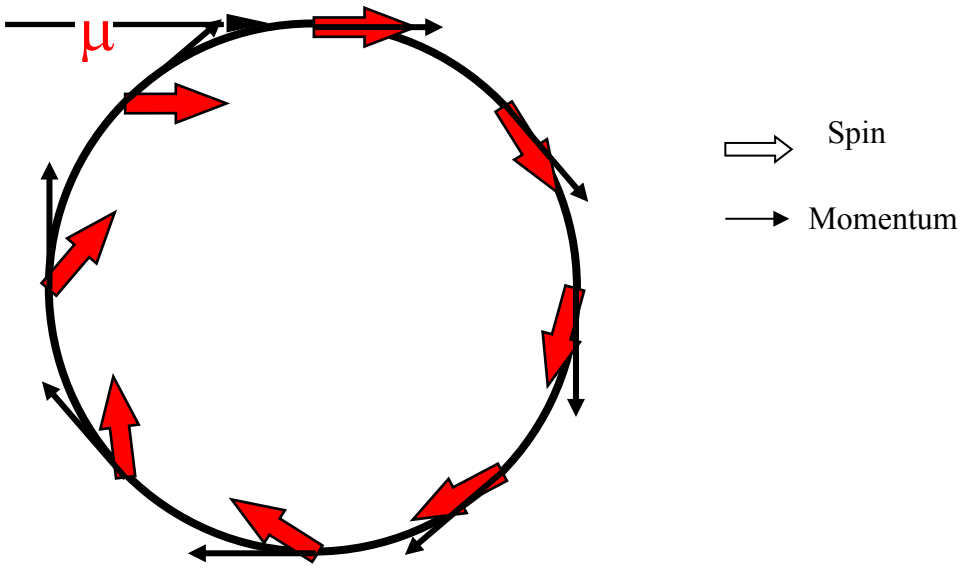

$$\Delta\omega = \left|\omega_L - \omega_c\right| = \left|(g-2)\frac{e}{2m_\mu}B\right| = \left|a\frac{e}{m_\mu}B\right|$$

- The frequency difference is proportional to g-2, independently of γ and of the focusing fields (at the magic momentum p_m).

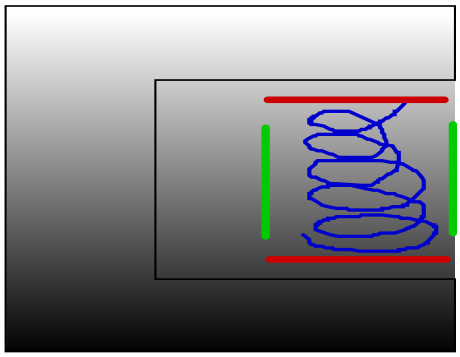

To obtain a vertical focussing of the circulating muons a weak field gradient in horizontal direction is necessary. This fact has a negative influence on the achievable precision. To determine *a* from $\Delta\omega$ it is necessary to know very precisely the field B averaged over the trajectory. Therefore, it is necessary to know the trajectory and the field map very well, which is achievable only to some extent. To avoid this source of error one uses a trick. An homogeneous magnetic field is generated along the trajectory and the vertical focusing is ensured by an electric quadrupole field $\vec{E}$.

Relativistically ($v_\mu \cong 0.99c$) Eq. [2-34] is to be replaced by

$$\Delta\omega = \frac{e}{m_\mu}\left[aB - (a - \frac{1}{\gamma^2 - 1})\vec{\beta} \times \vec{E}\right] \qquad [2\text{-}35]$$

with $\vec{\beta} = \frac{\vec{v}}{c}$ and $\gamma = \frac{1}{\sqrt{1-\beta^2}}$

The muon energy (or velocity) is chosen so that:

$\gamma^2 = 1 + \frac{1}{a^2}$

i.e. $\gamma = 29.30$, $E_\mu = 3.094$ GeV,

this way Eq. [2-35] reduces again to [2-34]. Since $\vec{B}$ is homogeneous (~1 ppm) it is not necessary in this case to know the μ-trajectory very precisely.

- Measurement of the spin direction

In the center of mass system:

$$\frac{dN_e}{dE_e d\Omega} = n(E)(1 + a(E)\cos\theta)$$

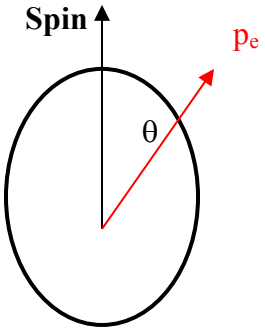

We measure:

$$N_{e^+}(t) = Ne^{-\frac{t}{\gamma\tau}}(1 + A\cos(\Delta\omega t)) \qquad [2\text{-}36]$$

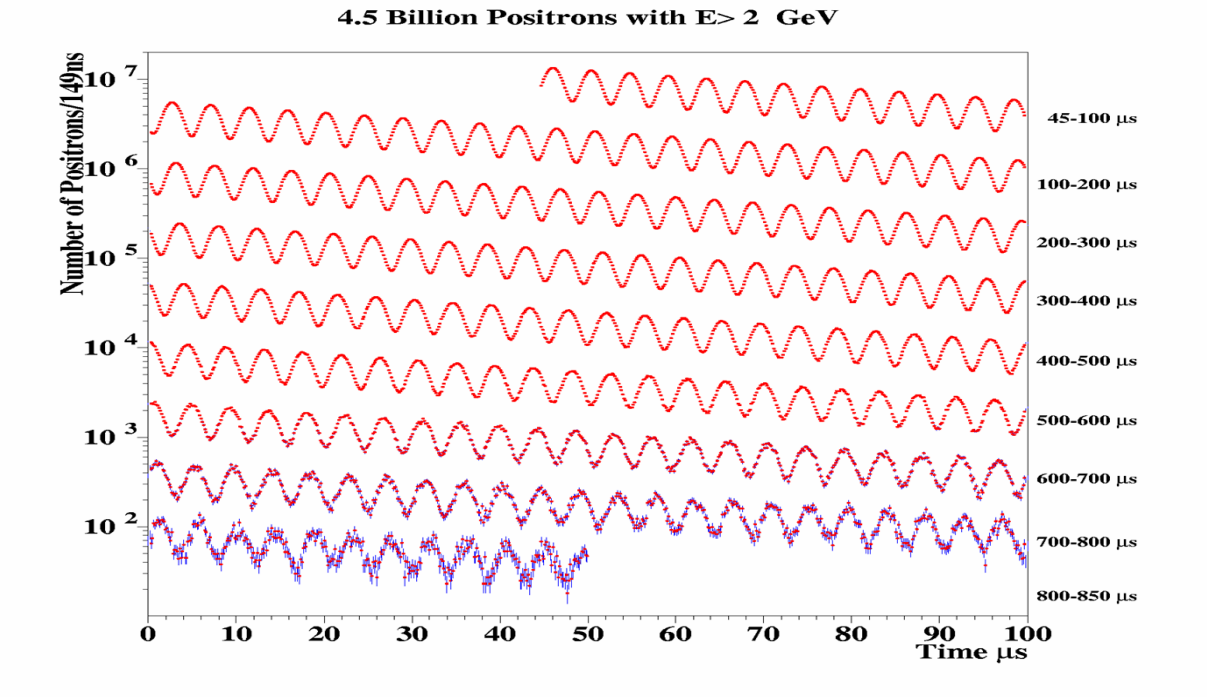

Fig. 2.3: Measured spectrum (see Eq. [2-36]). Note the increased lifetime due to relativistic time dilatation. The measuring interval extends over 14 lifetimes.

from [2-34] we have :

$$a = \frac{\Delta\omega\, m_\mu}{eB} \qquad [2\text{-}37]$$

$\Delta\omega$ is determined by fitting the spectra. The other quantities must be either known or determined with the necessary precision.

The B-field is obtained via proton NMR.

Zeeman splitting of the proton energy levels in B:

$$\Delta E = 2\mu_p B = \hbar\omega_p \qquad [2\text{-}38]$$

ω_p : NMR Resonance frequency (to determine B very precisely).

μ_p : magnetic moment of the proton.

m_μ : is expressed in terms of $\frac{\mu_\mu}{\mu_p}$, since this ratio is very well known.

with

$m_\mu = (a+1)\frac{e\hbar}{2\mu_\mu}$ in [2-37] and with [2-38], Eq. [2-37] becomes

$$a = \frac{\frac{\Delta\omega}{\omega_p}}{\frac{\mu_\mu}{\mu_p} - \frac{\Delta\omega}{\omega_p}} \qquad [2\text{-}39]$$

$\frac{\mu_\mu}{\mu_p}$ is obtained from other measurements (see Chapt. 3. Muonium and muonium spectroscopy):

$\frac{\mu_\mu}{\mu_p}$ = 3.183 345 107(84) (error 0.03 ppm) (newest value, PDG 2014)

The experiment at BNL gives following results for a mean value from μ^+ and μ^- measurement, (assuming CPT conservation):

a_{exp} = 116 592 091(54)(33) 10^{-11} (error 0.5 ppm) [2-40]
(stat.)(system. error)

(G.W. Bennett et al. in Phys. Rev. Lett. **92**, 161802(2004) and
G.W. Bennett et al., Phys. Rev. **D73**, 072003 (2006)).

The theoretical value is at the moment (2014, Particle Data Group)
a_{th} = 116 591 803(1)(42)(26) 10^{-11} (error 0.5 ppm) [2-41]

$a_{exp} - a_{th}$ = 288(63)(49) 10^{-11}

This means a 3.6σ deviation between theory and experiment (errors must be combined in quadrature). Does this point to „new physics“ beyond the Standard Model? To solve this puzzle new experiments are in preparation in USA and Japan with a statistical precision a factor of 5 better.

Another interesting effect, which contributes to the precision of the measurement is the relativistic muon life time dilatation.

$$\tau(3.09\text{GeV}) = \tau_\mu \frac{1}{\sqrt{1-\beta^2}} = \tau_\mu \gamma = 64.5\mu\text{s}$$

This prediction agrees to 99.9% with the measurement.

3 Theory versus experiment

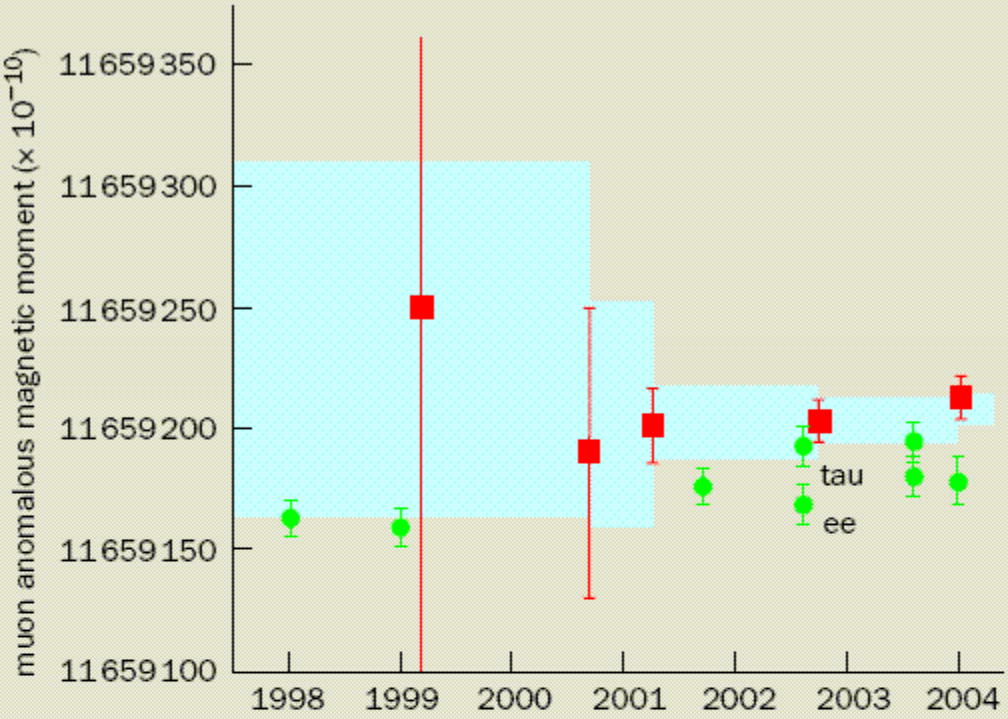

Measurements of the anomalous magnetic moment of the muon at the Brookhaven g – 2 experiment are now more precise than theoretical predictions. Red squares show the experimental values with their error bars, while the blue band represents the uncertainty in the world average experimental value. The centre of this band is therefore the most accurate measured value. The Standard Model prediction for the muon anomaly (green circles) has followed a somewhat bumpier path. Since the combined electron–positron (ee) collision and tau-decay results in 1998, various corrections to the theory have been made. In particular, the sign of the hadronic light-by-light contribution to the muon anomaly flipped in 2001, bringing the theory closer to experiment. The latest theory point is a recently suggested value in which the tau-decay results are not included (see text). Dates refer to the year in which the data or theory results were published. Earlier measurements of the muon anomaly from the CERN I, II and III experiments are not shown because their uncertainties are so large that the results no longer affect the world average.

From D. Hertzog, Physics World, March 2004.

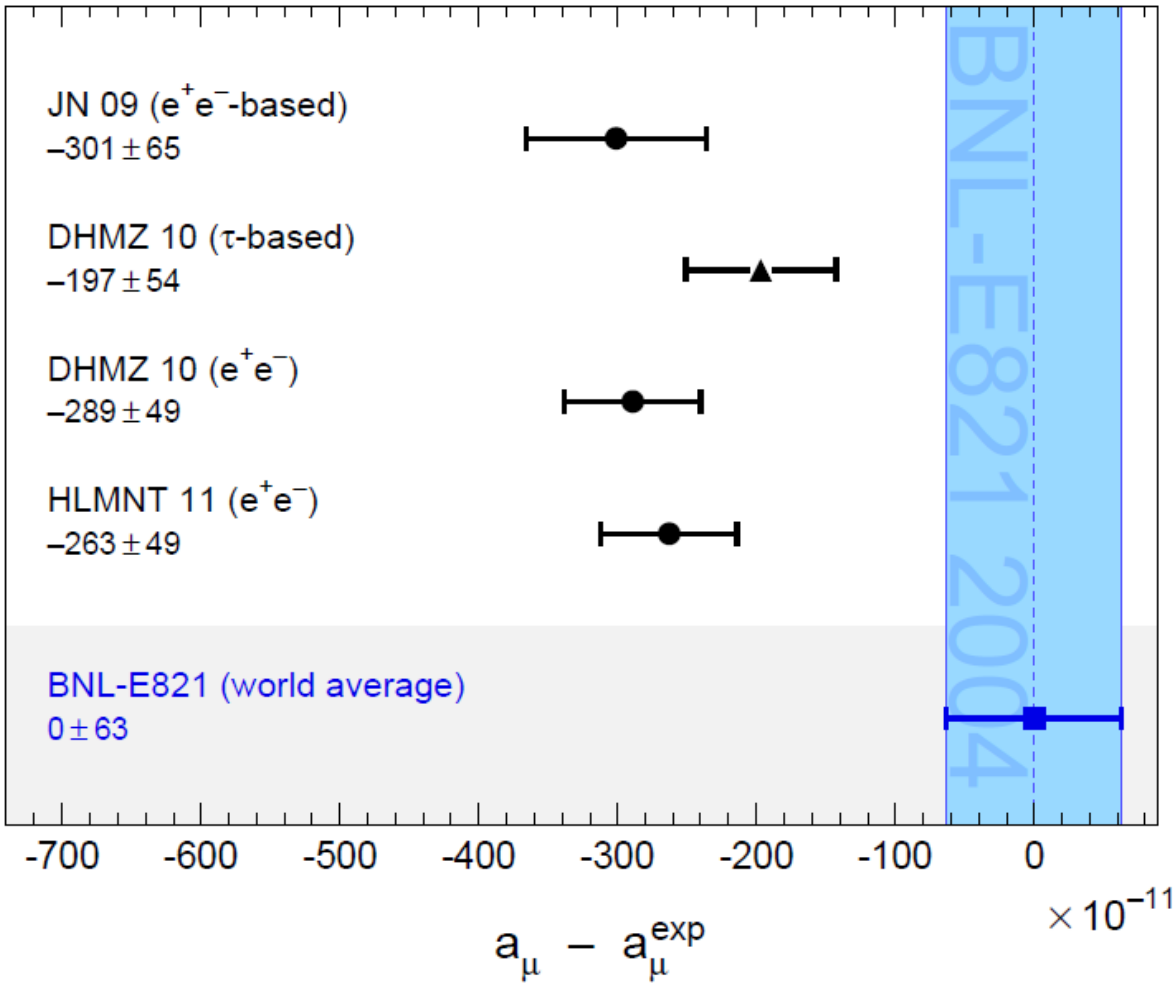

Fig. 2.4: Compilation of recent results for the theoretical value a_μ , subtracted by the central value of the experimental average. The shaded vertical band indicates the experimental error. (From K.A. Olive *et al.* (Particle Data Group), Chin. Phys. C **38**, 090001 (2014)). Note that the quoted errors in the figure do not include the uncertainty on the subtracted experimental value. To obtain for each theory calculation a result equivalent to Eq. [2-41], the errors from theory and experiment must be added in quadrature.

3. Muonium and muonium spectroscopy

3.1 Properties of muonium

Muonium, Mu $\equiv \mu^+ e^-$, is a true hydrogen isotope.

Mass: $m_{Mu} = 0.1131\, m_H = 207.77\, m_e$

Reduced Mass: $\bar{m}_{Mu} = 0.9956\, \bar{m}_H = (\frac{m_\mu m_e}{m_\mu + m_e}) \cong m_e$

Bohr Radius (n=1): $a_{Mu} = 1.0044\, a_0$ $\qquad a_{Mu} = \frac{4\pi\varepsilon_0 \hbar^2}{\bar{m}_{Mu} e^2} = 0.05315$ nm

$(a_0 = 4\pi\varepsilon_0 \frac{\hbar^2}{m_e e^2})$

generally (n-th level): $r_n = n^2 a_{Mu}$

Ionisation energy: $R_{Mu} = 0.9956\, R_y$ $\qquad R_{Mu} = \frac{\bar{m}_{Mu} e^4}{(4\pi\varepsilon_0)^2 2\hbar^2} = 13.54$ eV

$R_y = \frac{m_e e^4}{(4\pi\varepsilon_0)^2 2\hbar^2} = \frac{\alpha^2 m_e c^2}{2}$

for the n-th level: $\frac{R_{Mu}}{n^2}$

Hyperfine coupling: $A_{Mu} = 3.1423\, A_H$ $\qquad A_{Mu} = \frac{2}{3}\mu_0 g_e |\mu_B| g_\mu \mu_B^\mu \frac{1}{\pi\, a_{Mu}^3}$

$= h \cdot 4463.3$ MHz

"Nuclear "- gyromagnetic

factor: $\gamma_\mu = 3.18335 \gamma_p$ $\qquad \frac{\gamma_\mu}{2\pi} = 13.5534$ kHz / G $= 135.534$ MHz / T

Muonium gyromagnetic factor

in triplett state ($F = 1, M = \pm 1$): $\gamma_{Mu}^T = 1.0033\, \gamma_H^T$ $\qquad \gamma_{Mu}^T = \frac{1}{2}(\gamma_e - \gamma_\mu) =$

(in weak fields) $= 2\pi \cdot 1.3944$ MHz/G

$= 102.88\, \gamma_\mu$

A_{Mu} in cgs units: multiply with $\frac{4\pi}{\mu_0} \rightarrow \frac{8\pi}{3}$ instead of 2/3

R_y : Rydberg energy. Ionization energy of a H-Atom with infinitely heavy nucleus.
R_∞ : Rydberg constant, $R_y = hc\, R_\infty$
$R_y = 13.605\ 693\ 009(84)$ eV
$R_\infty = 10\ 973\ 731.568\ 508(65)\ m^{-1}$

Muonium is particularly interesting for spectroscopic investigations because:

- Simple, pure leptonic system.
- Only sensitive to weak, electromagnetic interaction, and gravitation.
- μ^+ : point like particle (from scattering experiments → dimension < 10^{-18} m=10^{-3} fm ~ 1/1000 proton radius).

Muonium can be used to test fundamental laws and symmetries and for precision measurements of fundamental parameters.

Examples are measurements of:

- Hyperfine structure → α, $\frac{\mu_\mu}{\mu_p}$, or $\frac{m_\mu}{m_e}$
- Muonium 1s-2s measurements → new determination of fine structure constant α
- Lamb shift ($2S_{1/2}$-$2P_{1/2}$) in Mu not yet precise enough for comparison with theory

Hydrogen

Electron g-2 factor or (g-2)/2=a_e and $\Delta\nu^H_{hfs}$ are among the best known quantities in physics.

E.g. a_e known to 0.23 ppb → α with 0.32 ppb error.

$\Delta\nu^H_{hfs}$ even known to 0.6 ppt (10^{-12}), but theoretical description is only possible at ppm level because of internal structure of the proton (radius, polarisibility). Similarly for $2S_{1/2}$-$2P_{1/2}$ Lamb shift.

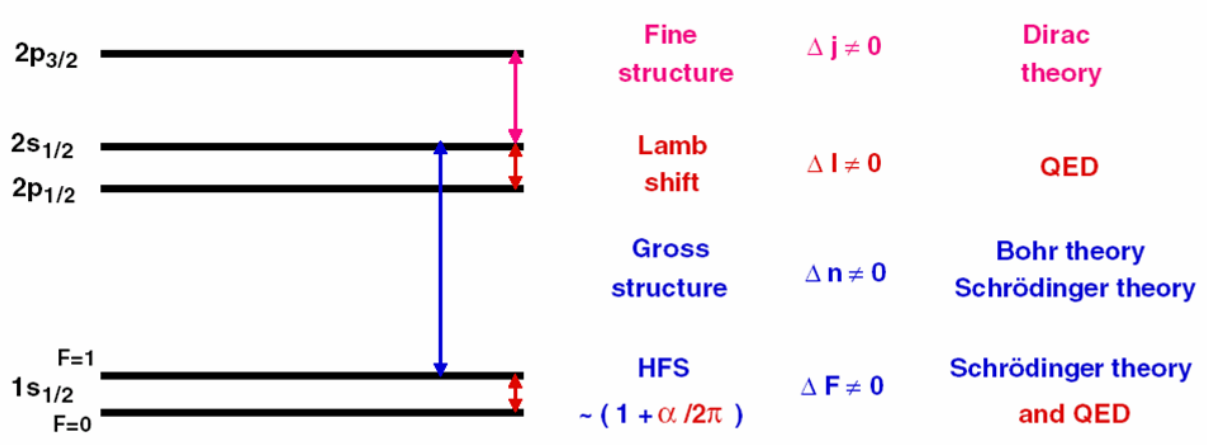

Fig. 3-1: Some low lying energy levels of hydrogen atom (or muonium), not to scale.

Energy level of muonium, n=1 und n=2

$$\vec{J} = \vec{L} + \vec{S}$$
$$\vec{F} = \vec{J} + \vec{I}$$

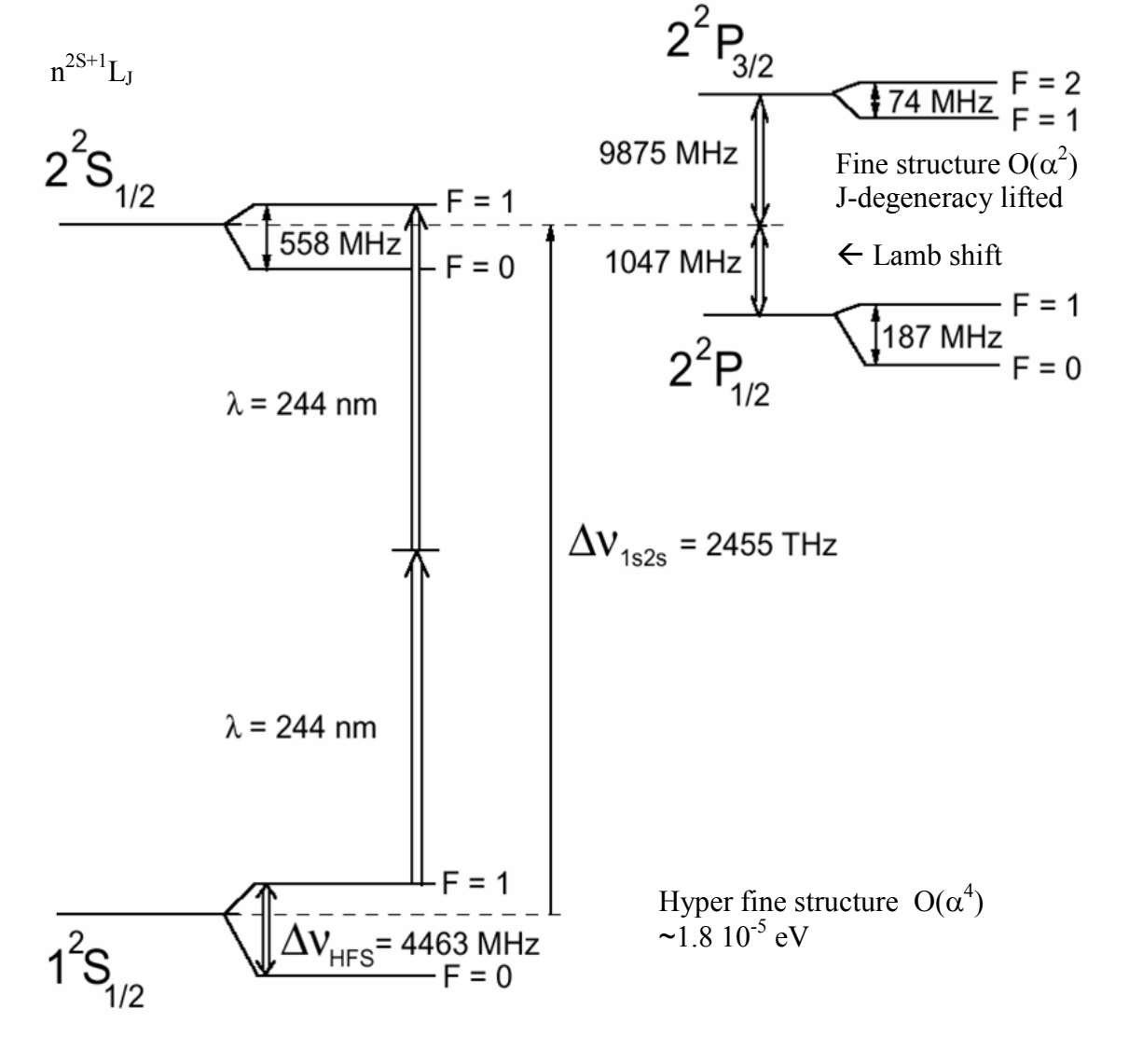

Life time $\tau_\mu = 2.2\,\mu s$, both ground state and excited state decay with this time constant → from uncertainty relation:

$\Delta E\tau = 2\hbar, \quad \Delta E = h\Delta\nu_{nat} \rightarrow \Delta\nu_{nat} = \frac{2}{2\pi\tau} \cong 145$ kHz (natural limit of precision)

3.2 Theory of the energy levels of a muonium atom

The total energy of an electron in a one-electron atom can be expressed in the following way:

$$E_{tot}(n; j; l; F) = E_D(n; j) + E_{RM}(n; j; l) + E_{QED}(n; j; l) + E_{HFS}(n; j; l; F; I) + E_{strong} + E_{weak} + E_{exotic} \quad [3\text{-}1]$$

E_D: Dirac energy for an electron in a point like infinite heavy nucleus with charge Z , which creates a potential $V = -Zq / r$. The Dirac theory of the gross and fine-structure for one-electron atom takes electron spin and fine structure into account. i.e. it contains effects such as spin-orbit coupling + relativistic effects and Darwin term, which originates from averaging the potential energy over the size of the electron wave.

$$E_D(n; j) = m_e c^2 \, (f(n; j) - 1) \quad [3\text{-}2]$$

$$f(n, j) = \left[1 + \left(\frac{Z\alpha}{n - \varepsilon} \right)^2 \right]^{-1/2} \quad [3\text{-}3]$$

$$\varepsilon = j + \frac{1}{2} - \sqrt{(j + \frac{1}{2})^2 - (Z\alpha)^2} \quad [3\text{-}4]$$

E_{RM} : Effects due to finite nuclear mass (relativistic and non-relativistic).

E_{QED} QED-Effects (Lamb shift): radioactive corrections to the electron propagator , (Electron self energy, anomalous magnetic moment), vacuum polarization.

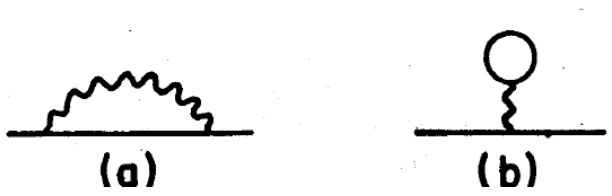

Fig. 3-2: Lowest order QED contributions to the Lamb shift. (a) Electron self energy. (b) Vacuum correction to the potential. The heavy lines represent the electron in an external static nuclear field.

E_{strong} Strong interaction → QED-effects of the vacuum polarization
E_{weak} Weak interaction (via Z-Boson exchange)
E_{HFS} Interaction between magnetic moment of the muon and electron
E_{exotic} Possible (non-Standard Model) exotic interaction between electron and „nucleus“

3.3 Hamilton function of the hyperfine interaction

The Hamilton function of an electron in the field of a muon is given by[5]:

$$H = \frac{1}{2m_e}\left[\vec{P} - e\vec{A}_I(\vec{R})\right]^2 + eU_I(\vec{R}) \underbrace{-g_e\mu_B(\frac{\vec{S}}{\hbar})\mathrm{rot}(\vec{A}_I(\vec{R}))}_{-\vec{\mu}_e\vec{B}} \qquad [3\text{-}5]$$

$\vec{R}$ and $\vec{P}$ are position and momentum of the electron, $\vec{S}$ its spin (in units of $\hbar$), e its charge. $\vec{I}$ is the nuclear spin (muon). Let's consider the terms, which originate from the vector potential $\vec{A}$.

$$\vec{A}_I(\vec{R}) = \frac{\mu_0}{4\pi}\frac{\vec{\mu}_\mu \times \vec{R}}{R^3} \qquad [3\text{-}6]$$

Where $\vec{\mu}_\mu$ is the magnetic moment of the muon.

The hyperfine Hamiltonian H_{hf} is obtained, if we retain in [3-5] only the terms linear in $\vec{A}_I$

$$H_{hf} = -\frac{e}{2m_e}\left[\vec{P}\cdot\vec{A}_I + \vec{A}_I\cdot\vec{P}\right] - g_e\mu_B\frac{\vec{S}}{\hbar}\mathrm{rot}(\vec{A}_I(\vec{R})) \qquad [3\text{-}7]$$

and put [3-6] in [3-7].

Coupling of the magnetic moment of the muon with the orbital momentum of the electron

Let's consider the first term in [3-7]. With

$$\vec{L} = \vec{R}\times\vec{P} \qquad [3\text{-}8]$$

and the fact that $\vec{\mu}_\mu$ with $\vec{R}$ and $\vec{P}$ commutes[6], we get:

$$H_{hf}^L = -\frac{\mu_0}{4\pi}\frac{e}{2m_e}2\frac{\vec{\mu}_\mu\cdot\vec{L}}{R^3} = -\frac{\mu_0}{4\pi}2\mu_B\frac{\vec{\mu}_\mu\cdot\frac{\vec{L}}{\hbar}}{R^3} = -\vec{\mu}_\mu\cdot\vec{B}_L \qquad [3\text{-}9]$$

This corresponds to the coupling between the magnetic moment $\vec{\mu}_\mu$ and the magnetic field (note *e* is negative)

[5] In this chapter we use [S]=[$\hbar$]

[6] Use: $\vec{P}\cdot\vec{A} \propto \vec{P}\cdot[\vec{\mu}_\mu\times\vec{R}] = \vec{\mu}_\mu\cdot[\vec{R}\times\vec{P}] = \vec{\mu}_\mu\cdot\vec{L}$ and similarly for $\vec{A}\cdot\vec{P}$

$$\vec{B}_L = \frac{\mu_0}{4\pi}\frac{e}{m_e}\frac{\vec{L}}{R^3} \qquad [3\text{-}10]$$

This field corresponds to the current generated by the orbiting electron.

(Biot-Savart law: $\vec{B}_L = -\frac{\mu_0}{4\pi} I \int \frac{\vec{R}\times d\vec{R}}{R^3}$, with $I=\frac{-ev}{2\pi R}$)

Coupling with electron spin:

Magnetic field created by the muon:

To avoid problems with singularities we consider first a muon with a finite radius ρ_0 and take $R > \rho_0$

With [3-6] and $\vec{B}^{dip} = rot\vec{A}_I$

$$\vec{B}^{dip}(\vec{R}) = \frac{\mu_0}{4\pi}\left[-\frac{\vec{\mu}_\mu}{R^3} + 3\frac{(\vec{\mu}_\mu \cdot \vec{R})\vec{R})}{R^5}\right] \qquad [3\text{-}11]$$

with $\vec{\mu}_\mu \| \hat{z}$, we get:

$$B_x = \frac{\mu_0}{4\pi} 3\mu_\mu \frac{xz}{R^5}$$

$$B_y = \frac{\mu_0}{4\pi} 3\mu_\mu \frac{yz}{R^5}$$

$$B_z = \frac{\mu_0}{4\pi} \mu_\mu \frac{3z^2 - R^2}{R^5}$$

[3-11] is also valid for R not much larger than ρ_0 , since a spin ½ particle creates a dipolar field.

The magnetic dipole term:

If we insert [3-11] in $-g_e\mu_B(\frac{\vec{S}}{\hbar})rot(\vec{A}_I(\vec{R}))$, we get for the magnetic dipole term (coupling between electron spin and magnetic field, which is generated by the dipole moment of the muon outside its "radius").

$$H_{hf}^{dip} = \frac{\mu_0}{4\pi}\frac{g_e\mu_B}{\hbar}\frac{1}{R^3}\left[\vec{S}\cdot\vec{\mu}_\mu - 3\frac{(\vec{S}\cdot\vec{R})(\vec{\mu}_\mu\cdot\vec{R})}{R^2}\right] = -\vec{\mu}_e \cdot \vec{B}^{dip} \qquad [3\text{-}12]$$

The contact term:

It takes into account the contribution of the „internal field " B_i (i.e. of the interaction between magnetic moment of the muon and electronic spin density at the muon site) $R \le \rho_0$: The field inside the nucleus (B_i) can be obtained by the explicit integration of the magnetic flux Φ over half a sphere surrounding the dipole, taking into account that the integral is zero.

$$B_i = \frac{\mu_0}{4\pi}\mu_\mu \frac{2}{\rho_0^3} \qquad [3\text{-}13]$$

Contact term in [3-5]:

$$-g_e\mu_B(\frac{\vec{S}}{\hbar})\mathrm{rot}(\vec{A}_I(\vec{R})) = -\vec{\mu}_e \cdot \vec{B}_i$$

The corresponding operator H_{hf}^c is obtained by calculating the matrix elements between the basis wave functions. We get (note μ_B is negative here):

$$H_{hf}^c = -\frac{\mu_0}{4\pi}\frac{8\pi}{3}\vec{\mu}_\mu \frac{g_e\mu_B\vec{S}}{\hbar}\delta(\vec{R}) = -\frac{2}{3}\mu_0\vec{\mu}_\mu\vec{\mu}_e\delta(\vec{R}) \qquad [3\text{-}14]$$

Note that the term is finite and does not depend on the choice of ρ_0.

With $H_{hf} = H_{hf}^L + H_{hf}^{dip} + H_{hf}^c$

and $\vec{\mu}_\mu = g_\mu\mu_B^\mu\frac{\vec{I}}{\hbar}$ [3-15]

With the three contributions, the Hamilton operator of the hyperfine interaction ($g_e = 2$) becomes:

$$H_{hf} = -\frac{\mu_0}{4\pi}\frac{2\mu_B\mu_B^\mu g_\mu}{\hbar^2}\left[\underbrace{\frac{\vec{I}\cdot\vec{L}}{R^3}}_{\text{e-Angular moment}} + \underbrace{3\frac{(\vec{I}\cdot\vec{R})(\vec{S}\cdot\vec{R})}{R^5} - \frac{\vec{I}\cdot\vec{S}}{R^3}}_{\text{Dipol (e-spin)}} + \underbrace{\frac{8\pi}{3}\vec{I}\cdot\vec{S}\delta(\vec{R})}_{\substack{\text{Contact term}\\ \text{(e-Spindensity}\\ \text{at the muon site)}}}\right] \qquad [3\text{-}16]$$

Dipolar and contact fields are also present in the solid. For instance, localized magnetic moments or nuclear moments produce dipolar fields and the spin density of conduction electrons (or delocalized electrons) generates a contact field at the muon site.

Calculation of the hyperfine structure of the 1s-level

For the 1s level the first two terms of [3-16] are zero, since
$< \vec{L} >$ and $< 1s \left| \text{dipolar term} \right| 1s >= 0$ because of the spherical symmetry of the 1s-state.
Only the contact term contributes.

Matrix element of the contact term:

with $\vec{\mu}_e = g_e \mu_B \frac{\vec{S}}{\hbar}$

$$< n=1, l=0, m_L=0, m_S, m_I \left| -\frac{2}{3}\mu_0 \vec{\mu}_\mu \vec{\mu}_e \delta(\vec{R}) \right| n=1, l=0, m_L=0, m_S, m_I > \qquad [3\text{-}17]$$

$$= A < m_S, m_I \left| \vec{I} \cdot \vec{S} \right| m_S, m_I > \qquad [3\text{-}18]$$

$$A = \frac{2}{3}\mu_0 g_\mu \mu_B^\mu g_e \left| \mu_B \right| \frac{1}{\hbar^2} \underbrace{< n=1, l=0 \left| \delta(\vec{R}) \right| n=1, l=0 >}_{|\varphi_{1s}(0)|^2} \qquad [3\text{-}19]$$

$$\text{with } < r \left| n=1, l=0 \right. >= \frac{1}{\sqrt{\pi a_{Mu}^3}} e^{-\frac{r}{a_{Mu}}} = \varphi_{1s}(r) \qquad [3\text{-}20]$$

$$< n=1, l=0 \left| \delta(\vec{R}) \right| n=1, l=0 >= \left| \varphi_{1s}(0) \right|^2 = \frac{1}{\pi a_{Mu}^3} \qquad [3\text{-}21]$$

$$A = \frac{2}{3}\mu_0 g_\mu \mu_B^\mu g_e \left| \mu_B \right| \frac{1}{\pi a_{Mu}^3} \frac{1}{\hbar^2} \qquad [A]=[\frac{\text{energy}}{\hbar^2}] \qquad [3\text{-}22]$$

With $a_{Mu} = \frac{4\pi\varepsilon_0 \hbar^2}{\bar{m}_{Mu} e^2}$ (Bohr radius), $\bar{m}_{Mu} = \frac{m_e m_\mu}{m_e + m_\mu} = \frac{m_e}{1 + \frac{m_e}{m_\mu}}$ (takes into account the finite "nuclear" mass), $\alpha = \frac{e^2}{4\pi\varepsilon_0 \hbar c}$ (fine structure constant in SI units) and $\varepsilon_0 \mu_0 = \frac{1}{c^2}$

For spectroscopy [3-22] can also be written in terms of precisely known quantities:

$$A = \frac{2}{3} g_\mu g_e \frac{m_e}{m_\mu} m_e c^2 \alpha^4 (1 + \frac{m_e}{m_\mu})^{-3} \frac{1}{\hbar^2} \qquad [3\text{-}23]$$

Summarizing the contact operator for the 1s state can be simplified to

$$H_{hf}^c = A\vec{I} \cdot \vec{S} \qquad [3\text{-}24]$$

With A>0 and $[I] = [S] = [\hbar]$

<u>Eigenvalues and eigenstates of the contact term of the 1s-level</u>

The degeneracy of the 1s-level is 4-fold. Instead of the basis

$$\left| S = \frac{1}{2}, I = \frac{1}{2}, m_S, m_I > \right. \qquad \text{(product basis)} \qquad [3\text{-}25]$$

we take the basis

$$\left| F, m_F > \right. \qquad \text{(coupled basis)} \qquad [3\text{-}26]$$

F is the total moment eigenvalue of the operator $\vec{F} = \vec{S} + \vec{I}$: [3-27]

$\vec{I} \cdot \vec{S}$ is diagonal in the basis [3-26]. With L=0 (1s level)

$$A\vec{I} \cdot \vec{S} = \frac{A}{2}(F^2 - I^2 - S^2) \qquad [3\text{-}28]$$

$$A\vec{I}\cdot\vec{S}\left|F, m_F\right> = A\frac{\hbar^2}{2}\left[F(F+1) - I(I+1) - S(S+1)\right]\left|F, m_F\right> \qquad [3\text{-}29]$$

$$= A\frac{\hbar^2}{4} \qquad F = 1$$

$$= -A\frac{3\hbar^2}{4} \qquad F = 0$$

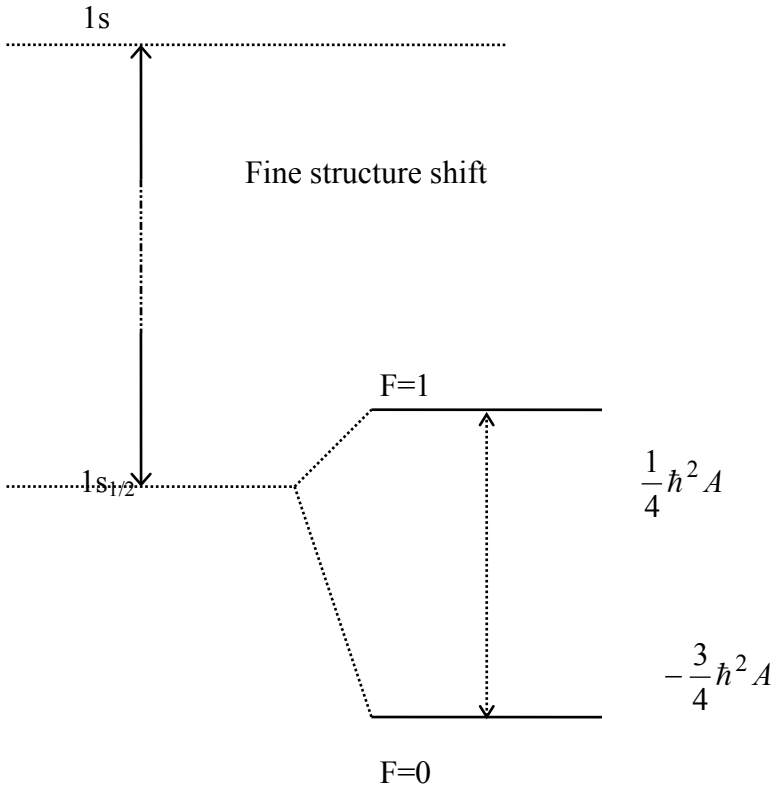

Eq. [3-23] is not accurate enough for high precision spectroscopy of muonium or of hydrogen and positronium. One has to consider additional correction terms arising from QED, weak interaction, and eventually exotic interactions.

However, the hyperfine-Hamilton function has still the form:

$$H_{hf}^{c} = A\vec{I}\cdot\vec{S} \qquad [3\text{-}30]$$

If we write the splitting in terms of frequency we get:

$$E_{hfs}(F=1) - E_{hfs}(F=0) = h\Delta\nu_{hfs} = \hbar^2 A \qquad [3.31]$$

$$\Delta\nu_{hfs}^{Mu} = \frac{16}{3}(Z\alpha)^2 \frac{R_y}{h}\frac{\mu_\mu}{\mu_B}\left[1+\frac{m_e}{m_\mu}\right]^{-3}\left(1+\varepsilon_{rad}+\varepsilon_{rec}+\varepsilon_{rad-rec}\right)+\Delta\nu_{weak}+\Delta\nu_{exotic} \qquad [3\text{-}32]$$

where $R_y = \frac{\alpha^2 m_e c^2}{2}$ and Z=1

Theoretical value:

$$\Delta\nu_{hfs}^{th} == \text{ 4 463 302 891 (272) Hz (63 ppb)} \qquad [3\text{-}33]$$

Better known for muonium than for H. For H one has to consider additional terms due to the proton structure:

$+ \varepsilon_{\text{nuclear radius}} + \varepsilon_{\text{nuclear polarization}}$.

The theoretical uncertainty is 560 ppb (whereas the experimental uncertainty is presently 0.6 ppt).

3.4 Spectroscopy of the hyperfine splitting in muonium

Method: Microwave spectroscopy of the ground state in an external magnetic field.

We consider the Zeeman effect on the 1s level.

Hamilton function:

$$H = -\vec{\mu}_\mu \cdot \vec{B} - \vec{\mu}_e \cdot \vec{B} + A\vec{I} \cdot \vec{S} \qquad [3\text{-}34]$$

with $\vec{B} \parallel \hat{z}$ and $\vec{\mu}_\mu = \gamma_\mu \vec{I}$ ($[I]=\hbar$)

and using the Larmor frequencies of muon and electron:

$$H = \omega_\mu I_z + \omega_e S_z + A\vec{I} \cdot \vec{S} \qquad [3\text{-}35]$$

where:

$$\omega_\mu = -\frac{g_\mu}{2}\frac{|e|}{m_\mu}B \quad , \quad \omega_\mu < 0$$
$$\omega_e = \frac{g_e}{2}\frac{|e|}{m_e}B \quad , \quad \omega_e > 0 \qquad [3\text{-}36]$$

To determine the energy eigenvalues, we must diagonalize the matrix of the Hamilton function *H* [3-35].

We obtain as energy eigenvalues:

$$E_1 = \frac{A\hbar^2}{4} + \frac{\hbar}{2}(\omega_e + \omega_\mu) = \frac{A\hbar^2}{4} + \frac{1}{2}(g_e|\mu_B| - g_\mu \mu_B^\mu)B$$
$$E_2 = \frac{A\hbar^2}{4} - \frac{\hbar}{2}(\omega_e + \omega_\mu) = \frac{A\hbar^2}{4} - \frac{1}{2}(g_e|\mu_B| - g_\mu \mu_B^\mu)B$$
$$E_3 = -\frac{A\hbar^2}{4} + \sqrt{(\frac{A\hbar^2}{2})^2 + \frac{\hbar^2}{4}(\omega_e - \omega_\mu)^2} = -\frac{A\hbar^2}{4} + \frac{A\hbar^2}{2}\sqrt{1+x^2} \qquad [3\text{-}37]$$
$$E_4 = -\frac{A\hbar^2}{4} - \sqrt{(\frac{A\hbar^2}{2})^2 + \frac{\hbar^2}{4}(\omega_e - \omega_\mu)^2} = -\frac{A\hbar^2}{4} - \frac{A\hbar^2}{2}\sqrt{1+x^2}$$

Breit-Rabi diagram

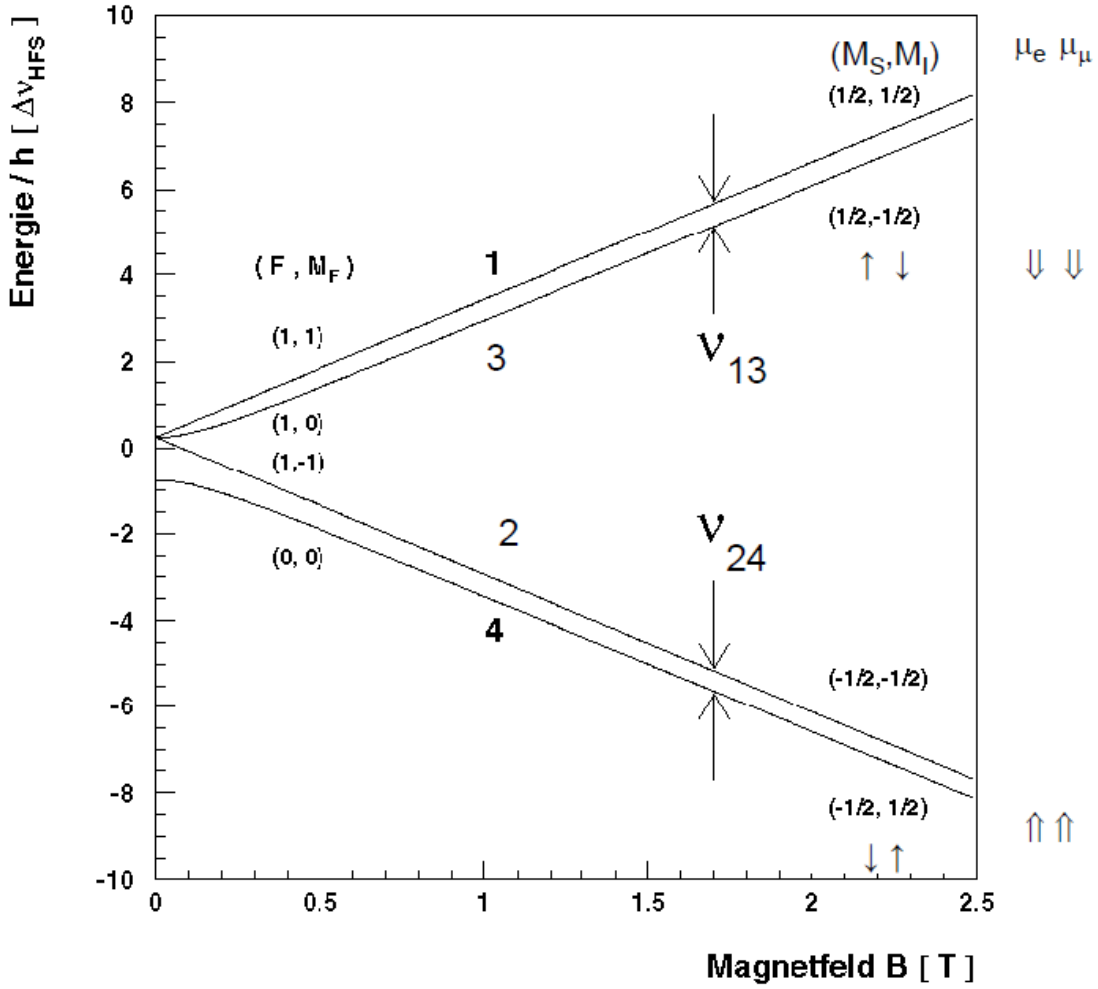

Fig. 3-3: Energy-level diagram for muonium in the $1^2S_{1/2}$ ground state in a magnetic field. At zero magnetic field the energy difference between the F=1 and F=0 states is the hyperfine splitting $h\Delta\nu_{hfs}$.

The field is generally expressed in terms of the dimensionless parameter

$$x = \frac{(g_e|\mu_B| + g_\mu \mu_B^\mu)B}{A\hbar^2} = \frac{(g_e|\mu_B| + g_\mu \mu_B^\mu)B}{h\Delta\nu_{hfs}} \equiv \frac{B}{B_0} \qquad [3\text{-}38]$$

B_0 is the field where the Zeeman splitting of the electron and the muon is equal to the hyperfine splitting. For muonium B_0=0.158 T.

In analogy we obtain the eigenstates:

$$
\begin{aligned}
&\mid 1>=\mid \ \mathrm{M_S}=\frac{1}{2},\mathrm{M_I}=\frac{1}{2}> \ =\mid \ \mathrm{F}=1,\mathrm{M_F}=1> \\
&\mid 2>=\mid \ \mathrm{M_S}=-\frac{1}{2},\mathrm{M_I}=-\frac{1}{2}> \ =\mid \ \mathrm{F}=1,\mathrm{M_F}=-1> \\
&\mid 3>=\sin\beta\mid \ \mathrm{M_S}=-\frac{1}{2},\mathrm{M_I}=\frac{1}{2}>+\cos\beta\mid \ \mathrm{M_S}=+\frac{1}{2},\mathrm{M_I}=-\frac{1}{2}> \\
&\mid 4>=\cos\beta\mid \ \mathrm{M_S}=-\frac{1}{2},\mathrm{M_I}=\frac{1}{2}>-\sin\beta\mid \ \mathrm{M_S}=+\frac{1}{2},\mathrm{M_I}=-\frac{1}{2}>
\end{aligned}
\qquad [3\text{-}39]
$$

where

$$\cos\beta=\frac{1}{\sqrt{2}}\left[1+\frac{x}{(1+x^2)^{1/2}}\right]^{1/2}$$

$$\sin\beta=\frac{1}{\sqrt{2}}\left[1-\frac{x}{(1+x^2)^{1/2}}\right]^{1/2}$$

We express the energy differences as frequencies:

$$\begin{aligned} E_1 - E_3 &= h\nu_{13} \\ E_2 - E_4 &= h\nu_{24} \end{aligned} \qquad [3\text{-}40]$$

Then we get for the sum or difference of the transition energies:

$$\begin{aligned} h\nu_{13} + h\nu_{24} &= h\Delta\nu_{hfs}^{Mu} = \hbar^2 A \\ h\nu_{13} - h\nu_{24} &= 2\mu_B^{\mu} g'_{\mu} B + h\Delta\nu_{hfs}^{Mu}\left[(1+x^2)^{1/2} - x\right] \end{aligned} \qquad [3\text{-}41]$$

$$x = \frac{(g'_e|\mu_B| + g'_\mu \mu_B^\mu)B}{h\Delta\nu_{hfs}^M}$$

To take into account the relativistic binding corrections in muonium we use in [3-41] g'_e and g'_μ instead of the values for free particles g_e and g_μ.

$$\begin{aligned} g'_\mu &= g_\mu[1 - \frac{\alpha^2}{3} + \frac{\alpha^2}{2}\frac{m_e}{m_\mu}] \\ g'_e &= g_e[1 - \frac{\alpha^2}{3} + \frac{\alpha^2}{2}\frac{m_e}{m_\mu} + \frac{\alpha^3}{4\pi}] \end{aligned} \qquad [3\text{-}42]$$

B can be expressed as a function of μ_p and of the NMR frequency.

$$h\nu_p = 2\mu_p B \qquad [3\text{-}43]$$

From the sum of the transition frequencies $\Delta\nu_{hfs}^{Mu}$ is determined and from the difference (Eq. [3-41]) by using $\mu_\mu = \frac{g_\mu \mu_B^\mu}{2}$ we obtain also the ratio of the muon and proton magnetic moments $\frac{\mu_\mu}{\mu_p}$.

Principle of the experiment (W. Lin et al., Phys. Rev. Lett. **82**, 711 (1999))

Stop polarized positive muons in Kr in a magnetic field $\vec{B}$ antiparallel to $\vec{I}$ (initial muon spin direction)
In Kr muonium is formed in the states (each with 50% probability since the electrons are unpolarized)

$|M_S = -\frac{1}{2}, M_I = -\frac{1}{2}>$ (level 2)

and $|M_S = +\frac{1}{2}, M_I = -\frac{1}{2}>$ (level 3)

With microwaves one induces the transitions in level 4 ($\rightarrow h\nu_{24}$)
and in level 1 ($\rightarrow h\nu_{13}$) .
The transition frequencies are determined from the positrons rates with and without microwave field (one can vary either the microwave frequency or the magnetic field)

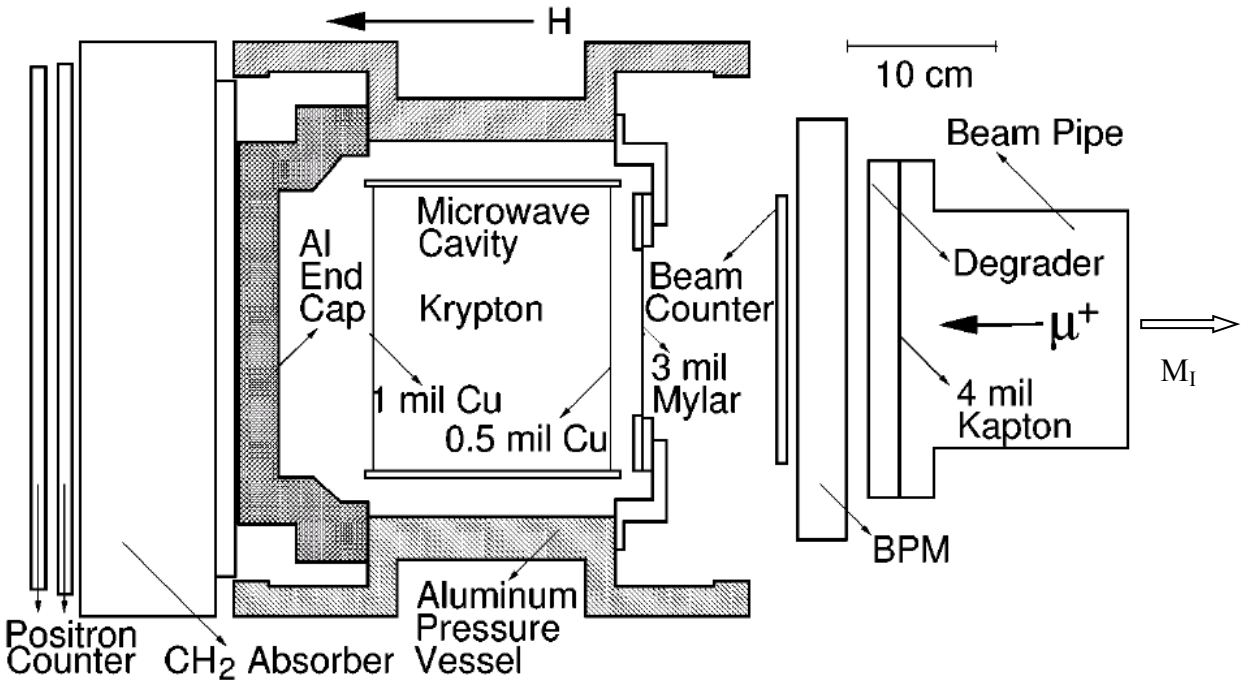

Fig. 3-4: A schematic view of the experimental apparatus

Positron signal (as a function of the magnetic field or of the microwave frequency)

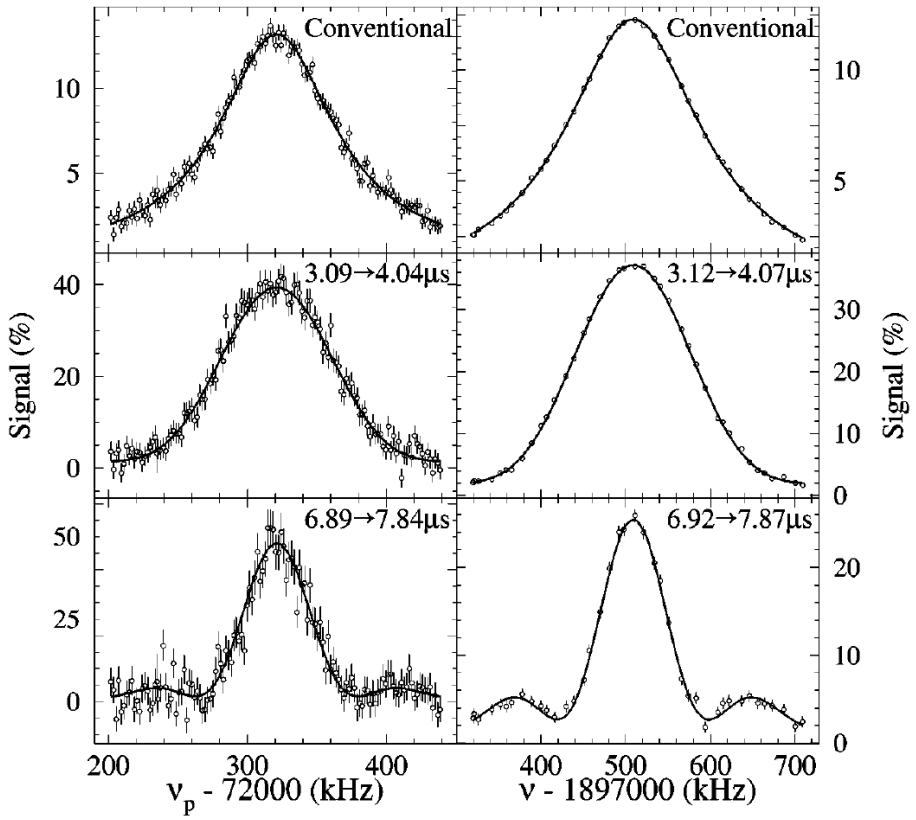

Fig. 3-5: Left: resonance curves obtained by sweeping the magnetic field and from different windows after muonium production. Right: microwave frequency sweep curves. The solid curves are fits to the theoretical line shape.

Results

$\Delta\nu_{hfs}^{exp}$ = 4 463 302 765(53) Hz (12 ppb) [3-44]

$\Delta\nu_{hfs}^{th}$ = 4 463 302 891 (272) Hz (63 ppb)

μ_μ/μ_p = 3.183 345 13(39) (122 ppb) [3-45]

(Ref. Liu et al., Phys. Rev. Lett. **82**, 711 (1999))

From [3-45] via $\frac{m_\mu}{m_e} = \frac{g_\mu}{2}\frac{\mu_p}{\mu_\mu}\frac{\mu_B^e}{\mu_p}$:

m_μ/m_e = 206.768 277(24) (120 ppb) can be determined [3-46]

Alternatively one can use m_μ/m_e or α as parameter in Eq. [3-32] and determine them from the experimental result for $\Delta\nu_{hfs}^{exp}$.
For instance with m_μ/m_e from [3-46] one gets:

α^{-1} = 137.0359963(80) (58 ppb)

Fine structure constant: summary of results

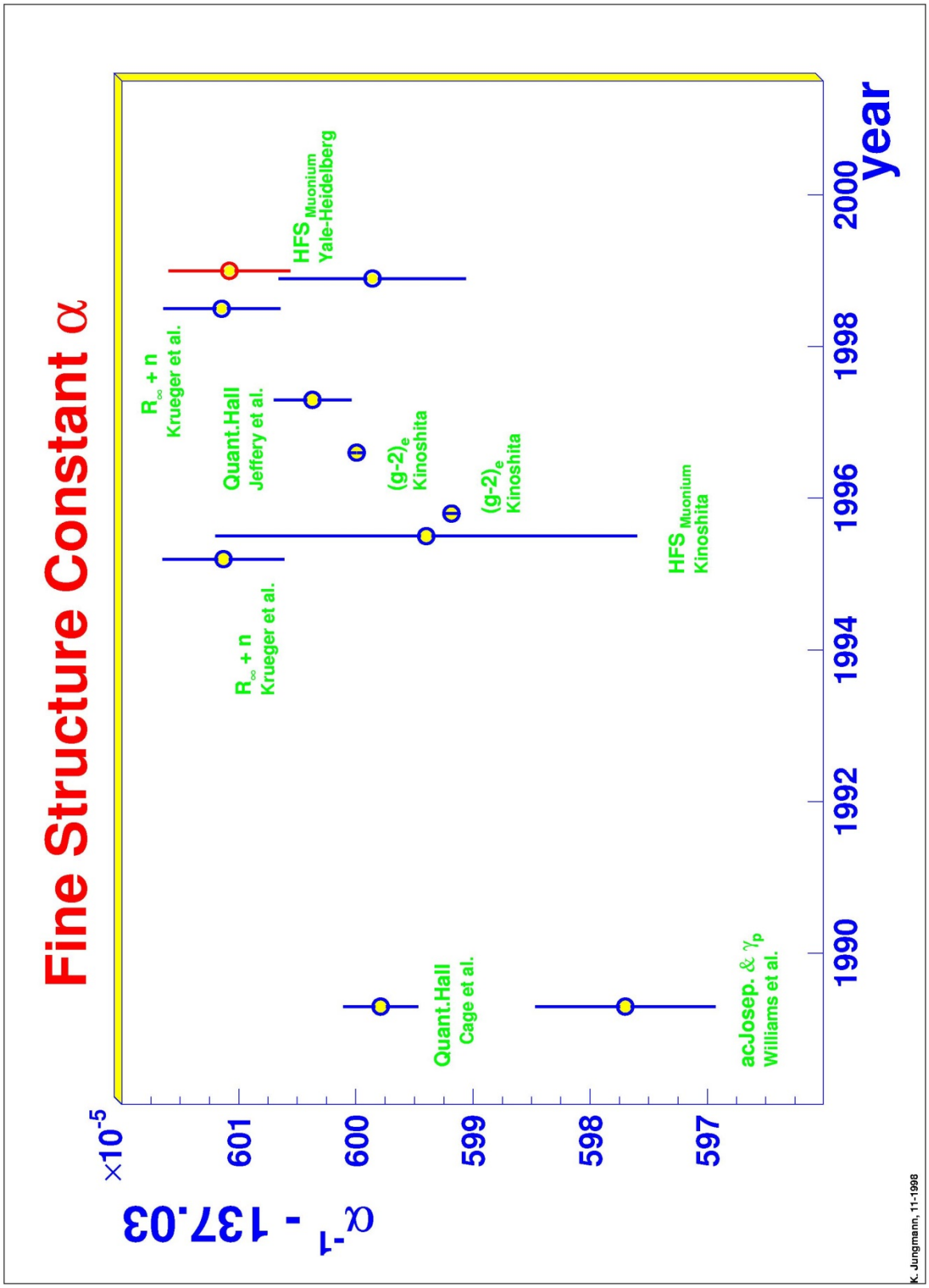

3.5 Measurement of the 1s-2s transition in muonium

(Doppler free 2-photons spectroscopy)

- 1 photon transition not allowed (because of $\Delta l = \pm 1$)
- Gross structure interval

$$\nu_{1s2s} = \frac{3}{4} cR_\infty \left(1 - \frac{m_e}{m_\mu}\right) = 2.45 \cdot 10^{15}\,\text{Hz} \qquad hcR_\infty \equiv R_y = m_e c^2 \frac{\alpha^2}{2} \qquad [3\text{-}47]$$

  R_∞ (Rydberg constant) is known to 8. 10^{-12}

- Natural width due to lifetime of the muon: ν_μ = 145 kHz → $\frac{\nu_\mu}{\nu_{1s2s}} \approx 6 \cdot 10^{-11}$
- A measurement of ν_{1s2s} at the 10^{-9} level allows an accuracy of $\frac{m_\mu}{m_e}$ determined by $10^{-9} \frac{m_\mu}{m_e} \approx 10^{-7}$

Measurement principle (Doppler free spectroscopy)

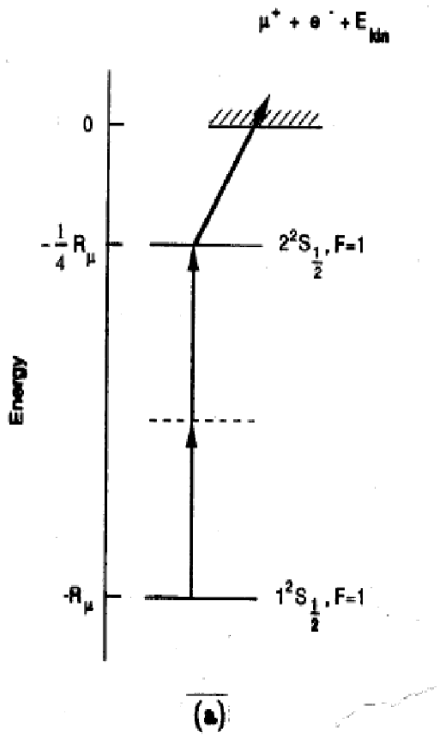

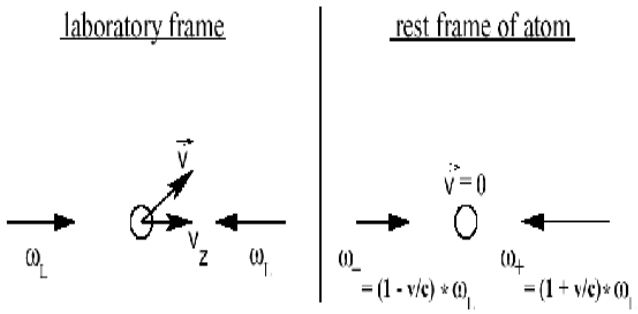

Principle of the 1s-2s muonium experiment. a) The transition between the 1s- and 2s- levels is induced by the absorption of two counterpropagating photons (λ= 244.2 nm). The metastable 2s-state is ionized by a third photon. b) The transition via two photon absorption is to first order Doppler free.

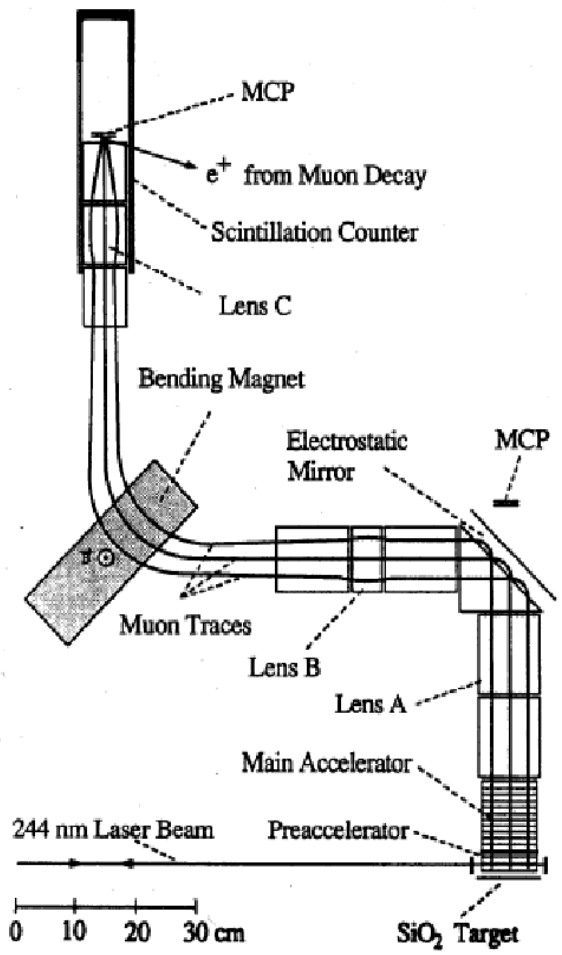

83

Apparatus for the 1s-2s experiment at the Rutherford Appleton Laboratory (pulsed muon source, UK).

Production of thermal muonium in vacuum. Efficiency for different materials. The beam momentum is optimized for maximum efficiency.

Target material	Target density [mg/cm^3]	Target Thickness [mg/cm^2]	Optimum muonium Fraction μ^+e^-/μ_{stop} [%]
SiO_2 powder	32	4.6	17(1)
SiO_2 powder	32	2.8	15.9(3.6)
SiO_2 powder	32	9.0	8.27(31)
SiO_2 aerogel	5	7.5	2.32(13)
SiO_2 aerogel	18	9	1.57(20)
W Foil (2130K)	19.3	96.5	4(2)
C_{60}/C_{70} Fullerenes	≈1400	≈210	1.85(23)
Cotton	10	3.6	2.25(16)
Cotton coated with SiO2 powder	17	5.8	11.43(31)
Microchannel Plate	≈2000	≈100	2.44(31)

Results

$\Delta\nu_{ls2s}^{Exp} = 2\ 455\ 528\ 941.0\ (9.8)$ MHz (4 ppb)

From the comparison with the theoretical value $\Delta\nu_{ls2s}^{Theor} = 2\ 455\ 528\ 934.5\ (3.6)$ MHz

$$\rightarrow \frac{m_\mu}{m_e} = 206.76838(16) \qquad (0.77\ \text{ppm})$$

or alternatively: from the comparison with the theory and the fact that the dominant term in [3-47] is proportional to $R_y \propto \alpha^2 \propto q_\mu{}^2 \cdot q_e{}^2 \propto (\frac{q_\mu}{q_e})^2 (\frac{q_e{}^4}{\alpha_{true}{}^2}) \propto (\frac{q_\mu}{q_e})^2$

$$\rightarrow (\frac{q_\mu}{q_e}) = -1 - 1.0(2.0)\cdot 10^{-9} \qquad (2.0\ \text{ppb})$$

This is a test of charge equality between two particle generations.

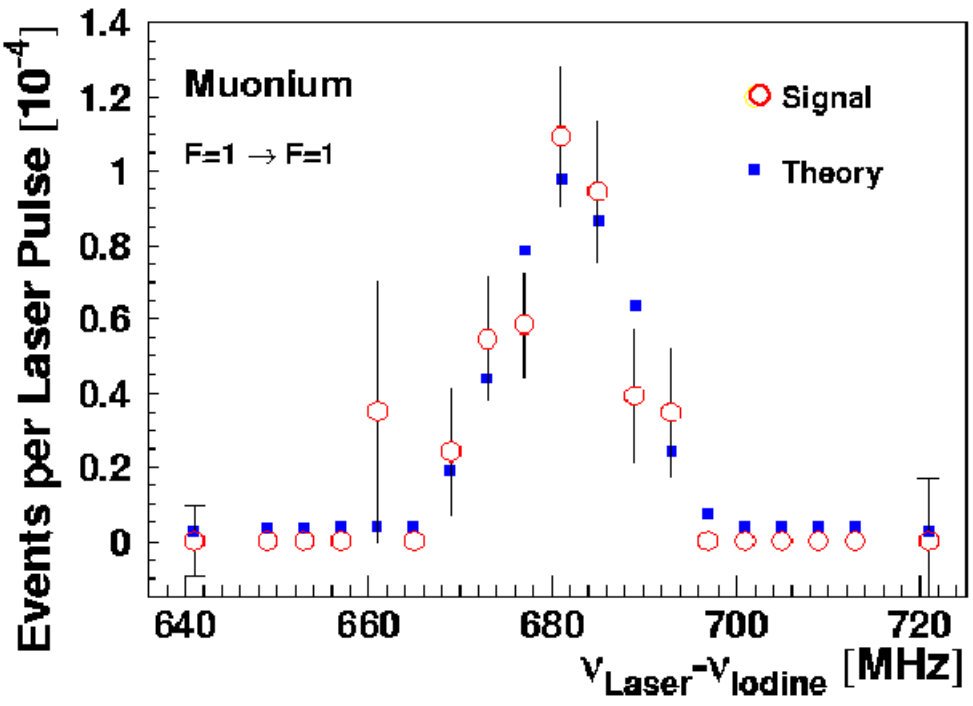
Muonium
F=1 → F=1
Signal
Theory
Events per Laser Pulse [10^-4]
1.4
1.2
1
0.8
0.6
0.4
0.2
0
640
660
680
700
720
ν_Laser-ν_Iodine [MHz]

Muon mass results, summary

Extracted from experiments:

$\frac{m_{\mu^+}}{m_e}$ (μSR Br) = 206.768 35 (11) (0.53 ppm)

$\frac{m_{\mu^+}}{m_e}$ (μ^- Atoms) = 206.768 30 (64) (3.1 ppm)

$\frac{m_{\mu^+}}{m_e}$ (M 1s-2s) = 206.768 38 (16) (0.77 ppm)

$\frac{m_{\mu^+}}{m_e}$ (μ_μ) = 206.768 270 (24) (0.12 ppm)

Using the muonium hyperfine structure measurement and the theory:

$\frac{m_{\mu^+}}{m_e}$ (M_{hfs}) = 206.768 267 0 (55) (0.027 ppm)

Value in Particle Data Book (2014):

$\frac{m_{\mu^+}}{m_e}$ = 206.768 284 3(52) (0.025 ppm)

Summary of precision experiments

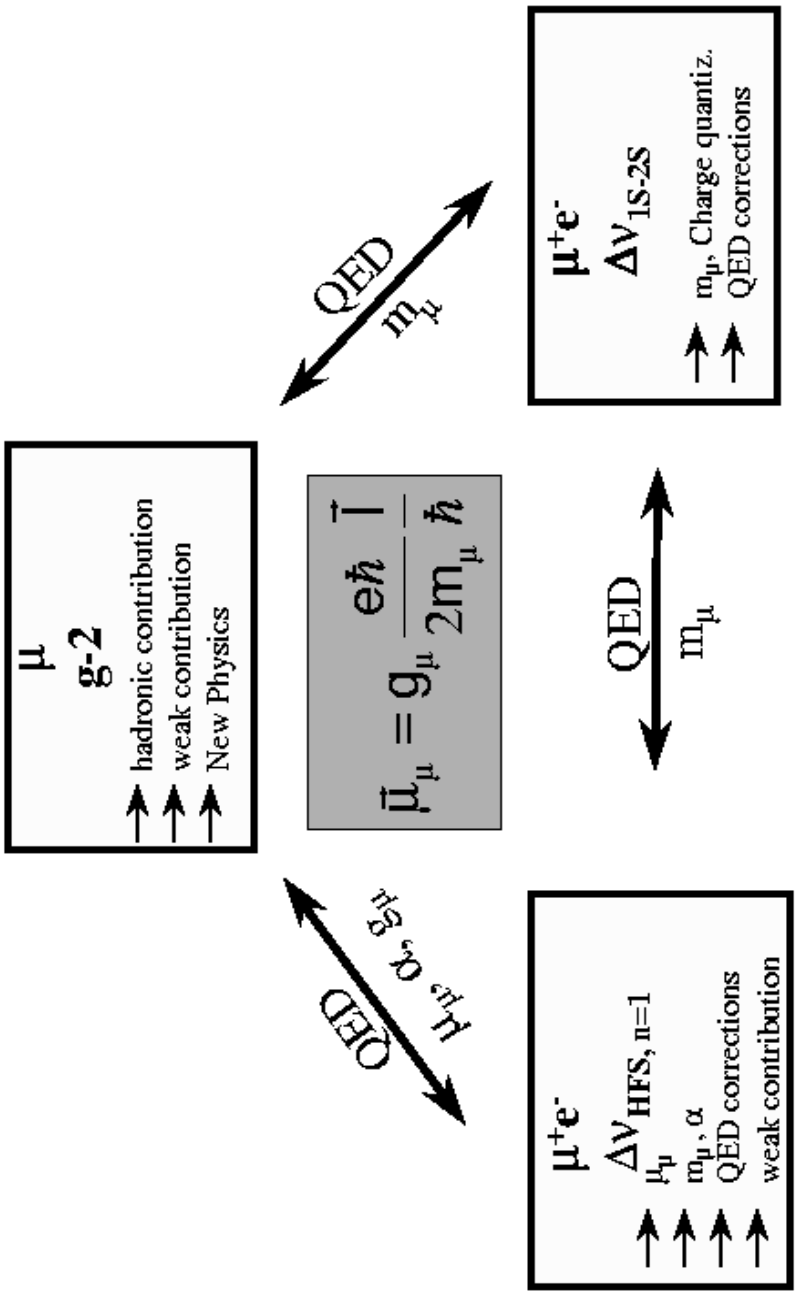

4. Positive and negative muons in matter

4.1 Energy loss of charged particles in matter

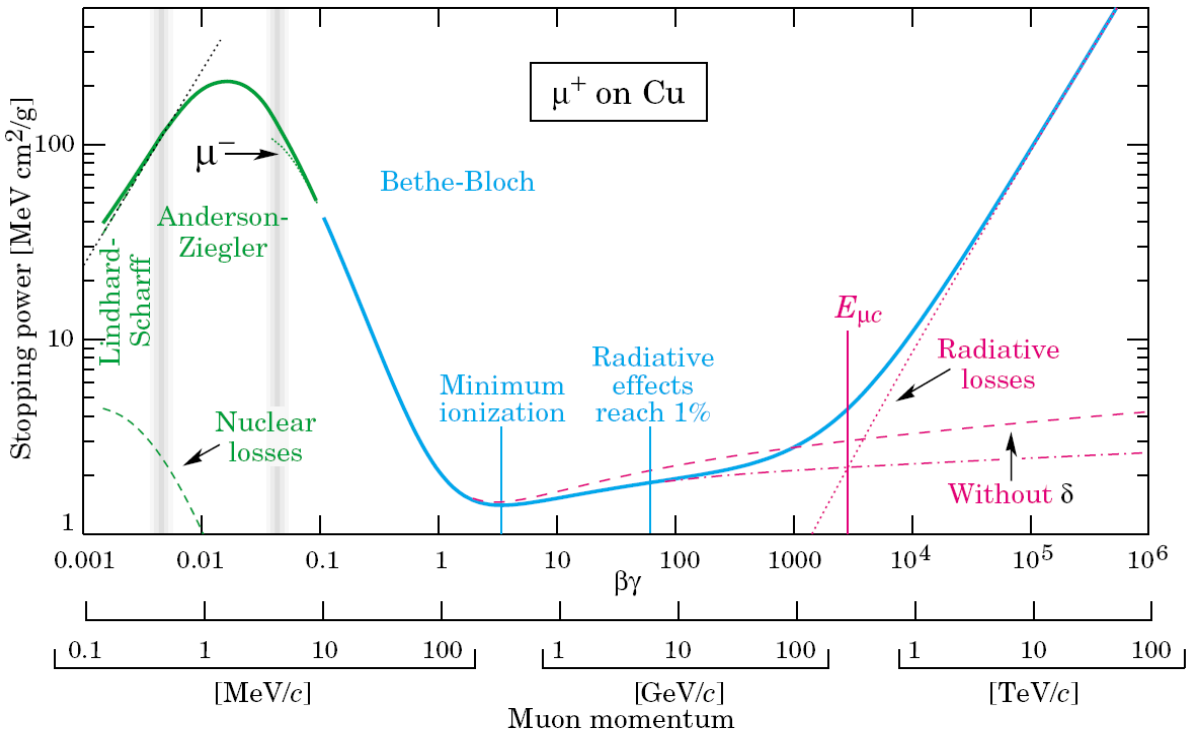

Fig. 4-1: Stopping power (= < −dE/dx>) for positive muons in copper as a function of $\beta\gamma = p/m_\mu c$ over nine orders of magnitude in momentum (12 orders of magnitude in kinetic energy). Solid curves indicate the total stopping power. Vertical bands indicate boundaries between different approximations. The short dotted lines labeled μ^- illustrate the "Barkas effect", the dependence of stopping power on projectile charge at very low energies.

Interaction between a charged particle and matter leads to energy loss and scattering.

Energy loss:

$$\frac{dE}{dx} = \frac{dE}{dx}_{electronic} + \frac{dE}{dx}_{nuclear} + \ldots \qquad [4\text{-}1]$$

The energy loss is proportional to the density. Therefore, often the density is included in the length, $x = l.\rho$ $\quad [x]=[g/cm^2]$

The most important contribution is the so-called electronic energy loss arising from inelastic collisions with electrons (ionization, excitation,..).

Generic Bethe-Bloch formula for electronic energy loss:

$$-\frac{dE}{dx_{electronic}} = K\frac{Z}{A}z^2\frac{1}{\beta^2}\left[\frac{1}{2}\ln\left(\frac{2m_e c^2\beta^2\gamma^2 T_{max}}{I}\right) - \beta^2 - \frac{\delta}{2}\right] \qquad \left[\frac{MeV\cdot cm^2}{g}\right] \qquad [4\text{-}2]$$

Z : Target atomic number
A: Target atomic mass [g/mol]
M: Target mass
z : Charge of incoming particle
I : Mean excitation energy
T_{max}: Maximum energy transfer to a free electron in one collision

$$T_{max} = \frac{2m_e c^2\beta^2\gamma^2}{1 + 2\gamma\frac{m_e}{M} + \left(\frac{m_e}{M}\right)^2} \qquad \text{Non relativistically:} \quad T_{max} = 2m_e v^2 \qquad [4\text{-}3]$$

For $v >> v_e$ (v: Projectile velocity, v_e: velocity of the electron to be ionized) and $z << Z$, the energy loss can be calculated classically (non-relativistic Bethe-Bloch formula).

$$-\frac{dE}{dx_{electronic}} \propto \frac{1}{v^2} \qquad [4\text{-}4]$$

Energy loss occurs via inelastic collisions with the shell electrons of the material.

Assume $M >> m_e$ and electrons at rest before collisions:

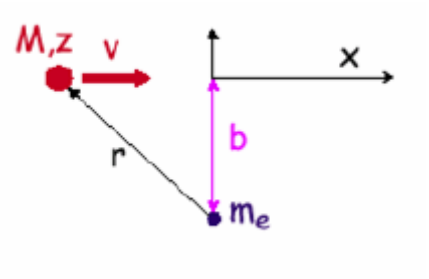

Momentum transfer:

$$\Delta p = \int_{-\infty}^{+\infty} F_{Coul} dt$$

Longitudinal component of force averages out. Only the transverse component contributes to the integral:

$$F_{Coul}^{\perp} = F_{Coul} \frac{b}{|\vec{r}|} = F_{Coul} \frac{b}{\sqrt{b^2 + x^2}}, \quad \text{b impact parameter}$$

with

$$\Delta p = \int_{-\infty}^{+\infty} \frac{ze^2}{b^2 + x^2} \frac{b}{\sqrt{b^2 + x^2}} \frac{dx}{v} = \frac{2ze^2}{vb}$$

$$\Delta E(b) = \frac{\Delta p^2}{2m_e} = \frac{2z^2 e^4}{m_e v^2 b^2}$$

where v and z are velocity and charge of the projectile.

Determine minimum and maximum impact parameter from maximum and minimum energy transfer.

Maximum energy transfer:

$$\Delta p_{max} = 2m_e v$$

$$\Delta E_{max} = \frac{\Delta p_{max}{}^2}{2m_e} = 2m_e v^2 = \Delta E(b_{min}) = \frac{2z^2 e^4}{m_e v^2 b_{min}^2}$$

$$\rightarrow b_{min} = \frac{ze^2}{m_e v^2}$$

Minimum energy transfer: from $\Delta E_{min} = I$ (mean excitation energy of the atom)

$$\rightarrow b_{max} = \frac{ze^2}{v} \sqrt{\frac{2}{m_e I}}$$

Energy loss in a collision with one atom (Z electrons, atomic number A, density ρ):

$$dE = Z \int_{b_{min}}^{b_{max}} \Delta E(b) 2\pi b db = Z \int_{b_{min}}^{b_{max}} \frac{2z^2 e^4}{m_e v^2 b^2} 2\pi b db$$

On a length $d\ell$ there are $\rho \frac{N_A}{A} d\ell$ atoms per cm^2. With $dx = \rho d\ell$ we have finally (and introducing a minus sign to take into account that energy is lost in the collisions):

$$\frac{dE}{dx_{electronic}} = -\frac{4\pi z^2 e^4 Z}{m_e v^2} \frac{N_A}{A} \ln \sqrt{\frac{2m_e v^2}{I}}$$

which is the classical derivation of Bohr of the Bethe-Bloch formula (Eq. [4-2]).

For $v << v_e$ a quantum mechanical calculation is necessary (for instance energy loss in an electron gas). At low velocities the energy loss is linearly proportional to the velocity.

$$\frac{dE}{dx} \propto v \qquad [4\text{-}5]$$

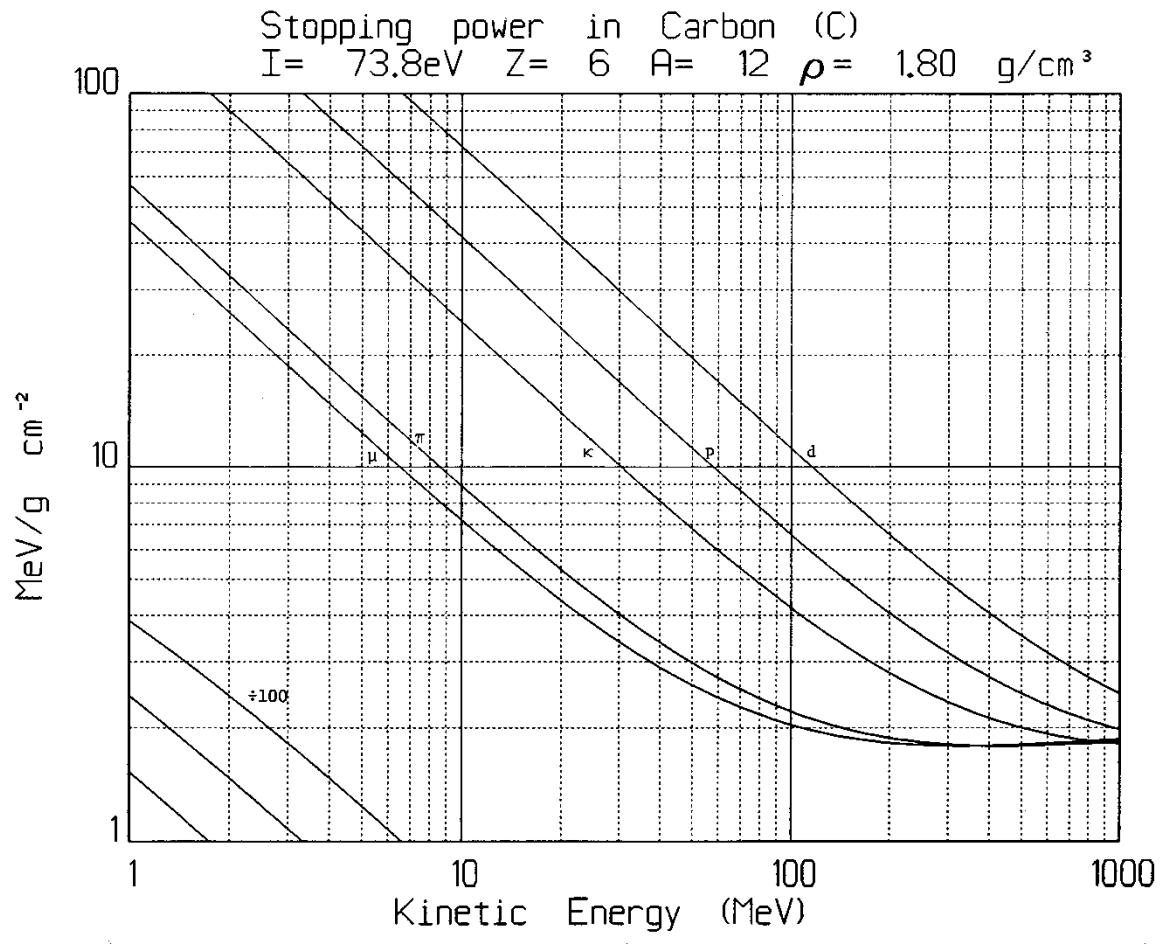

Fig. 4-2: Stopping power in Carbon.

4.2 Range of muons

Total range

$$R_{tot} = \int_{E_{in}}^{0} \frac{1}{dE/dx} dE \qquad [4\text{-}6]$$

Important for practical purposes is the projected range along the incoming trajectory.
Projected range and range straggling of surface muons:

$$R = ap^{3.5} \qquad p \text{ in MeV/c}$$

$$\frac{\Delta R}{R} = \sqrt{(0.1)^2 + (3.5\frac{\Delta p}{p})^2} \qquad [4\text{-}7]$$

For surface muons (p~ 30 MeV/c) R is typically 130 mg/cm^2, $\Delta p/p \cong 0.03$ and $\Delta R \cong 15$ % of R. Typical values of R lie therefore between 0.1 and 1 mm.
Surface muons stop in the bulk of a sample. For higher ranges (e.g. for pressure cell experiments) muons from pion-decay in-flight are used (see Chapt. 1. Introduction). For thin films we use the so called low energy muons obtained by moderation of surface muons (see Chapt. 9. Thin film and heterostructure studies with low energy muons).

Slowing down or thermalization time t

$$\frac{dE}{d\ell} = \frac{dE}{vdt} \Rightarrow t = \int dt = \int_{v_{in}}^{0} \frac{d\ell}{v} = \int_{E_{in}}^{0} \frac{dE}{v\frac{dE}{d\ell}} = \int_{E_{in}}^{0} \frac{dE}{v\frac{dE}{dx}\rho} \approx 10^{-11} \text{ s in solids}$$

$$\propto \rho^{-1} \text{ (density)}^{-1} \qquad [4\text{-}8]$$

$$\uparrow \ell = \frac{x}{\rho} \qquad [x] = [\frac{mg}{cm^2}]$$

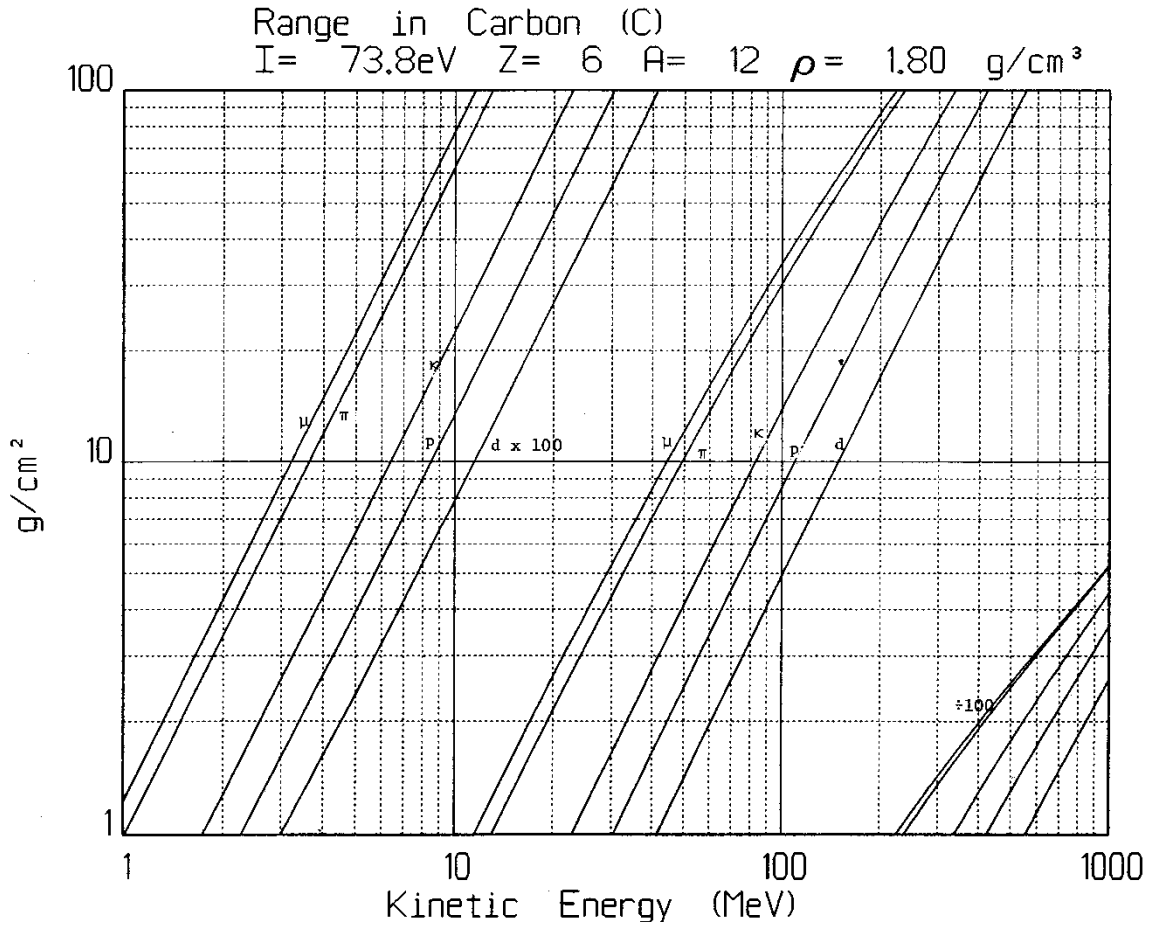

Fig. 4-3: Range in Carbon.

Range scaling:

$$R \propto \int \frac{dE}{\frac{dE}{dx}}$$

$$\frac{dE}{dx} \propto \frac{1}{v^2} \propto \frac{m}{E}$$

$$\rightarrow R \propto \int \frac{E}{m} dE \propto \frac{E^2}{m} \qquad [4\text{-}9]$$

Energy for which $R_\mu = R_p \rightarrow \frac{E_\mu{}^2}{m_\mu} = \frac{E_p{}^2}{m_p} \quad \Rightarrow \quad \frac{E_\mu}{E_p} = \sqrt{\frac{m_\mu}{m_p}} \approx \frac{1}{3}$

Range at the same energy $E \rightarrow R_p = \frac{m_\mu}{m_p} R_\mu \quad \Rightarrow R_p \approx \frac{1}{9} R_\mu$

Multiple scattering

A charged particle traversing a material experiences many small scattering events.
Therefore, the angular distribution resulting from Coulomb scattering can be approximated by a Gauss distribution.

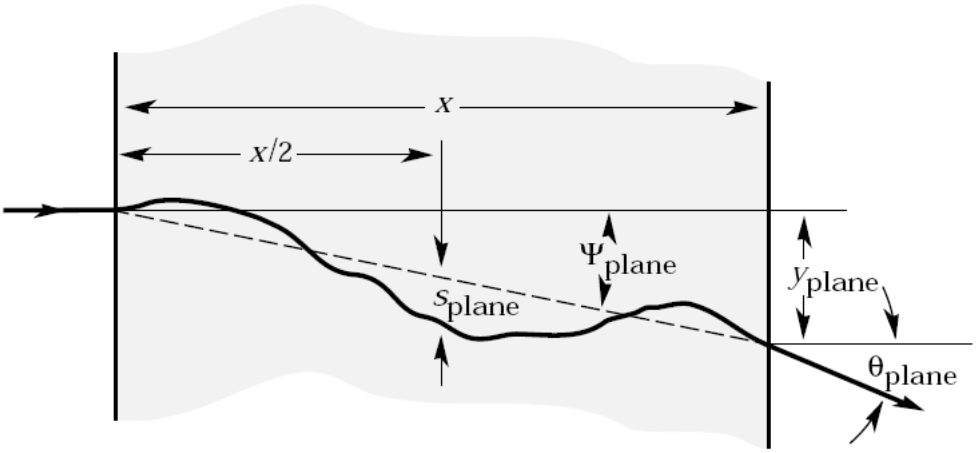

Quantities used to describe multiple Coulomb scattering. The particle is incident in the plane of the figure.

The spatial and projected angular distributions are given by:

$$\frac{1}{2\pi\theta_0^2}\exp\left(-\frac{\theta_{\text{space}}^2}{2\theta_0^2}\right)d\Omega \qquad [4\text{-}10]$$

$$\frac{1}{2\pi\theta_0}\exp\left(-\frac{\theta_{\text{plane}}^2}{2\theta_0^2}\right)d\Omega \qquad [4\text{-}11]$$

$$\text{With } \theta_0 = \theta_{\text{plane}}^{\text{rms}} = \frac{1}{\sqrt{2}}\theta_{\text{space}}^{\text{rms}} \qquad [4\text{-}12]$$

$$\theta_0 = \frac{13.6\text{MeV}}{\beta cp} z\sqrt{\frac{x}{X_0}}\left(1+0.038\ln\left(\frac{x}{X_0}\right)\right)$$

$$\text{Non relativistically:} \qquad [4\text{-}13]$$

$$\theta_0 \propto \frac{1}{mv^2} \propto \frac{1}{E_{\text{kin}}}$$

$\frac{x}{X_0}$ is the thickness of the material expressed in so called „radiation lengths“.

Radiation length: Mean distance where the energy of an energetic electron is reduced to 1/e of the initial energy by bremsstrahlung.

X_0 is a material property, $\quad X_0 = \frac{716.4A}{Z(Z+1)\ln(287/\sqrt{Z})}\ \left[\frac{g}{cm^2}\right]$ [4-14]

4.3 Thermalization of muons in gases

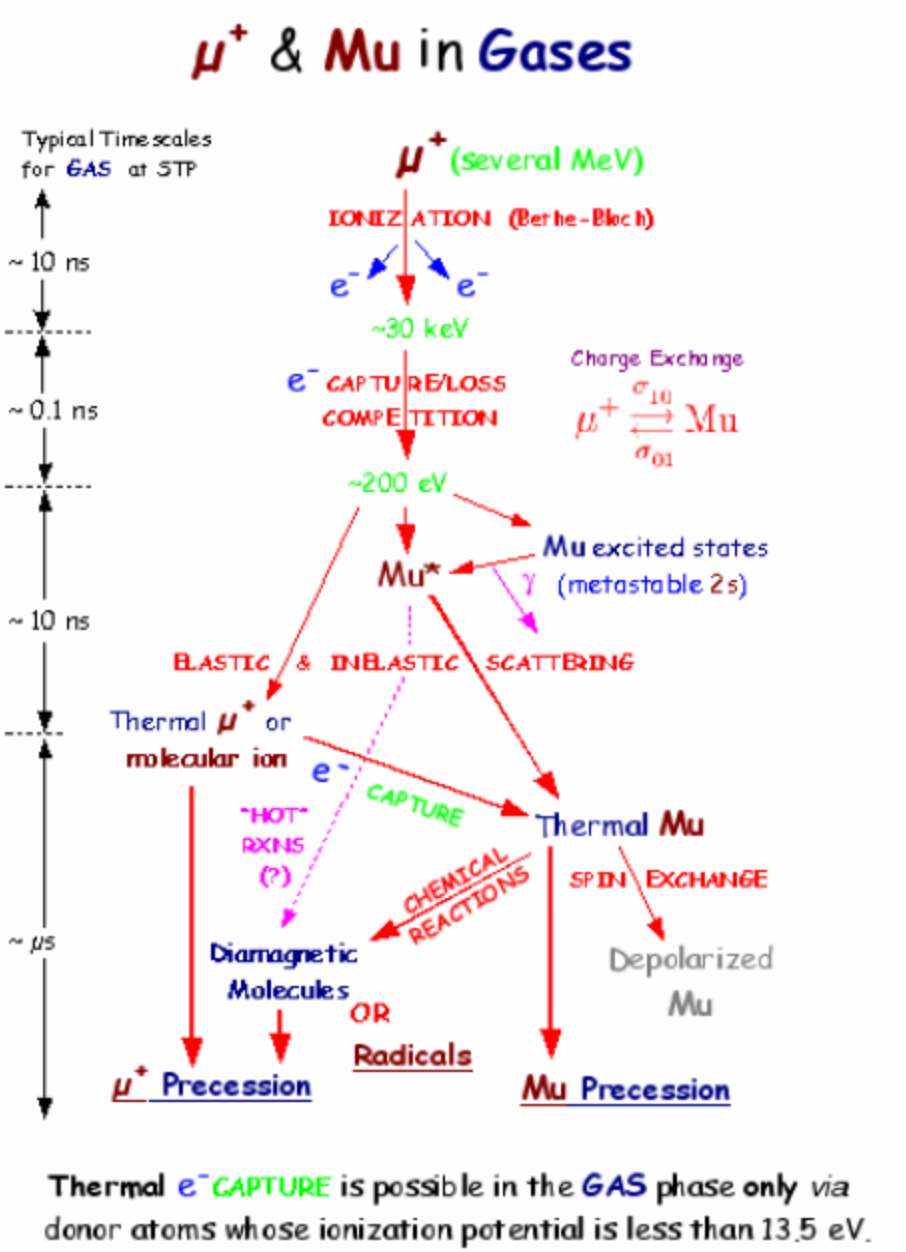

(graphics J. Brewer, UBC)

Electronic collision processes contributing to the energy loss (gas model)

Process:	Energy loss or gain:	
Ionization:		
$\mu^+ + A \rightarrow \mu^+ + A^+ + e$	$\Delta E \cong$ Ion. energy of A	[4-15]
$Mu + A \rightarrow Mu + A^+ + e$	$\Delta E \cong$ Ion. energy of A	
Electron capture (Mu formation):		
$\mu^+ + A \rightarrow Mu + A^+$	$\Delta E \cong$ Ion. energy of A - Ion. energy of Mu	
Electron loss (Break-up)		
$Mu + A \rightarrow \mu^+ + A + e$	$\Delta E \cong$ Ion. energy of Mu=13.6 eV	[4-16]

Processes involving Mu^- (negatively charged muonium) can be neglected.

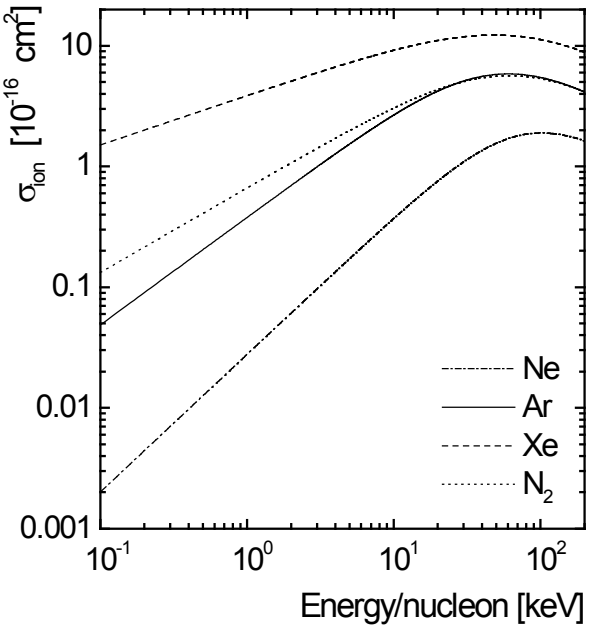

Fig. 4-4: Ionization cross sections in different gases.

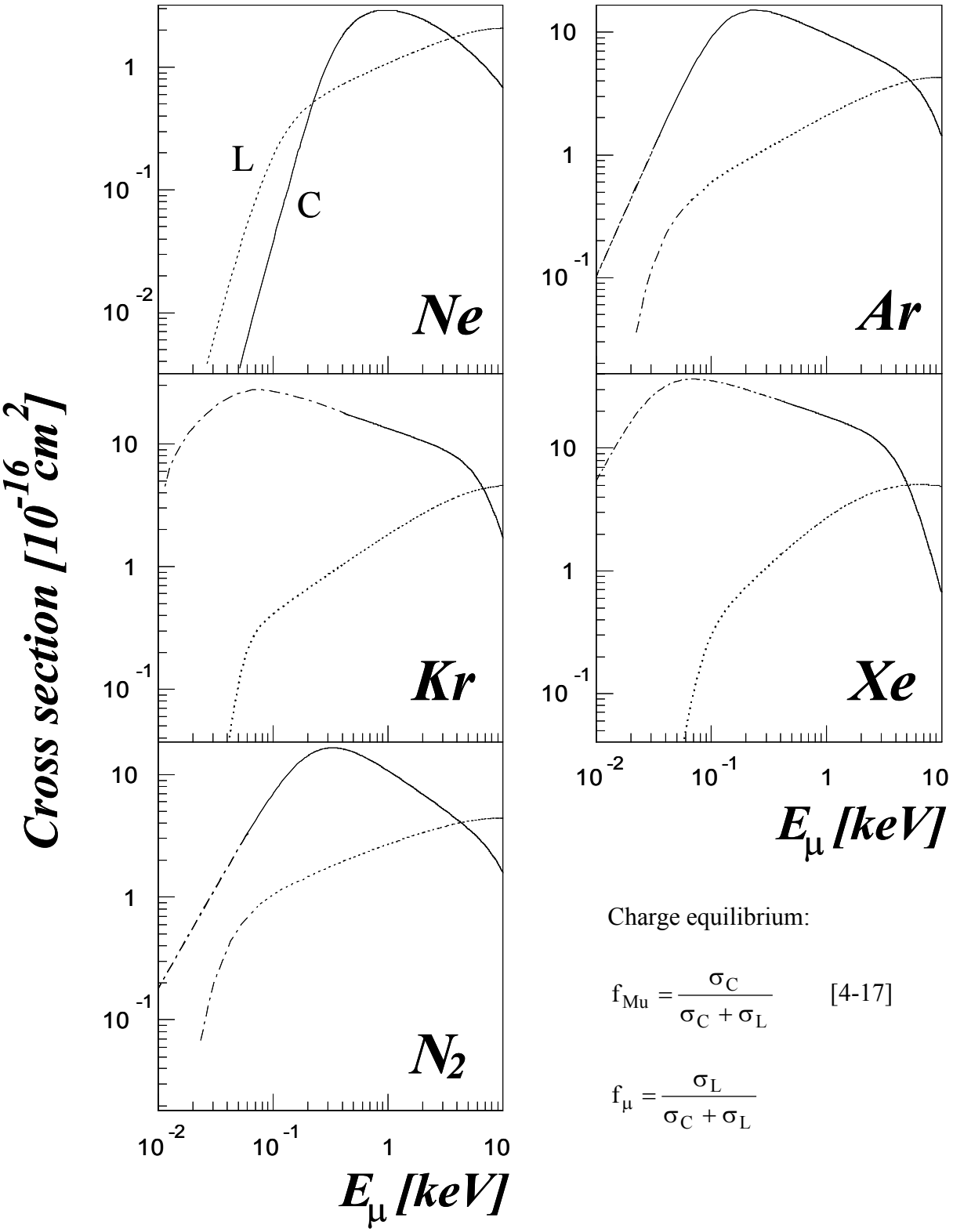

Charge equilibrium:

$$f_{Mu} = \frac{\sigma_C}{\sigma_C + \sigma_L} \qquad [4\text{-}17]$$

$$f_{\mu} = \frac{\sigma_L}{\sigma_C + \sigma_L}$$

Fig. 4-5: Muonium formation (C: electron capture, solid line) and breakup (L: electron loss, dotted line) as a function of muons energy.

Energy transfer in elastic collisions („nuclear stopping power“)

Stopping cross section (energy loss per atom/cm^2):

$$S_n = \frac{dE}{d\ell}\frac{1}{N} = \frac{dE}{d\ell}\frac{A}{N_A\rho} = \frac{dE}{dx}\frac{A}{N_A} \qquad [S_n] = [\mathrm{eV.cm^2}] \qquad [4\text{-}18]$$

N: Atomic density [Atoms/cm^3], A: Atomic weight in g, N_A: Avogadro number.

$$S_n(E) = \int T\frac{d\sigma}{d\Omega}d\Omega \qquad [4\text{-}19]$$

T kinetic energy transfer, E initial energy. From kinematics:

$$T = \frac{4m_\mu m_{tgt}}{(m_\mu + m_{tgt})^2} E\sin^2\frac{\theta}{2} = \frac{2m_\mu m_{tgt}}{(m_\mu + m_{tgt})^2} E(1-\cos\theta) \qquad [4\text{-}20]$$

$$S_n = \frac{2m_\mu m_{tgt}}{(m_\mu + m_{tgt})^2} E\int \frac{d\sigma}{d\Omega}(1-\cos\theta)d\Omega \qquad [4\text{-}21]$$

$$S_n \cong \frac{2m_\mu}{m_{tgt}} E\ \sigma_{el}(1-<\cos\theta>) \cong \overline{\Delta E}\cdot\overline{\sigma_{el}} \qquad [4\text{-}22]$$

A calculation with a screened Coulomb potential gives:

$$S_n(E_\mu) = \frac{8.462\cdot 10^{-15} Z_{tgt} m_\mu}{(m_\mu + m_{tgt})(1+Z_{tgt}^{0.23})} S_n(\varepsilon) \quad [\frac{\mathrm{eV\cdot cm^2}}{\mathrm{atom}}] \qquad [4\text{-}23]$$

Where ε is a reduced energy and $S_n(\varepsilon)$ the reduced energy loss:

$$\varepsilon = \frac{32.53 m_{tgt} E_\mu}{Z_{tgt}(m_\mu + m_{tgt})(1+Z_{tgt}^{0.23})} \cong \frac{32.53 E_\mu[\mathrm{keV}]}{Z_{tgt}(1+Z_{tgt}^{0.23})} \qquad [4\text{-}24]$$

$$S_n(\varepsilon) = \frac{0.5\ln(1+1.1383\varepsilon)}{(\varepsilon + 0.01321\varepsilon^{0.21226} + 0.19593\varepsilon^{0.5})} \qquad [4\text{-}25]$$

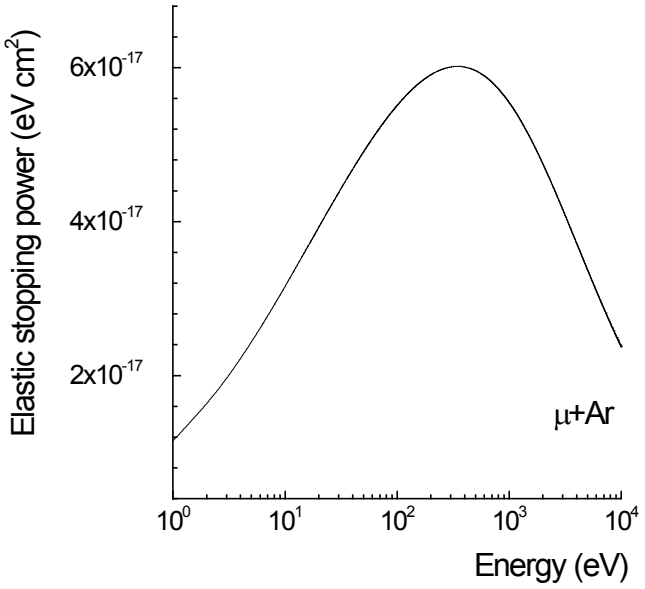

Fig. 4-6: Elastic energy loss (nuclear stopping power) of muons in Ar.

The elastic (or "nuclear") stopping power is important only at very low energies. It can be neglected for the stopping processes of surface muons. However, it is important in the mechanisms leading to the generation of low energy muons (see Chapt. 9. Thin film and heterostructure studies with low energy muons).

4.4 Muonium formation in gases (prompt or epithermal muonium formation)

TABLE II. Relative fractions (in percent) of muonium (f_{Mu}) and of diamagnetic μ^+ (f_μ) found in different gases.

Target gas	Pressure or range in pressure (atm)	f_μ	f_{Mu}	f_H^b
He	1.2—3.1	100±1	0±1	15
	50[a]	99±5	1±5	
Ne	1.2	93±5[c]	7±5[c]	20
	26[a]	100±2	0±2	
Ar	1.0—2.8	26±4	74±4	85
	30[a]	35±5	65±5	
Kr	0.4—0.95	0±5	100±5	100
Xe	0.4—0.65	0±4	100±4	100
	4.4[a]	10±5	100	
H_2	3.0	39±4	61±4	95
N_2	1.0—2.4	16±4	84±4	90
NH_3	2.8	9±4	91±4	100
CH_4	1.2—3.0	13±4	87±4	100

[a]Higher-pressure values from earlier study of Stambaugh *et al.*, Ref. 17.
[b]Expected neutral fraction from proton-charge-exchange studies (Refs. 3 and 4).
[c]Taken from the research grade Ne result of Table I which gives the most reliable μ^+ and Mu amplitude.

$$f_\mu + f_{Mu} = 1$$

The thermalized muonium fraction f_{Mu} increases with decreasing ionization energy.

Gas	Ionization potential [eV]	f_{Mu}
He	24.5	0
Ne	21.6	0.06±0.05
Ar	15.8	0.74±0.04
Kr	14.0	1.0±0.05
Xe	12.1	1.0±0.04
N_2	15.6	0.84±0.04

TABLE III. Number of charge-changing cycles and slowing-down times for the μ^+ in gases.

Gas	N_c[a]	Pressure (atm)	$t_1(ns)$[b]	$t_n(ns)$[c]	$t_3(ns)$[d]
He	111	3.1	30	0.077	0.63
Ne	53	1.2	18	no data	8.2
Ar	76	1.0	14	0.014	19.1
Kr	95	0.8	10	0.014	50.2
Xe	no data	0.6	11	$\lesssim$.014[e]	101
H_2	71	3.1	30	0.043	0.32
N_2	77	1.0	18	0.030	13.4

[a]$E_i > 35$ keV, $E_f = 1$ keV, except in case of Ne where available proton data extends down only to an equivalent 4.4-keV μ^+ energy.
[b]Bethe-Bloch ionization, from 3 MeV to 35 keV.
[c]Time spent as neutral during the charge-exchange regime, from 35 to 1 keV. The actual total time t_2 spent in this region would be a factor of 2—3 longer.
[d]Final thermalization time from 50 eV to 0.035 eV (300 K) assuming elastic collisions only and an energy-independent cross section of 10^{-15} cm^2.
[e]Complete data not available, but t_n expected to be less than in Kr.
(from D.G. Fleming, et al., Phys. Rev. **A 26,** 2527 (1982)).

4.5 Thermalization of muons in solids

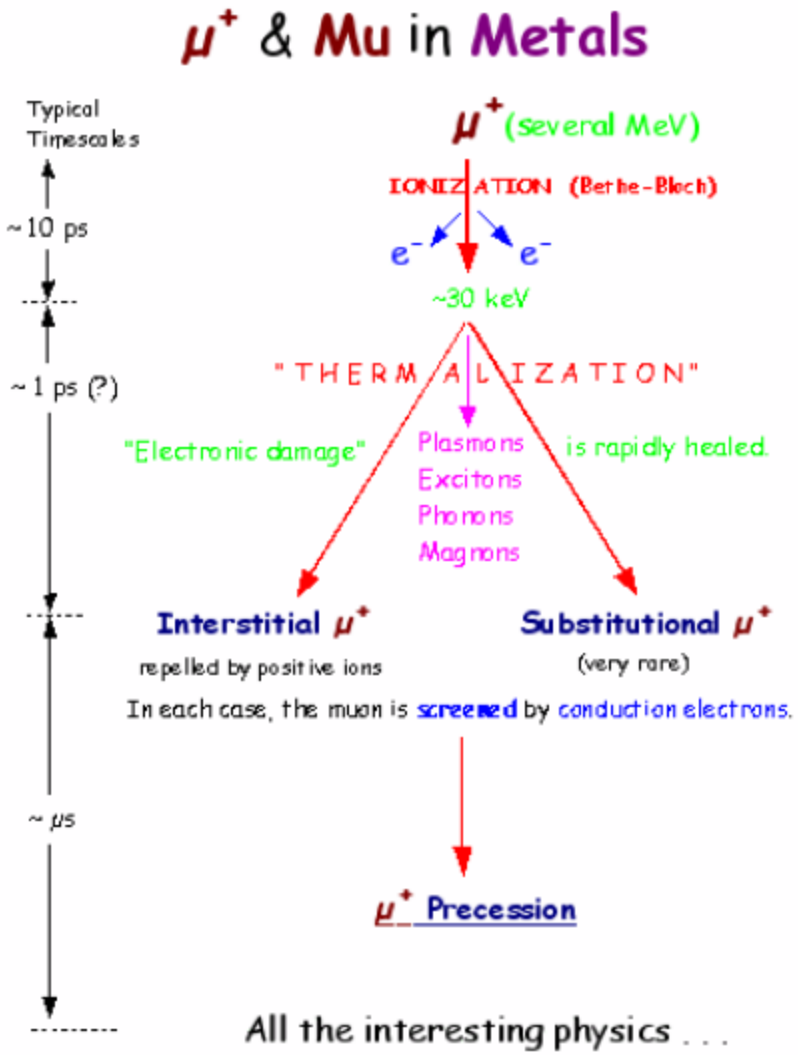

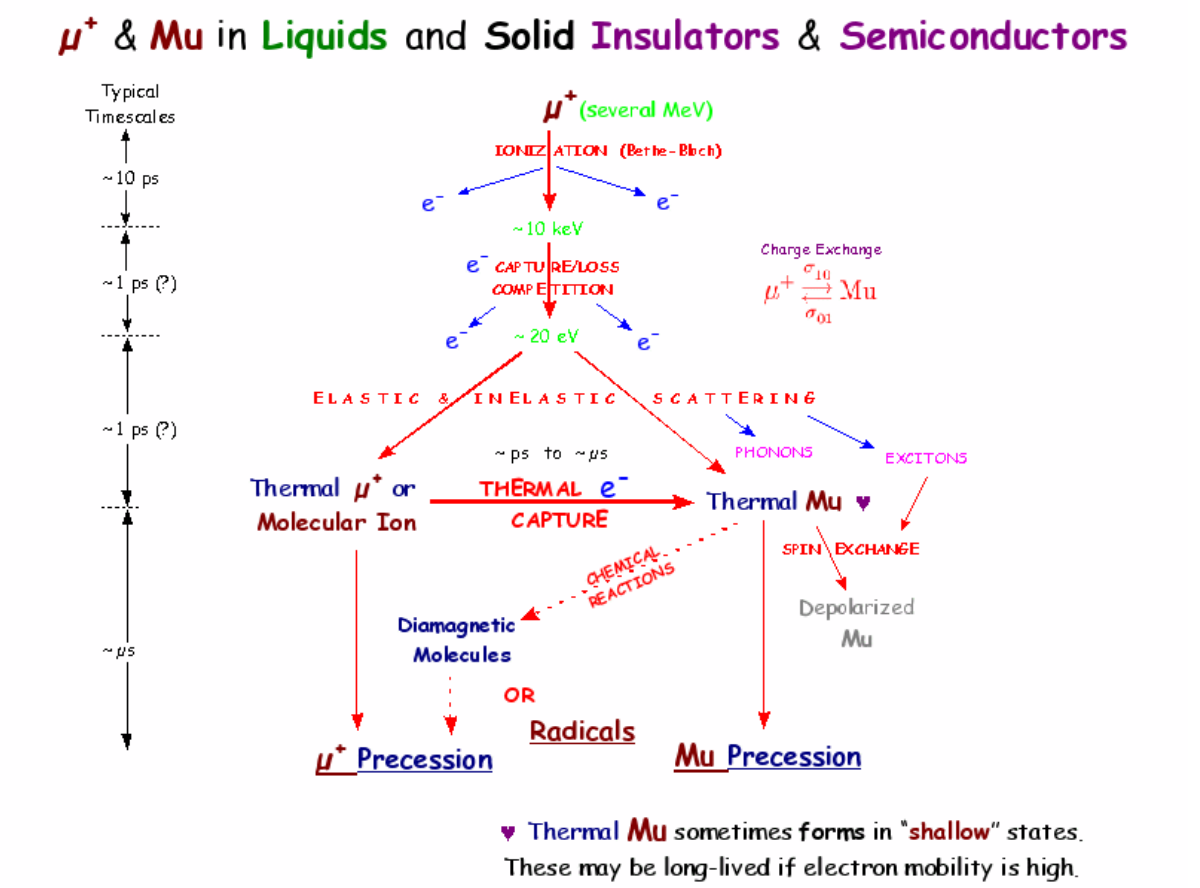

(graphics J. Brewer, UBC)
More similar to slowing down processes in gases.

The Coulomb attraction between a thermalized positive muon and an electron from the track may lead to "delayed" muonium formation, i.e. muonium formation after thermalization of the muon. The formation probability depends on the electron transport properties in the corresponding medium.

Consider the thermalization track in insulators and semiconductors:

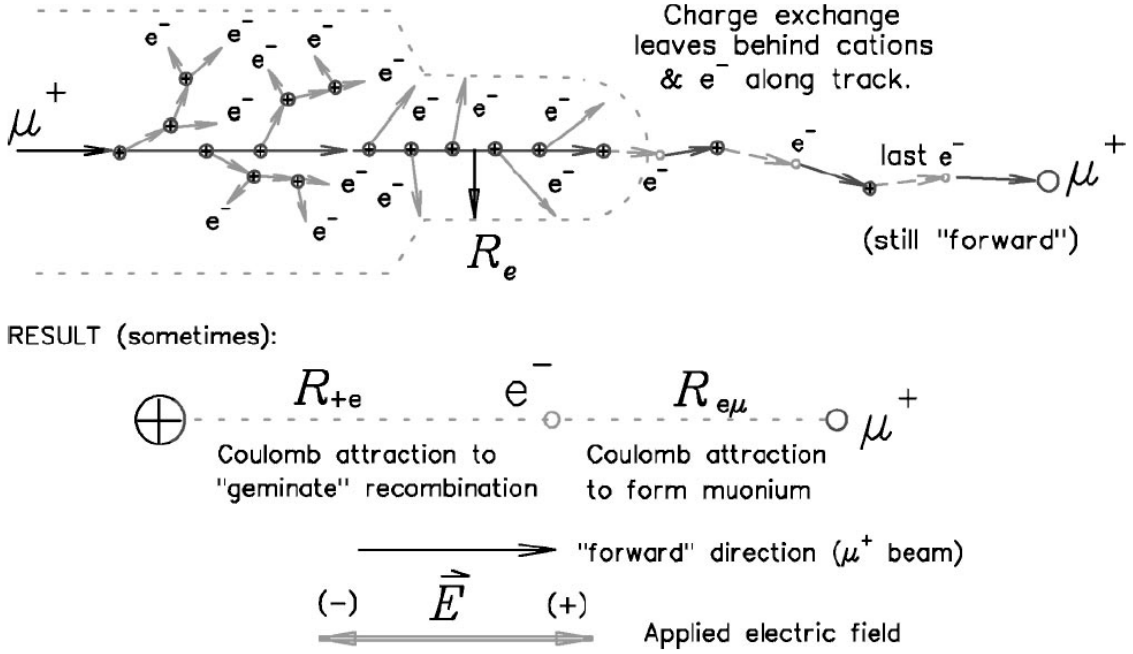

Fig. 4-7: Model for processes occurring at the end of the muon track in a frozen Van der Waals gas. (from D. Eshchenko et al., Phys. Rev. B **66**, 035105 (2002)).

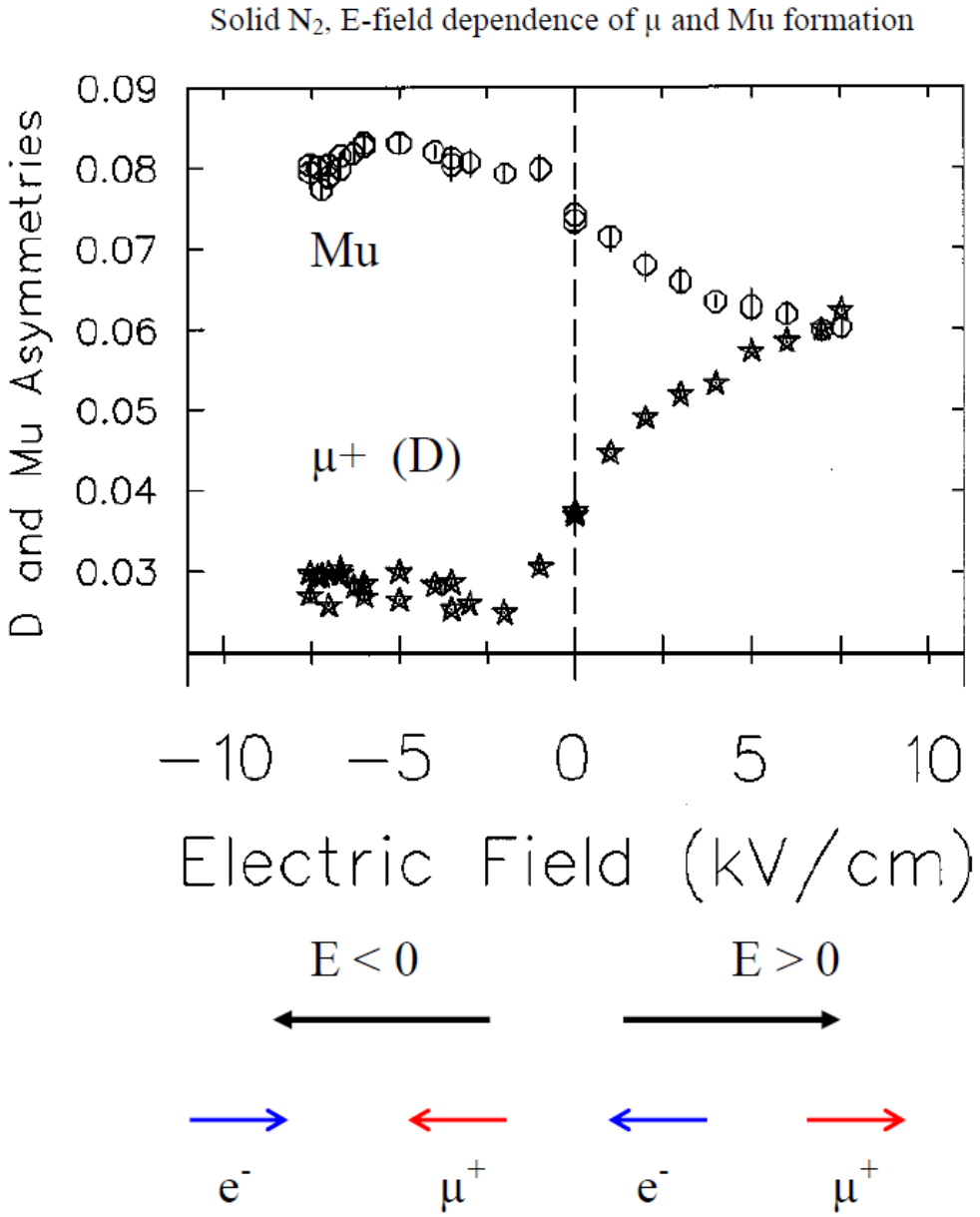

$R_{e\mu}$ (mean distance between electron and muon) and τ (muonium formation time) can be determined from the field dependence of the muonium formation probability (proportional to the muonium initial asymmetry $A_{Mu}(0)$). In α-N_2 at 20K one obtains $\langle R_{e\mu} \rangle \approx 50$ nm. From this experiment the electron mobility b_e can de derived microscopically ($\vec{v}_e = b_e \vec{E}$) and the state of the electron investigated (V. Storchak et al., Phys. Rev. B **59**, 10559 (1999)).

Example:
β-N_2 (hcp), τ=30 ns, $R_{e\mu}$ = 25 nm, $b_e \sim 10^{-3}$ $cm^2/V/s$ (T> 35.6 K)
→ Electron localized
α-N_2 (fcc), τ<<1 ns, $R_{e\mu}$ = 50 nm, $b_e > \approx 10^2 cm^2/V/s$ (T<35.6 K)
→ very large electron mobility, e.g. electron is delocalized

4.6 Positive muon in metals

A positive muon represents a positively charged impurity at a generally interstitial position of the lattice. To first approximation the muon behaves like a proton (but with different zero point energy, quantum mechanical effects...). The charge and spin of the muon change local the electron and electron spin density.

Electron- and spin distribution around a μ^+ (p) in a metal:

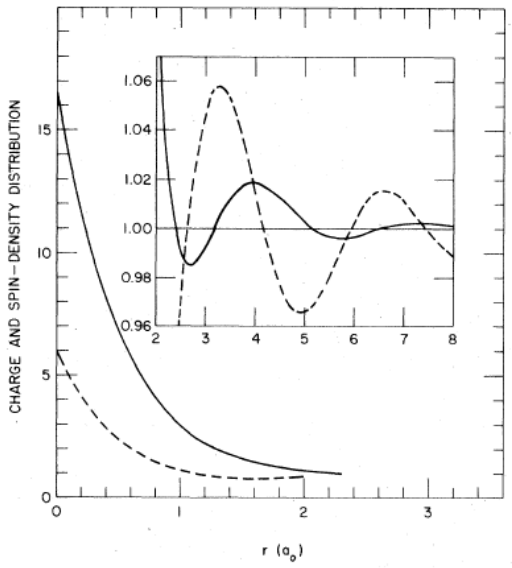

Fig. 4-8: Charge- and spin-density distribution around a positive muon in a spin-polarized electron gas with r_s=2 and polarization ξ_0 =0.17. The solid and dashed curves correspond respectively to normalized charge density $n(r)/n_0$ and normalized spin density $\frac{n^{\uparrow}(r)-n^{\downarrow}(r)}{n_0^{\uparrow}-n_0^{\downarrow}}$. From P. Jena et al., Phys. Rev B **17**, 301 (1978).

n_0: free electron density. Definition of r_s : Radius of a sphere (in units of Bohr radius), which contains one electron: $n_0 = \frac{1}{\frac{4}{3}\pi(r_s a_0)^3}$, a_0 : Bohr Radius

The charge impurity represented by the muon increases the electron density at the muon site (see figure 4-8) from n_0 to n(r) and modifies the spin polarization of a spin polarized gas from $\xi_0 = \frac{n_0^{\uparrow}-n_0^{\downarrow}}{n_0}$ to $\xi(r) = \frac{n^{\uparrow}(r)-n^{\downarrow}(r)}{n(r)}$.

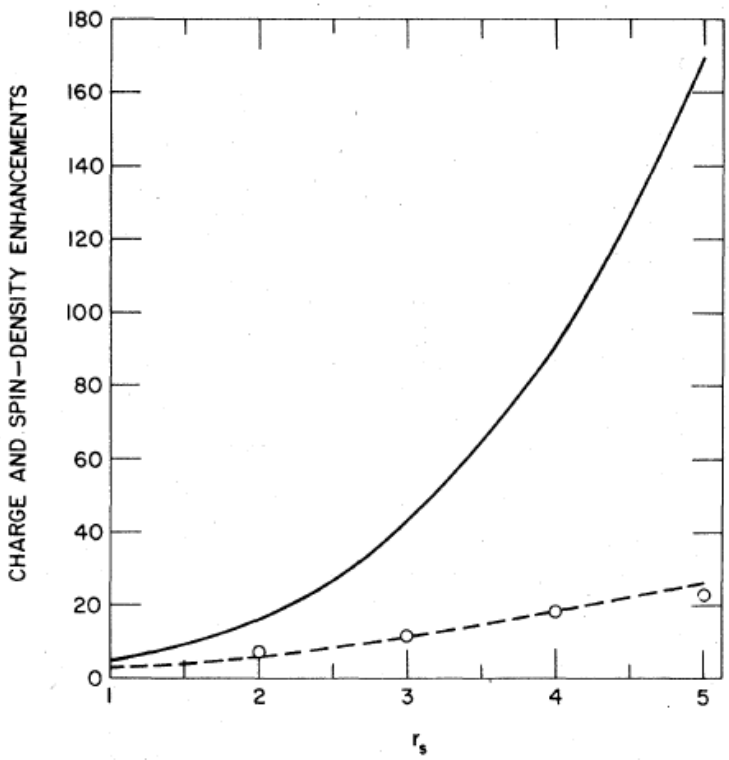

Fig. 4-9: Charge- and spin-density enhancements at a μ^+ site for bulk densities $1< r_s<5$. The solid and dashed curves correspond respectively to normalized charge density $n(0)/n_0$ and normalized spin density $\frac{n^{\uparrow}(0)-n^{\downarrow}(0)}{n_0^{\uparrow}-n_0^{\downarrow}}$. From P. Jena et al., Phys. Rev B **17**, 301 (1978).

Note that the spin density at the origin is enhanced over the ambient polarization to a much lesser degree than the charge density.

Comparison of local electron densities:

- Electron gas (undisturbed) with r_s=2 (typical): $n_0(r_s=2)=\frac{1}{\frac{4}{3}\pi(2a_0)^3}$

- Electron gas with muon impurity (see Fig. [4-8]): $n(0)=16n_0=\frac{16}{\frac{4}{3}\pi(2a_0)^3}$

- Free muonium (density at muon site): $\frac{1}{\frac{4}{3}\pi a_0{}^3}=\frac{1}{2}n(0)$

In a metal the electron density at the muon site is comparable to the value in muonium. In spite of this, if we stop muons in a metal we do not observe muonium formation: the screening of the Coulomb potential hinders its formation and the scattering of the electron with the conduction electrons makes such a state very short lived. A short lived „bound state" with two electrons (Mu^-) and very small binding energy is however in principle possible.

Screening in a metallic medium

Macroscopically there is no electric field inside a metal. This means that a single positive charge must be screened within a few Angstroems.
The semi-classical Thomas-Fermi approximation describes the static screening response ($\omega=0$) at long wavelengths ($k << k_F$), which corresponds to a slowly varying potential as a function of position *r* relative to the impurity charge.

In this approximation the dielectric constant can be approximated as:

$$\varepsilon(0,\vec{k}) = 1 + \frac{k_{s,TF}^{\ 2}}{k^2} \quad \text{(see e.g. Kittel, Solid state physics)} \qquad [4\text{-}26]$$

and the screened Coulomb potential becomes:

$$V_{scr}(\vec{r}) = -\frac{e^2}{4\pi\varepsilon_0}\frac{e^{-\vec{k}_{s,TF}\vec{r}}}{|\vec{r}|} \qquad [4\text{-}27]$$

In this potential the long-range nature of the bare Coulomb potential is exponentially suppressed with a screening length scale of $l_{scr} = 1/k_{s,TF}$.

For a 3D free electron gas

$$l_{scr} \approx 0.5\left(\frac{n_c}{a_0^{\ 3}}\right)^{-1/6} \qquad [4\text{-}28]$$

For a typical metal (e.g. Cu) we get $l_{scr} \approx 0.054$ nm. This indicates that the Coulomb potential range is cut off within a lattice parameter. In a semiconductor, the screening length can be considerably longer because the carrier concentration is much smaller; for a typical value of $n_c = 10^{14}$ cm^{-3}, $1/k_{s,TF} \approx 1.7$ nm.

A refinement to the original Thomas-Fermi calculations was done by Lindhard (J. Lindhard, Kgl. Danske Videnskab. Selskab Mat.-Fys. Medd., **28** (1954)) predicting a lesser degree of screening and an oscillating structure at larger distances from the impurity.
Since the Thomas-Fermi approximation is a long-range approximation it cannot adequately describe the response of the electron gas to a short-range perturbation caused by a point-like charge. In order to get a more accurate description, Lindhard replaced the T-F dielectric function with:

$$\varepsilon(0,\vec{k}) = 1 + \frac{k_{s,TF}^{\ 2}}{k^2} F\left(\frac{k}{2k_F}\right) \qquad [4\text{-}29]$$

where

$$F(x) = \frac{1-x^2}{4x}\log\left|\frac{1+x}{1-x}\right| + \frac{1}{2} \qquad [4\text{-}30]$$

and obtained the following expression for the screened impurity potential

$$V_{scr}^{L} \propto \frac{x}{(2+x^2)^2}\frac{\cos(2\vec{k}_F\vec{r})}{r^3} \qquad x \equiv \frac{k_{s,TF}}{2k_F} \qquad [4\text{-}31]$$

The main feature of this potential is the oscillatory $1/r^3$ behaviour also known as Friedel or RKKY oscillations (see Chapt. 6. Some applications in magnetism).

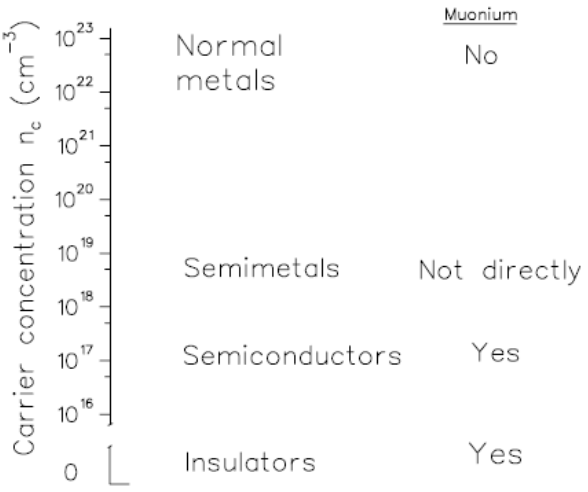

Fig. 4-10: Range of carrier concentrations in various groups of material with their characterization with respect to experimentally observed muonium (from J. Chakhalian, PhD Thesis, UBC 2002).

4.7 Negative muons in matter: muonic atoms $\mu^- Z$

A thermalized μ^- is captured by the Coulomb potential of the atoms and forms an excited muonic atom. The negative muon behaves as a heavy electron (capture in an atomic shell, followed by cascade de-excitation via Auger and X-ray emission). After the cascade the muon can be captured in the nucleus.
The thermalized μ^- will be captured in an excited state with similar energy and size as the 1s-level of the corresponding hydrogen-like atom. Initial state of the muonic atom:

Bohr radius: $r_n{}^e = \frac{a_0}{Z} n^2, \qquad r_n{}^\mu = \frac{a_0}{Z}\frac{m_e}{m_\mu} n^2$

from $r_1{}^e = r_n{}^\mu \quad \rightarrow \quad n = \sqrt{\frac{m_\mu}{m_e}} \cong 14$

The formation of muonic atoms leads to depolarization as a consequence of spin-orbit coupling, cascade and hyperfine interaction with the nucleus $I \neq 0$.
(This is one of the reasons why negative muons are less useful than positive muons for muon spin rotation and relaxation experiments).

Estimate of depolarization:

Classically the initial polarization P_{in} is reduced by a factor 3 because of the spin orbit (LS) coupling (here $\vec{S}_\mu$: μ^- spin, $\vec{L}$: angular momentum of the atomic shell of capture):

$$P_{in}\frac{\int_{-1}^{1}(\cos\theta)^2 d(\cos\theta)}{\int_{-1}^{1} d(\cos\theta)} = \frac{1}{3}P_{in} \qquad ,(\cos\theta)^2 \propto (\vec{L}\cdot\vec{S}_\mu)(\vec{L}\cdot\vec{S}_\mu)$$

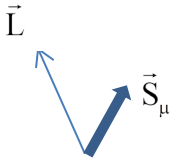

The analog quantum mechanical expression is:

$$P = \frac{1}{3}P_{in}\left(1 \pm \frac{2}{2L+1}\right), \qquad \text{for } J = L \pm \frac{1}{2}$$

Atomic capture of μ^-

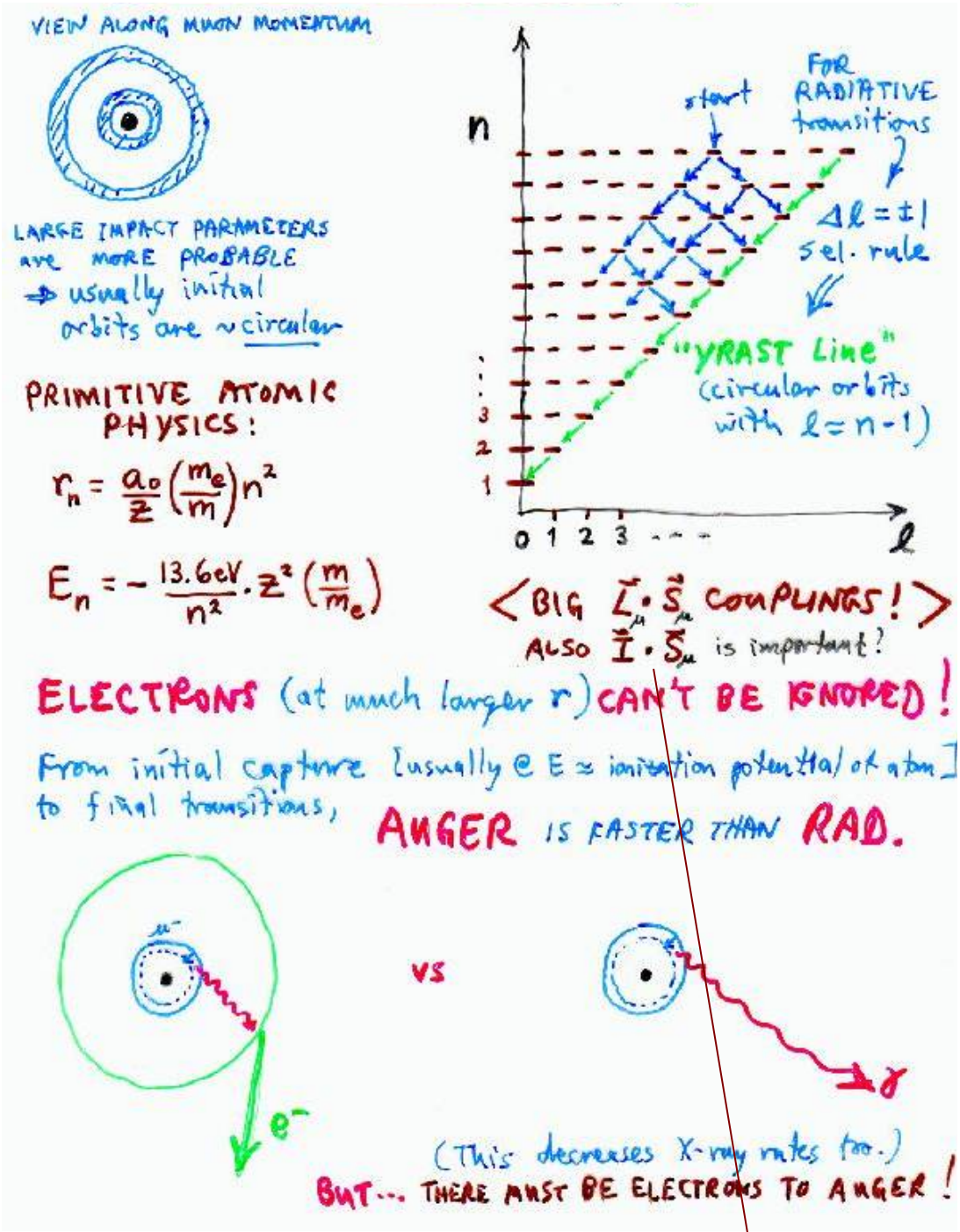

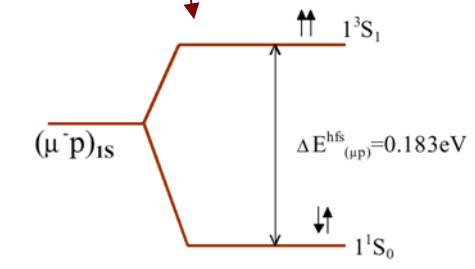

$A \propto |\varphi(0)|^2$

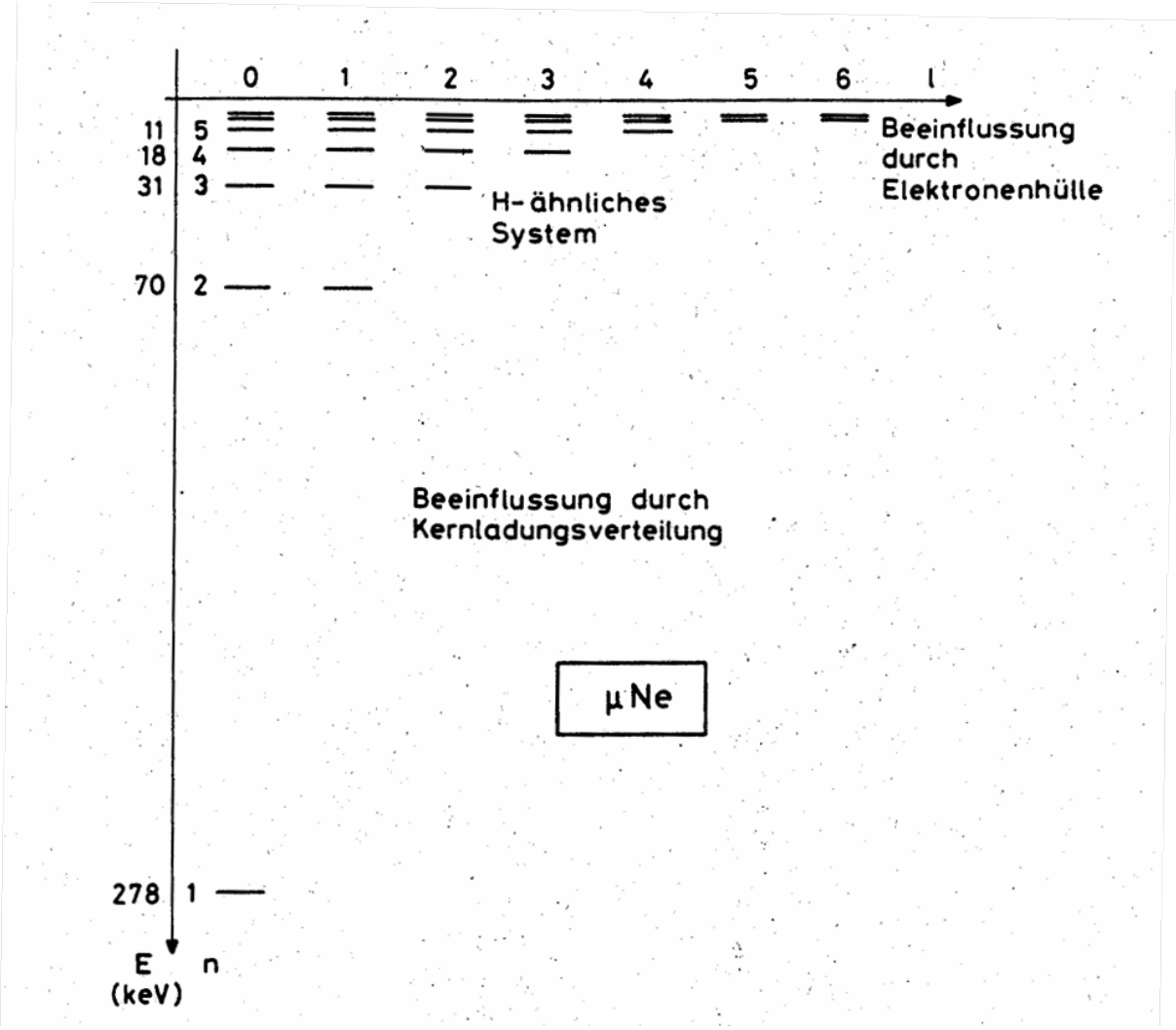

Fig. 4-11: Energy levels of hydrogen-like muonic neon.

Comparison of binding energies in electronic and muonic atoms:

Bohr model:

$$E_n^e = 13.6\frac{Z^2}{n^2} \quad [eV]$$

$$E_n^\mu = 13.6\frac{Z^2}{n^2}\frac{m_\mu}{m_e} \quad [eV] \qquad [4\text{-}32]$$

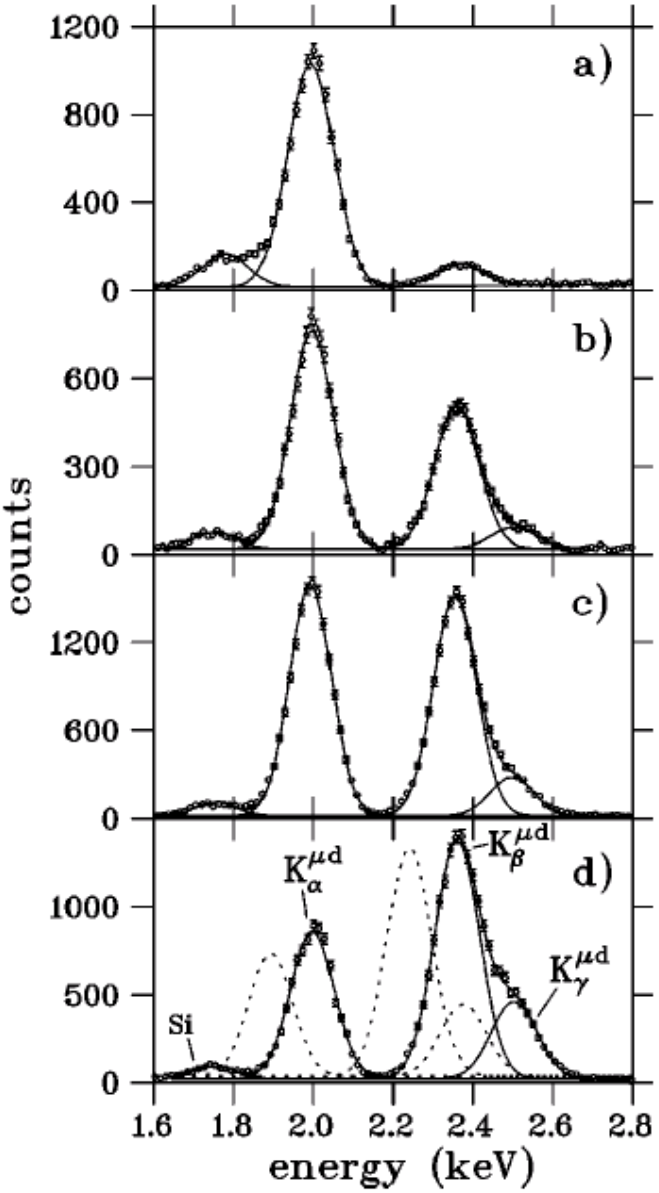

Fig. 4-12:

Energy spectra of muonic x rays observed in deuterium at various target densities Φ (given in units of LHD): (a) Φ = 1.145, (b) Φ = 0.0783, (c) Φ = 0.0399, (d) Φ = 0.0133. The lines corresponding to the $K_\alpha^{\mu d}$, $K_\beta^{\mu d}$, and $K_\gamma^{\mu d}$ transitions are separated. The solid lines indicate Gaussian fits. The density dependence of the line intensities is clearly visible. The x-ray peak at 1.74 keV is due to fluorescence excitation of the detector's silicon material. The isotopic energy shift compared to muonic hydrogen is demonstrated in (d), where the dotted lines display the corresponding $K^{\mu p}$ lines which were observed in muonic hydrogen [8].

Life time of negative muons in muonic atoms. The capture process

$\mu^- + p \rightarrow n + \nu_\mu$

shortens the natural lifetime of μ^-.

Muon capture probability in the nucleus as a function of atomic number Z:

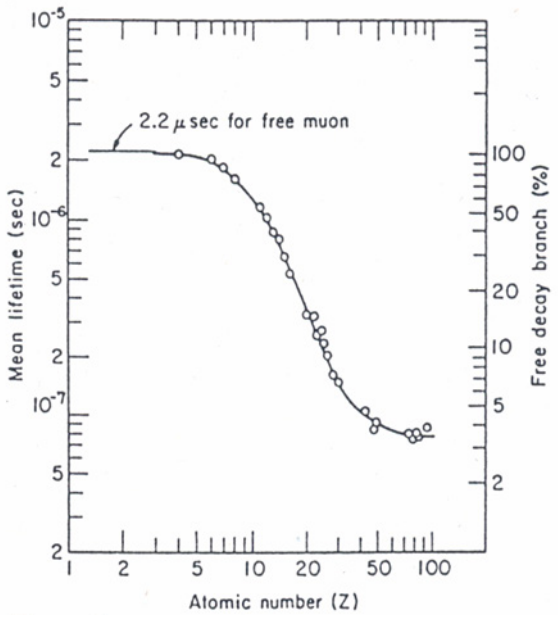

Fig. 4-13: Negative lifetime and free decay branch as a function of atomic number.

Up to Z ≈ 10 the total rate is comparable with the decay rate.
The decay rate (1/lifetime in matter) is proportional to the probability to find a negative muon in the volume of the nucleus, where it is then captured:

$$\int_{\text{Nucl. vol.}} |\phi^{1s}(r)|^2 d^3r \approx |\phi^{1s}(0)|^2 R^3_{\text{Nucleus}}$$

$$R_{\text{Nucleus}} \cong 1.75\, Z^{\frac{1}{3}}\,[\text{fm}]$$

$$\phi^{1s}(r) = \frac{1}{\sqrt{\pi a^3}} e^{-r/a}, \quad a = \frac{a_0}{Z}\left(\frac{m_e}{m_\mu}\right) \quad a_0 = 0.053\ \text{nm}$$

$$|\phi^{1s}(0)|^2 = \frac{1}{\pi a^3}$$

$$|\phi^{1s}(0)|^2 R^3_{\text{Nucleus}} \propto Z^3 Z \qquad \Rightarrow \text{ capture probability } \propto Z^4$$

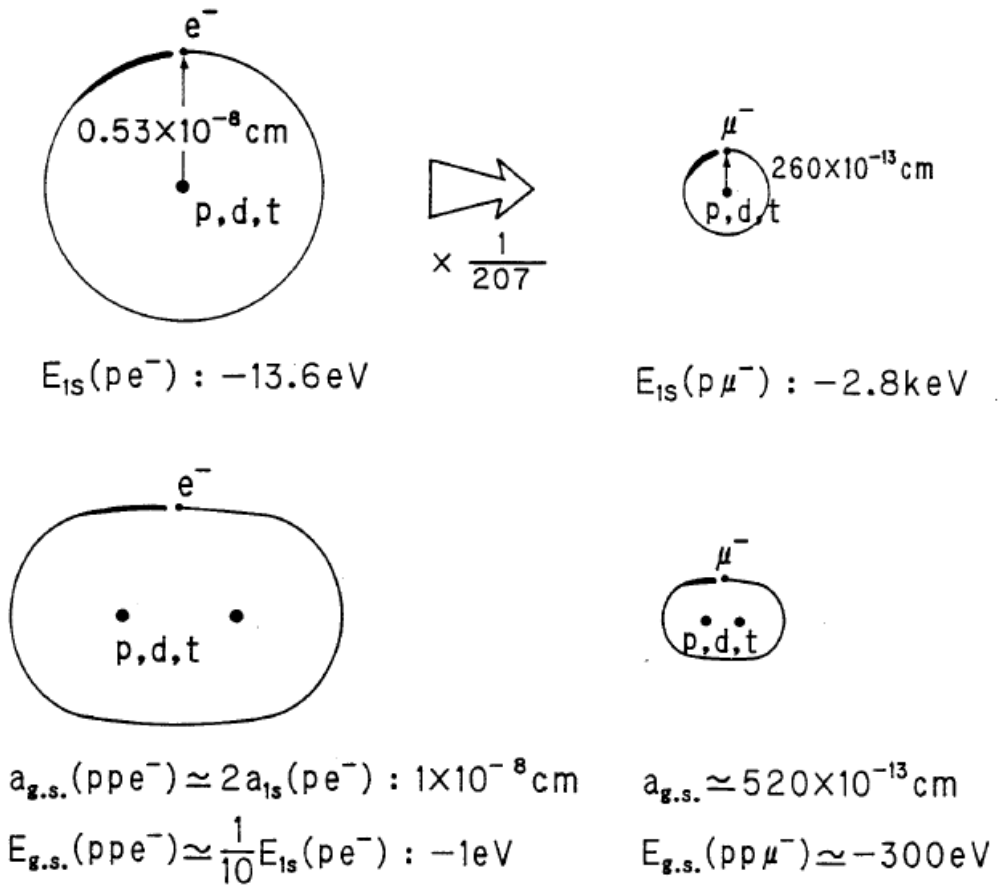

Fig. 4-14: Basic properties of the muonic hydrogen atom and of the muonic hydrogen molecular ion.

4.8 Muon Catalyzed Fusion (μCF)

Muon catalyzed fusion: Idea: induce nuclear fusion via formation of muonic molecules and muon capture. Can we gain energy by this process?

Fusion rate is determined by:

- Collisions between muonic atoms and atoms
- Elastic collisions
- μ^- - Transfer
- Resonant processes (depend on hyperfine state of the molecule)

Energy cycle:

$$d\mu t \rightarrow \mu\alpha + n$$

(3.5 MeV) (14.1 MeV)

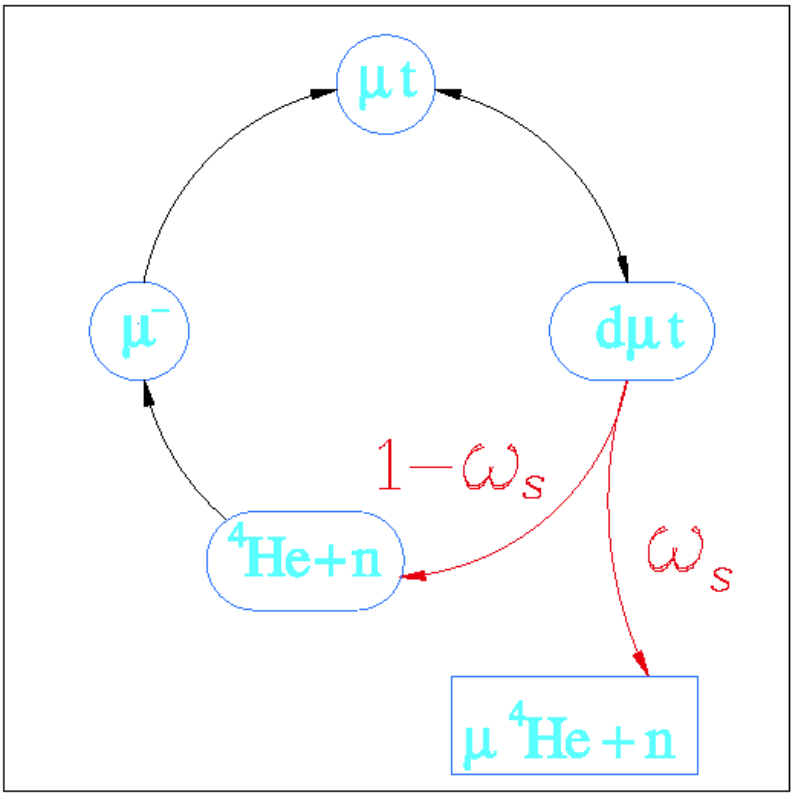

ω_s Sticking probability

Other possible reactions:
p+d → ^{3}He + γ (5.5 MeV)
p+t → ^{4}He + γ (19.8 MeV)

Energy production via μCF ?

The fusion yield is limited by the sticking process.

Fusion yield per muon:

$$Y_n = \frac{1}{(\frac{\lambda_0}{\lambda_c} + W)}$$

$\lambda_0 = \frac{1}{\tau_\mu}$ muon decay rate

λ_c cycling rate

$W \sim \omega_s$

for $W \to 0$ $\quad Y_n \to \frac{\lambda_c}{\lambda_0} \approx 430$

for $\lambda_c >> \lambda_0$ $\quad Y_n \to \frac{1}{W} \approx 175 \;\Rightarrow\; 17.6\ \text{MeV} \cdot 175 \cong 3\ \text{GeV}$ per muon

Energy production?

Assume a flux of 10^{16} μ^-/sec

Power: $10^{16}/\text{s} \cdot 3 \cdot 10^9\ \text{eV} = 3 \cdot 10^{25}\ \text{eV/s} \cdot 1.6 \cdot 10^{-19}\ \text{J/eV}$ → 5 MW

(To compare: the Leibstadt nuclear power plant delivers 1275 MW).

5. Principles of Muon Spin Rotation/Relaxation/Resonance

The expression μSR is the acronym for Muon Spin Rotation/Relaxation/Resonance and underlines the analogy with NMR (Nuclear Magnetic Resonance). There are, however, important differences (see key features of μSR, next page). For instance with μSR it is possible to perform measurements without applying a magnetic field (so called zero field μSR, ZF) a big advantage with respect to NMR because this allows to investigate magnetic systems without perturbation. NQR (Nuclear Quadrupole Resonance) is also a zero field technique, but for magnetic investigations less direct than zero field μSR.

The method is based on the observation of the time evolution of the polarization P(t) of an ensemble of muons implanted in a sample. This quantity contains the physical information about the interaction of the muon magnetic moment with its local environment. P(t) is obtained from the intensity of decay positrons as a function of time after implantation.

The muon acts as a local very sensitive magnetic probe. Value ($\omega_L = \gamma_\mu B_{loc}$), direction, distribution and dynamics of internal (microscopic) magnetic fields can be measured. Such fields may be produced by electronic moments, nuclear moments or local currents as those in superconductors. With μSR it is also possible to determine magnetic, non-magnetic, and superconducting fractions. Muonium acts as a Hydrogen isotope, e.g., in chemical reactions or as impurity in semiconductors and insulators and gives information about its electronic environment.

In a μSR experiment one measures the positron rate with scintillators, which are placed around the sample.

The positron is emitted preferentially in the spin direction of the muon at the moment of the decay.

$$\frac{dN_{e^+}(t)}{d\Omega} \propto (1 + AP\cos\theta) = (1 + A\vec{P}(t)\cdot\hat{n}) \qquad [5\text{-}1]$$

A: Asymmetry parameter (the theoretical decay asymmetry averaged over the positron energy is 1/3, see Chapt. 1. Introduction). $\hat{n}$ is the direction of observation, defined by the position of the detectors.

After detecting the positrons from several 10^6 stopped muons, one obtains histograms as in Fig. 5-1, which in the ideal case have following dependence (t=0 is the implantation time, N_{bg} is a time independent background):

$$N_{e^+}(t) = N_0 e^{-\frac{t}{\tau_\mu}}(1 + A_0\vec{P}(t)\hat{n}) + N_{bg} \qquad [5\text{-}2]$$

The recorded events in the positron histograms reflect the time evolution of the polarization of the muon ensemble. A_0 is the experimentally observable maximum asymmetry, generally smaller than 1/3.

5.1 Key features of μSR

Muons are **purely magnetic** probes (I = ½, no quadrupolar effects[7])

Local information, mainly **interstitial** probe → complementary to NMR

Large magnetic moment: $\mu_\mu = 3.18\ \mu_p = 8.89\ \mu_n$ → **sensitive** probe

Particularly suitable for:
Very weak effects, small moment magnetism ~ $10^{-3}\ \mu_B$ /Atom
Random magnetism (e.g. spin glasses)
Short range order (where neutron scattering is not sensitive)

Independent determination of **magnetic moment** and of **magnetic volume fraction**

Determination of magnetic/non-magnetic/superconducting fractions

Full polarization in zero field, independent of temperature → unique measurements without disturbance of the system (typical polarization in NMR $< I_z >= \frac{\gamma_N \hbar I(I+1)}{3k_B T} B$ is very small. NMR needs high magnetic fields and low temperatures)

Single particle detection → extremely high sensitivity

No restrictions in choice of materials to be studied

Fluctuation time window: $10^{-5} < t < 10^{-11}$ s

Bound state: μ^+e^- muonium, used as H-Isotope for spectroscopy, impurity studies, radical chemistry, reaction kinetics

Other features:

Number of implanted muons << number of atoms → negligible sample damage
No perturbation of the system (unlike spin probes in EPR)
No special isotope is needed (as in NMR, Mössbauer)

---

[7] $Q =< I, M_I = I \left| 3z^2 - r^2 \right| I, M_I = I >$ since $3z^2 - r^2 \propto Y_{2,0}$ (irreducible tensor operator), by Wigner-Eckart theorem: $Q =< I, I \left| 3z^2 - r^2 \right| I, I >= C < I, I \left| 3I_z^2 - I^2 \right| I, I >= C \cdot I(2I-1)$, i.e. Q=0 for I=0 or I=1/2 (see C. Slichter, Principles of Magnetic Resonance, Chapter 9).

5.2 Experimental details

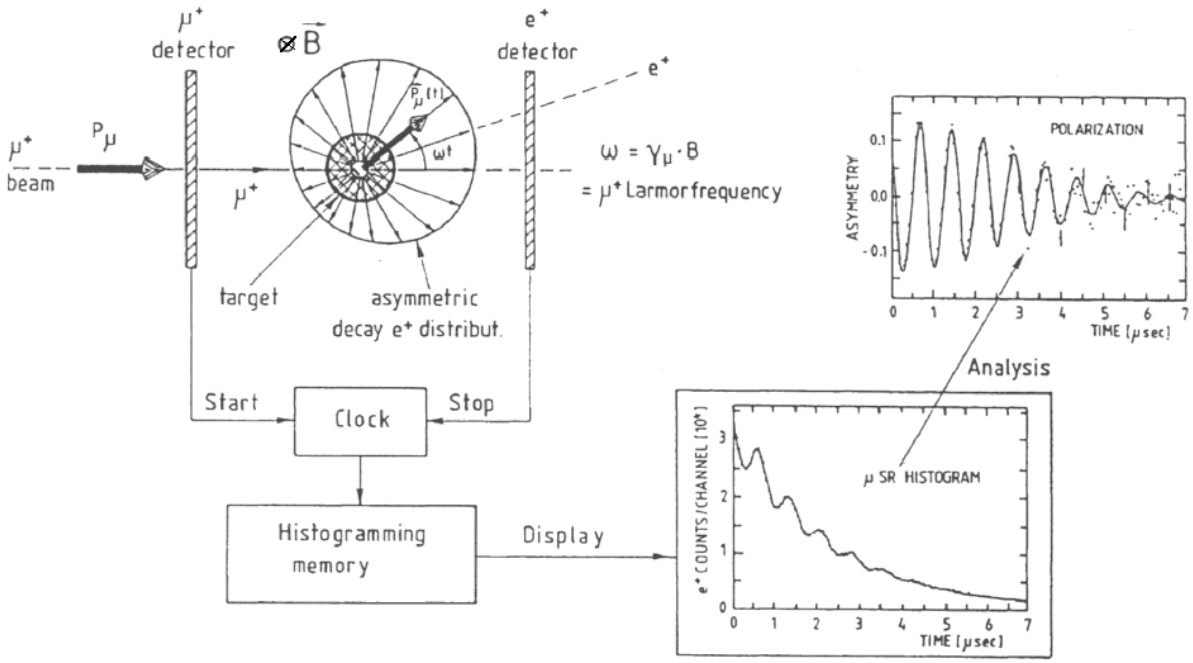

Fig 5-1: Principle of a μSR-measurement in transverse field (TF) (Time differential μSR).

a)

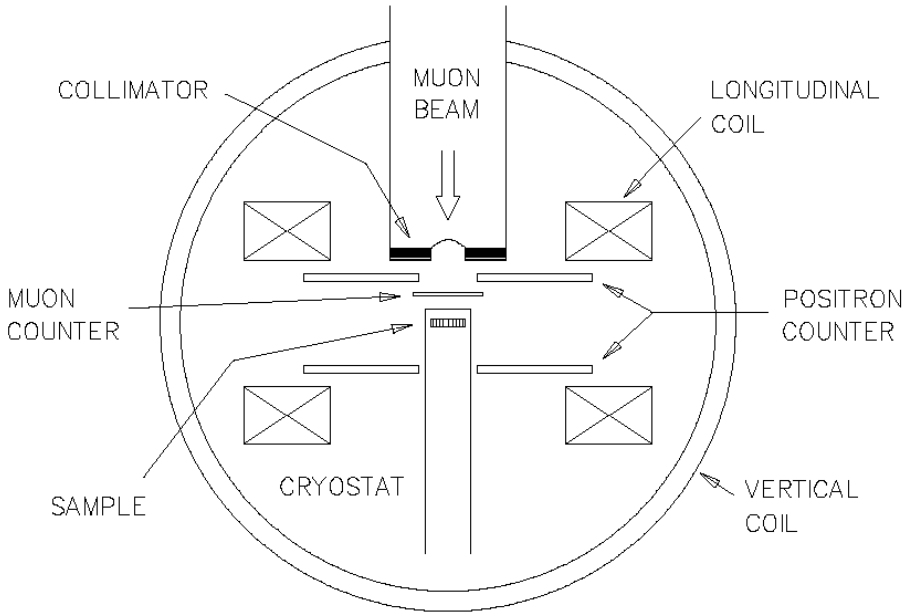

b)

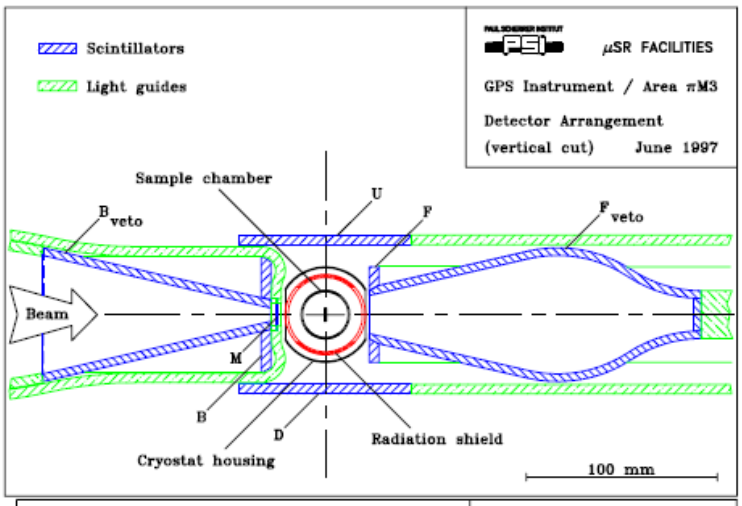
Scintillators
Light guides
μSR FACILITIES
GPS Instrument / Area πM3
Detector Arrangement
(vertical cut) June 1997
Sample chamber
U
B veto
F
F veto
Beam
M
B
D
Radiation shield
Cryostat housing
100 mm

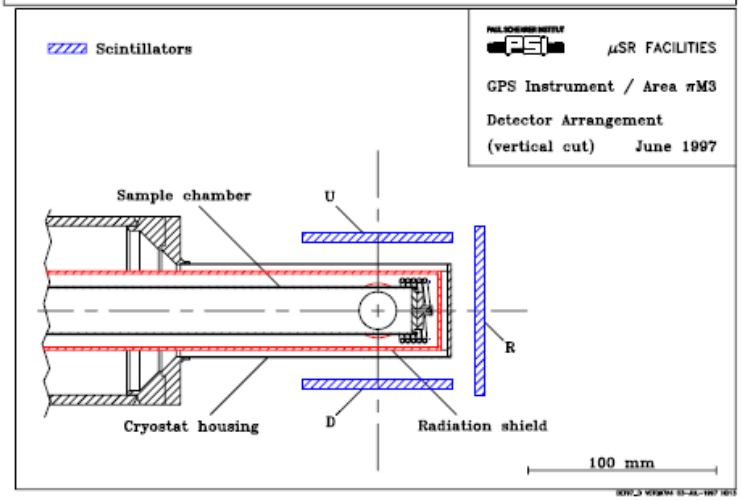
Scintillators
μSR FACILITIES
GPS Instrument / Area πM3
Detector Arrangement
(vertical cut) June 1997
Sample chamber
U
R
Cryostat housing
D
Radiation shield
100 mm

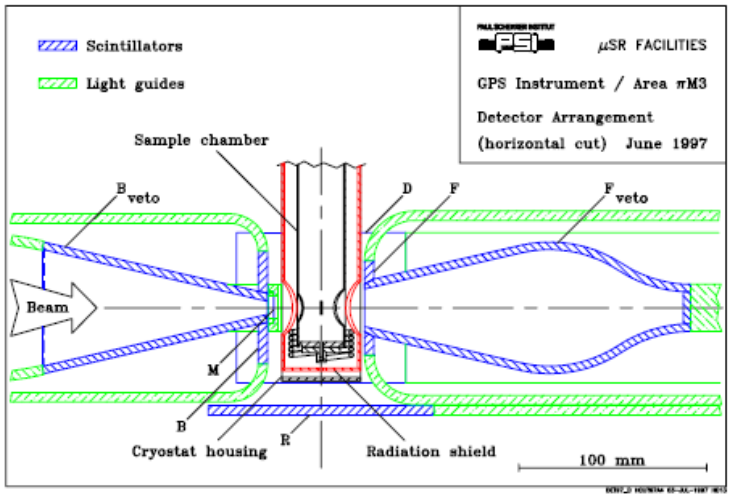
Scintillators
Light guides
μSR FACILITIES
GPS Instrument / Area πM3
Detector Arrangement
(horizontal cut) June 1997
Sample chamber
B veto
D
F
F veto
Beam
M
B
R
Cryostat housing
Radiation shield
100 mm

c)

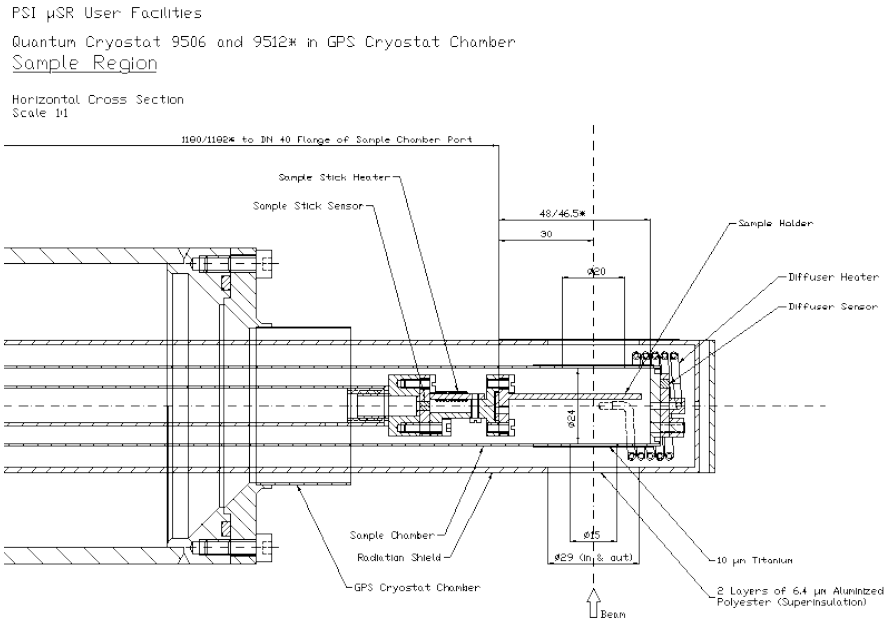

Fig 5-2: a) Schematic of a µSR apparatus, top view. b) Detailed view of detectors and c) sample region of the General Purpose Spectrometer (GPS) at PSI.

One distinguishes between continuous muon beams (PSI and TRIUMF, Canada) and pulsed beams (ISIS/RAL, UK and J-PARC, Japan).
At PSI the accelerator time structure (50 MHz microstructure) and the pion lifetime (26 ns) leads to a practically continuous surface muon beam:

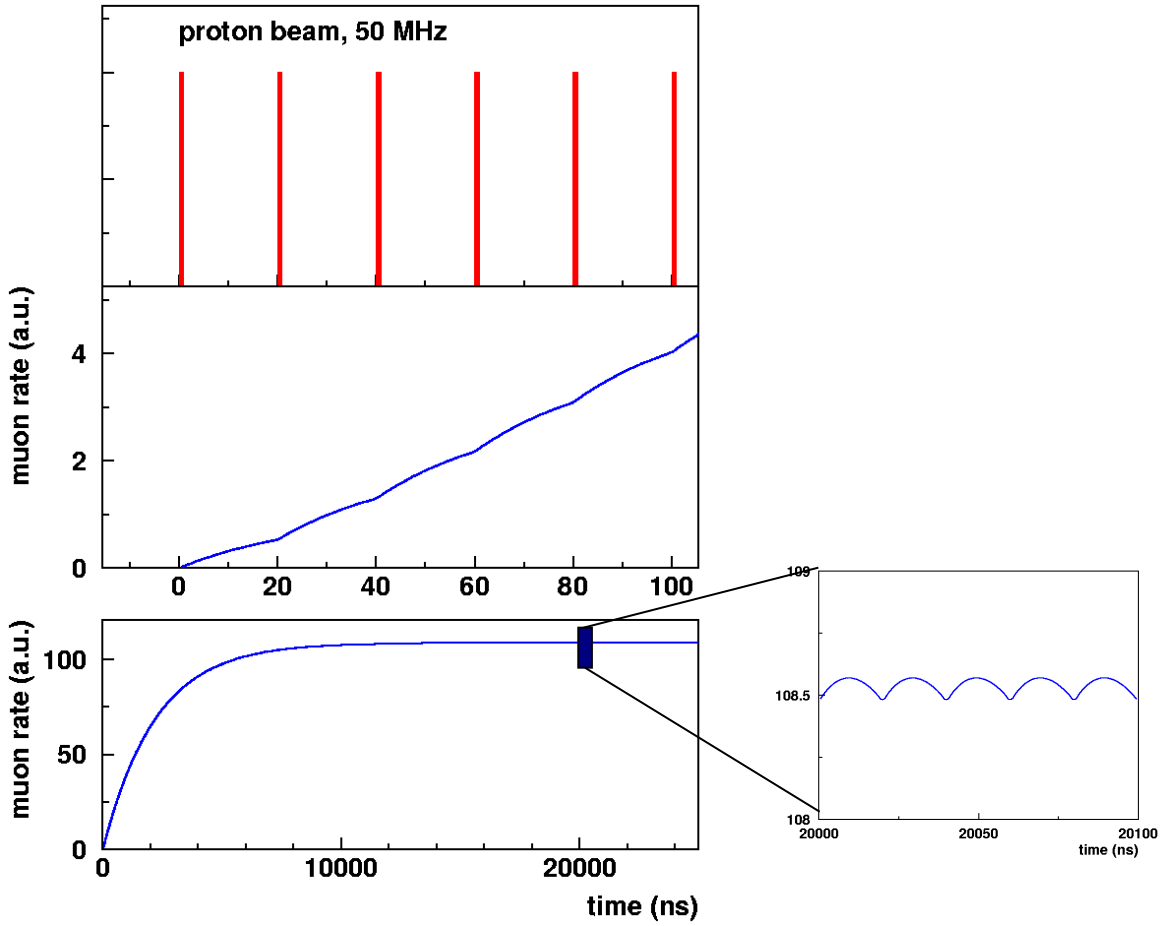

Fig. 5-3: Build-up of the muon rate at PSI.

In a μSR experiment with continuous beam one has to take care that only one muon at a time is present in the sample before decaying, otherwise the time correlation between muon and its decay positron is lost (see Fig. 5-1). This is done electronically (rejection of second muon event by analysis of the timing diagram) and by limiting the incoming muon rate.

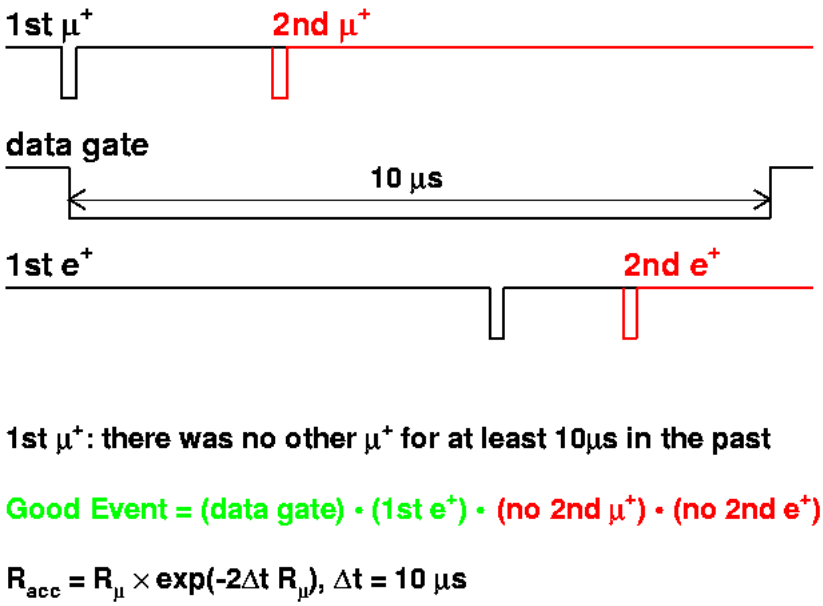

Fig 5-4: Timing diagram of a μSR experiment at a continuous muon beam facility such as PSI.

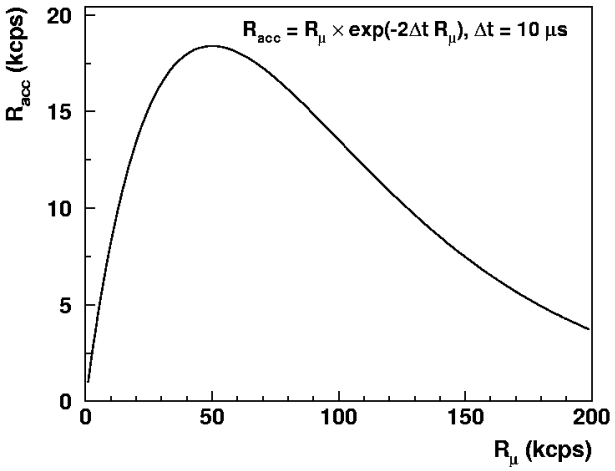

Fig. 5-5: Accepted rate as a function of incoming rate for a time window of 10 µs. $\exp(-2\Delta t R_\mu)$ is the probability that there is no second event in an interval Δt if the rate is R_μ.

At a pulsed machine all the muons are contained in a pulse (50-100 ns wide) with low repetition rate (25-50 Hz). The implantation time is given by this pulse. All the decay positrons of a pulse are measured at once. This allows a higher rate. However, one has to take care either to have only one positron in a detector within the observation time, or if there are more than one to get the time stamp for each one. This requires a high segmentation of the positron spectrometer.
A big disadvantage of a pulsed machine is that the time resolution is given by the pulse width (50-100 ns), whereas at a continuous beam line the time resolution is determined by the muon counter which is typically better than 1 ns.
A pulsed beam has in principle a lower background than a continuous beam and allows a better exploitation of a pulsed environment. At PSI, the so-called muon on request electrostatic kicker device (MORE) allows only one muon at the time in the apparatus. This reduces the background, while keeping the excellent time resolution of the continuous beam.

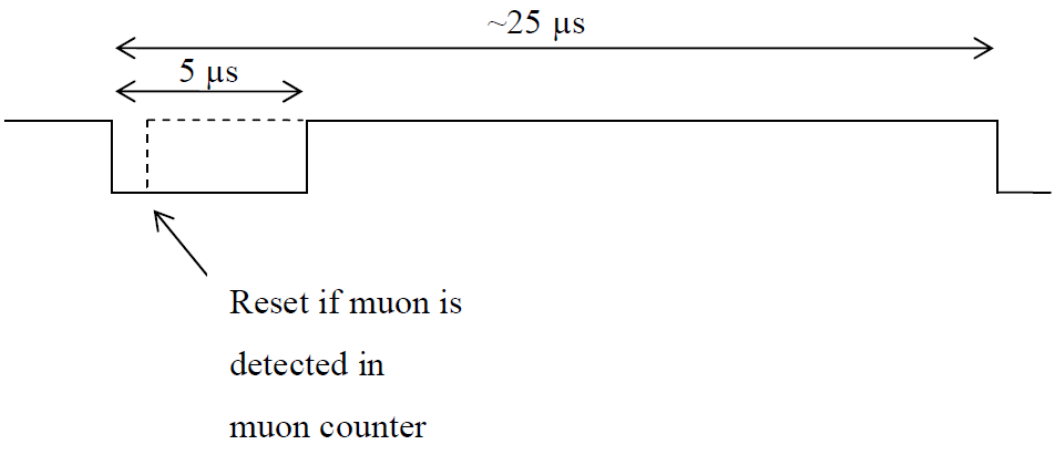

In the MORE mode the muon detector (M-counter) in the spectrometer (GPS or LTF) is used to trigger the kicker. The kicker is switched to the spectrometer running in "MORE mode" (say, GPS) for a maximum of 5µs at a fixed repetition rate (max. 40 kHz). The signal of the first muon hitting the trigger detector (M-counter) after a minimum delay of 200ns is used to switch the kicker back to the spectrometer running in "parasitic mode" (Low Temperature Facility, LTF in this case). The delay is necessary to avoid damage to the power switches.

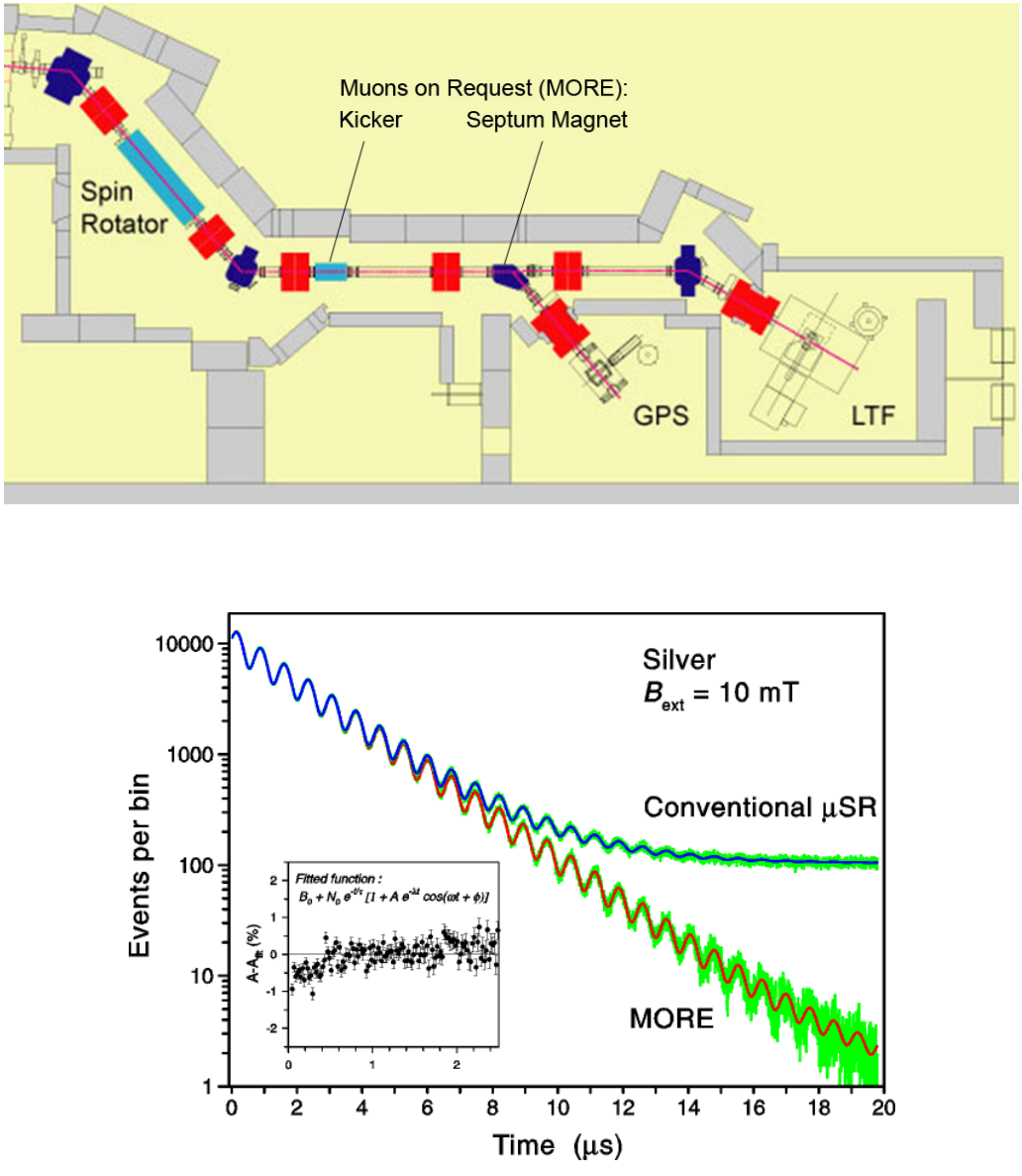

Fig. 5-6: Top: Layout of the GPS/LTF beam areas at PSI with spin rotator and MORE. Bottom: Example of µSR in silver in an external magnetic field of 10mT, taken with the GPS instrument (General Purpose Spectrometer) at PSI in MORE mode. For comparison a conventional spectrum taken at the same event rate is shown. The background in MORE mode is at least a factor of 100 lower than in conventional mode, thus easily allowing the study of muon-spin precession and relaxation up to 20 µs. Insert: Reduced asymmetry plot for the first 2µs in MORE mode.

	Conventional	MORE	Pulsed μSR
Trigger	none	GPS	50 Hz
B_0/N_0 [10^{-5}]	660	8.7	ca. 1
Time resol. [ns]	<1	<1	80
Event. rate [10^6/h]	12	20	20-100

Table: Comparison of results obtained with GPS in conventional and in MORE mode (using the GPS muon-counter as trigger). Values for pulsed μSR (at ISIS Rutherford Appleton Laboratory, UK) are also shown.

After background subtraction the number of events in a detector placed in direction $\hat{n}$ (normally defined by the direction of the incoming muon beam or of the initial polarization):

$$N_{e^+}(t) = N_0 e^{-\frac{t}{\tau_\mu}}(1 + A_0\vec{P}(t)\hat{n}) \qquad [5\text{-}3]$$

$$\vec{P}(t)\hat{n} = P(t) = \frac{<\vec{I}(t)\cdot\hat{n}>}{|\vec{I}(0)|} \qquad < \; > : \text{ Average is over the muon ensemble}$$

e.g. for forward (F: forward with respect to muon spin $\vec{I}$) and backward (B) detectors we have:

$$N_F(t) = N_0 e^{-\frac{t}{\tau_\mu}}(1 + A_0\vec{P}(t)\cdot\hat{n}_F)$$
$$N_B(t) = N_0 e^{-\frac{t}{\tau_\mu}}(1 + A_0\vec{P}(t)\cdot\hat{n}_B) = N_0 e^{-\frac{t}{\tau_\mu}}(1 - A_0\vec{P}(t)\cdot\hat{n}_F) \qquad [5\text{-}4]$$

The asymmetry A(t) is obtained from:

$$A(t) = A_0 P(t) = \frac{N_F(t) - N_B(t)}{N_F(t) + N_B(t)} \qquad [5\text{-}5]$$

A_0 is a parameter to be determined experimentally. It depends on factors such as detector solid angle, efficiency, absorption and scattering of positrons in the materials on the way from sample to detector. Generally, $A_0 < 1/3$ (intrinsic decay asymmetry). Typical values lie between 0.25 and 0.3.
The function A(t) contains the information about the physics. In a real spectrometer one has to consider that the solid angles and efficiencies of the detectors may be different. This is taken care of by introducing in [5-5] one or two additional (fit) parameters (so called α, most important, and β parameters) (see exercise).

One distinguishes between transverse field- (TF) ($\vec{B}_{ext} \perp \vec{P}(0)$ longitudinal field- (LF, $\vec{B}_{ext} \parallel \vec{P}(0)$) or zero field measurements (ZF, $\vec{B}_{ext}=0$).

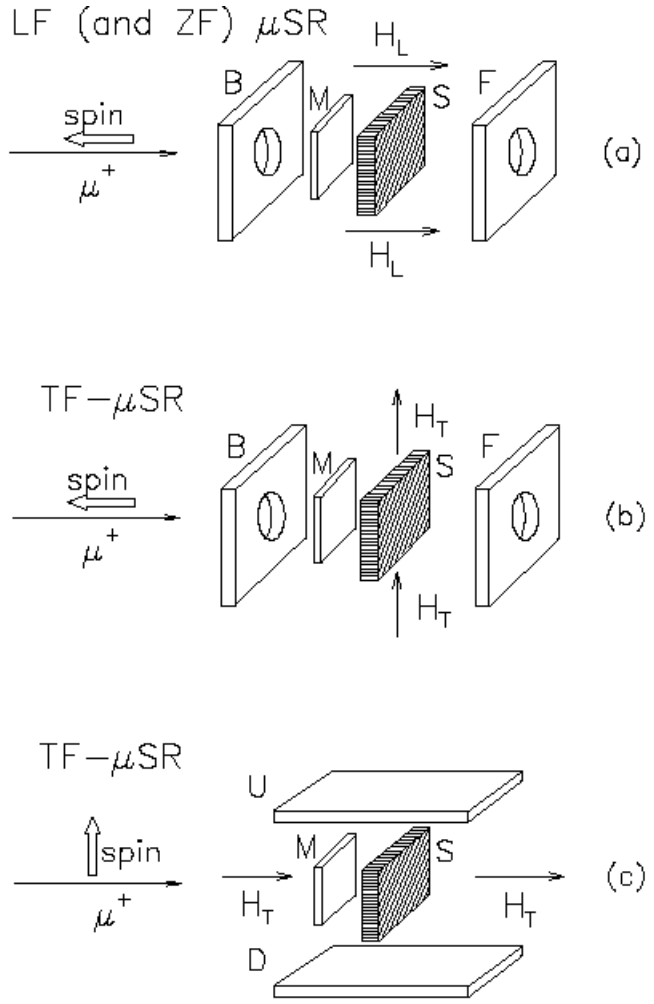

Fig. 5-7: a) Longitudinal (LF) and zero field geometry (ZF). b) and c) Transverse field geometry (TF).

Often the direction of $\vec{B}_{ext}$ is taken as z-axis. With $\vec{P}(0) \parallel \hat{n}$ then the measured polarization directions are indicated as:

In LF und ZF: $P_z(t)$
In TF $P_x(t)$

TF- spectrum and polarization function:

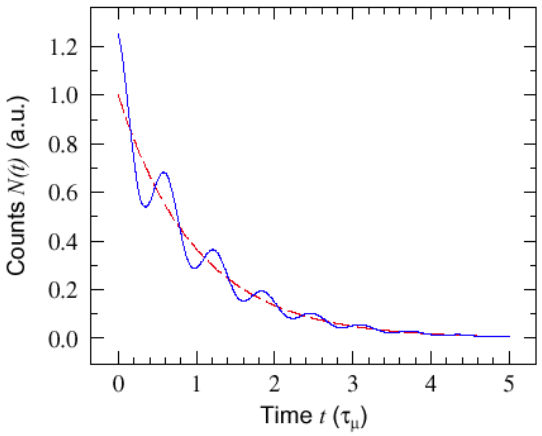

Positron count $N(t)$.

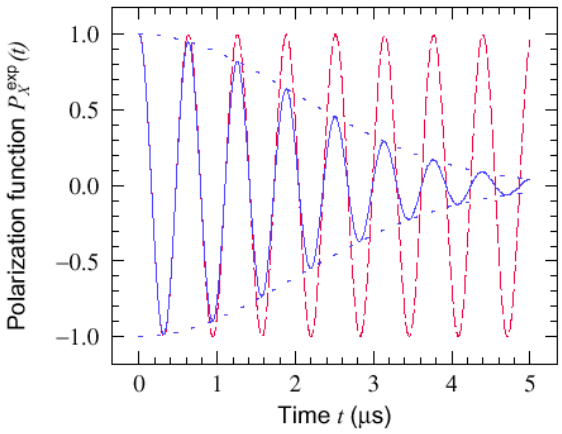

Two examples of transverse field polarisation function $P_X^{\exp}(t)$.

ZF and LF spectra and polarization function:

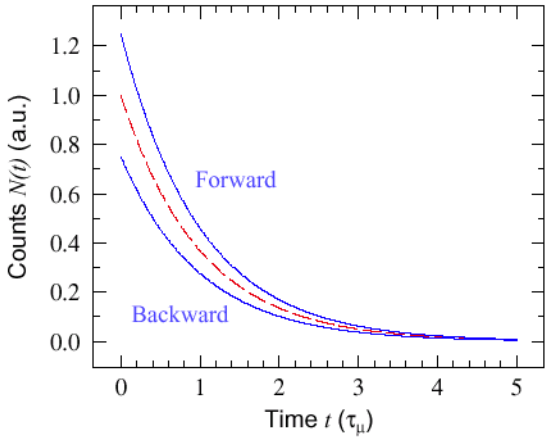

Positron counts $N_{\mathrm{F}}(t)$ and $N_{\mathrm{B}}(t)$.

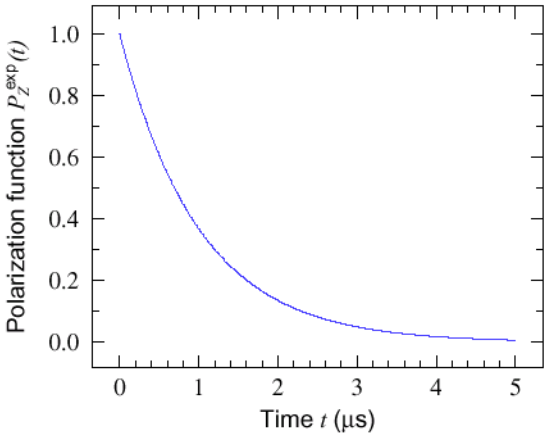

An example of a longitudinal field polarisation function $P_Z^{\exp}(t)$.

Fig. 5-8: Examples of μSR spectra and polarization functions.

5.2 Polarization and relaxation functions for static fields

Spin precession in a static field.
Static means: the local field experienced by the muon is constant over times $t \gtrsim 5\text{-}20\ \tau_\mu$.

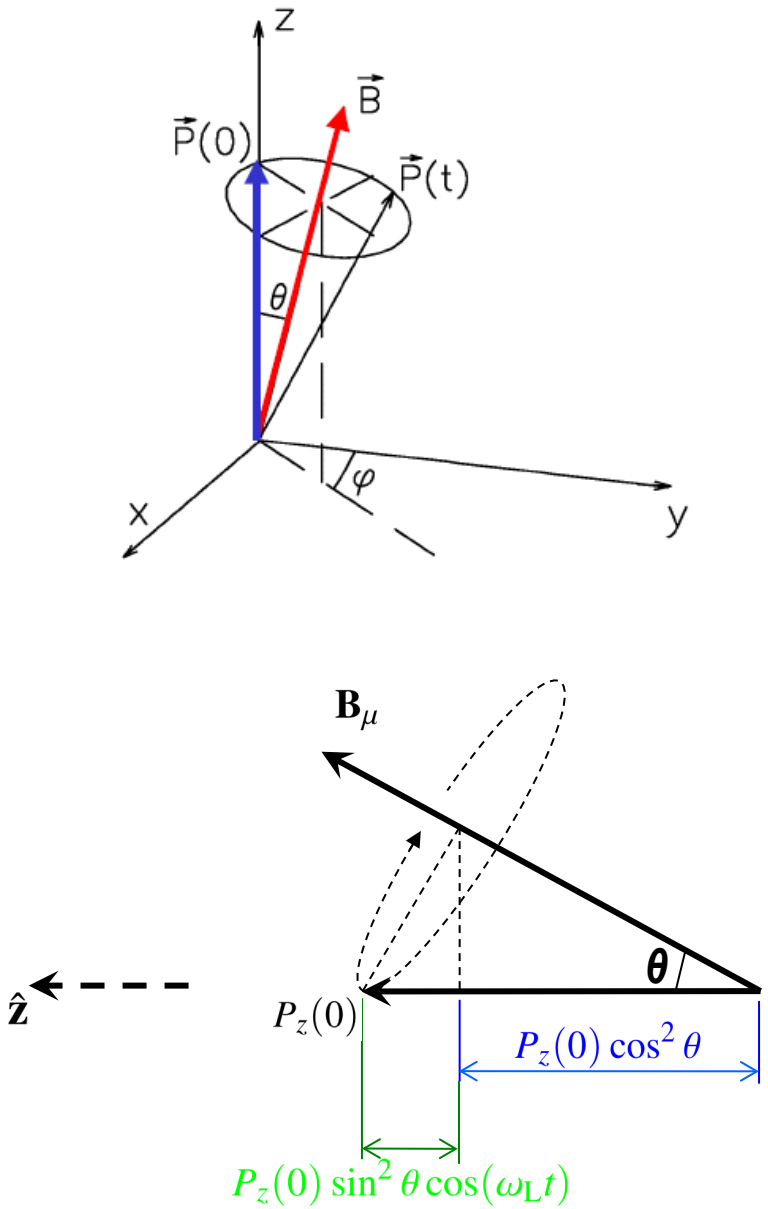

Fig. 5-9: Muon spin precession in a constant field ($\vec{B}$ or $\vec{B}_\mu$). The initial polarization is along the z-axis, which is also the observation direction ($\hat{n}$).

$$P(t) = \frac{< \vec{I}(t) \cdot \vec{I}(0) >}{\left|\vec{I}(0)\right|^2} \qquad [5\text{-}6]$$

$$P(t) = P_z(t) \equiv P_{\vec{B}}(t) = \cos^2\theta + \sin^2\theta\cos(\omega_L t) = \frac{{B_z}^2}{B^2} + \frac{{B_x}^2 + {B_y}^2}{B^2}\cos(\gamma_\mu Bt)$$

$$P_y(t) = \frac{1}{2}\sin 2\theta \sin\varphi(1-\cos(\omega_L t)) - \sin\theta\cos\varphi\sin(\omega_L t) \qquad [5\text{-}7]$$

$$P_x(t) = \frac{1}{2}\sin 2\theta \cos\varphi(1-\cos(\omega_L t)) + \sin\theta\sin\varphi\sin(\omega_L t)$$

$$B = \sqrt{{B_x}^2 + {B_y}^2 + {B_z}^2}$$

By making use of Eq. [5-7], with a single crystal sample one can determine the direction of the internal fields from the angular dependence of the amplitudes of the oscillating components.

An example is a measurement of the tetragonal heavy fermion compound $CeRhIn_5$ (A. Schenck et al., Phys. Rev. B **66,** 144404 (2002)).

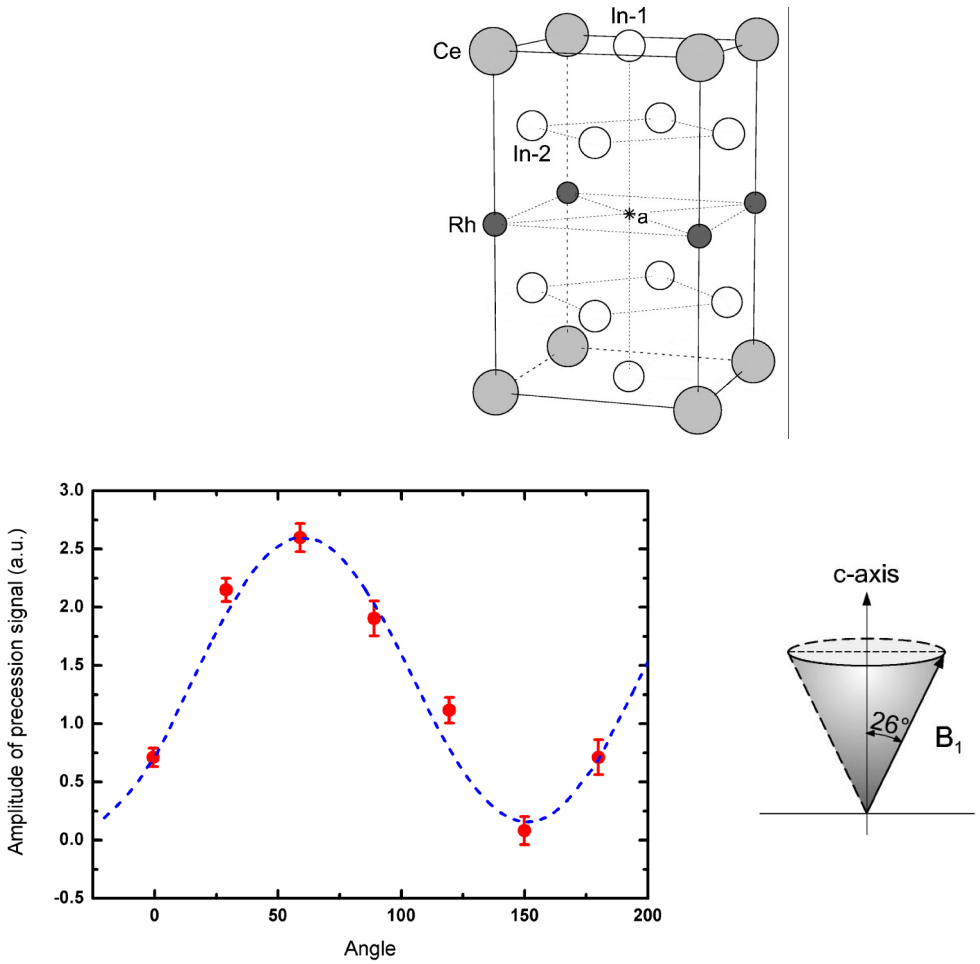

Fig. 5-10: Crystal structure of $CeRhIn_5$. Amplitude of the precession signal as a function of the rotation angle of the crystal. From the measurement a local field pointing at 26° with respect to the c-axis is determined. The local field in this case is produced by an incommensurate helical structure of the Ce moments and also induced moments at the Rh sites.

If the field distribution probed by the muon ensemble $p(\vec{B})$ is known we can calculate the corresponding polarization function:

$$P_z(t) = \frac{\int P_{\vec{B}}(t) p(\vec{B}) d^3B}{\int p(\vec{B}) d^3B}$$

This expression can be used to calculate the muon spin polarization in several special very useful cases.

A) Zero Field case with $\left|\vec{B}\right|$ constant, random direction isotropically distributed (e.g. in domain structures of magnetic materials or in ferromagnetic or antiferromagnetic powder samples).

In this case:

$$p(\vec{B})d^3B = \frac{1}{4\pi}\delta(B - B_\mu)dBd\Omega$$

$$P(t) = \frac{1}{4\pi}\int\left(\cos^2\theta + \sin^2\theta\cos(\gamma_\mu B_\mu t)\right)d(\cos\theta)d\phi = \frac{1}{3} + \frac{2}{3}\cos(\gamma_\mu B_\mu t) \qquad [5\text{-}8]$$

If the fields are isotropic in the xz or yz planes, we obtain $P_z(t) = \frac{1}{2} + \frac{1}{2}\cos(\gamma_\mu B_\mu t)$

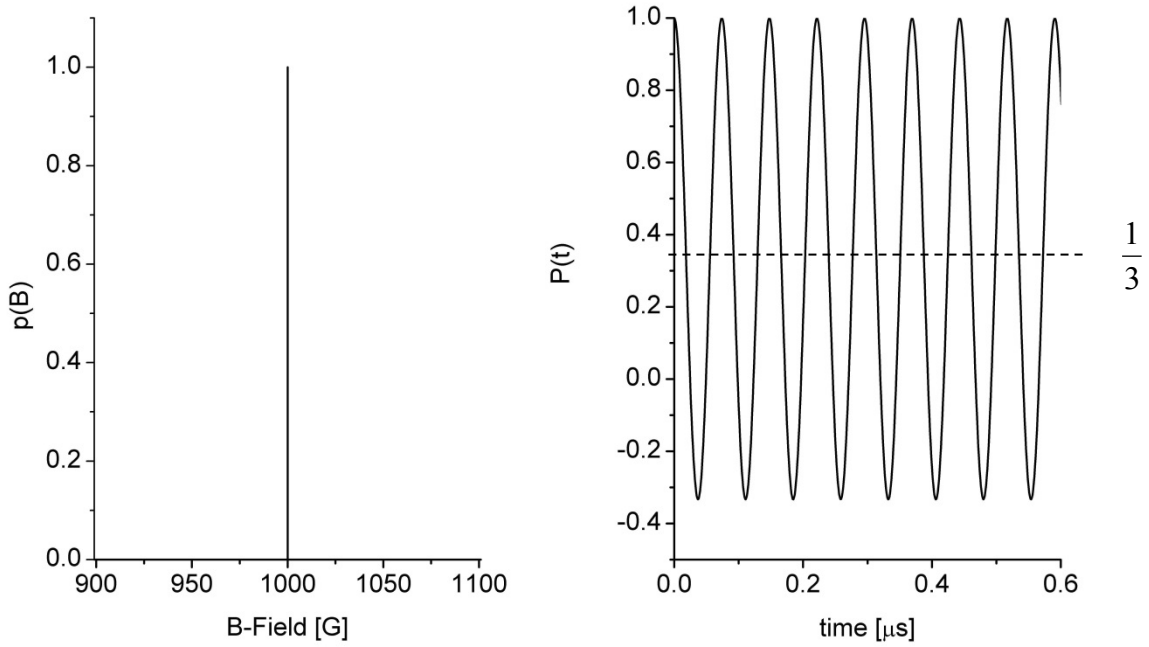

Fig 5-11: Polarization and corresponding magnetic field distribution in the case of equation [5-8].

Eq. [5-8] and Fig. 5-11 correspond to the ideal case. In the real case, there is distribution of fields around a mean value; i.e. the field distribution is not a delta function but has a finite width, better described e.g. by a Gaussian or Lorentz distribution. In the case of a Gaussian field distribution of width $<\Delta B_x^2>=<\Delta B_y^2>=<\Delta B_z^2>\equiv<\Delta B^2>$ small compared to the average field B_μ, [5-8] becomes for instance:

$$P(t)=\frac{1}{3}+\frac{2}{3}e^{-\frac{1}{2}\gamma_\mu^2\langle\Delta B^2\rangle t^2}\cos(\gamma_\mu B_\mu t)$$

$<\Delta B^2>=<(B_i-<B_i>)^2>$, i=x,y,z $<\Delta B_x^2>=<\Delta B_y^2>=<\Delta B_z^2>$

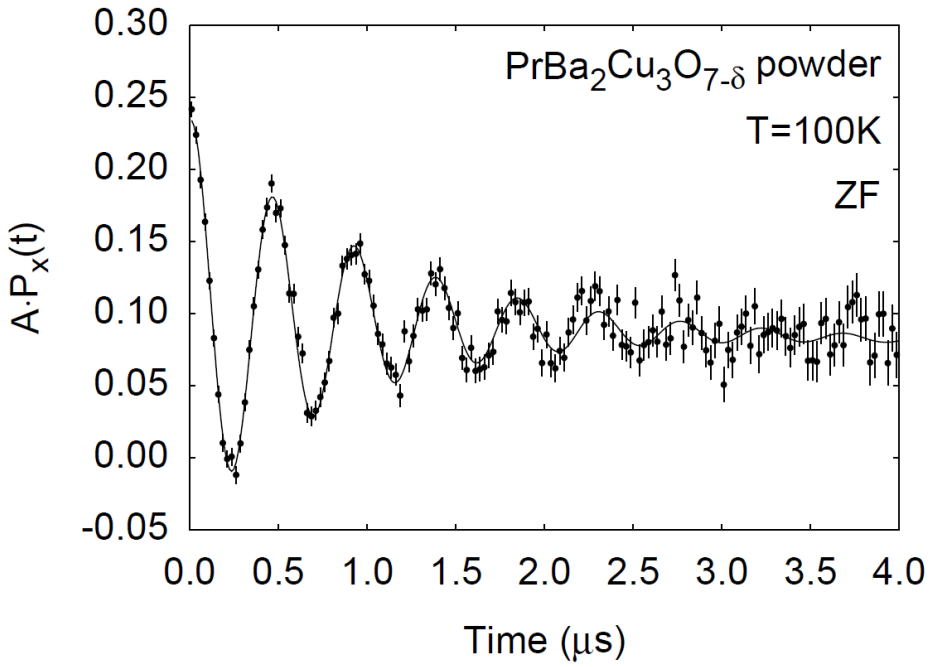

Fig 5-12: Polycrystalline $PrBa_2Cu_3O_{7-\delta}$, ZF measurement, AF order of the Cu moments. The asymmetry shows the 2/3 precessing component (damped) and the 1/3 non-precessing component (B.M. Wojek et al, Physica B **404**, 720 (2009)).

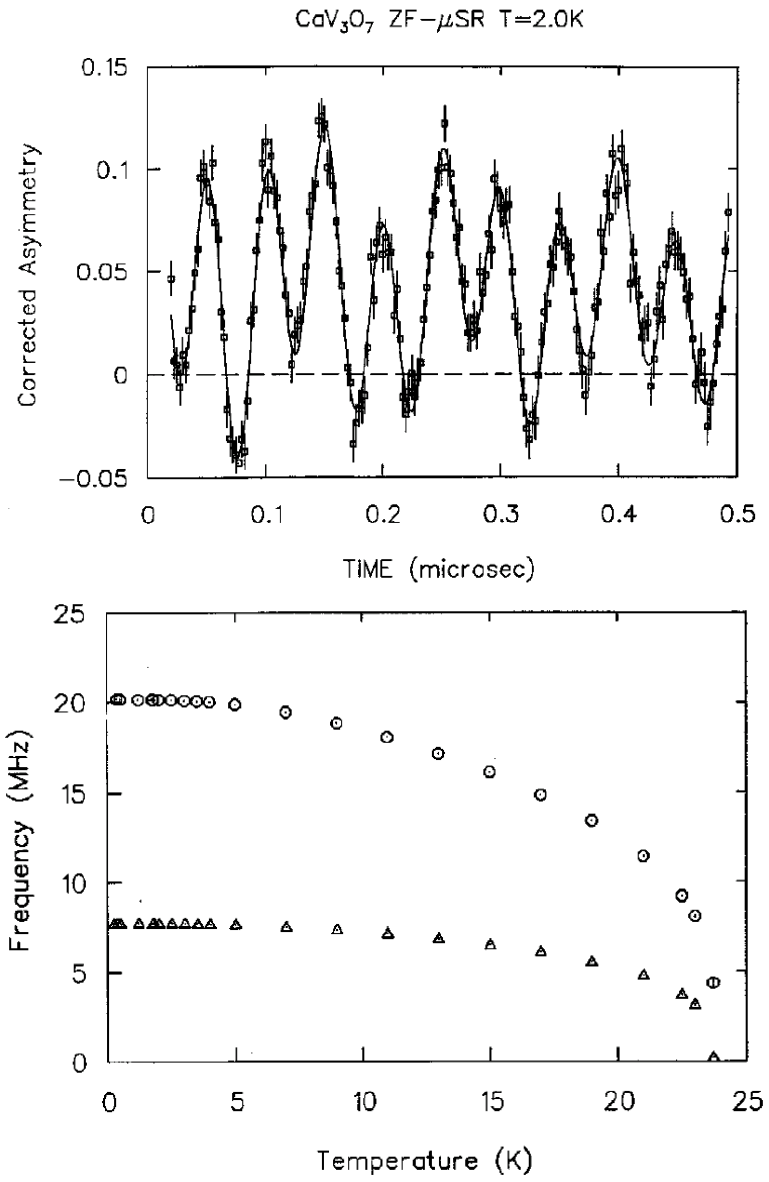

Fig 5-13: ZF μSR spectra in the CaV_3O_7 antiferromagnet. The local field is a consequence of the AF order of the V moments. We observe two precession signals corresponding to two different muon sites and in addition the non-precessing 1/3 component. The bottom curve shows the corresponding microscopic magnetization curve (R.E. Walstedt, L.R. Walker, Phys. Rev. **9** 4857 (1974)).

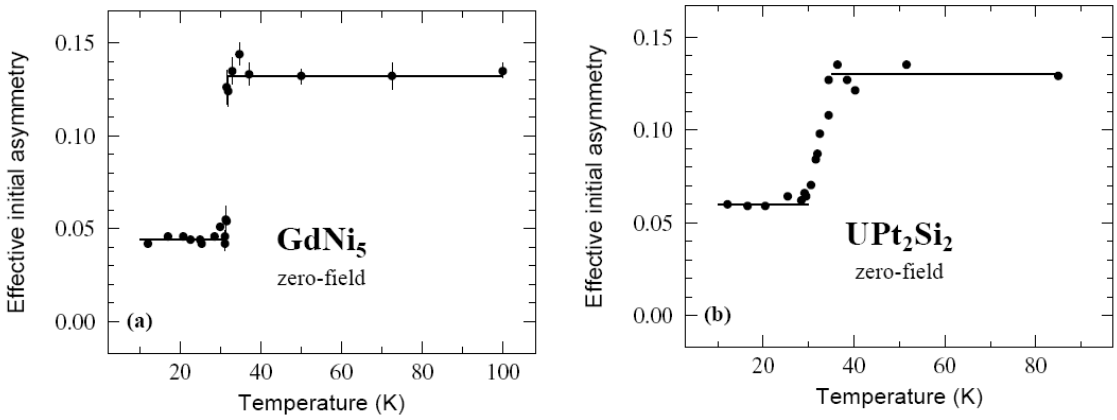

Fig 5-14: Zero field measurement. Initial asymmetry A(0) as a function of temperature in two polycrystalline samples. a) $GdNi_5$ (ferromagnet) b) UPt_2Si_2 (antiferromagnet). At T_c and T_N respectively the asymmetry falls to 1/3 (from P. Dalmas de Réotier, A. Yaouanc, Journal of Physics, Cond. Matt. **9**, R9113 (1997)). The origin of the jump can be the formation of large local fields or of fluctuating moments, so that the precessing 2/3 part of the polarization is suppressed.

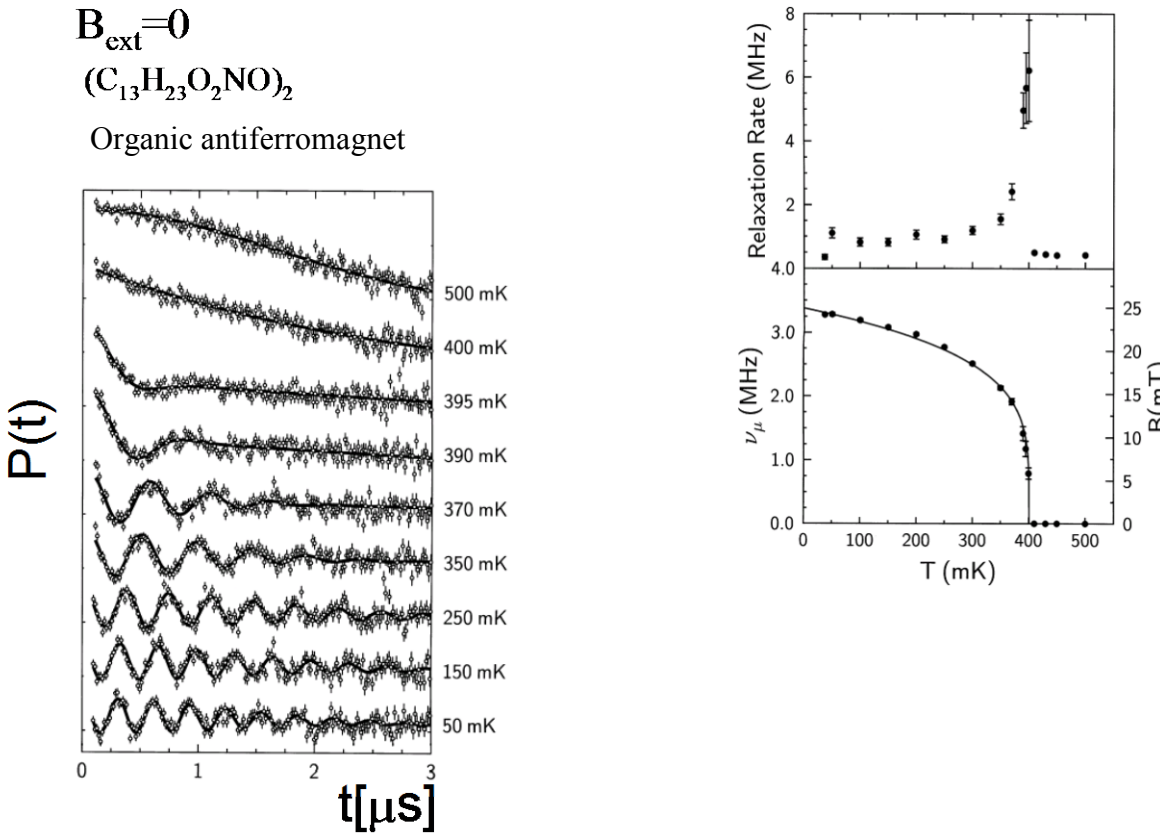

Fig 5-15: ZF μSR spectra in an organic antiferromagnet, showing the magnetic phase transition (S. Blundell et al., Physica B **289**, 115 (2000)). The T-dependence of the spontaneous precession frequency gives the local magnetization. The peak in the relaxation rate λ(T) at T_N is typical of a phase transition. In this case only the local magnetization is of interest so that $P(t) \approx A_L + A_T e^{-\lambda(T)t} \cos(2\pi\nu_\mu(T)t + \varphi)$.

B) $\vec{B}$ Gauss distributed in x, y and z direction

$< B_i >=0$ and $i = x,y,z$

$$< \Delta B_i^2 >=< (B_i - < B_i >)^2 > = < B_i^2 > - < B_i >^2 = < B_i^2 > = \frac{\sigma^2}{\gamma_\mu^2} \qquad [5\text{-}9]$$

A Gauss distribution of fields is obtained in the case of a dense arrangement of randomly oriented moments (for example nuclear moments, which on the μSR time scale can be considered as static) and is justified by the central limit theorem.

Magnetic field distribution:

$$p^G(B_i) = \frac{\gamma_\mu}{\sqrt{2\pi}\sigma} e^{-\frac{\gamma_\mu^2 B_i^2}{2\sigma^2}} \qquad i = x,y,z \qquad [5\text{-}10]$$

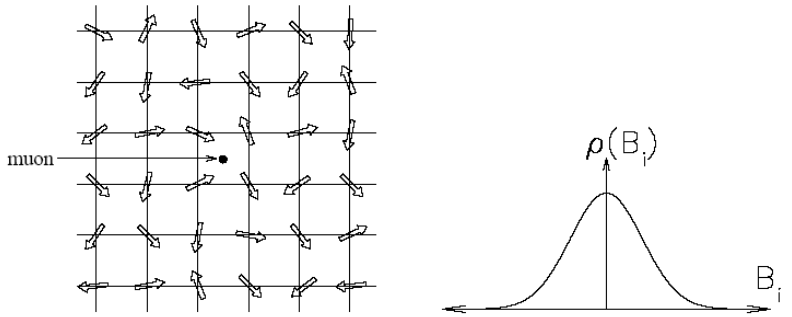

Fig. 5-16 a) Randomly oriented dense moments. b) Resulting distribution of fields projected onto an axis. The projection is a Gaussian distribution in each of the field components.

The distribution function for the absolute value $|\vec{B}| \equiv B$ is

$$p^G(B)dB = (\frac{\gamma_\mu}{\sqrt{2\pi}\sigma})^3 e^{-\frac{\gamma_\mu^2 B^2}{2\sigma^2}} \cdot 4\pi B^2 dB \qquad [5\text{-}11]$$

Which is a Maxwell distribution with maximum at $B = \sqrt{2}\frac{\sigma}{\gamma_\mu}$ and $< B >\approx \sqrt{\frac{8}{\pi}}\frac{\sigma}{\gamma_\mu}$.

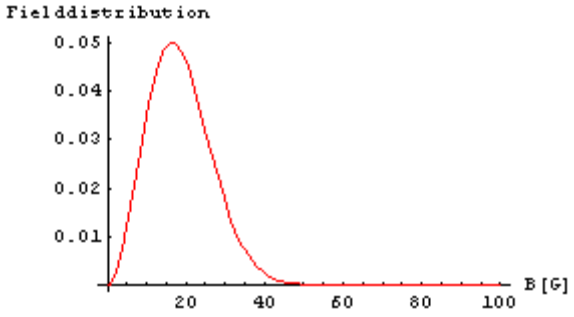

Fig. 5-17: Distribution of the field value p(B) for Gauss distributed B_x, B_y and B_z (σ=1 μs^{-1}).

The relaxation function is obtained in this case from:

$$P^{G-KT}(t) = \int p^G(B_x)p^G(B_y)p^G(B_z)P_{\vec{B}}(t)dB_x dB_y dB_z \qquad [5\text{-}12]$$

Where $P_{\vec{B}}(t)$ is given by [5-7].

The integration in [5-12] can be explicitly performed, by using for instance spherical coordinates. We obtain the well-known Kubo-Toyabe relaxation function (Fig. 5-19) (R. Kubo and T. Toyabe in *Magnetic Resonance and Relaxation*, edited by R. Blinc . North-Holland, Amsterdam, 1967):

$$P^{G\text{-}KT}(t) = \frac{1}{3} + \frac{2}{3}(1-\sigma^2t^2)e^{-\frac{\sigma^2t^2}{2}} \qquad [5\text{-}13]$$

Damped oscillation (with damping σ, relaxation rate) around maximum of $|\vec{B}|$

On average one third of the muons does not precess or relax.

The 1/3 and 2/3 components can be qualitatively understood by considering that the local field is random in all directions: about 1/3 is parallel or antiparallel to the muon spin and about 2/3 is perpendicular.

In the paramagnetic state, a Kubo-Toyabe function is very often observed reflecting the field distribution of the small fields created by the nuclear moments.

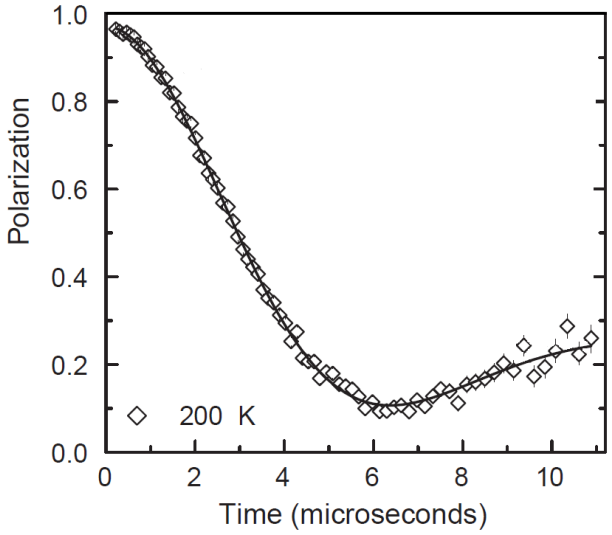

Fig. 5-18: Observation of a Gauss Kubo-Toyabe relaxation in semiconducting InN, Y.G. Celebi et al., Physica B 340-342, 385 (2003).

C) If the local fields instead of Gauss are Lorentz distributed:

$$p^{L}(B)dB = \left(\frac{\gamma_\mu^3}{\pi^2}\right) \frac{a}{(a^2+\gamma_\mu^2 B^2)^2} \cdot 4\pi B^2 dB$$

One obtains the so called static Lorentz Kubo-Toyabe function (ZF):

$$P^{L-KT}(t) = \frac{1}{3} + \frac{2}{3}(1-at)e^{-at} \qquad [5\text{-}14]$$

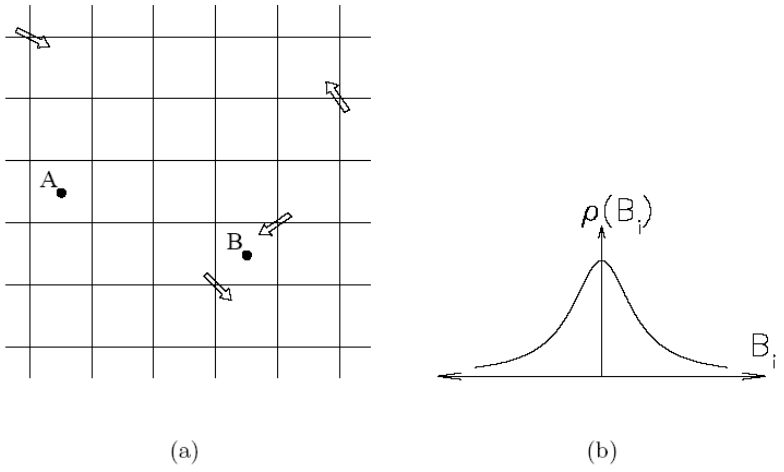

Fig. 5-19: a) Randomly oriented dilute moments. Muons at site A feel weak fields, while those at B feel stronger fields. b) Resulting distribution of fields projected onto an axis. The projection is a Lorentzian distribution.

It holds:

$$p^L(B_x) = \int\int p^L(B)dB_y dB_z = (\frac{\gamma_\mu}{\pi})\frac{a}{(a^2+\gamma_\mu^2 B_x^2)}$$

$$(\frac{a}{\gamma_\mu} = \text{HWHM})$$

and in analogy for B_y and B_z.

But differently from the Gaussian case:

$$p^L(B)dBd\Omega \neq p^L(B_x)p^L(B_y)p^L(B_z)dB_x dB_y dB_z$$

Sometimes a general relaxation function, which in the limiting case gives the Gauss and Lorentz Kubo-Toyabe function, is used:

$$P^{Gen-KT}(t) = \frac{1}{3} + \frac{2}{3}(1-\lambda^\alpha t^\alpha)e^{-\frac{\lambda^\alpha t^\alpha}{\alpha}} \qquad 1 \le \alpha \le 2$$

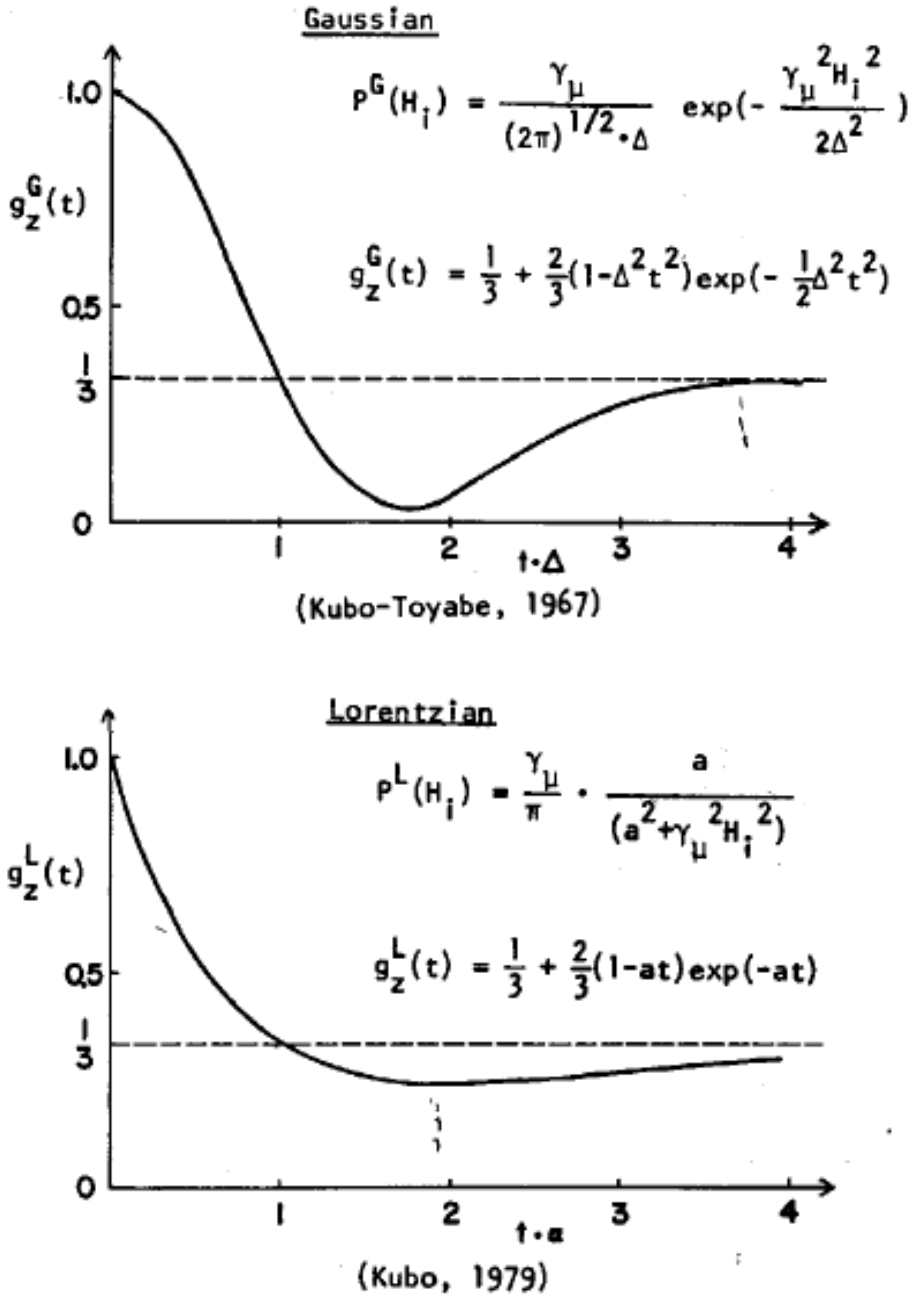

Fig. 5-20: Static ZF polarization functions, corresponding to Gaussian and Lorentzian field distributions.

D) Longitudinal field case

LF Gauss KT: as example B) but in addition an external field $\vec{B}_{ext} \| \hat{z}$ is applied. In this case the (total) field distribution modifies to:

$$p^{G}(B_z) = \frac{\gamma_\mu}{\sqrt{2\pi\sigma}} e^{-\frac{\gamma_\mu^2 (B_{ext} - B_z)^2}{2\sigma^2}} \qquad [5\text{-}15]$$

The B_x and B_y distributions remain unchanged and the B_z distribution is offset. If we integrate [5-12] with the new distribution we get the so called Gauss-Kubo-Toyabe relaxation in longitudinal field (R.S. Hayano et al., Phys. Rev. **B20**, 850 (1979)).

$$P^{G-KT}(t, B_{ext}) = 1 - \frac{2\sigma^2}{(\gamma_\mu B_{ext})^2}\left[1 - e^{-\frac{\sigma^2 t^2}{2}} \cos(\gamma_\mu B_{ext} t)\right] + \frac{2\sigma^4}{(\gamma_\mu B_{ext})^3} \int_0^t e^{-\frac{\sigma^2 t^2}{2}} \sin(\gamma_\mu B_{ext} t')dt' \qquad [5\text{-}16]$$

If B_{ext} is large with respect to the local fields the spin will be aligned along the z-direction (so called *decoupling* of static fields). LF measurements are used to distinguish between static and dynamic contributions to the relaxation.

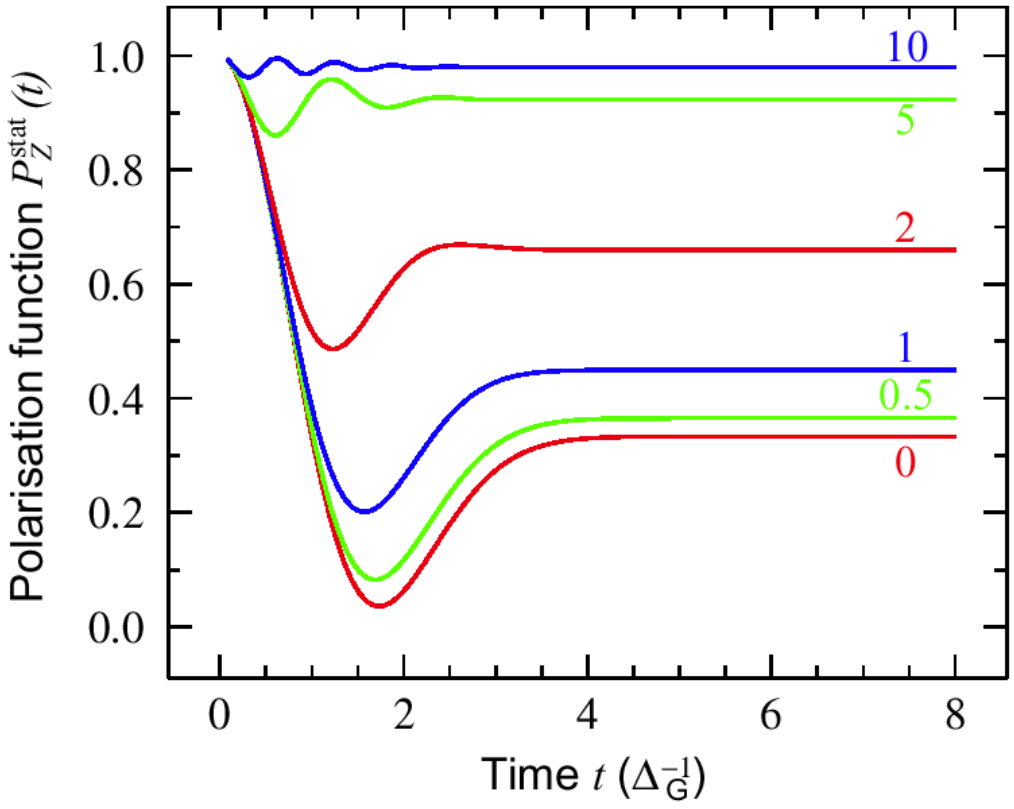

Fig. 5-21: Field dependence of the polarization function for isotropic Gauss distributed fields. Time scale in units of $1/\sigma$ (here indicated as Δ_G^{-1}). B_{ext} in units of σ/γ_μ.The zero field curve corresponds to the Kubo-Toyabe function.

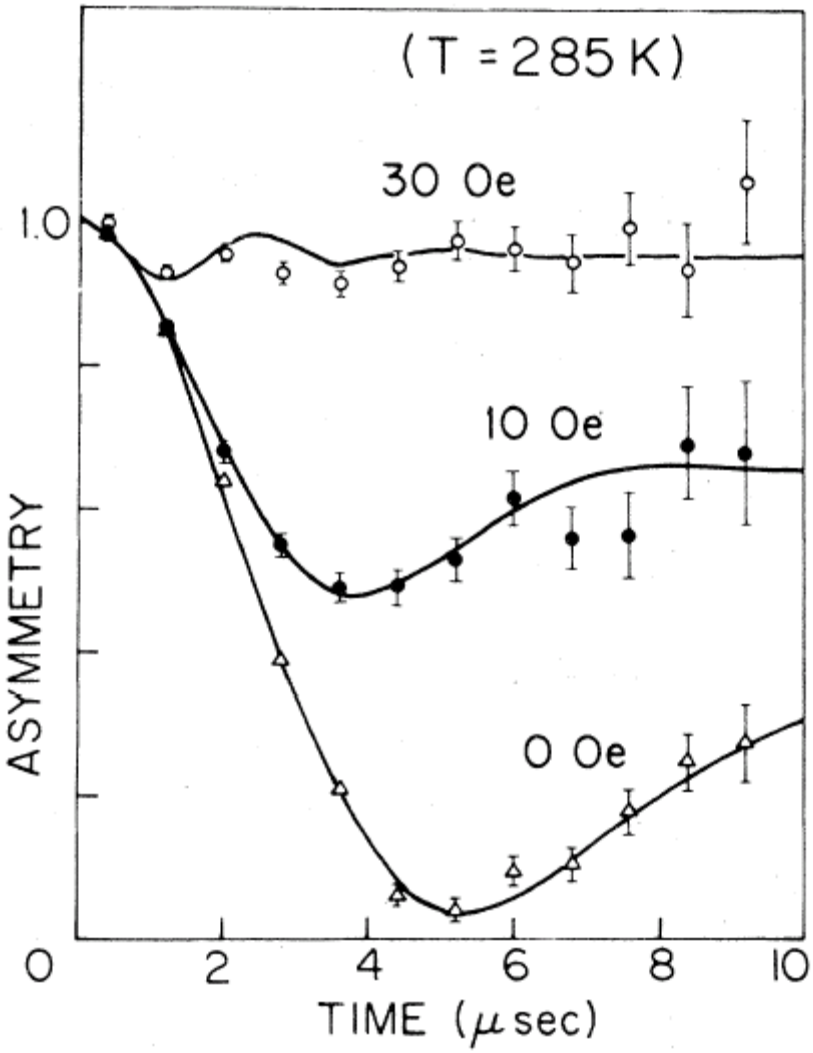

$$t_{min} = \frac{\sqrt{3}}{\sigma} \quad \left(P(t_{min}) = 0.03583\right)$$

Fig 5-22: Example of Gauss Kubo-Toyabe relaxation and longitudinal field-decoupling: Muon spin relaxation in the paramagnetic phase of MnSi (R.S. Hayano et al., Phys. Rev B **20**, 850 (1979)). The local field is produced in this case mainly by the Mn nuclear moments. The electronic Mn moments fluctuate very fast and do not contribute to the muon spin relaxation.

The behavior of the LF relaxation can be understood qualitatively by considering that the 1/3 component of Eq. [5-8] corresponding to the muons with spin parallel or antiparallel to the local field is increased in B_{ext}, whereas the 2/3 component is reduced while still showing indication of a precession around the external field.

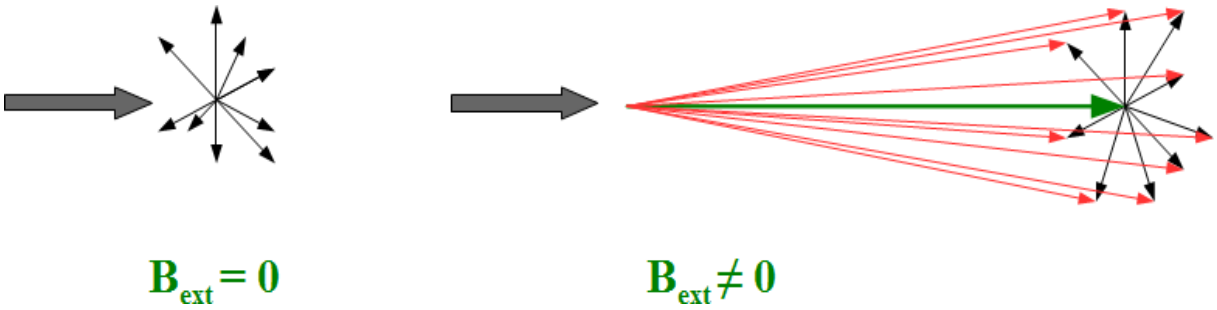

E) LF with Lorentz distributed local fields, $\vec{B}_{ext} \parallel \hat{z}$.

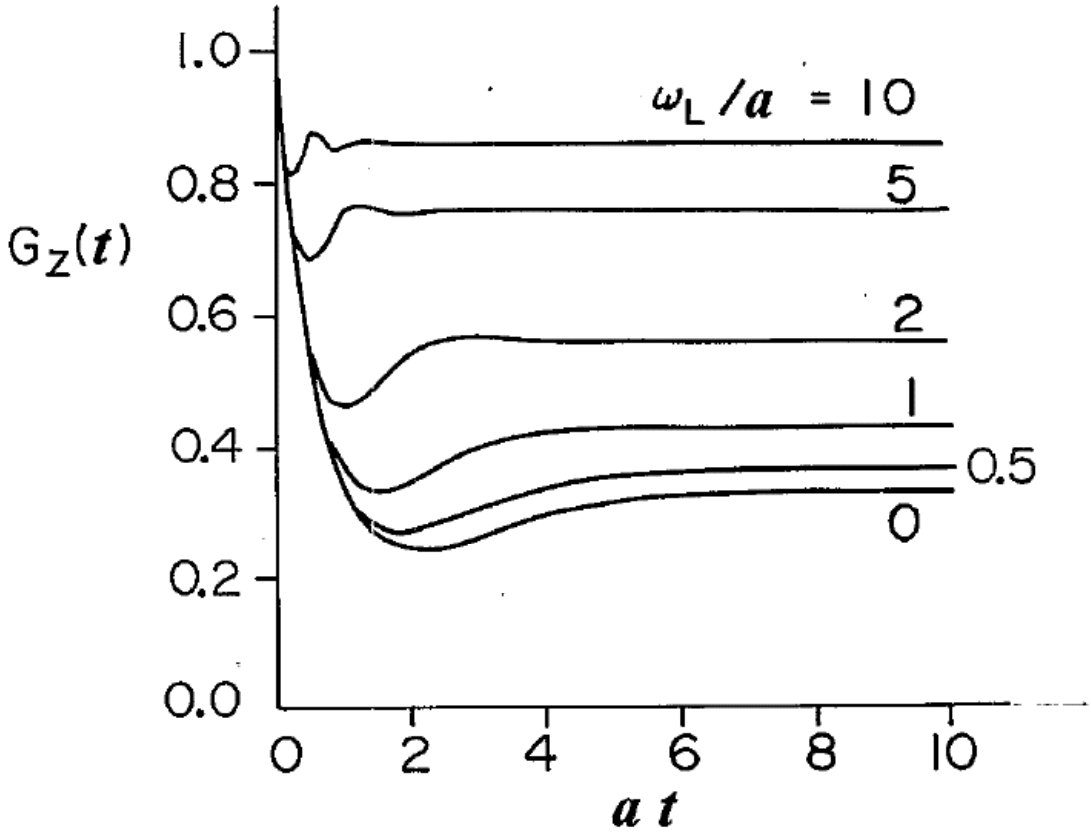

Fig. 5-23: $G_z(t)$: Muon spin polarization in random distributed Lorentz fields as function of the external field (ω_L / γ_μ) (Y. Uemura et al., Phys. Rev. B **31**, 546 (1985)).

$$P^{L-KT}(t,B_{ext}) = 1 - \frac{a}{(\gamma_\mu B_{ext})} j_1(\gamma_\mu B_{ext} t) e^{-at} - (\frac{a}{\gamma_\mu B_{ext}})^2 \left[j_0(\gamma_\mu B_{ext} t) e^{-at} - 1 \right]$$
$$- \left[1 + (\frac{a}{\gamma_\mu B_{ext}})^2 \right] a \int_0^t j_0(\gamma_\mu B_{ext} t') e^{-at'} dt' \qquad [5\text{-}17]$$

j_0 and j_1 are spherical Bessel functions.

F) Transverse field case. Relaxation in an external field: $\vec{B}_{ext} \perp \vec{P}(0)$ and $\| \hat{z}$.

If the internal fields are Gauss distributed, we have

$$p^G(\vec{B}) = \frac{\gamma_\mu}{\sqrt{2\pi}\sigma} e^{-\frac{\gamma_\mu^2 B_x^{\,2}}{2\sigma^2}} \frac{\gamma_\mu}{\sqrt{2\pi}\sigma} e^{-\frac{\gamma_\mu^2 B_y^2}{2\sigma^2}} \frac{\gamma_\mu}{\sqrt{2\pi}\sigma} e^{-\frac{\gamma_\mu^2 (B_{ext}-B_z)^2}{2\sigma^2}} \qquad [5\text{-}18]$$

with $\left|\vec{B}_{ext}\right| >> \frac{\sigma}{\gamma_\mu}$, in [5-7]: For all fields $\theta \cong 90^o$, $P_{\vec{B}}(t) \cong \cos(\gamma_\mu B t)$ and $\gamma_\mu B \cong \gamma_\mu B_z$

$$P^{G-TF}(t) = \int p^G(B_z) p^G(B_y) p^G(B_x) P_{\vec{B}}(t) dB_x dB_y dB_z$$
$$\cong \left[\int (\frac{\gamma_\mu}{\sqrt{2\pi}\sigma})^3 e^{-\frac{\gamma_\mu^2 (B_{ext}-B_z)^2}{2\sigma^2}} \cos(\gamma_\mu B_z t) dB_z \int e^{-\frac{\gamma_\mu^2 B_y^2}{2\sigma^2}} e^{-\frac{\gamma_\mu^2 B_x^2}{2\sigma^2}} dB_y dB_x \right] = \qquad [5\text{-}19]$$
$$= e^{-\frac{\sigma^2 t^2}{2}} \cos(\gamma_\mu B_{ext} t)$$

The Gauss relaxation does not depend on B_{ext} if $\left|\vec{B}_{ext}\right| >> \frac{\sigma}{\gamma_\mu}$. Fig. 5.8a shows an example of Gauss relaxation (depolarization due to dephasing, inhomogeneous broadening).

G) If the local field is Lorentz- instead of Gauss distributed, we obtain:

$$P^{L-TF}(t) = e^{-at} \cos(\gamma_\mu B_{ext} t) \qquad [5\text{-}20]$$

In both cases the oscillation frequency gives the average local field (in this case B_{ext}) and the damping gives the local field width.

Depending on the physical conditions, there may be various contributions to the average field, which is then not given simply by the external field. An example is the Knight shift K where $B_{ext} \rightarrow B_{ext}(1+K)$, another example is the vortex state in a superconductor, where $B_{ext} \rightarrow \langle B \rangle$, average field generated by the vortices, see Chapt. 7. μSR studies of superconductivity.

In the static TF case, when $< B_z > \; >> \; \frac{\sigma}{\gamma_\mu} = \sqrt{< \Delta B_z^2 >}$, a Gauss relaxation reflects a Gauss distribution of local fields and an exponential relaxation reflects a Lorentz distribution of local fields (polarization and field distribution are related via a cosine Fourier transform).

5.3 Special cases of polarization functions

In some cases the interaction with nuclear dipoles can give rise to coherent muon spin precession in ZF even if the nuclear dipoles are randomly oriented. This has been observed in materials, where there the muon is close to one or two nuclear spins. In ferroelectric potassium dihydrogen phosphate KH_2PO_4 (KDP) and antiferroelectric ammonium dihydrogen phosphate $NH_4H_2PO_4$ (ADP), the muon forms an oxygen-hydrogen-like bond and is relatively close to a proton which is responsible for the hydrogen bond between two adjacent phosphate tetrahedra.

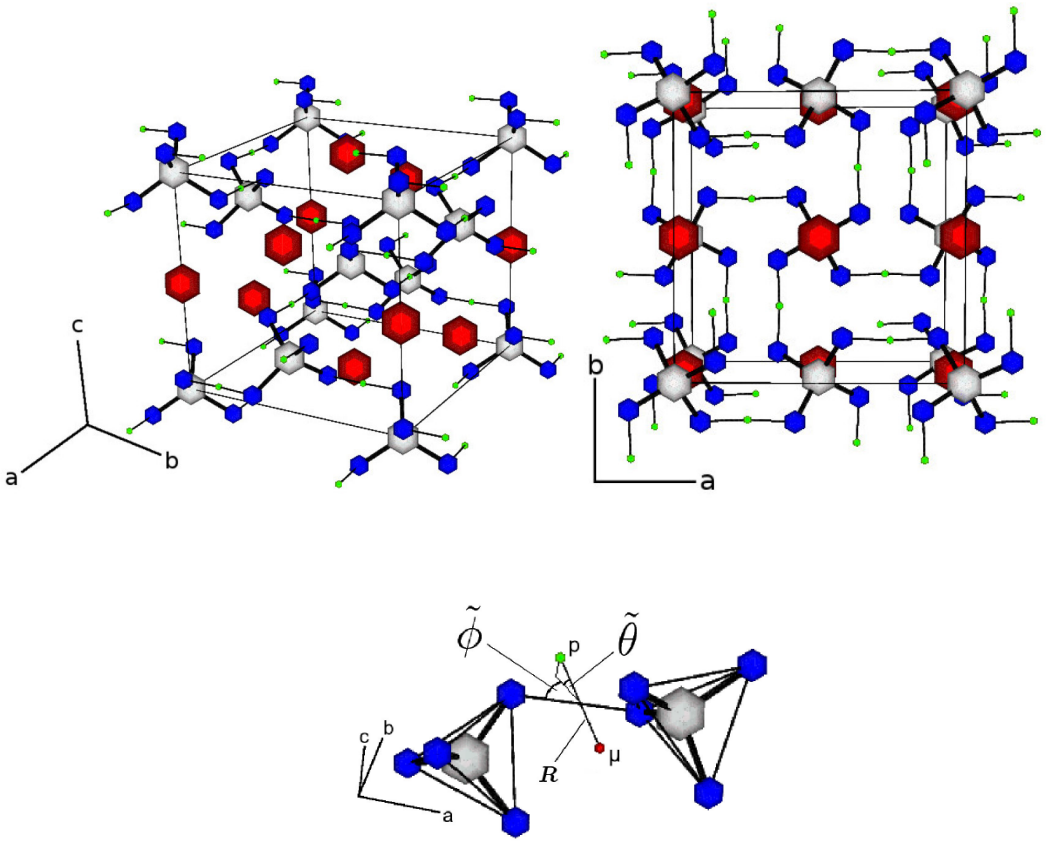

Fig. 5-24: Top: Unit cell of KDP in the paraelectric phase (K: red, P: grey, O: blue, H: green). The muon forms an O-μ bond and probes the dipole field of the nearest H nucleus. Bottom: Possible muon and proton sites between oxygen atoms of neighboring phosphate groups.

The time evolution of the polarization of a muon interacting with a single proton's dipolar field is obtained by solving the Hamilton operator of the dipolar interaction between two spin 1/2 particles:

$$H^{dip} = -\vec{\mu}_\mu \cdot \vec{B}_p = \frac{\mu_0}{4\pi}\frac{1}{R^3}\left[\vec{\mu}_\mu \cdot \vec{\mu}_p - 3\frac{(\vec{\mu}_\mu \cdot \vec{R})(\vec{\mu}_p \cdot \vec{R})}{R^2}\right] \qquad [5\text{-}21]$$

Where $\vec{R} = R\vec{n}$ defines the μ-p axis direction and $\vec{\mu}_\mu$ and $\vec{\mu}_p$ are the magnetic moments of muon and proton. Expressing the magnetic moments with the gyromagnetic ratio and the spins (in units of $\hbar$), the operator can be written as:

$$H^{dip} = \hbar\omega_D \frac{1}{\hbar^2}\left[\vec{I}_\mu \cdot \vec{I}_p - 3(\vec{I}_\mu \cdot \vec{n})(\vec{I}_p \cdot \vec{n})\right] \qquad [5\text{-}22]$$

with $\omega_D = \frac{\mu_0}{4\pi}\frac{\hbar\gamma_\mu\gamma_p}{R^3}$, $\quad \omega_D = 2\pi \cdot 0.00038238 \text{ MHz } \frac{nm^3}{R^3}$

The eigenvalues of [5-22] are 0, $-0.5\omega_D$, $-0.5\omega_D$, ω_D . Three components with definite frequencies (0, $0.5\omega_D$, ω_D and $1.5\ \omega_D$) should be observed at an arbitrary angle θ between the muon spin and the muon–proton bond direction (see P-F. Meier, Hyperfine Interactions, **17-19**, 427 (1984) and K. Nishiyama et al., Hyperfine Interactions, **106**, 111 (1997)).

$$P_z(t) = (\cos\theta)^2 P_{||}(t) + (\sin\theta)^2 P_\perp(t) \qquad [5\text{-}23]$$

Where $P_{||}(t)$ and $P_\perp(t)$ are the time dependent polarization (for initial spin parallel or perpendicular to $\hat{z}$, taken here as the muon-proton axis direction $\vec{n}$)[8]:

$$P_{||}(t) = \frac{1}{2}\left[1 + \cos(\omega_D t)\right]$$
$$P_\perp(t) = \frac{1}{2}\left[\cos(\frac{\omega_D}{2}t) + \cos(\frac{3\omega_D}{2}t)\right] \qquad [5\text{-}24]$$

[8] The muon spin precession frequency and depolarization depend on the temperature. This opens the possibility to study ferroelectric and antiferroelectric transitions with a magnetic probe (B. Wojek, Diplomarbeit, ETH Zürich, 2006 and E. Morenzoni et al., Physica B **388**, 274-277 (2007)).

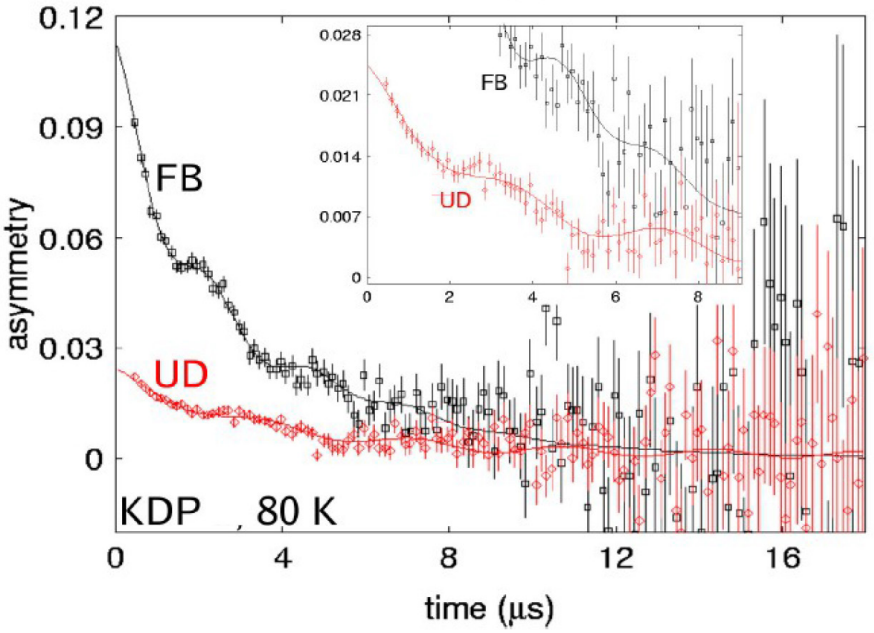

Fig. 5-25: Asymmetry spectrum in KDP at T=80 K, showing the spontaneous oscillations observed along different directions. $\vec{P}(0) \perp$ c-axis, c axis in plane (B. Wojek, Diplomarbeit, ETH Zürich, 2006).

Another special case is the formation of the so called F-μ-F complex, where the muon is located between two F ions (^{19}F has high electronegativity and a small spin ½ nucleus with high nuclear moment and ~ 100% abundancy). This leads to coherent oscillations.

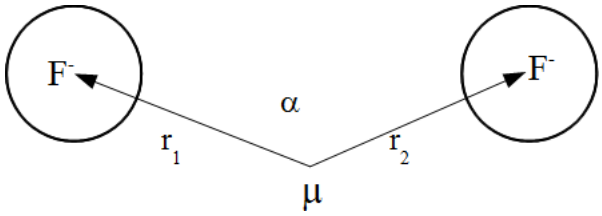

Assuming $r_1 = r_2$ and $\alpha = 180°$ one has the analytic solution for a powder averaged polarization ($\omega_D = \frac{\mu_0}{4\pi}\frac{\hbar\gamma_\mu\gamma_F}{R^3}$)

$$P_z(t) = \frac{1}{6}\left[3 + \cos(\sqrt{3}\omega_D t) + (1 - \frac{1}{\sqrt{3}})\cos(\frac{3-\sqrt{3}}{2}\omega_D t) + (1 + \frac{1}{\sqrt{3}})\cos(\frac{3+\sqrt{3}}{2}\omega_D t)\right] \qquad [5\text{-}25]$$

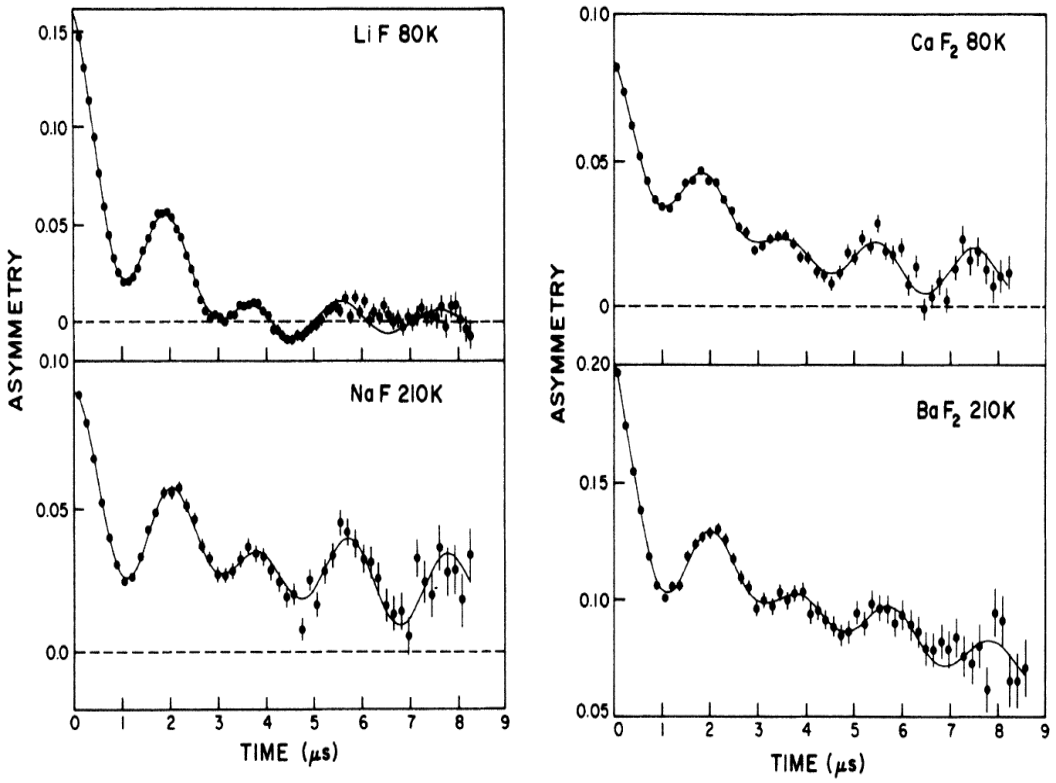

Fig. 5-26: ZF asymmetry spectra for several metal fluoride crystals (<100> axis parallel to P(0)). The solid line is a fit to Eq. 5-25 including a multiplicative relaxation function and a background contribution (from J. Brewer et al., Phys. Rev B **33**, 7813 (1986)).

Details of the μSR spectra are very sensitive to the relative distance r_1 and r_2 from the two F ions and the angle α between r_1 and r_2. This property has been used to identify various classes of sites that occur in molecular magnets (T. Lancaster et al., Phys. Rev. Lett. **99**, 267601 (2007)).
Comparing the experimental data with the refined structure obtained by Density Functional Theory (DFT) the correct location and shape for the F-μ+-F complex has been predicted in YF_3 (F. Bernardini et al, Phys. Rev. B **87**, 115148 (2013)).

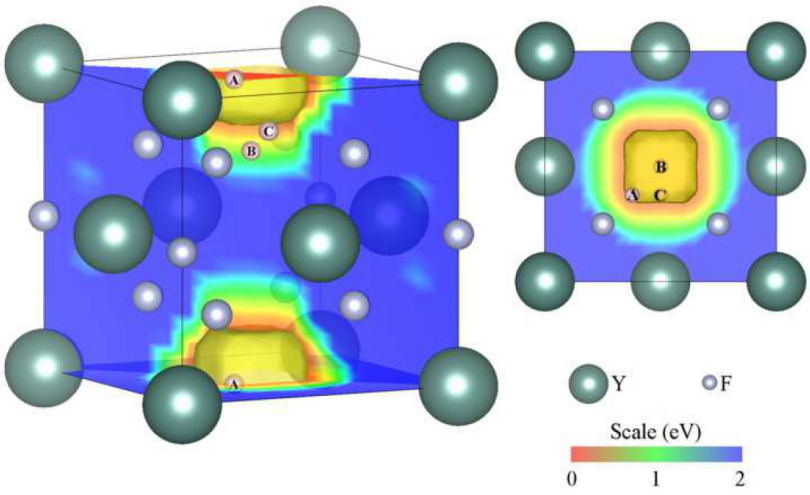

Fig. 5-27: Possible muon sites in YF_3. The label A identifies the expected site. The localization volume surface is shown in dark yellow.

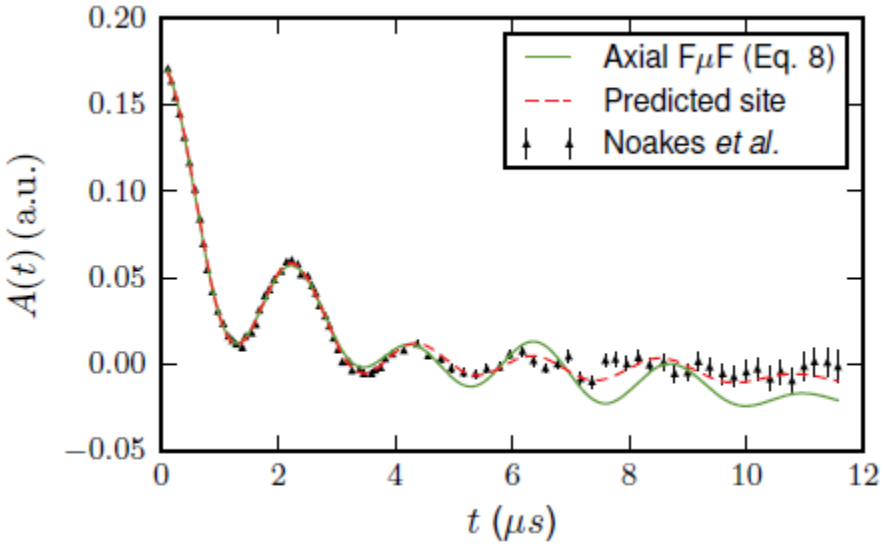

Fig. 5-28: Fit of YF_3 data (D. R. Noakes et al., J. Phys. Chem. Solids **54**, 785 (1993)) with the conventional axial F-μ^+-F model (Eq. 5-25) and with the depolarization calculated for the DFT predicted site in the fully relaxed structure (from F. Bernardini et al, Phys. Rev. B **87**, 115148 (2013)).

5.4 Example of TF-spectroscopy: paramagnetism of the conduction electrons (Knight-shift)

The magnetic properties of simple metallic systems are determined essentially by the conduction electrons. The magnetic response and susceptibility is determined by the Pauli paramagnetism (related to the spin of the conduction electrons) and Landau diamagnetism (related to the orbital moment of the conduction electrons).
The local spin susceptibility can be probed by NMR or μSR via the so-called Knight-shift measurement.

Experimentally, one measures in TF the small shift of the muon spin precession in a well-known external field B_{ext} (accuracy needed 1-10 ppm).

In systems without localized electronic moments the shift is determined by the contact interaction between μ^+ spin and spin of the conduction electrons (in the presence of localized moments, e.g. rare earth, additional dipolar and hyperfine terms have to be considered):

$$B_{exp} = B_{ext} + < B_{hf}^{c} > \qquad [5\text{-}26]$$

In our case the Knight-shift K is then:

$$B_{exp} = B_{ext}(1+K) \qquad [5\text{-}27]$$

$$K = \frac{< B_{hf}^{c} >}{B_{ext}} \qquad [5\text{-}28]$$

It is proportional to the density of conduction electrons at the muon site (which gives the strength of the contact interaction, see contact interaction in muonium) and to the Pauli susceptibility (which reflects how much the conduction electrons are polarized by an external magnetic field).

Pauli susceptibility

In a free electron gas, the density of states is:

$$D(E) = \frac{3}{2}\frac{n}{E_F^{3/2}}\sqrt{E} \qquad [5\text{-}29]$$

n: Electron density
E_F: Fermi energy

Without external field, spin up and spin down states are equally populated.
If a field B_{ext} is applied, the band with magnetic moment parallel to B_{ext} will be lowered by $\mu_B B_{ext}$ and the band with antiparallel moment will be raised by the same amount. Since both bands are filled up to E_F, there is an overweight of electrons with magnetic moment parallel to B_{ext}. As a consequence the metal develops a weak spin polarization.

Electron density for both states:

$$n^{\uparrow} = \frac{1}{2}\int D(E+\mu_B B_{ext})F(E)dE \qquad [5\text{-}30]$$

$$n^{\downarrow} = \frac{1}{2}\int D(E-\mu_B B_{ext})F(E)dE \qquad [5\text{-}31]$$

$F(E) = \frac{1}{e^{\frac{E-\mu}{kT}}+1}$, F(E) Fermi-Dirac distribution, μ chemical potential[9]

For small B_{ext} the magnetization becomes:

$$M = \mu_B(n^{\uparrow}-n^{\downarrow}) \cong \mu_B{}^2 B_{ext}\int_0^{\infty}\frac{dD}{dE}F(E)dE = \mu_B{}^2 B_{ext}\left(\overbrace{D(E)F(E)\Big|_0^{\infty}}^{D(0)=0,F(\infty)=0} - \overbrace{\int_0^{\infty}\frac{dF}{dE}D(E)dE}^{\cong -\delta(E-E_F)} \right) \qquad [5\text{-}32]$$

$$\cong \mu_B{}^2 B_{ext} D(E_F)$$

$$M \cong \frac{3}{2}\frac{n\mu_B{}^2}{E_F}B_{ext} \qquad [5\text{-}33]$$

The Pauli susceptibility is:

$$\chi_P = \frac{M}{H_{ext}} = \frac{\mu_0 M}{B_{ext}} = \mu_0 \frac{3}{2}\frac{n\mu_B{}^2}{E_F} \qquad [5\text{-}34]$$

The magnetization of the conduction electrons can be also expressed in terms of their average spin $\langle s_z \rangle$:

$$M = n g_e \mu_B \langle s_z \rangle = \chi_P \frac{B_{ext}}{\mu_0} \quad \rightarrow \quad \langle s_z \rangle = \frac{B_{ext}}{n\mu_B g_e \mu_0}\chi_P \qquad [5\text{-}35]$$

---

[9] $\mu = E_F\left[1 - \frac{\pi^2}{12}(\frac{k_B T}{E_F})^2 + O\left((\frac{k_B T}{E_F})^4\right)\right]$, at T=0, μ=$E_F$

the average spin polarization $<s_z>$ can be written[10] in terms of the average hyperfine contact field $<B_{hf}^c>$

With $A\vec{I}\cdot\vec{s} = -\vec{\mu}_\mu \cdot \vec{B}_{hf}^c$ and $A = \frac{2}{3}\mu_0 g_\mu \mu_B^\mu g_e \mu_B \left|\varphi(0)\right|^2$ (equation [3-19]):

$$< B_{hf}^c >= \mu_0 \frac{2}{3} g_e \mu_B < s_z > \left|\varphi(0)\right|^2 \quad \propto \; A \qquad [5\text{-}36]$$

and $K = \frac{< B_{hf}^c >}{B_{ext}}$ we obtain[11]:

$$K = \frac{2}{3}\chi_P \frac{\left|\varphi(0)\right|^2}{n} \qquad [5\text{-}37]$$

Up to a factor 2/3, K is equal to the Pauli susceptibility multiplied with the enhancement factor $\frac{\left|\varphi(0)\right|^2}{n}$, which gives the ratio between the electron density at the muon site (in μSR measurements) or at the nuclear site (in the case of NMR measurements) and the average density of electrons.

---

[10] Here is the spin dimensionless

[11] In general the hyperfine field at the muon site from the polarized conduction electrons can contain other contributions and is given by:

$$B_{hf,i}(\vec{R}_\mu) = \frac{\mu_0}{4\pi}\int d^3r \; D_{ij}(\vec{r} - \vec{R}_\mu) M_i(\vec{r})$$

where $\vec{M}(\vec{r})$ is the conduction electron magnetization and D_{ij} is the tensor expressing the coupling to it:

$$D_{ij}(\vec{x}) = (\nabla_i \nabla_j - \frac{1}{3}\delta_{ij}\Delta)\frac{1}{x} - \frac{2}{3}\delta_{ij}\Delta\frac{1}{x}$$

The first term expresses the dipolar coupling (see Eq. [3-16]). Polarized conduction electrons can also produce dipolar fields if the corresponding magnetization (or spin density distribution) is not of spherical or cubic symmetry with respect to the muon site. Since the first term transforms as a spherical harmonics of order 2, for a spherical symmetric screening cloud only the second term contributes to the hyperfine field. With $\Delta\frac{1}{|\vec{x}|} = -4\pi\delta(\vec{x})$ the second term yields the contact term:

$\vec{B}_{hf}^c(\vec{R}_\mu) = \frac{2}{3}\mu_0\vec{M}(\vec{R}_\mu)$ with $\vec{B}_{ext} \parallel \hat{z}$ and $M_z(\vec{R}_\mu = 0) \cong g_e\mu_B < s_z > |\varphi(0)|^2$ we obtain [5-36] and [5-37]. A more accurate way to write the Knight shift is the following:

$K = \frac{2}{3}\chi_P \frac{n^\uparrow(\vec{R}_\mu) - n^\downarrow(\vec{R}_\mu)}{n_0{}^\uparrow - n_0{}^\downarrow} = \frac{2}{3}\chi_P \alpha(\vec{R}_\mu)$, where $n^\uparrow(\vec{R}_\mu) - n^\downarrow(\vec{R}_\mu)$ is the actual (up and down spin) electron density at the muon site and $n_0{}^\uparrow - n_0{}^\downarrow$ is the corresponding average density (see Chapt 4.6). The spin enhancement factor $\alpha(\vec{R}_\mu)$ has to be provided by theory.

$\frac{|\varphi(0)|^2}{n} \equiv \alpha$ is the so called „spin density enhancement factor“.

Since $|\varphi(0)|^2$ is proportional to the hyperfine coupling A (Eq. [3-21] and [3-23]), it holds:

$$K \propto A\chi_P \qquad [5\text{-}38]$$

Often the units are chosen in such a way that:

$$K = \frac{A\chi}{N_A \mu_B} \qquad [5\text{-}39]$$

χ is the molar susceptibility ([emu/mol=erg/(G mol)] in cgs), N_A the Avogadro number and A is in Gauss (given as G/μ_B because of $1/\mu_B$ in [5-39]). Measurements of the Knight-shift contribute to the understanding of the local electronic structure of hydrogen in metals.

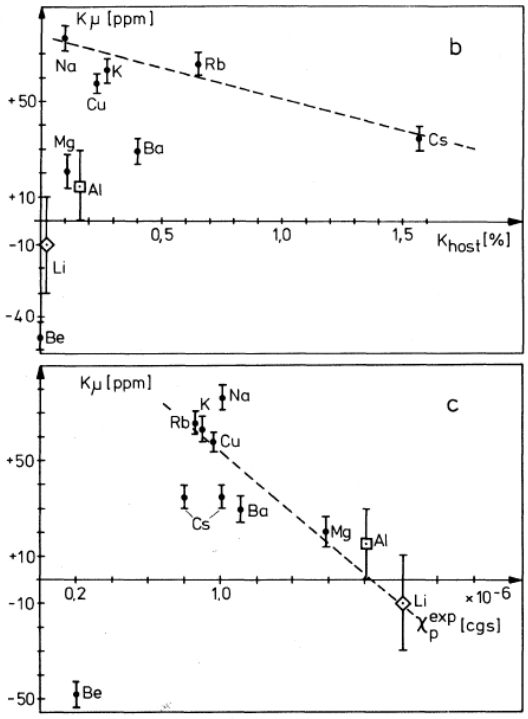

Fig. 5-29: Top: Knight-shift at muon site (K_μ) as a function of the Knight-shift at the nuclear (lattice) site (K_{host}) plotted for various metals. Bottom: Muon Knight-shift as a function of the electron spin susceptibility from M. Camani et al, Phys. Rev. Lett. **42,** 679 (1979).

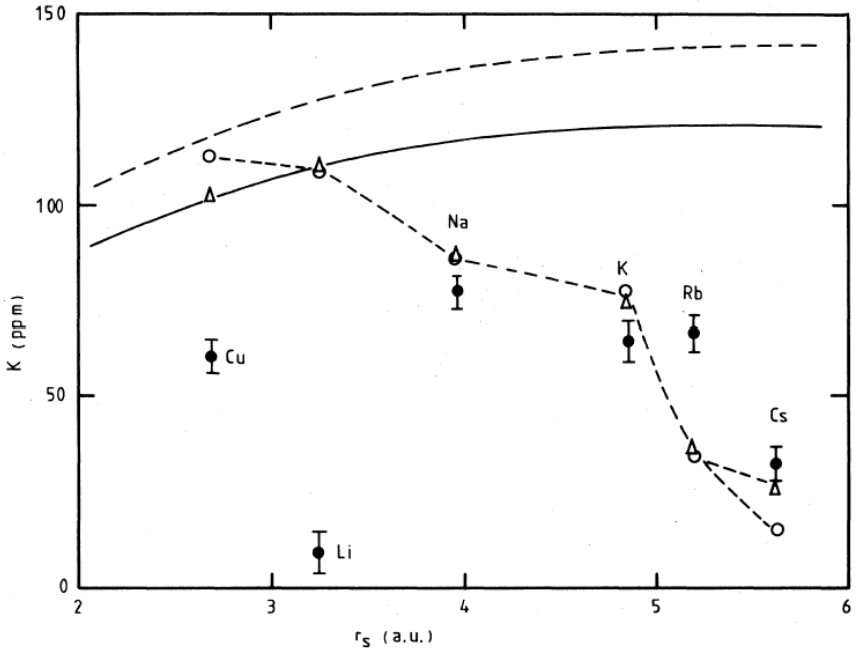

FIG. 1. Muon Knight shift in monovalent metals. The black dots are the experimental results from Ref. 3. The open circles and triangles are the calculated Knight shifts for the octahedral and tetrahedral interstitial sites, respectively. The solid line shows the jellium result, and the dashed line is the jellium result without the diamagnetic shielding.

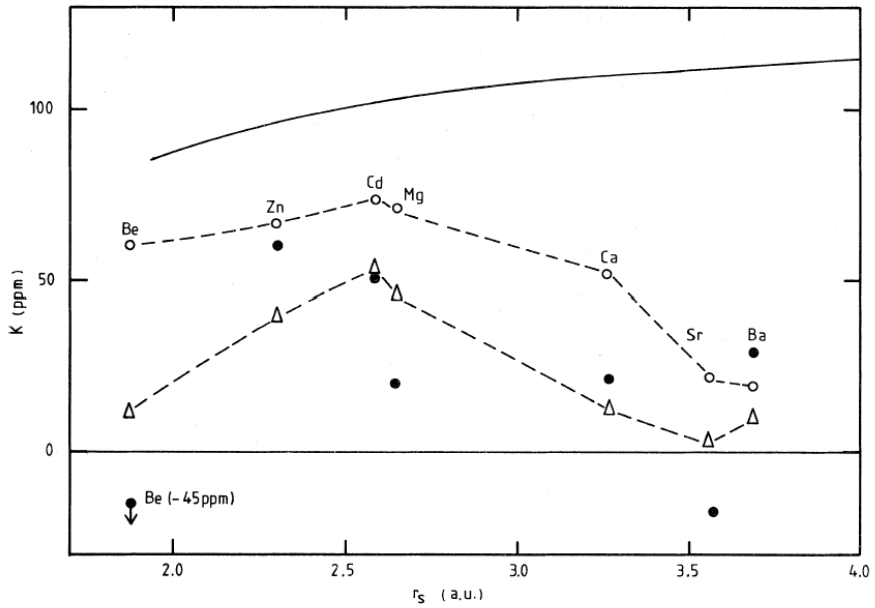

FIG. 2. Muon Knight shift in divalent metals. The black dots are the experimental results from Ref. 3. The open circles and triangles are the calculated Knight shifts for the octahedral and tetrahedral interstitial sites, respectively. The solid line shows the jellium result.

Fig. 5-30: Self consistent calculations of the Knight-shift in mono- and bivalent metals. (M. Manninen, Phys. Rev. B **27,** 53 (1983)).

5.5 Example of field distribution: field distribution from the sum of dipolar fields produced by nuclear moments

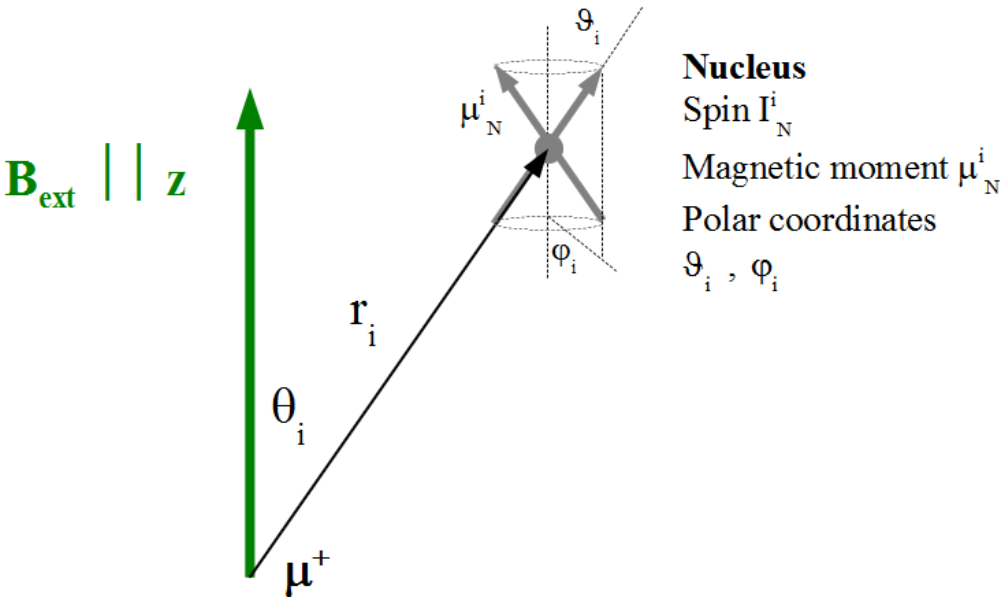

Fig. 5-31: Muon in the field of a nuclear dipole.

Magnetic field from a nuclear dipole with spin I_N:

$$\vec{B}_{dip}(\vec{r}) = \frac{\mu_0}{4\pi}\hbar\gamma_N \frac{3(\vec{I}_N\cdot\vec{r})\cdot\vec{r} - \vec{I}_N r^2}{r^5} \qquad [5\text{-}40]$$

Dipole-dipole coupling of the μ^+ with all nuclear spins (lattice sum over i):

$$H_{dip} = -\vec{\mu}_\mu \sum_i \vec{B}^i_{dip}(\vec{r}_i) = \sum_i H^i_{dip}$$

$$H^i_{dip} = \frac{\mu_0}{4\pi}\frac{\hbar^2\gamma_\mu\gamma_N}{r^3}\left(\vec{I}_\mu\cdot\vec{I}^i_N - \frac{3(\vec{I}_\mu\cdot\vec{r}_i)(\vec{I}^i_N\cdot\vec{r}_i)}{r^3}\right) \qquad [5\text{-}41]$$

If B_{ext} is large with respect to the nuclear dipole fields (~ 10^{-4} T) and to the muon dipole field at the nuclear site (e.g. $H_{Zeeman} >> H_{dip}$), then the nuclear dipoles also precess around $\vec{B}_{ext}$.
Only $\langle I_z\rangle \neq 0$, whereas $\langle I_x\rangle = \langle I_y\rangle = 0$ (time averaged).
Therefore, one has to consider only the z-components of the spins and the effective Hamiltonian contains only such terms:

$$H^i_{dip} = \frac{\mu_0}{4\pi}\frac{\hbar^2\gamma_\mu\gamma_N}{r_i^3}[I_{\mu,z}\cdot I^i_{N,z}(1-3\cos^2\theta_i)] = -\gamma_\mu\hbar I_{\mu,z}B^i_{dip,z} \qquad [5\text{-}42]$$

A quantum mechanical calculation of the second moment of the field distribution, which is Gauss like, gives (for a classical derivation see Eq. [5-45]-[5-47]):

$$\sigma^2 = \gamma_\mu^2 < \Delta B_{dip}^2 >= \frac{I_N(I_N+1)}{3}\left(\frac{\mu_0}{4\pi}\right)^2 \hbar^2 \gamma_\mu^2 \gamma_N^2 \sum_i \frac{1}{r_i^6}(1-3\cos^2\theta_i)^2 \qquad [5\text{-}43]$$

σ^2 depends on the μ^+ site and, in single crystals, also on the orientation of the crystal with respect to $\vec{B}_{ext}$. Formula [5-43] (Van Vleck formula) can be used to determine the muon site. For polycrystalline samples we integrate the angular dependent part of [5-43] over all possible directions. This gives:

$$< (1-3\cos^2\theta_i)^2 >= \frac{4}{5} \qquad [5\text{-}44]$$

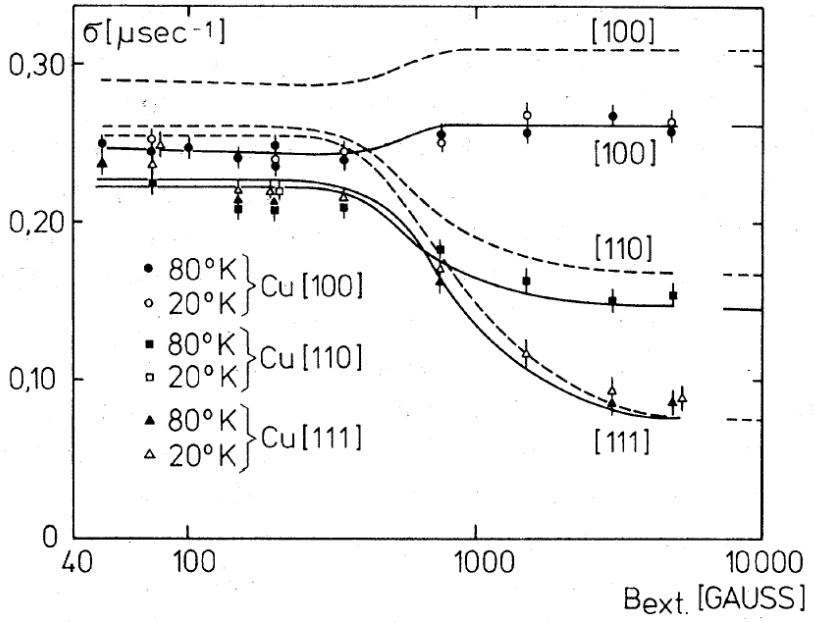

Fig. 5-32: Relaxation rate σ in Cu as a function of the external field for different crystal orientations (M. Camani et al., Phys. Rev. Lett., **39**, 836 (1977)). The Van Vleck value (right lines) is reached at large fields. If the nuclei have also a quadrupolar moment as in Cu (I=3/2), then at small fields the precession of the nuclear spins is around a new axis determined by the electric field gradient and $\vec{B}_{ext}$ and not simply around $\vec{B}_{ext}$ (O. Hartmann, Phys. Rev. Lett., **39**, 832 (1977)).

From this experiment it follows:

- Muon site determination: in fcc Cu μ^+ is at an octahedral position (see Chapt. 5.7)
- The next Cu neighbors around the muon shift 5% away from their undisturbed position (solid curve in Fig. 5-32: calculation with shifted Cu atoms; dotted curve: without shift).
- The electronic field gradient generated by μ^+ interacts with the Cu quadrupole moment.

5.5 Classical calculation of nuclear dipolar broadening in transverse and zero field

Muon in the field of a nuclear moment (see Fig. 5-31).

We calculate classically the field width at the muon position (origin of coordinate system).

Dipolar field at the origin generated by a classical nuclear moment $\vec{\mu}_{N,i}$:

$$\vec{B}_i = \frac{\mu_0}{4\pi}\mu_{N,i}\frac{3(\hat{\mu}_{N,i}\cdot\hat{r}_i)\cdot\hat{r}_i - \hat{\mu}_{N,i}}{{r_i}^3} \qquad \text{where } \hat{\mu}_{N,i} = \frac{\vec{\mu}_{N,i}}{\mu_{N,i}} = \frac{\vec{\mu}_{N,i}}{|\vec{\mu}_{N,i}|} \quad \text{and } \hat{r}_i = \frac{\vec{r}_i}{|\vec{r}_i|}$$

The total field is given by the lattice sum over all dipoles:

$$\vec{B} = \sum_i \vec{B}_i = \sum_i \frac{\mu_0}{4\pi}\mu_{N,i}\frac{3(\hat{\mu}_{N,i}\cdot\hat{r}_i)\cdot\hat{r}_i - \hat{\mu}_{N,i}}{{r_i}^3}$$

Consider only z- component (parallel to $\vec{B}_{ext}$).

With:

$$\hat{r}_i^{\,z} = \cos\theta_i, \quad \hat{\mu}_{N,i}^{\,z} = \cos\vartheta_i, \quad \hat{\mu}_{N,i}\cdot\hat{r}_i = \cos\vartheta_i\cos\theta_i + \sin\vartheta_i\cos\varphi_i\sin\theta_i$$

$$(B_i)_z = \frac{\mu_0}{4\pi}\frac{\mu_{N,i}}{{r_i}^3}\left[(3\cos^2\theta_i - 1)\cos\vartheta_i + 3\sin\theta_i\cos\theta_i\sin\vartheta_i\cos\varphi_i\right] \qquad [5\text{-}45]$$

TF case with $\gamma_N B_{ext} >> \gamma_\mu B_i$

$B_{ext} >> \frac{\gamma_\mu}{\gamma_N}B_i$ → Larmor precession of $\vec{\mu}_{N,i}$ around B_{ext} averages out the second term of [5-45] (so called non secular term).

Mean square of the secular component along $\vec{B}_{ext} \parallel \hat{z}$ is given by:

$$\sigma_{TF}^2 \equiv (\sigma^2)_z = \gamma_\mu^2\left[<(\sum_i B_{i,z}\ )^2> - <\sum_i B_{i,z}>^2\right] \qquad [5\text{-}46]$$

Average is over all possible orientations of $\vec{\mu}_{N,i}$ (i.e. over ϑ_i, φ_i).

The second term in [5-46] is zero since average gives terms of the form $\sum_i \int_{-1}^{1} \cos\vartheta_i d(\cos\vartheta_i)$.

The first term contains only sum of squared term $\sum_i \int_{-1}^{1} \cos^2\vartheta_i d(\cos\vartheta_i)$ which properly averaged gives $\frac{1}{3}$.

$$\rightarrow \sigma_{TF}^2 \equiv (\sigma^2)_z = \frac{1}{3}(\frac{\mu_0}{4\pi})^2 \hbar^2 \gamma_\mu^2 \gamma_N^2 I_N^2 \sum_i \frac{(3\cos^2\theta_i - 1)^2}{r_i^6}$$

Substituting I^2 with the quantum mechanical value I(I+1) we get Equation [5-43]

$$\sigma_{TF}^2 \equiv (\sigma^2)_z = \frac{1}{3}(\frac{\mu_0}{4\pi})^2 \hbar^2 \gamma_\mu^2 \gamma_N^2 I_N (I_N+1) \sum_i \frac{(3\cos^2\theta_i - 1)^2}{r_i^6} \qquad [5\text{-}47]$$

where θ_i is the polar angle of the position of the i-th dipole (with $B_{ext} \parallel z$). This value of the width is the so called van Vleck value.

Polycrystalline average (with average of $(3\cos^2\theta_i - 1)^2 = \frac{4}{5}$) we have:

$$\sigma_{TF,Poly}^2 \equiv \frac{4}{15}(\frac{\mu_0}{4\pi})^2 \hbar^2 \gamma_\mu^2 \gamma_N^2 I_N (I_N+1) \sum_i \frac{1}{r_i^6} \qquad [5\text{-}48]$$

ZF case

In this case the non-secular term cannot be dropped and the muon spin feels the full magnitude of $\vec{\mu}_{N,i}$.

The mean-square of the full magnitude of $\vec{\mu}_{N,i}$ is given by:

$$\sigma_{tot}^2 = \gamma_\mu^2 \left[< (\sum_i \vec{B}_i\ )^2 > - < \sum_i \vec{B}_i >^2 \right] = \sum_i < \vec{B}_i{}^2 >$$

or

$$\sigma_{tot}^2 = (\sigma_{ZF}^2)_x + (\sigma_{ZF}^2)_y + (\sigma_{ZF}^2)_z$$

For the z-component we have for instance

$$(\sigma_{ZF}^2)_z = \gamma_\mu^2 \sum_i < B_{i,z}{}^2 > ,$$

where now for $B_{i,z}$ the non-secular components have to be taken into account (see [5-45]). This gives terms of the form:

$$\left[(3\cos^2\theta_i - 1)^2 \cos^2 \vartheta_i + 9 \sin^2 \theta_i \cos^2 \theta_i \sin^2 \vartheta_i \cos^2 \varphi_i \right]$$

to be averaged over $d(\cos \vartheta_i)$ and $d\varphi_i$.

One obtains:

$$(\sigma_{ZF}^2)_z = \frac{1}{3} (\frac{\mu_0}{4\pi})^2 \hbar^2 \gamma_\mu^2 \gamma_N^2 I_N (I_N + 1) \sum_i \frac{(3\cos^2 \theta_i + 1)}{r_i^6} \qquad [5\text{-}49]$$

Similarly, for the x and y components in the crystal case:

$$(\sigma_{ZF}^2)_x + (\sigma_{ZF}^2)_y = \frac{1}{3} (\frac{\mu_0}{4\pi})^2 \hbar^2 \gamma_\mu^2 \gamma_N^2 I_N (I_N + 1) \sum_i \frac{(5 - 3\cos^2 \theta_i)}{r_i^6} \qquad [5\text{-}50]$$

Polycrystalline average or if the muon site has cubic symmetry (in both cases $< \cos^2 \theta >= \frac{1}{3}$)

$$\sigma^2_{ZF,Poly} = \frac{1}{3}\left[(\sigma^2_{ZF})_x + (\sigma^2_{ZF})_y + (\sigma^2_{ZF})_z\right] = \frac{2}{3}(\frac{\mu_0}{4\pi})^2 \hbar^2 \gamma_\mu^2 \gamma_N^2 I_N (I_N + 1) \sum_i \frac{1}{r_i^6} \quad [5\text{-}51]$$

Note also that

$$\sigma^2_{ZF,Poly} = \frac{5}{2}\sigma^2_{TF,Poly} = \frac{5}{2}\sigma^2_{VV,Poly} \quad [5\text{-}52]$$

The results obtained here are also valid quantum mechanically (see R. Hayano et al. Phys. Rev. B **20**, 850 (1979).

The prediction of equation [5-52] is confirmed experimentally in the ZrH_2 system, by comparing $G_z(t)$ the relaxation at zero field and $G_x(t)$ the relaxation at high transverse field (B_{ext}= 5 kG).
ZrH_2 is ideal because there is no electric quadrupole moment, the dipolar field created by the protons is large and the muon is diffusing very slowly. From the experiment
(R. Hayano et al. Phys. Rev. B **20**, 850 (1979) one obtains:

$$\frac{\sigma^2_{ZF,Poly}}{\sigma^2_{TF,Poly}} = 2.4 \pm 0.1$$

which is in good agreement with the prediction of [5-52].

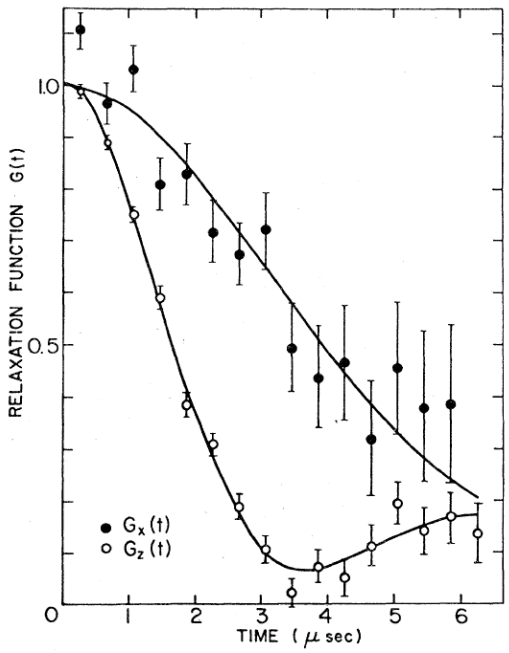

Fig. 5-33: Observed zero-field relaxation $G_z(t)$ and high-field transverse relaxation $G_x(t)$ in ZrH_2 at room temperature.

5.6 Dynamic spin relaxation

In the previous chapter we considered the muon and the local fields as static during the observation time. In this chapter we consider the effect of dynamic and of fluctuations on the polarization of the muon ensemble.

A) Simple model: Brown motion of the phase

The muon stays at a site where the field fluctuates with correlation (or fluctuation) time τ between the random values $+B_1$ or $-B_1$ ($\vec{B}_1 \perp \vec{P}(0)$). Analog is the case where the muon jump after a time τ (average dwelling time) from a position to another where the field can take the random values $+B_1$ or $-B_1$.
The phase of the muon spin precession Φ makes a „random walk“ with step:

$$\delta\Phi = \gamma_\mu B_1 \tau = \sigma\tau \qquad [5\text{-}53]$$

After N steps (time $t = N\tau$) the variance of the phase is:

$$\langle (\Phi - \langle\Phi\rangle)^2 \rangle = \langle \Phi^2 \rangle = \left(\sum_N \pm\delta\Phi \right)^2 = \sum_N \delta\Phi^2 = N(\delta\Phi)^2 = N(\sigma\tau)^2 = \sigma^2 \tau\, t \qquad [5\text{-}54]$$

($\uparrow = 0$)

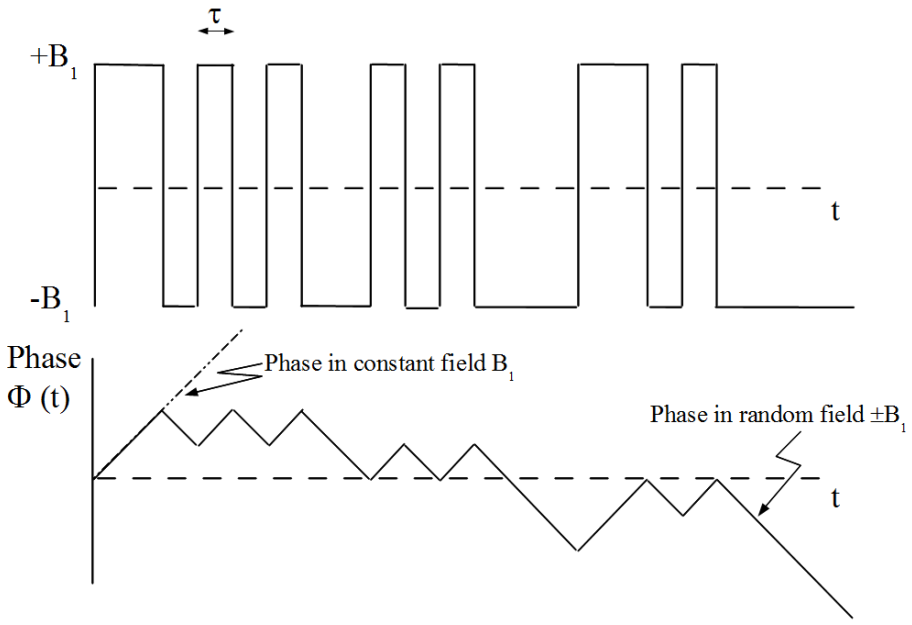

Fig.5-34: Phase of the spin in a constant field, compared with the case where the muon experiences a field randomly fluctuating between two values.

The increase of the phase variance leads to a loss of polarization of the muon ensemble. We estimate the relaxation time T as the time after which the phase variance reaches the value of one radian i.e.

$$\frac{1}{T} = \sigma^2 \tau = \frac{\sigma^2}{\nu} \qquad [5\text{-}55]$$

where $\nu = 1/\tau$ is the fluctuation rate of the local fields, experienced by the muon, or it is the hopping rate in case of muon diffusion.

Eq. [5-55] has more general validity. It is obtained also in the case that the fluctuating fields are Gauss distributed (Eq. [5-10]) and an external field $\vec{B}_0 \perp \vec{P}(0)$ is applied (dynamic TF relaxation).

The polarization function becomes:

$$P(t) = e^{-\frac{\sigma^2}{\nu}t} = e^{-\sigma^2 \tau t} \qquad [5\text{-}56]$$

Higher fluctuation rate (or hopping rate) leads to an averaging of the field distribution → reduction of the damping or relaxation (so called "motional narrowing").

In the TF case fast fluctuations are described by an exponential relaxation:

$$P(t) = e^{-\frac{t}{T_2}} \qquad T_2\text{: relaxation time} \qquad [5\text{-}57]$$

B) <u>Better model: Strong Collision Approximation (SCA)</u>

Assumption: The muon jumps between different sites with an average rate ν (muon diffuses, filed is static). The same model can be used in the case that the muon is immobile and that the local field changes its value with an average rate ν (muon static, field dynamic).The probability that the muon after time t is at the same position or experiences the same local field is $e^{-\nu t}$.
After one „jump" (or „collision"), the local field is randomly chosen from the field distribution $p(\vec{B})$. There is no correlation between the fields before and after the jump (with the exception of possible external fields).
The field correlation function is given by:

$$< B_i(t) B_j(0) >= \delta_{ij} < B_i^2(0) > e^{-\nu t} \qquad i,j=x,y,z \qquad [5\text{-}58]$$

The muon polarization at time t is the sum of the contributions from muons which have experienced no jump, one, two or more jumps:

$$P(t,\nu) = \sum_i g_i(t) \qquad [5\text{-}59]$$

No „jump“: $g_0(t) = e^{-\nu t} G_z(t)$ [5-60]

Where $e^{-\nu t}$ is the probability that no „jump" occurred within the time t and $G_z(t)$ is the static relaxation function corresponding to the field distribution $p(\vec{B})$ (i.e. in ZF the Kubo-Toyabe function, Eq. [5-13], if we have Gauss distributed fields).

1 „jump“: $$g_1(t) = \nu \int_0^t dt_1 e^{-\nu t_1} G_z(t_1)\, e^{-\nu(t-t_1)} G_z(t-t_1) = \nu e^{-\nu t} \int_0^t dt_1 G_z(t_1)\, G_z(t-t_1)$$ [5-61]

2 „jumps“:

$$g_2(t) = \nu^2 e^{-\nu t} \int_0^t dt_2 \underbrace{\int_0^{t_2} dt_1 G_z(t_1) G_z(t_2 - t_1)}_{\propto\ g_1(t_2)} G_z(t - t_2)$$ [5-62]

and so on.

The higher terms can be calculated recursively:

$$g_n(t) = \nu \int_0^t dt' g_0(t') g_{n-1}(t - t')$$

The dynamic relaxation (Eq. [5-59]) can be calculated numerically for any field distribution (e.g. Gauss or other, with or without external field).

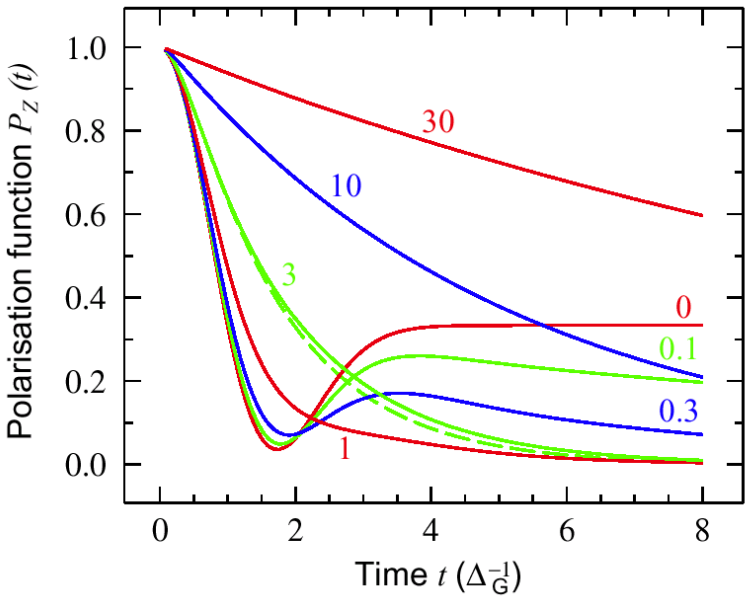

Fig 5-35: Dynamic Gauss Kubo-Toyabe in ZF case: Strong Collision Model for an isotropic Gauss distribution of fields (with variance σ), B_{ext}=0. The fluctuation rate ν is given in units of σ. The dashed curve is the motional narrowing limit (exponential) for $\frac{\nu}{\sigma} = 3$.

Special cases:

a) „Motional narrowing limit“ in ZF ($\nu >> \sigma$):

$$P_z(t) \cong e^{-\frac{2\sigma^2}{\nu}t} = e^{-2\sigma^2 \tau t} = e^{-\lambda t} \qquad [5\text{-}63]$$

(exponential relaxation, see [5-56])

In an external field (LF) (with $\omega_L = \gamma_\mu B_{ext}$):

$$P_z^{LF} = e^{-\lambda_{LF} t} \qquad [5\text{-}64]$$

where

$$\lambda_{LF} = \frac{2\sigma^2 \tau}{1 + \omega_L^2 \tau^2} \qquad [5\text{-}65]$$

b) Quasi static case in ZF ($\nu << \sigma$):

$$P_Z(t) \cong \frac{1}{3} e^{-\frac{2}{3}\nu t} + \frac{2}{3}(1 - \sigma^2 t^2) e^{-\frac{\sigma^2 t^2}{2}} \qquad [5\text{-}66]$$

The first term (damping of the „1/3 tail“) depends only on ν. This fact can be used to investigate slow dynamics (time window ~ 10 μs) also in systems where σ is large. However, some caution is due. The Kubo-Toyabe expression does not take into account the coupling of the muon moment with the surrounding moments (e.g. nuclear moments).
A classical or quantum mechanical treatment of this effect may lead to deviation from a pure 1/3 behavior (see P. Dalmas de Réotier et al., Phys. Lett. A **162**, 206 (1992), M. Celio and P.F. Meier, Phys. Rev B **27**, 1908 (1993)).

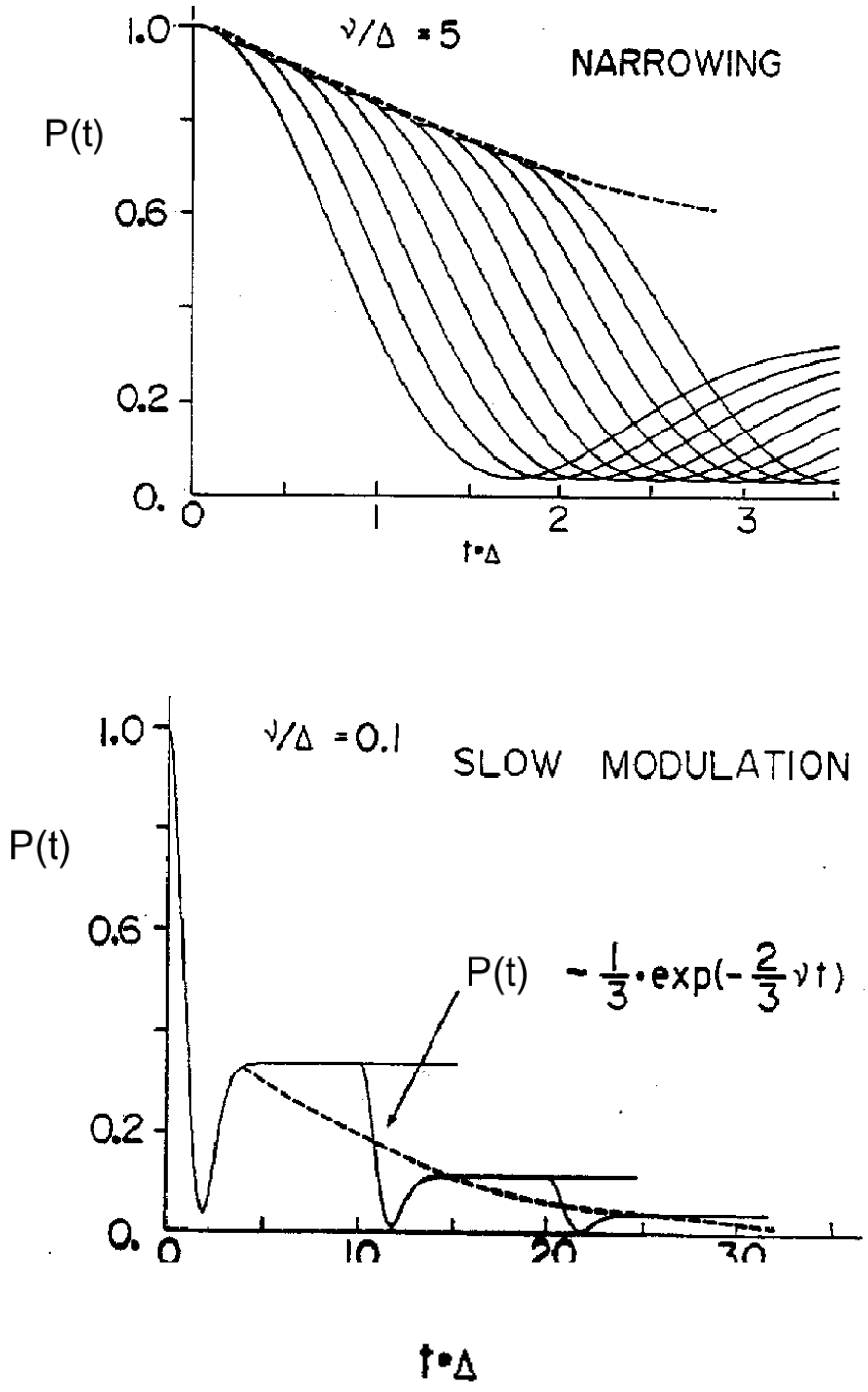

Fig 5-36: Schematic representation of the time evolution of the average muon spin polarization in the SCA model for Gauss fields. The behavior of the dynamic relaxation can be obtained from the envelope of the static functions.

Hopping (or fluctuation) effect on the relaxation function of Cu (Fig. 5-32). At small rate (compared to $\sigma \approx 0.25\ \mu s^{-1}$, see Fig. 5-32) there is no sizeable effect on the ZF relaxation up to large times ($t \approx 6\ \mu s$), whereas, in weak LF, changes appear at an earlier stage.

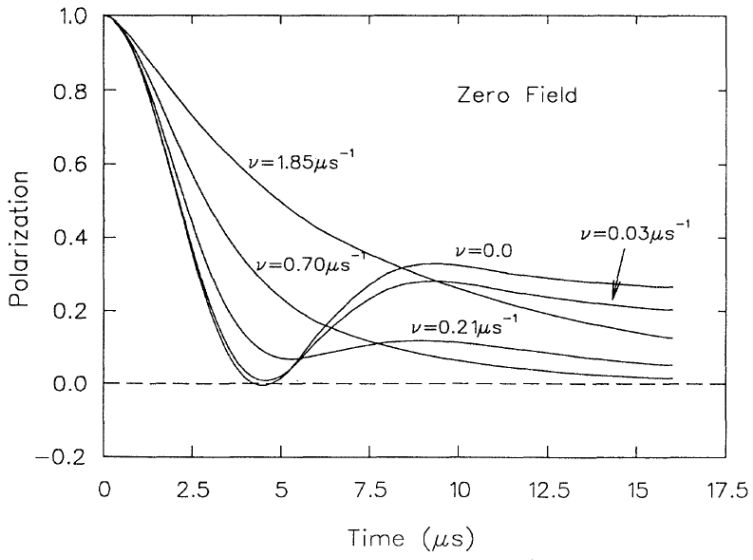

Fig. 5-37a: **Muon polarization in zero field (ZF) for several muon hop rates, calculated from static relaxation function using the strong collision model.**

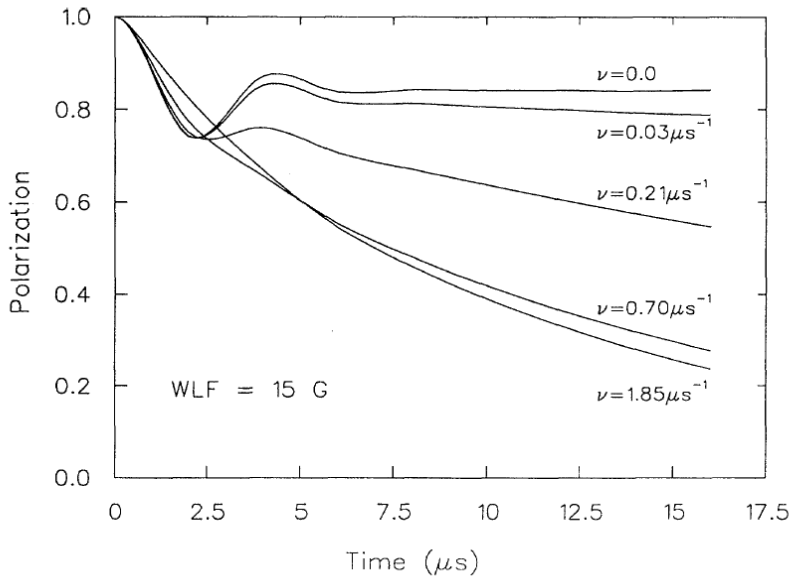

Fig. 5-37b: **Muon-polarization function in weak longitudinal field (WLF) at several muon hop rates, calculated using the strong collision model.**

G.M Luke et al., Phys. Rev B **43**, 3284 (1991)

In the TF case a relaxation function, which describes static as well as dynamic processes, is the so-called Abragam function:

$$P_x(t) \equiv G_x(t) = e^{-\Gamma(t)t}$$
$$\Gamma(t)t = \Delta^2\tau^2\left(e^{-\frac{t}{\tau}} - 1 + \frac{t}{\tau}\right) \qquad [5\text{-}67]$$

Dynamic limit:

$\tau \to 0,\ t >> \tau$ $\qquad P_x(t) \to e^{-\Delta^2\tau t} \equiv e^{-\lambda t}$ (as in Eq. [5-65] up to a factor 2)

Static limit:

$\tau \to \infty$ $\qquad P_x(t) \to e^{-\frac{\Delta^2 t^2}{2}}$

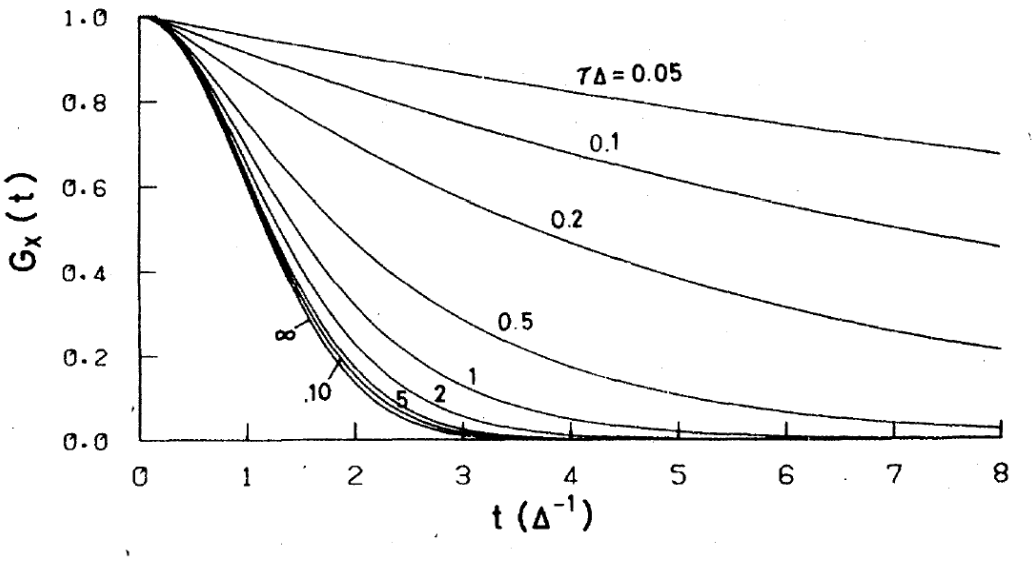

Fig. 5-38: Transverse relaxation function in high fields according to [5-67] for different correlation times τ. Δ is the field width. Contrary to ZF measurements, from these curves it is difficult to extract information about slow fluctuations ($\tau\Delta >> 1$). From R. Hayano et al. Phys. Rev. B **20**, 850 (1979).

5.7 Example of dynamic relaxation: muon diffusion in Cu, quantum diffusion

The muon diffuses between nuclear moments. As a consequence the local field is a stochastic function of time. From the muon spin relaxation one can obtain the jump rate $\nu = \frac{1}{\tau}$ and its temperature dependence.

Jump rate and diffusion constant are related by (Random-walk model, Einstein):

$$D = \frac{1}{C} a^2 \frac{1}{\tau} \qquad [5\text{-}68]$$

C: Constant, depends on geometry of the diffusion jumps (for instance for jumps between octahedral sites in a fcc crystal C=36, a: lattice constant).

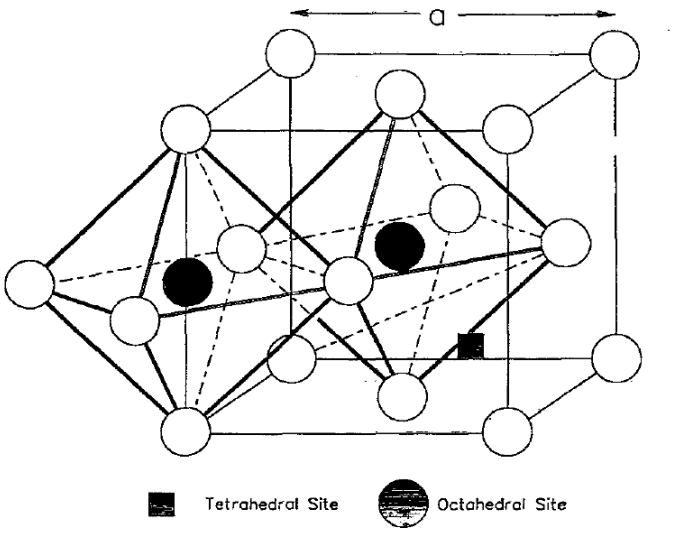

Fig. 5-39: Muon site in Cu in the center of an octahedron. Shown is also the tetrahedral site.

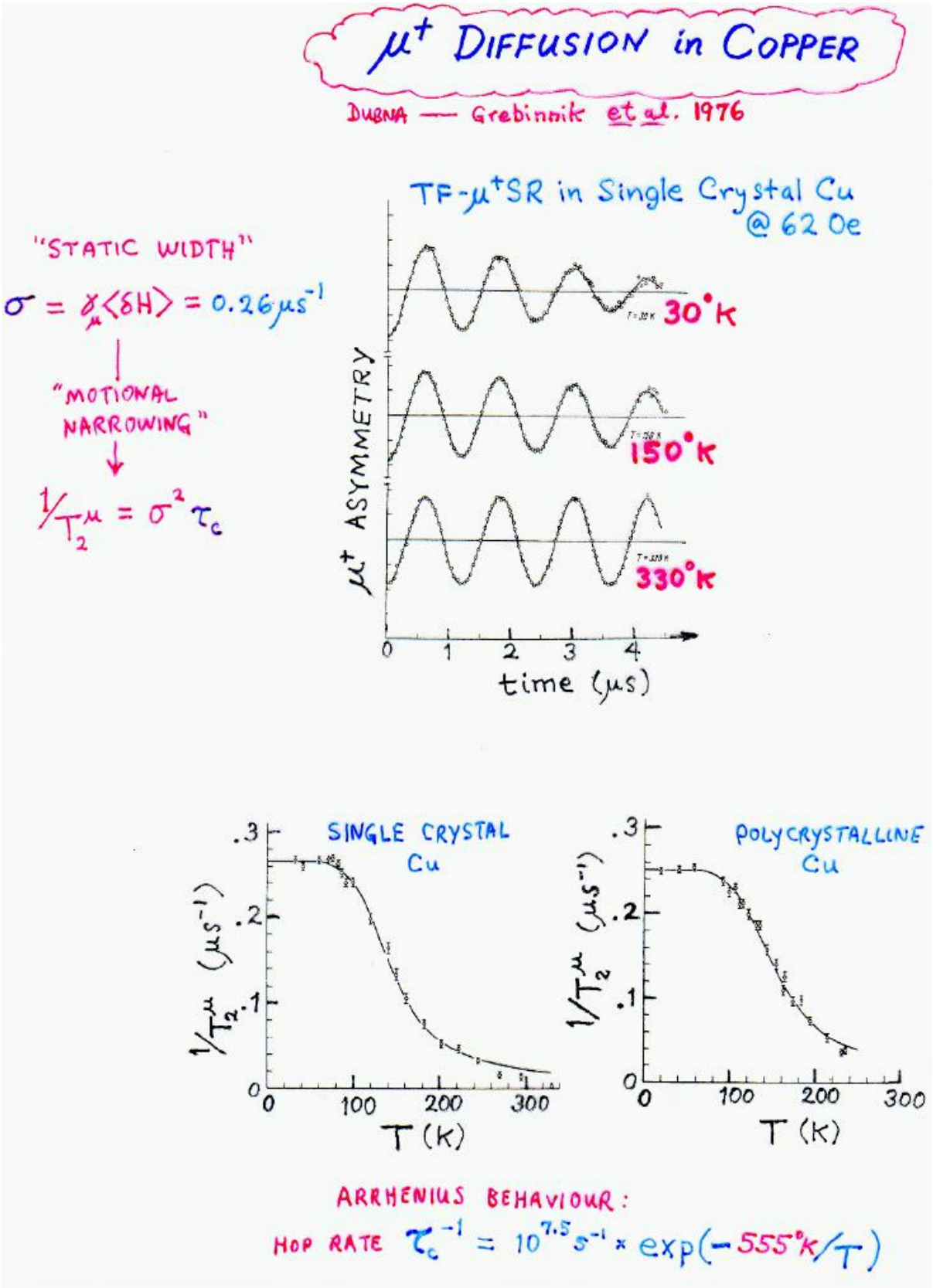

In the early measurements the temperature dependence of the hop rate was obtained from measurements of the TF relaxation rate (graphics J. Brewer, UBC).

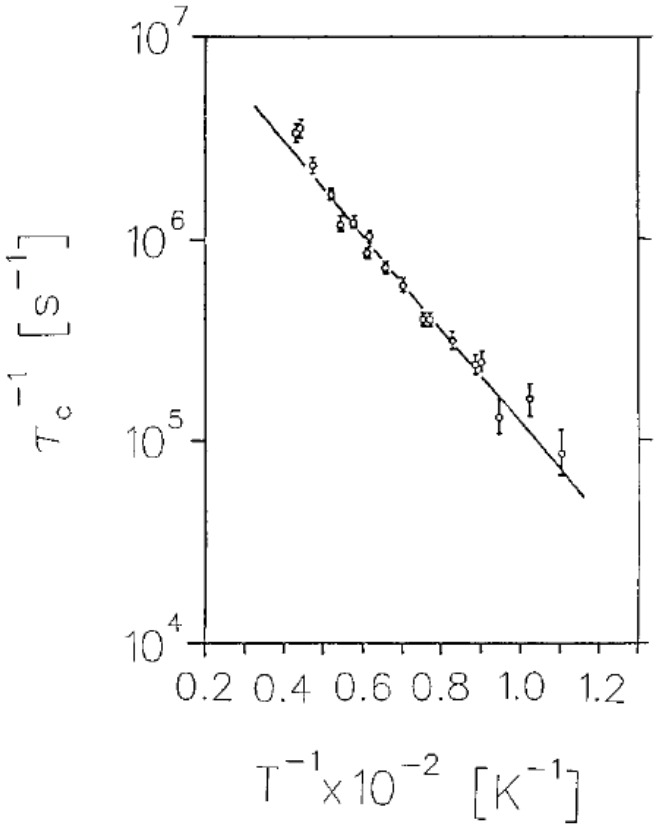

Fig. 5-40: Temperature dependence (90 K < T < 250 K) of the muon hop rate in Cu (V.G. Grebinnik et al., Sov. Phys. JETP **41**, 777 (1975)).

For classical diffusion we expect an Arrhenius law:

$$\frac{1}{\tau} = \nu_0 e^{-\frac{E_A}{kT}} \qquad [5\text{-}69]$$

ν_0 = local vibration frequency (attempt frequency) of the μ^+ in a potential well
E_A = Potential threshold = Activation energy

The values from Fig. 5-40 indicate a quantum nature of the process.[12]
Quantum diffusion of a light particle such as the muon or the proton is based on:

- Tunnel effect ($E < E_A$)
- Small polaron picture (= μ^+ + lattice distortion) → Phonon assisted tunneling (Energy levels in occupied and non-occupied states in the potential well must be degenerate for tunneling to take place. This degeneracy can occur as a consequence of lattice vibration, phonons, see Fig. 5-41).

[12] The value for ν_0 is too small to be valid classically, where ν_0 should be of the order of the vibration frequency 10^{13}/s.

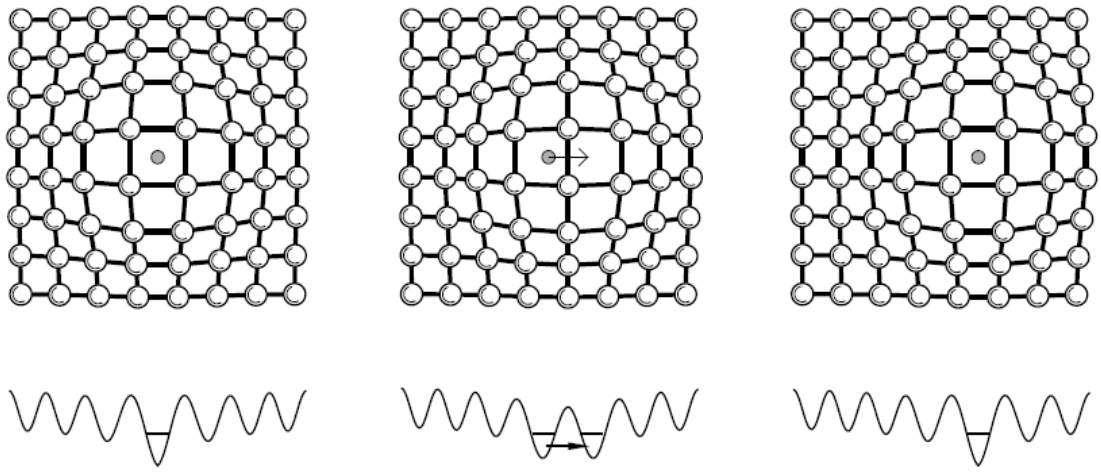

Fig. 5-41: Local lattice distortion and phonon assisted tunneling.

At the lowest temperatures the μ^+ can move in a band state as a Bloch wave (coherent motion). The rate is given by the finite range of the motion, which is limited by lattice defects. Important is the dissipation due to the concomitant motion of the electronic screening cloud.

More precise determination of the hop rate is obtained in weak LF fields (see Fig. 5-37):

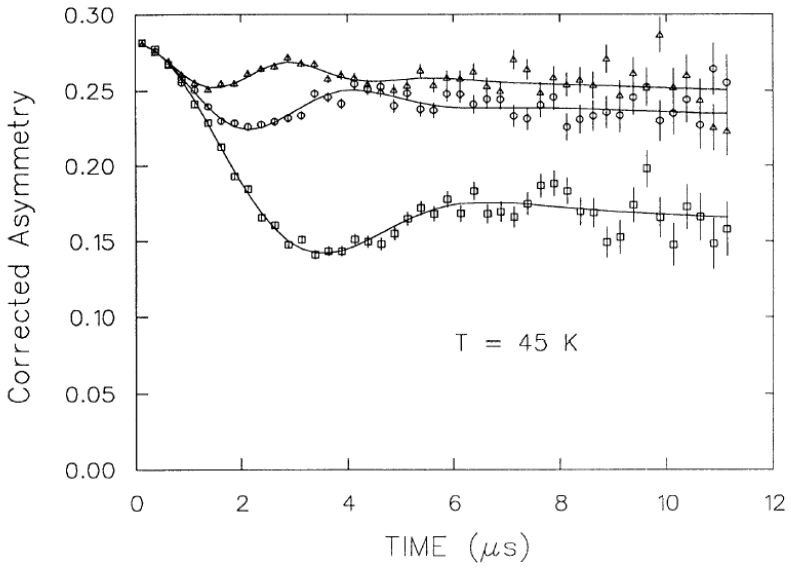

Fig. 5-42a: **WLF time-differential μSR spectra for applied fields 8 (squares), 16 (circles), and 24 G (triangles). Muons are nearly static: T=45 K.**

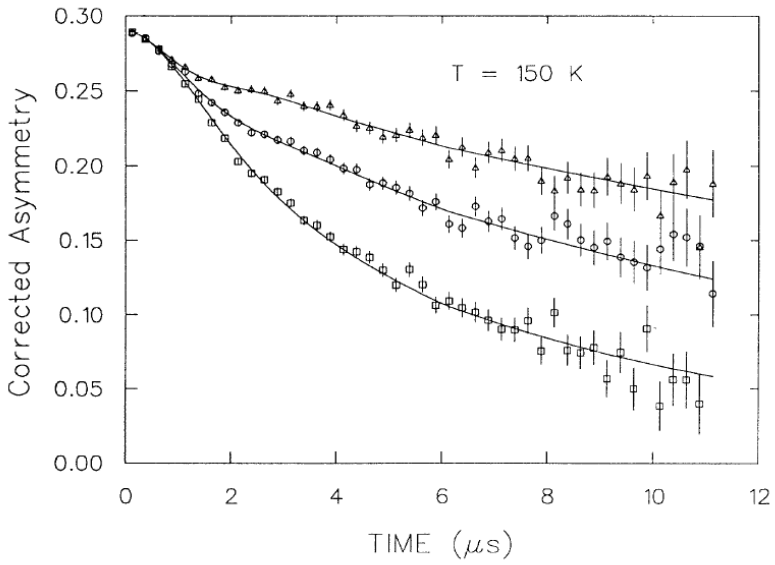

Fig. 5-42b: **WLF time-differential μSR spectra for applied fields 8 (squares), 16 (circles), and 24 G (triangles). Muons are diffusing rapidly: T=150 K.**

G.M Luke et al., Phys. Rev **B43**, 3284 (1991)

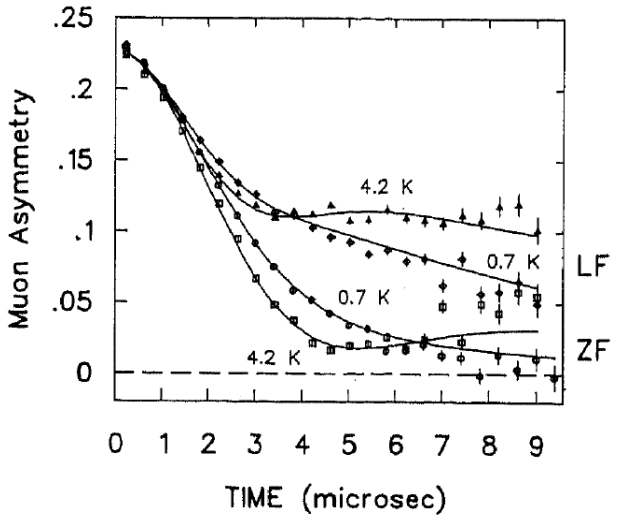

Fig. 5-42c Positive muon relaxation functions in Cu crystal for zero applied field (ZF) at 4.2 K (squares) and 0.7 K (circles) and for 9 G longitudinal field (LF) at 4.2 K (triangles) and 0.7 K (diamonds). The data were fitted with one common value of $\Delta = 0.380(4)\ \mu s^{-1}$ and with common values of μ^+ hop rates $\tau_c^{-1}(4.2\ K) = 0.158(13)\ \mu s^{-1}$ and $\tau_c^{-1}(0.7\ K) = 0.432(14)\ \mu s^{-1}$.

J.H. Brewer et al., Phys. Lett. **120**A, 199 (1987)

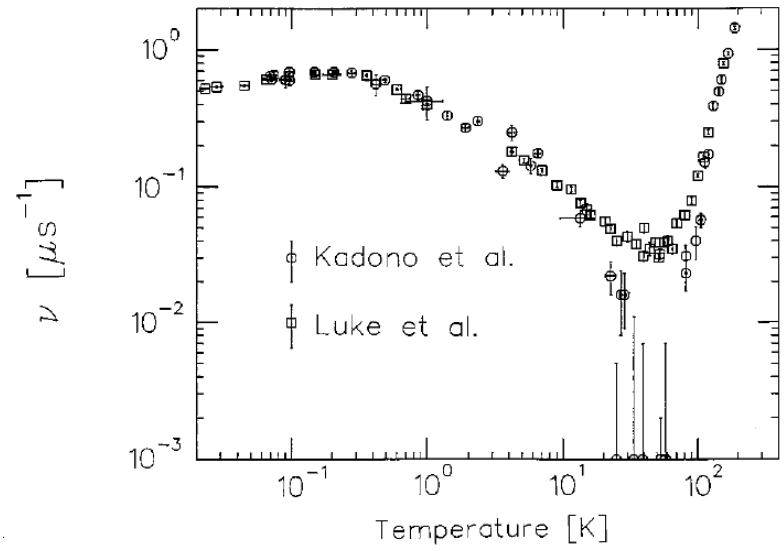

Fig. 5-43: Muon hop rate in Cu from ~ mK to room temperature. Different mechanisms determine the motion in the various temperature intervals (for an overview see V.G. Storchak, N. V. Prokofev, Review of Modern Physics **70**, 929 (1998)).

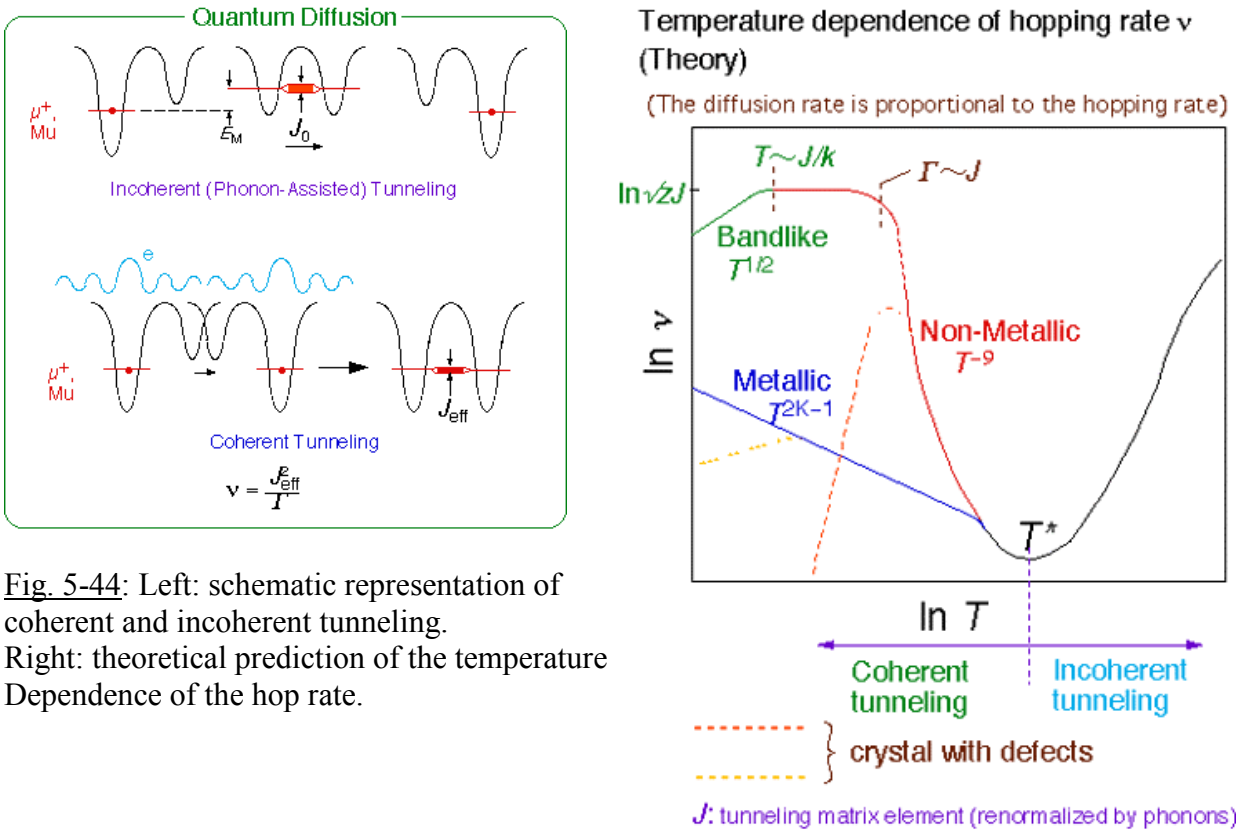

Fig. 5-44: Left: schematic representation of coherent and incoherent tunneling.
Right: theoretical prediction of the temperature Dependence of the hop rate.

The behavior $\nu \propto T^{-\alpha}$ is theoretically predicted (Kondo in Perspectives of Meson Science, T. Yamazaki Editor, North Holland, 1992). The theory predicts a smaller exponent α for muons in metals than in insulators. This is a consequence of the additional dissipation by electronic mechanisms in metals („electron drag“).

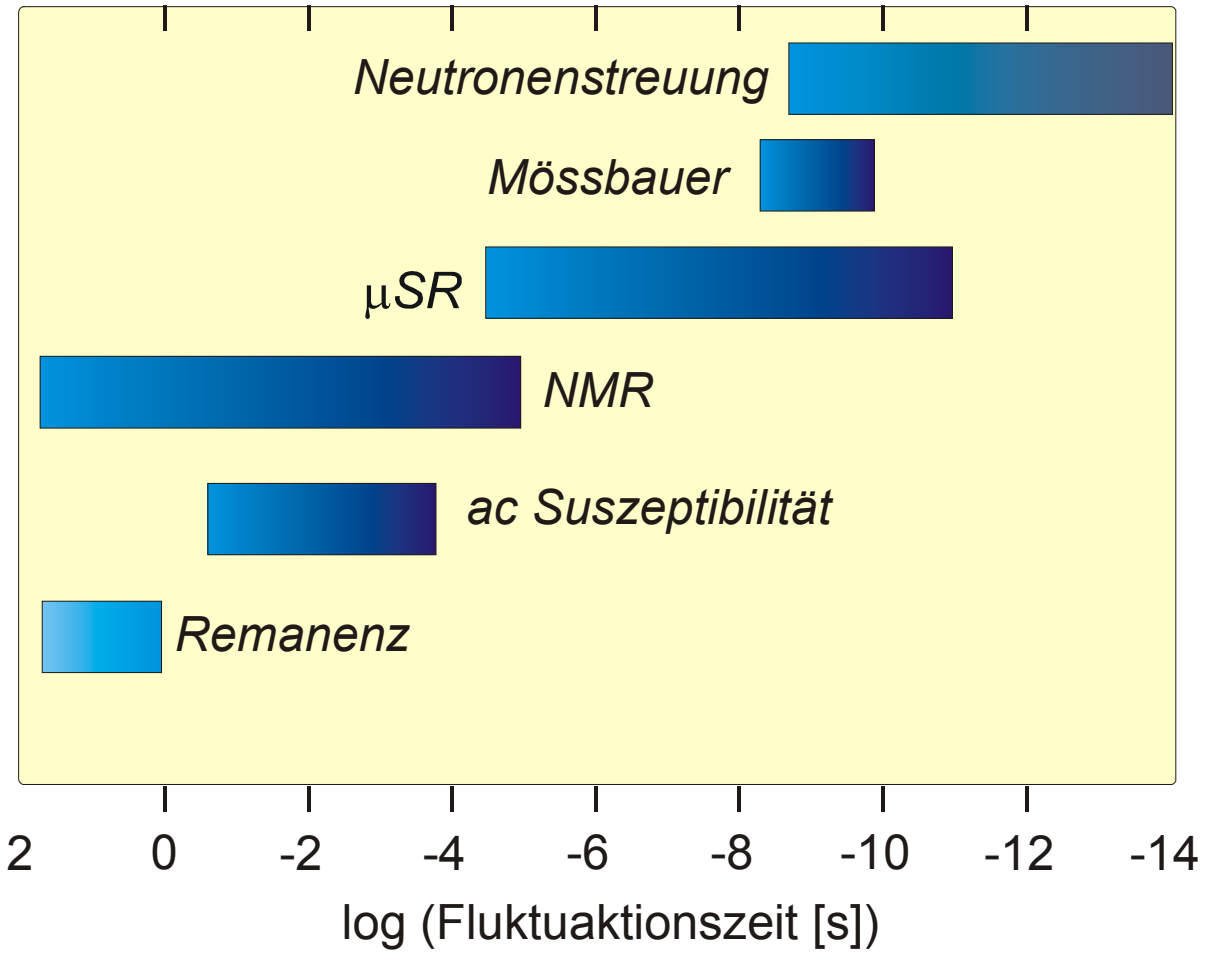

Fig. 5-45: Time window of different methods for magnetic fluctuation and relaxation phenomena, showing the complementarity between μSR and neutron scattering and NMR.

6. Some applications in magnetism

6.1 Local magnetic fields in magnetic materials

As a magnetic probe the μ^+ is well suited to investigate local magnetic fields and fluctuations.

The internal field is generally a combination of dipolar fields and contact hyperfine fields.

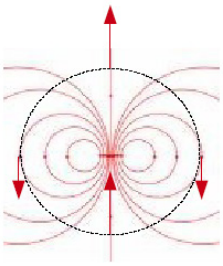

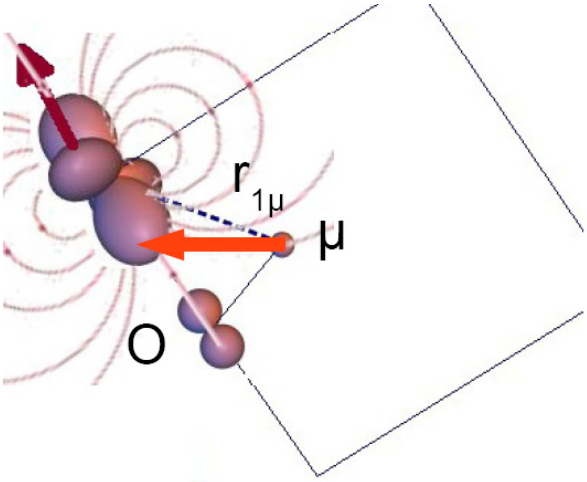

$$\vec{B}_{dip}(\vec{r}_i) = \frac{\mu_0}{4\pi}\frac{3(\vec{\mu}_i \cdot \vec{r}_i)\cdot \vec{r}_i - \vec{\mu}_i r_i^2}{r_i^5}$$

$$B_{dip} \approx \frac{\mu_0}{4\pi}\frac{\mu_i}{r_{1\mu}{}^3} \approx \frac{\mu_i[\mu_B]}{d^3[A^3]}\ T$$ Typically some 0.1 T (kG)

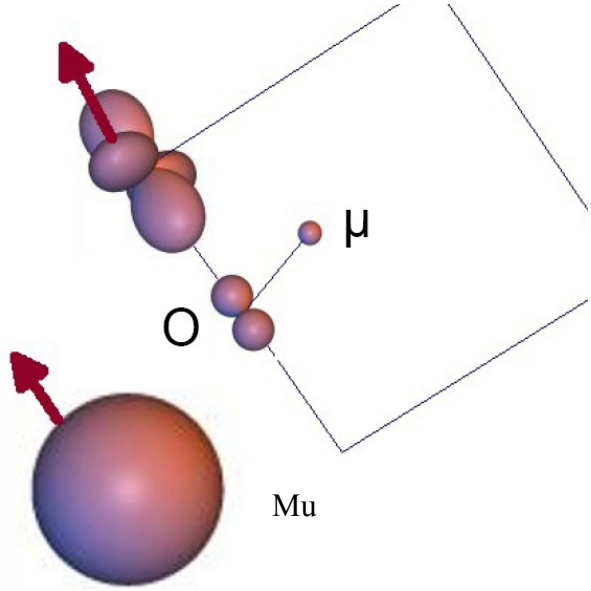

Mu

The contact field is usually smaller than the dipolar field. However, note that for Mu in the 1s state it corresponds to a field $B_{hf}(r_\mu)$=32.8 T. This large value is more similar to the NMR case, where the spin probe is at a lattice site and the electronic s-wave component is large.

Contact interaction:

$$\vec{B}_{hf}(\vec{r}_\mu) = \frac{2\mu_0}{3} g_e \mu_B \rho_{spin}(\vec{r}_\mu) \cong \frac{2\mu_0}{3} g_e \mu_B \left|\varphi(\vec{r}_\mu)\right|^2 \langle \vec{s} \rangle$$

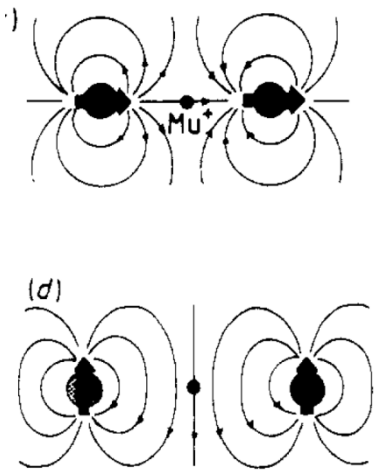

The dipolar field is anisotropic. The field at the muon site is not necessarily parallel to the magnetization.

The measured field value and direction depend on the muon position in the lattice. Fig. 6-1 shows the dipolar field in MnSi.

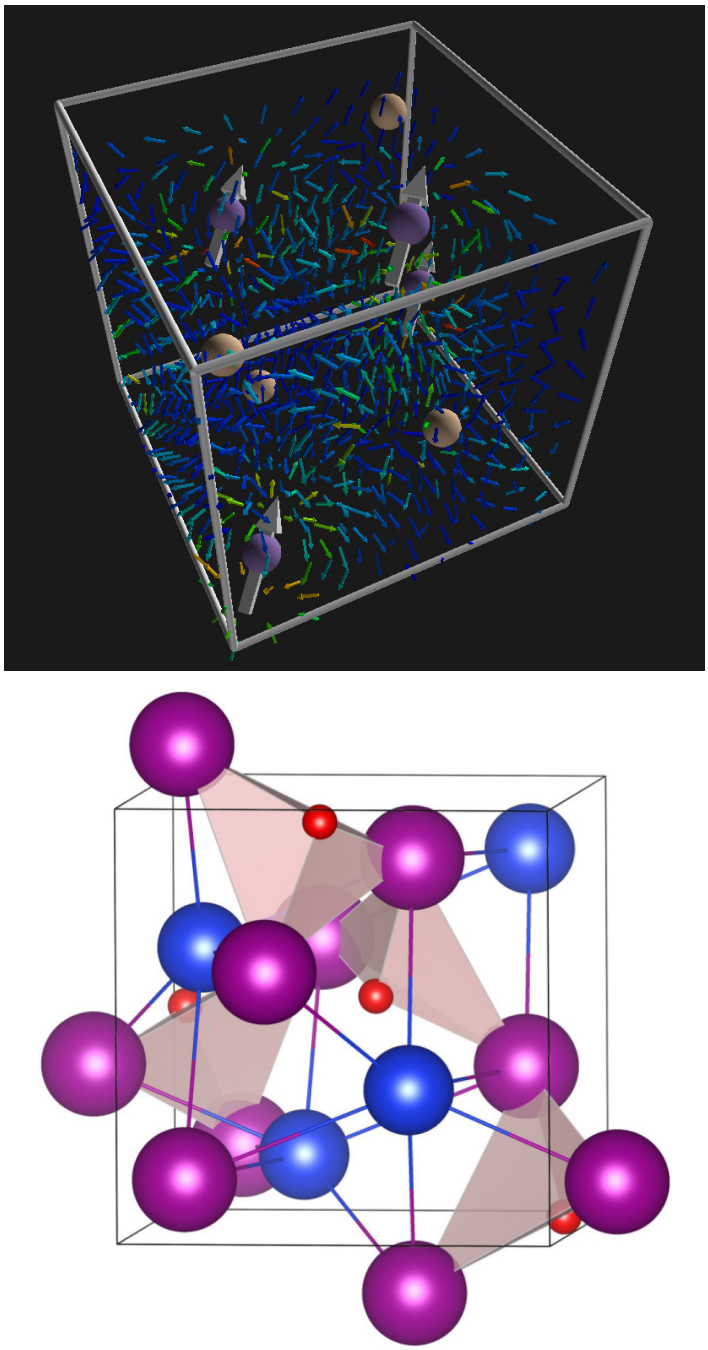

Fig. 6-1: a) Dipolar field in MnSi arising from Mn magnetic moments of 0.3 μ_B in the FM phase. b) Sketch of the crystallographic structure of MnSi (Mn ions are drawn in purple, Si ions in blue. Note that six Mn ions, which do not belong to the primary unit cell, are also displayed. The muon position (0.532,0.532,0.532), in units of the lattice constant, is also indicated (red) as well as the other three equivalent sites. There are totally 4 equivalent crystallographic positions in the unit cell (corresponding to the so called Wycoff position 4a): $(x,x,x),\ (\frac{1}{2}-x,\bar{x},\frac{1}{2}+x),\ (\frac{1}{2}+x,\frac{1}{2}-x,\bar{x}),\ (\bar{x},\frac{1}{2}+x,\frac{1}{2}-x)$, giving rise to up to four different muon precession frequencies (from A. Amato et al., Phys. Rev. B **89**, 184425 (2014)).

In a magnetic material the total local magnetic field $\vec{B}_{loc}$ at the muon site can be generally written as:

$$\vec{B}_{loc} = \vec{B}_{ext} + \vec{B}_{dem} + \vec{B}_{Lor} + \vec{B}_{dip} + \vec{B}_{hf} \qquad [6\text{-}1]$$

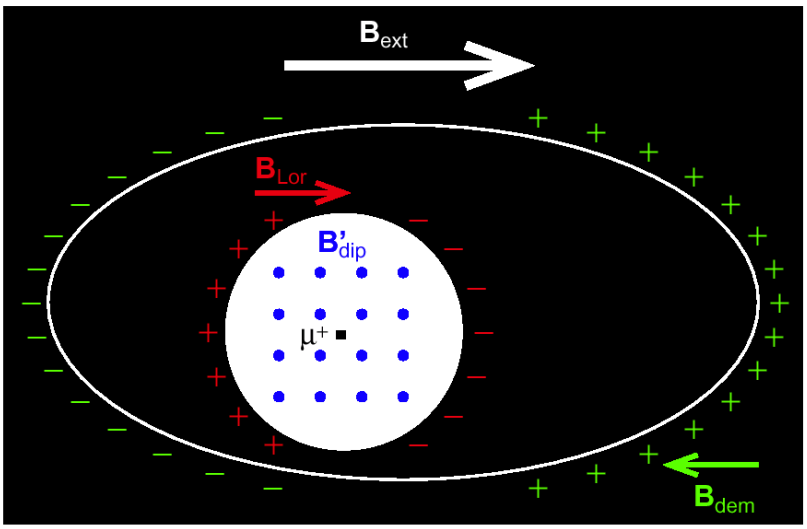

Fig. 6-2: Schematic representation of the different contributions for a ferromagnetic material in saturation (sample of ellipsoidal shape). This representation is also applicable to polarized paramagnets.

$\vec{B}_{ext}$: Applied external magnetic field

$\vec{B}_{dem}$: Demagnetizing field

$\vec{B}_{dem} = -N\mu_0\vec{M}$ N: Demagnetization factor. It depends on the sample form. In the general case it is a tensor and can depend on position.

For a sphere $N = \frac{1}{3}$. Another important example is an infinite plate (an ellipsoid with two of its axes going to infinity) which has N = 1 in a direction normal to the plate and N=0 in parallel orientation.

$\vec{M}$: Macroscopic magnetization of the sample

$\vec{B}_{Lor}$: Lorentz field; Field of a hypothetical hollow sphere (Lorentz sphere)

$$\vec{B}_{Lor} = \frac{1}{3}\mu_0\vec{M}_S \qquad [6\text{-}2]$$

$\vec{M}_S$: Saturation magnetization in a ferromagnet or vector sum of the magnetic moments inside the Lorentz sphere divided by its volume.

$\vec{B}_{dip}$: Field of the dipoles in the Lorentz sphere

$$\vec{B}_{dip}(\vec{r}) = \frac{\mu_0}{4\pi}\sum_i \frac{3(\vec{\mu}_i \cdot \vec{r}_i)\cdot \vec{r}_i - \vec{\mu}_i r_i^2}{r_i^5} \qquad [6\text{-}3]$$

$\vec{\mu}_i$: Dipole moment of the lattice atoms

$\vec{r}_i$: Vector radius from muon site to dipole

$\vec{B}_{hf}$: Hyperfine field or Fermi-contact field

$$\vec{B}_{hf}(\vec{r}_\mu) = \frac{2\mu_0}{3} g_e \mu_B \rho_{spin}(\vec{r}_\mu) \cong \frac{2\mu_0}{3} g_e \mu_B \left|\varphi(\vec{r}_\mu)\right|^2 \langle \vec{s} \rangle \qquad [6\text{-}4]$$

$\rho_{spin}(\vec{r}_\mu) = \rho_\uparrow(\vec{r}_\mu) - \rho_\downarrow(\vec{r}_\mu)$: Electron spin density at the muon site

Most of the μSR-measurements in a ferromagnet are performed without external field. Then we have $\vec{B}_{ext} = \vec{B}_{dem} = 0$.

$$\vec{B}_{loc} = \vec{B}_{Lor} + \vec{B}_{dip} + \vec{B}_{hf} \qquad [6\text{-}5]$$

At a muon site with cubic symmetry $\vec{B}_{dip} = 0$, so that

$$\vec{B}_{loc} = \vec{B}_{Lor} + \vec{B}_{hf} \qquad [6\text{-}6]$$

For an antiferromagnet, $\vec{B}_{dem}$ and $\vec{B}_{Lor}$ are zero so that

$$\vec{B}_{loc} = \vec{B}_{dip} + \vec{B}_{hf}$$

If a saturated FM sample has a spherical shape Lorentz field and demagnetizing field cancel each other $\vec{B}_{Lor} = -\vec{B}_{dem}$.

$$\vec{B}_{loc} = \vec{B}_{dip} + \vec{B}_{hf}$$

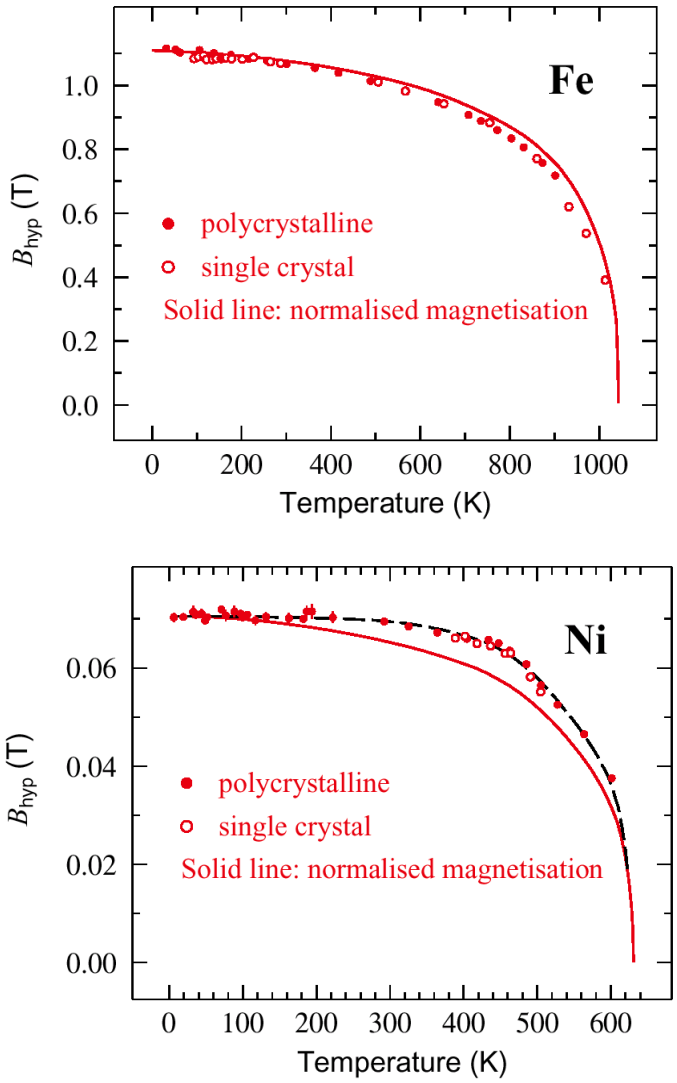

Fig. 6-3: Absolute value of the hyperfine field in Fe and Ni as a function of temperature.

Nickel has a cubic face centered structure (fcc). The dipole field at octahedral and tetrahedral sites is zero because of the cubic symmetry.

T=0: $\vec{B}_{loc} = +\ 0.148\ (1)$ T

$\vec{B}_{Lor} = +\ 0.221$ T

$\vec{B}_{hf} = -\ 0.071$ T

$\vec{B}_{hf}$ is not strictly proportional to $\vec{M}$ (in Ni $\mu_0 M(0)=0.66$ T). Possible reasons:

- Spin density at the muon site is not simply linearly proportional to $\vec{M}$
- Zero point motion of the muon
- Thermal volume expansion

The sign of $\vec{B}_{loc}$ can be obtained from a measurement of $\vec{B}_{loc}$ as a function of $\vec{B}_{ext}$.

Example: Magnetic order in organic compounds (containing only C,O,N,H)

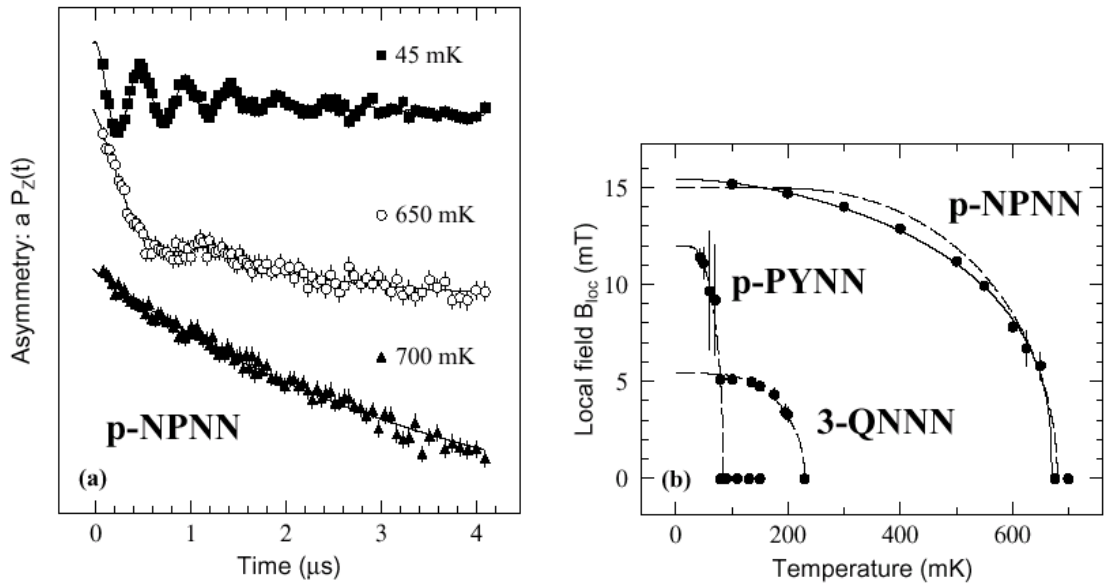

Fig. 6-4: (Left) ZF spectra for p-NPNN with fits. (Right) Temperature dependence of the local magnetic field at the muon site B_{loc}. The solid line is a fit with $B_{loc}(T) \propto \left[1-(\frac{T}{T_C})^{\alpha}\right]^{\beta}$. The dashed lines are fits with a molecular-field model with spin S=1/2 (S. Blundell et al., Europhys. Lett. **31**, 573 (1995)).

- μSR gave the first observation of magnetic order in p-NPNN.
- The compound are based on the nitronyl nitroxid group (N-O) (ex. p-NPNN $C_{13}H_{16}N_3O_4$).
- An unpaired electron is associated with this group.
- The residual molecules ensure the overlap of the correct orbitals with the neighboring molecules so that 3D FM order appears.
- The transition temperature depends strongly on the crystal structure.
- Critical behavior of $\vec{B}_{loc}(T)$ consistent with 3D- Heisenberg magnet.

$B_{loc}(T) \propto (1-(\frac{T}{T_C})^{\alpha})^{\beta}$ describes the spin-wave region ($T<<T_C$) as well as the critical region ($T \approx T_C$) (α =1.7(4), β =0.36(5)).

6.2 Magnetic volume fraction

With a so called weak transverse field experiment (wTF), it is possible to determine the fraction of a magnetic phase and the transition temperature.
The amplitude of the muon signal precessing at a frequency corresponding to B_{ext} reflects the volume fraction of the sample, which is paramagnetic or not ordered magnetically. Muons stopping in the magnetically ordered regions will experience a broader field distribution, which leads to a rapid decay of the muon-spin asymmetry at early times. Therefore, the amplitude of the muon signal precessing at a frequency corresponding to B_{ext} will start to decrease at the magnetic transition and reach a level determined by the non-magnetic phase (which can also include some background signal).
The magnetic volume fraction is the given by

$$V_{Mag} = (1 - \frac{A_{TF}^{0}(T)}{A_0}) \qquad A_{TF}(t) = A_{TF}^{0}(T)R(t)\cos(\gamma_\mu B_{ext} + \varphi) \quad [6\text{-}7]$$

A_0 is the experimental asymmetry of the spectrometer, R(t) takes into account some field broadening.

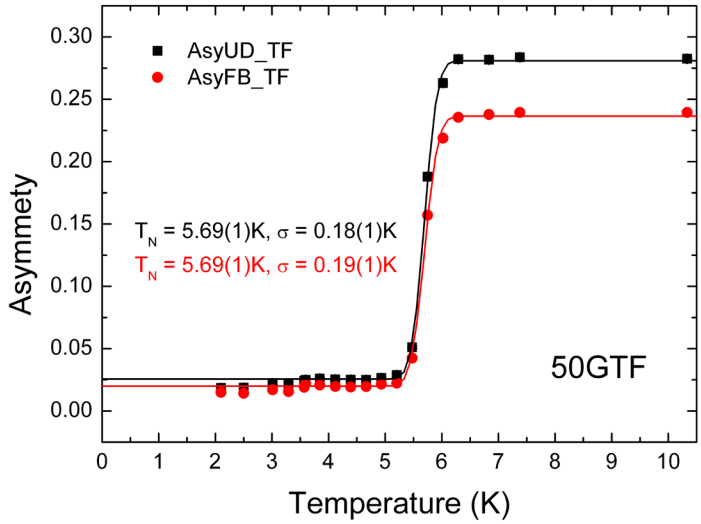

Fig. 6-5: Example of temperature scan in a wTF, used to determine the magnetic transition and corresponding volume fraction in $CeNi_{0.768}Bi_2$.

Also from ZF data it is possible to determine the magnetic volume fraction. However, one needs to know the depolarization function appropriate for the physical situation (see details below).

Example: *Magnetism in ferromagnetic semiconductors*

An example is shown for Li(Zn,Mn)As, which is as a new generation ferromagnet based on a I–II–V semiconductor (Z. Deng et al., Nature Communications **2**, 422 (2011)).

Magnetization measurements show FM behavior (Fig. 6-6).

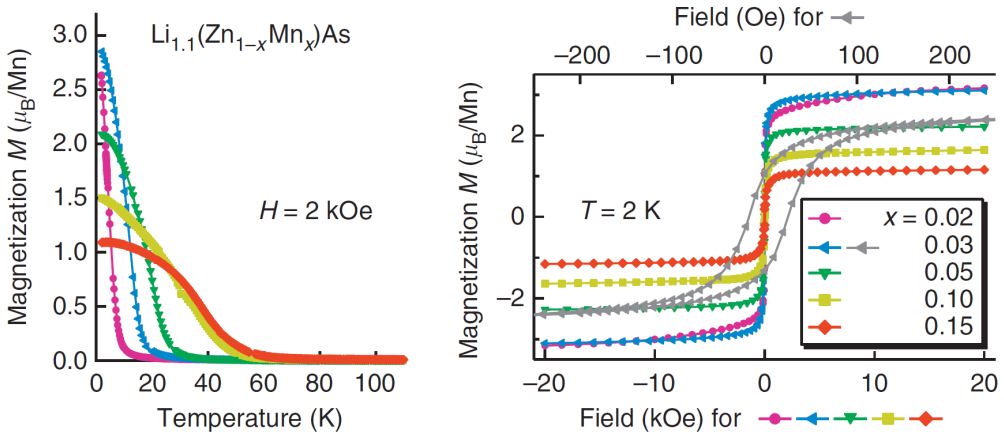

Fig. 6-6: Magnetization M(H,T) results of $Li_{1.1}(Zn_{1-x}Mnx)As$ with x = 0.0–0.15 showing (left) the T dependence of M in H = 2 kOe (no difference in Field Cooled and Zero Field cooled procedures) and (right) M at T = 2 K in various values of external field H. The grey symbols show a hysteresis loop in x = 0.03 system plotted for small field regions (top horizontal axis), which demonstrate a very small coercive field of 30–100 Oe.
From μSR measurements (Fig. 6-7 and 6-8) one can deduce that the FM is homogeneous and that the magnetic volume fraction reaches 100% at low temperatures.

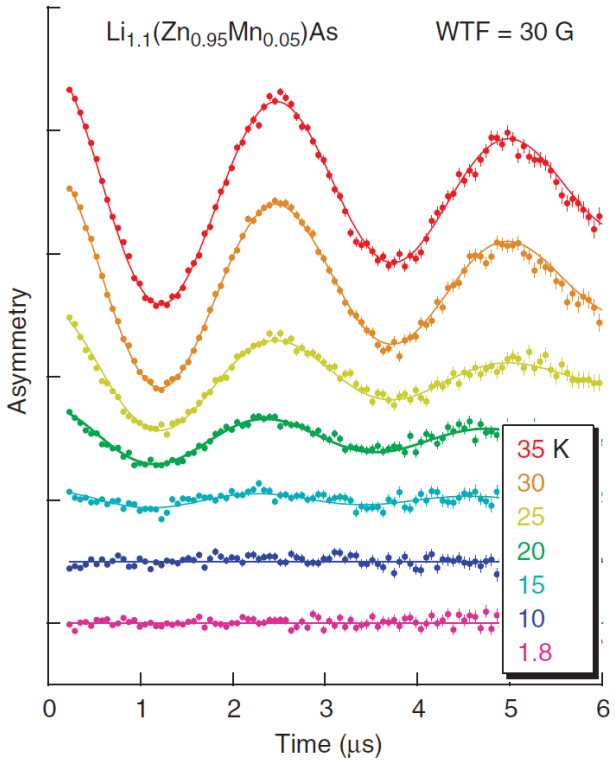

Fig. 6-7: μSR time spectra in the wTF of 30 G in $Li_{1.1}(Zn_{0.95}Mn_{0.05})As$. The oscillation amplitude corresponds to the paramagnetic volume faction. See Fig. 6-8c (Z. Deng et al., Nature Communications **2**, 422 (2011)).

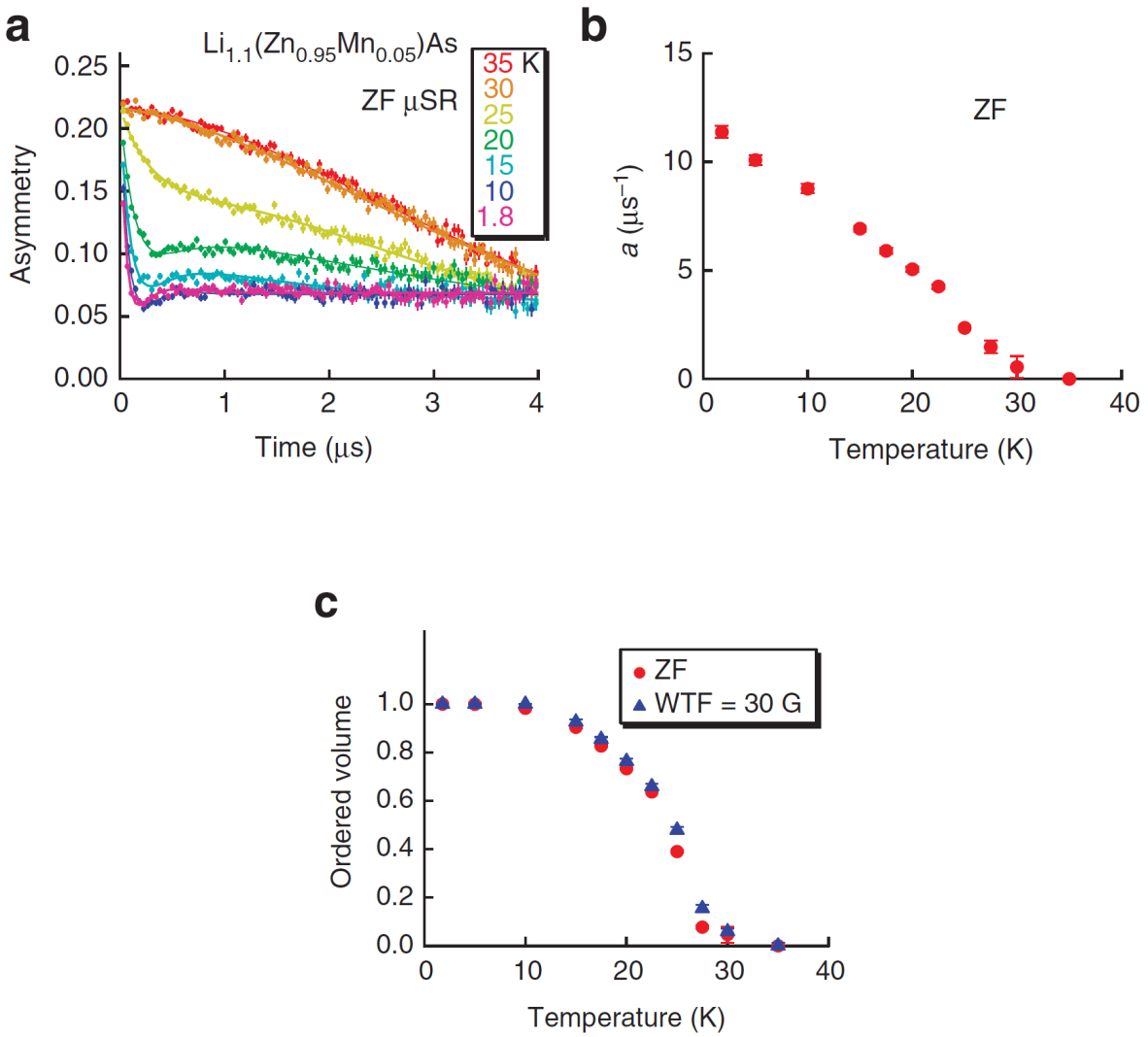

Fig. 6-8: Results of μSR measurements in sintered polycrystalline specimens of $Li_{1.1}(Zn_{0.95}Mn_{0.05})As$: (a) time spectra in zero field that exhibit onset of extra relaxation below T~30 K. The solid lines represent fits to the relaxation function for dilute spin systems in zero field for the static case (often used for dilute-alloy spin glasses), which exhibits a fast relaxation, plus a non-relaxing paramagnetic component (b) the depolarization rate a of the signal that exhibits fast relaxation; (c) the volume fraction of the magnetically ordered region, derived from the the wTF measurement (Fig. 6-6) and from the amplitude of the fast relaxing signal.

Details about the analysis of ZF muon spin relaxation spectra

For the analysis of the zero-field (ZF) μSR time spectra in polycrystalline sample of $Li_{1.1}(Zn_{0.95}Mn_{0.05})As$ one assumes a two component function:

$$A_{Mag}G^{L-KT}(t) + A_{pm}e^{-(\lambda t)^{\beta}}$$
$$G^{L-KT}(t) = \frac{1}{3} + \frac{2}{3}(1-at)e^{-at} \qquad [6\text{-}8]$$

$G_{L\text{-}KT}$ is the relaxation function for a static magnetic field with Lorentzian distribution (see Eq. [5-14]). a/γ_{μ} represents a field amplitude for the half-width at half-maximum. The Lorentzian field distribution is expected for dilute Mn moments randomly substituting Zn sites.
The first and second terms of Eq. [6-8] represent the magnetically ordered and paramagnetic volumes, respectively (β is a temperature-independent parameter). The ZF spectra above 30 K can be fitted to the second term of Eq. [6-8] without the first term. The ZF spectra below 10 K can be fitted to the first term alone. As shown in Fig. 6-8, however, both terms are needed to fit spectra in the temperature region between 15 and 25 K, suggesting coexistence of the paramagnetic and magnetically ordered volumes.

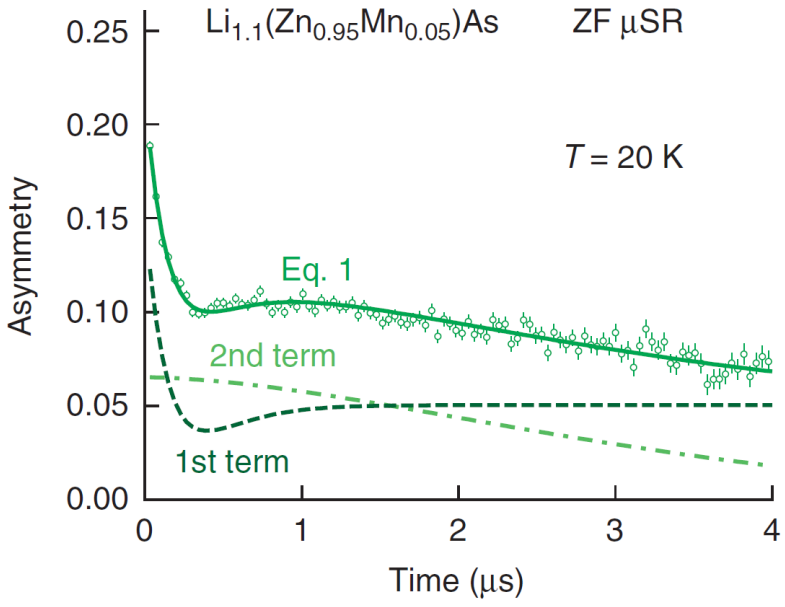

Fig. 6-9: μSR time spectra in zero-field. ZF μSR time spectra in $Li_{1.1}(Zn_{0.95}Mn_{0.05})As$ at T = 20 K (open circles). The solid line represents the best fit to Eq. [6-8]. The black and green broken lines show the first and the second terms, respectively, of this fitting function.

6.3 Magnetic ordering in spin chains and ladders

The μSR technique has been used to determine the magnetic properties of the ground state of systems consisting of one-dimensional chains and ladders of copper and oxygen atoms with the aim of eventually learn about the high-T_c superconductors where Cu–O planes play an important role.

The oxides $Sr_{n-1}Cu_{n+1}O_{2n}$ (n=3, 5,..) are realizations of such ladders. Indeed, one observes that the geometries of the ladder structure and of the CuO square lattice layer are related.

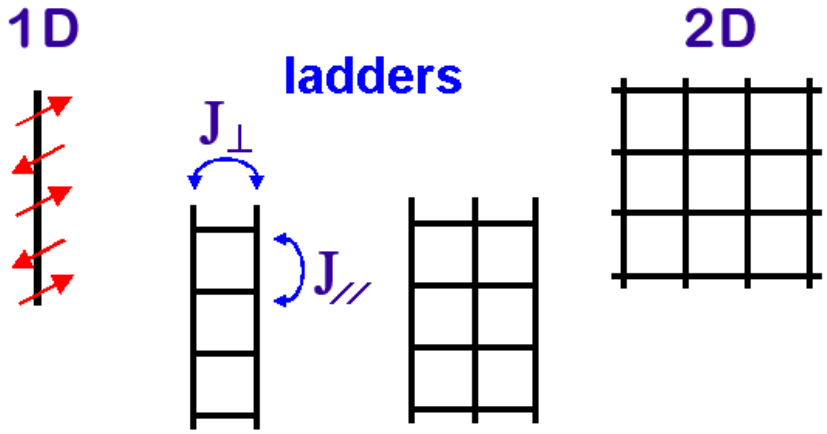

The lattice structure is composed of (n+1)/2-leg spin ladders, namely strips of CuO_2 square lattice which have (n+1)/2 Cu^{2+} ions across their width (Fig. 6.10, for a three-leg structure). Each Cu^{2+} ion has spin ½ with AF coupling in the "rung" and "leg" direction (strength J). In the two directions, differences in the coupling strength are presumably small, because the Cu-O-Cu bond lengths are almost equal in both directions. Neighboring ladders are displaced by half a lattice constant, making the interladder interactions small and FM (– J' , J'/J ≈ 0.1-0.2). The spin of the end of the ladder are frustrated because of the triangular structure with two FM and one AF interaction.

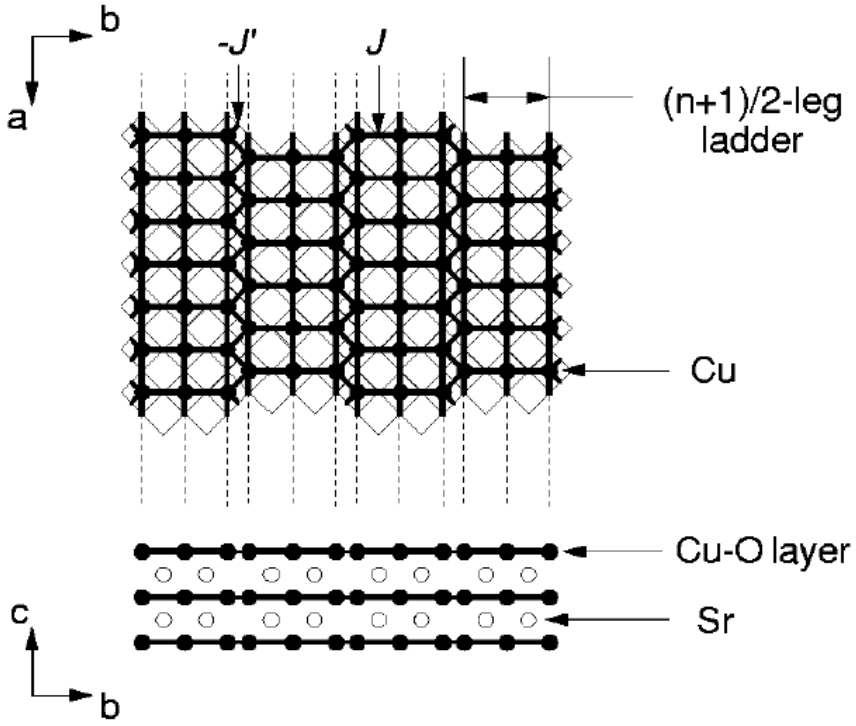

Fig. 6-10: The three-leg ladder structure (n=5, $Sr_4Cu_6O_{10}$) (from Kojima et al 1995). Oxygen ions locate at each corner of the drawn squares. The ferromagnetic interladder interaction J' is much smaller than the antiferromagnetic intraladder interaction J.

A key theoretical prediction is that only ladders with even numbers of legs have a singlet ground state separated from the triplet state by a large spin gap. The odd-leg systems are expected to reach a magnetically ordered ground state in the presence of interladder interactions. Zero-field and longitudinal field μSR measurements have tested these theoretical predictions for $Sr_4Cu_6O_{10}$ and $Sr_2Cu_4O_6$ (K. Kojima et al, Phys. Rev. Lett. **74**, 812 (1995)).

In Fig.6-11 spectra recorded on the three-leg system are presented. The strong depolarization of the zero-field spectra at low temperature shows that the ground state is magnetic. Since no wiggles are detected (in contrast to the observations for the organic magnets; see section 6.1), the disorder in the compound is important or the number of muon localization sites with different local fields are large. Comparing the spectra recorded at 50 K and 60 K, one infers that a 3D magnetic phase transition occurs between these temperatures. The longitudinal field measurements confirm the interpretation of the zero-field spectra, i.e. the ground state of the three-leg system with interladder interactions is a conventional static ordered state rather than a spin-liquid system.

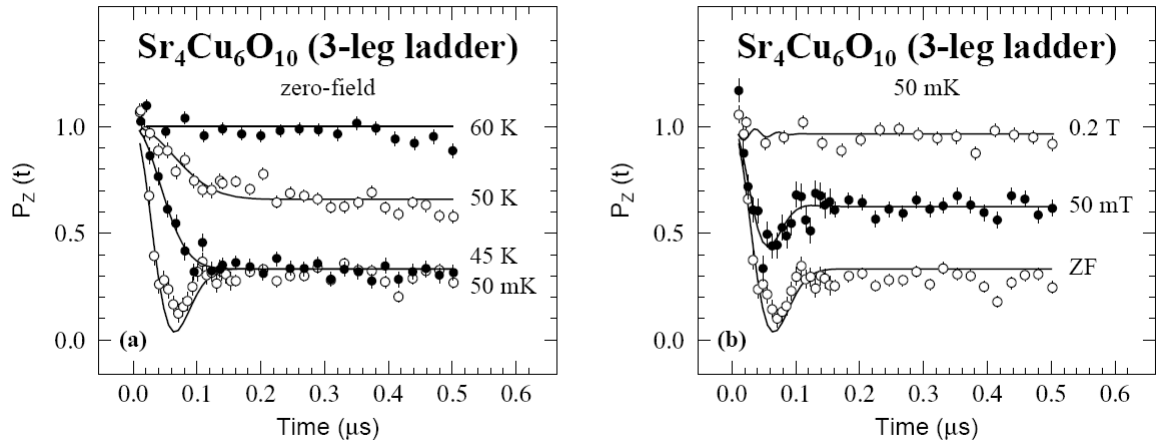

Fig. 6-11: μSR-spectra recorded on $Sr_4Cu_6O_{10}$ which has a three-leg spin ladder structure. The solid lines are fits (From K. Kojima et al.).

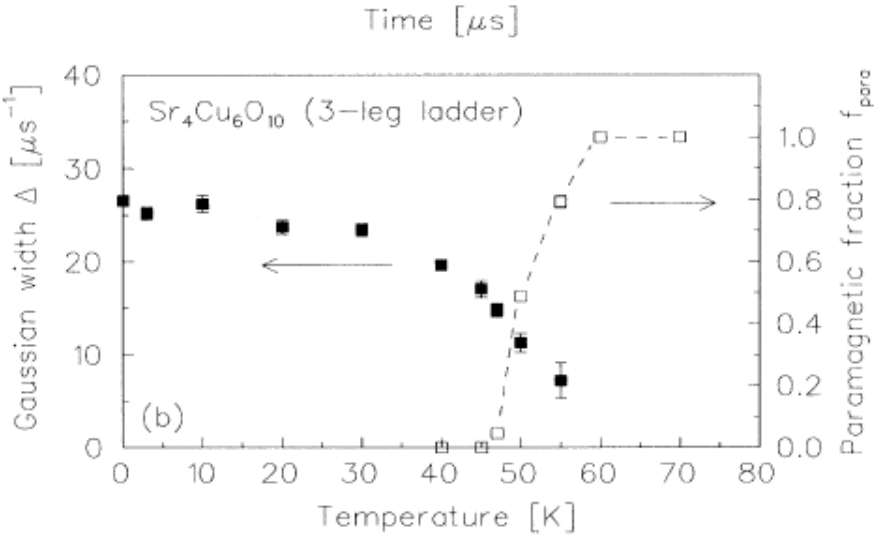

Fig. 6-12: Temperature dependence of the Gaussian field distribution width and of the paramagnetic volume fraction.

The data can be analyzed with a functional form of

$$P_z(t) = f_{para} + (1 - f_{para}) G_{static}(t, \Delta)$$

f_{para} is the paramagnetic volume fraction in the sample and G is the static Gaussian Kubo-Toyabe function for T<30K or static Gaussian function $\frac{1}{3} + \frac{2}{3} e^{-\frac{\Delta^2 t^2}{2}}$ at T≳ 40K. Δ is proportional to the size of the static component of Cu moments. From Fig. 6-12 one determines an ordering temperature of about 52 K with a distribution of ± 5K.

The absence of muon spin precession in Fig. 6-11 suggests that the magnetic order of the 3-leg ladder system is random freezing of moments rather than true Néel order. A possible source of randomness is the frustration at the edge of the ladder.

The magnetic behaviors of the two-leg and three-leg ladder systems differ remarkably as seen in Figure 6-13.

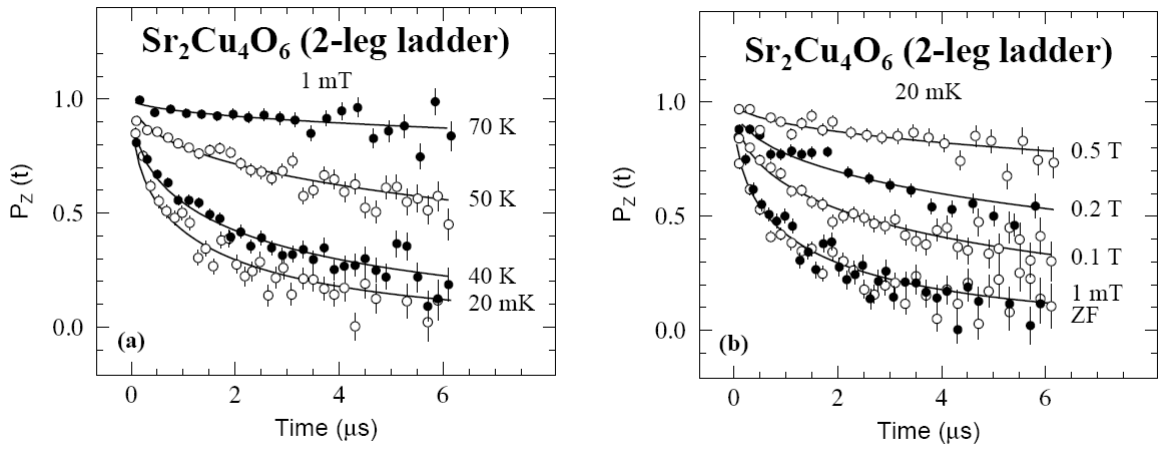

Fig. 6-13: Some spectra recorded on $Sr_2Cu_4O_6$ (n=3) which has a two-leg spin ladder structure. The solid lines are fits (from Kojima et al 1995). Note that the horizontal scales are ~10 times larger than in Fig. 6-11.

The depolarization functions are described with a square-root exponential function, $\propto e^{-\sqrt{\lambda t}}$, appropriate for dilute fluctuating moments. Therefore no static magnetic ordering is detected. The depolarization originates from dilute unpaired spins which may be associated with defects in the sample. In conclusion, the work of Kojima *et al.* confirms the theoretical predictions (M. Rice et al. Europhys. Lett. **23**, 445 (1993)) that a three-leg system becomes magnetic at low temperature but a two-leg system does not.

6.4 Spin Density Wave

In general, the periodicity of a magnetic structure can be expressed as a rational fraction of the periodicity of the underlying crystal lattice (commensurate magnetic structure) or as an irrational number (incommensurate magnetic structure). A well-known example for an incommensurate magnet is metallic chromium, whose magnetic structure below 123 K is described in terms of a longitudinal spin-density wave characterized by an incommensurate wave vector and magnetic moments parallel to the [100] axis of the body-centered-cubic structure.
In the commensurate case a discrete number of local fields will be experienced by a muon for a given interstitial site (Fig. 6-14a).
For the incommensurate structure we consider here the simple case of an amplitude (cosine) modulated magnetic structure (Fig. 6-14b).

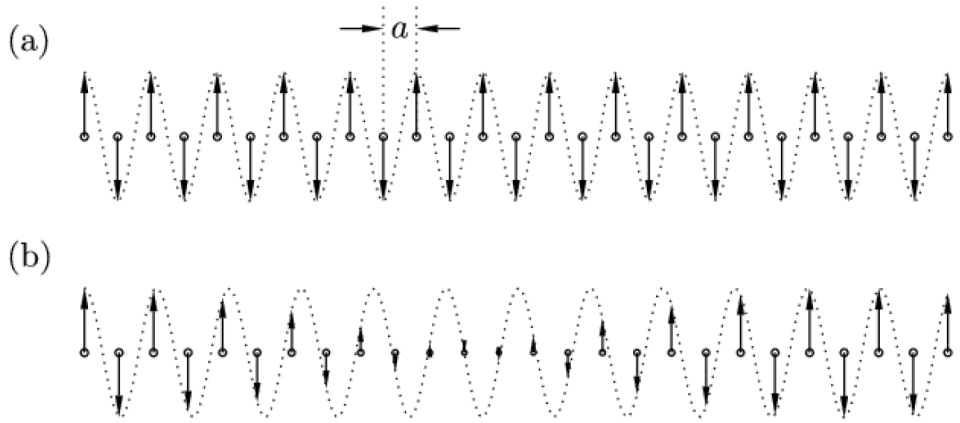

Fig. 6-14: a) Commensurate magnetic structure b) incommensurate magnetic structure.

Crystallographically equivalent muon sites will probe different magnetic fields corresponding to the different phases of the cosine-modulation. Instead of a single or a finite number of discrete values of the local field B, as in the case of commensurate magnetic structures, we expect a continuous set of local fields for the incommensurate ones.

We assume the local field to be proportional to the magnetic moments and
to be directed along the y axis and describe the modulation as a spin-density wave.
The field can be expressed as:

$$B(x) = B_0 \cos(x) \qquad [6\text{-}9]$$

The probability to find a field B(x) is given by the (uniform) probability that the muon probes a phase x, i.e.

$$dx = \frac{dx}{dB} dB = p(B) dB \propto \frac{1}{\sin(x(B))} dB$$

The field distribution normalized to one becomes

$$p(B) = \frac{1}{\pi} \frac{1}{\sqrt{B_0^{\,2} - B^2}} \qquad [6\text{-}10]$$

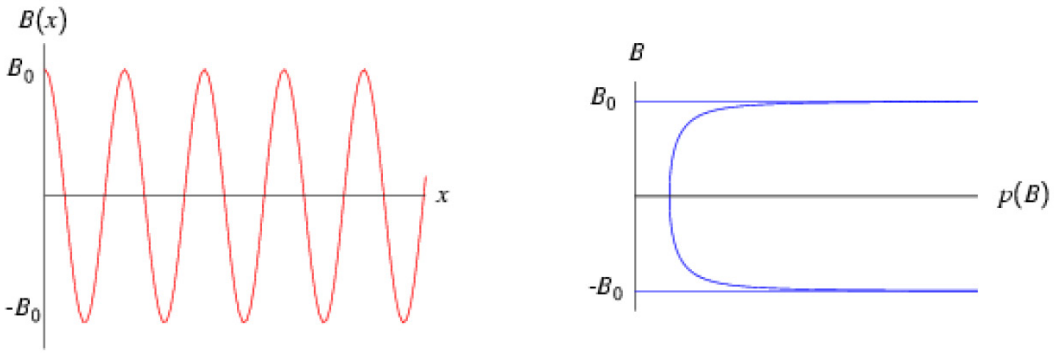

Fig. 6-15: Field and field distribution of an amplitude modulated spin density wave.

This distribution is also called Overhauser distribution and is displayed in Fig. 6-15. It is a symmetric continuous distribution with an appreciable weight at B = 0 $p(B=0) = \frac{1}{\pi B_0}$. This means that there is a finite probability for a vanishing local magnetic field at the muon site. Following our assumption that the field is along the y axis we have for the polarization

$$P_x(t) = \int p(B)\cos(\gamma_\mu B t)dB = J_0(\gamma_\mu B_0 t)$$

Where J_0 is the zeroth-order Bessel function of the first kind.
When t is large relative to $1/\gamma_\mu B_0$ we can use the approximation

$$J_0(\gamma_\mu B_0 t) \cong \sqrt{\frac{2}{\pi \gamma_\mu B_0 t}} \cos(\gamma_\mu B_0 t - \frac{\pi}{4}) \qquad [6\text{-}11]$$

Thus a weakly damped precession with negative phase shift of 45 degrees appears when the field at the muon site is modulated according to Eq. [6-9]. Eq. [6-11] is a very good approximation to the Bessel function even at quite small times.

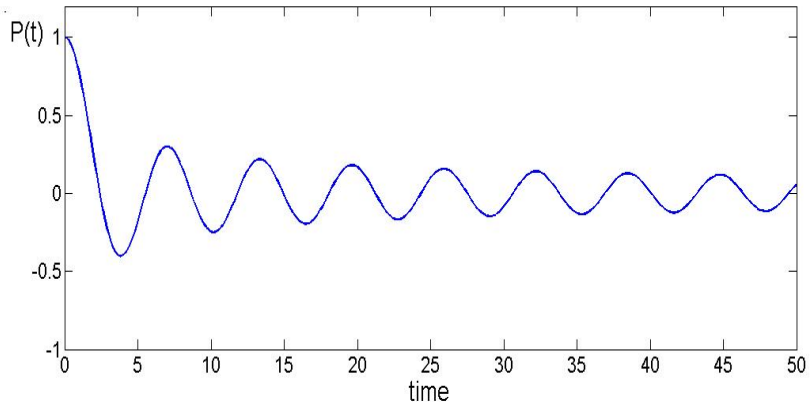

Fig. 6-16: Polarization function for a cosine modulated magnetic field at the muon site. Time is in unit of $1/\gamma_\mu B_0$.

Note that whereas a single k incommensurate amplitude-modulated magnetic structure leads to Bessel-like oscillations, the converse is not always true, i.e. the observation of such oscillations does not unambiguously guarantee that the magnetic structure is incommensurate.

Example: Spin-density-wave (SDW) phase in $(TMTSF)_2$-X

One of the first observations of a SDW behavior by μSR is in the tetramethyltetraselenafulvalene $(TMTSF)_2$-X family where X denotes a monovalent anion (X = PF_6, NO_3, and $C1O_4$). These conducting organic compounds display many fascinating properties, such as spin-density-wave magnetism, superconductivity, anion ordering, field-induced spin-density-wave states. The interplay and competition between different ground-state are related to the highly anisotropic electronic structures of these compounds.

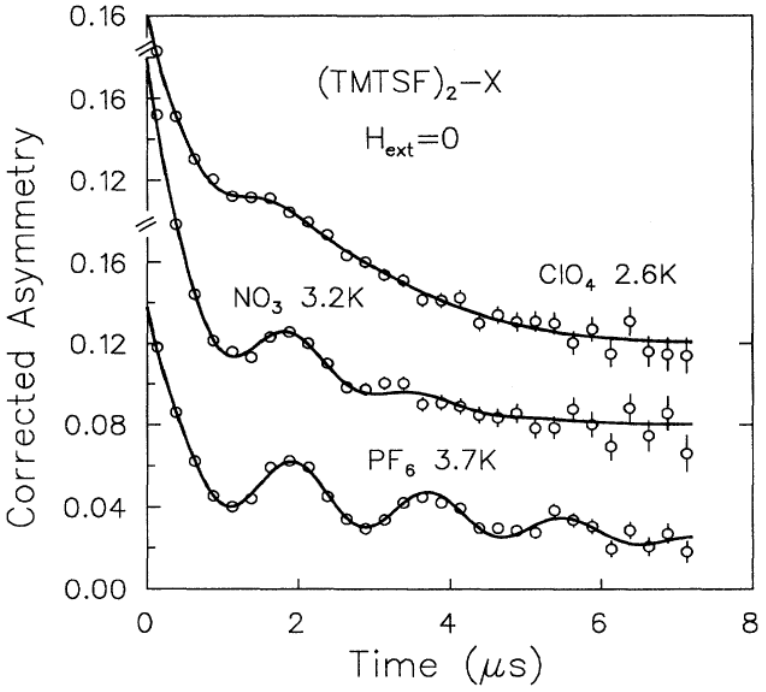

Fig. 6-17: ZF-μSR time spectra observed in $(TMTSF)_2$-X below T_{SDW}. The depolarization and oscillation due to SDW magnetic order are seen in the PF_6, $N0_3$, and $C10_4$ systems.
From L. P. Le et al. Phys. Rev. B **48**, 7284 (1993).

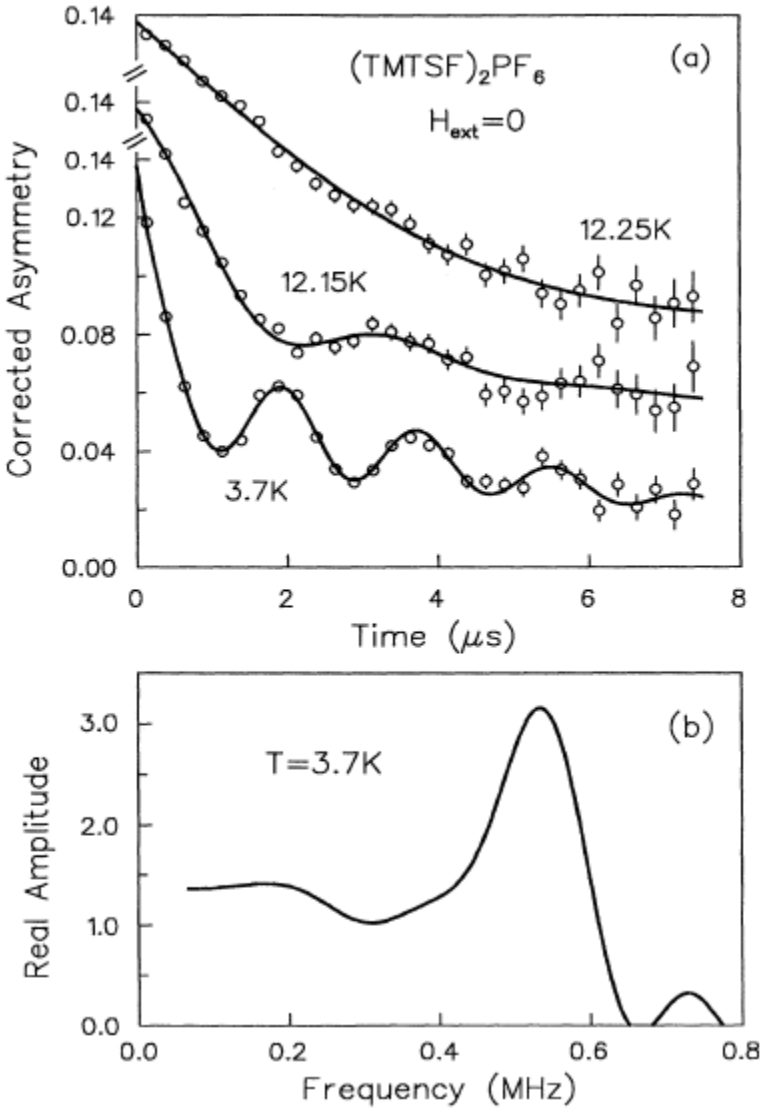

Fig. 6-18: ZF spectra at T = 3.7 K, 12.15 K, and 12.25 K in $(TMTSF)_2PF_6$. The clear onset of depolarization due to static magnetic order is seen below T_{SDW} = 12.2 K. (b) Fourier transform of the time spectrum at 3.7 K. The real part of the Fourier transform reflects the local-field distribution and corresponds to the expected distribution (Fig. 6-15) folded around B=0 and including nuclear moments broadening (L. P. Le et al. Phys. Rev. B **48**, 7284 (1993)).

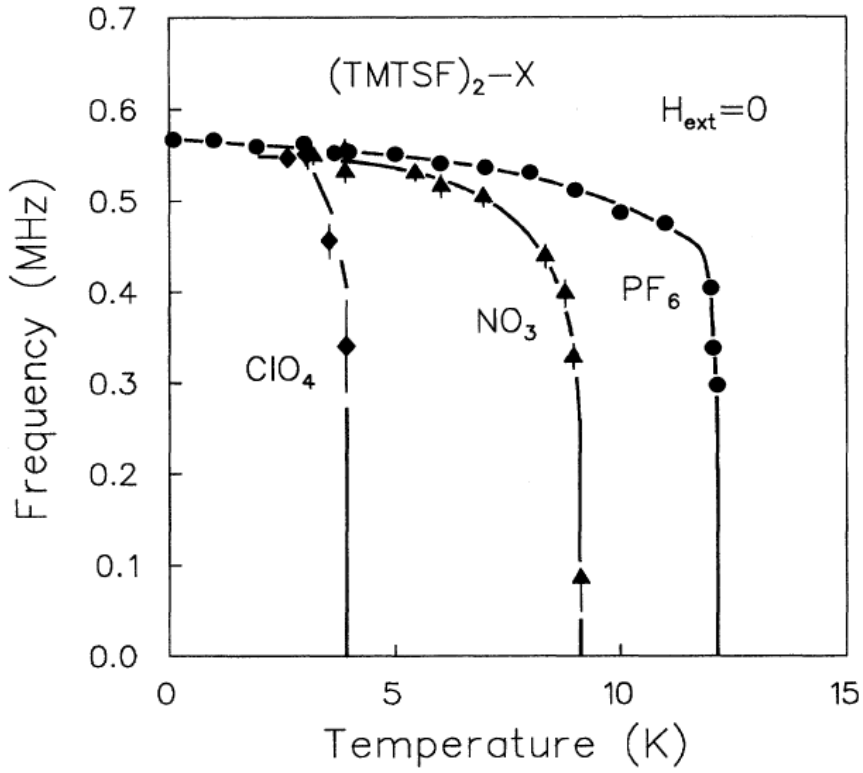

Fig. 6-19: Temperature dependence of the muon-spin precession frequency in zero field observed in $(TMTSF)_2$-X. Note the first order like phase transition. The magnitude of the internal field at T=0 is approximately the same for the three systems, suggesting a common SDW amplitude in these systems. Overall the data (e.g. spin stiffness) are incompatible with a Heisenberg model for a localized spin system and demonstrate the importance of using an itinerant-electron picture to describe the magnetic behavior of this system.

6.5 Relaxation via fluctuating fields (stochastic theory)

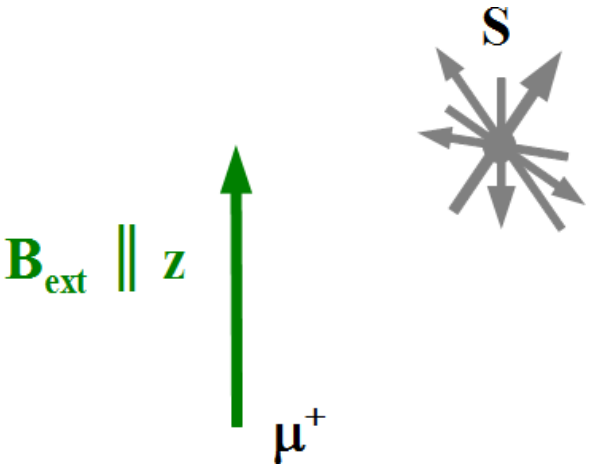

Consider a muon in the environment of fluctuating internal fields B_i. We have:

$< B_i(t) > = 0$ but

$< \Delta B_i^2(t) > \neq 0$

In addition an external static field is applied

$\vec{B}_{ext} \| \vec{P}(0) \| \hat{z}$.

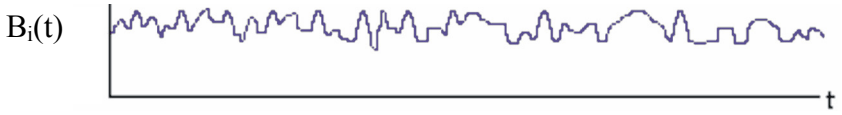

Zeeman splitting of a spin ½ level:

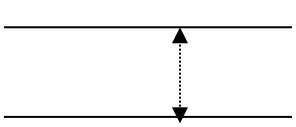

The total Hamiltonian is then:

$$H = -\gamma_\mu (\vec{B}_{ext} + \vec{B}_i(t)) \hbar \vec{I} \qquad [6\text{-}12]$$

Where $\vec{B}_i(t)$ is a stochastic function of time. The fluctuating field induces transitions between the two Zeeman levels, so that the initial muon spin polarization is lost (spin relaxation via spin flip)

$$P(t) = e^{-\lambda t} = e^{-\frac{t}{T_1}} \qquad [6\text{-}13]$$

T_1: is the so-called spin-lattice relaxation (NMR concept, where the spin-lattice (or longitudinal) relaxation time T_1 quantifies the rate of transfer of energy from the nuclear spin system to the neighboring molecules (the lattice). This is relaxation in the z-direction and leads to restoration of Boltzmann equilibrium in the nuclear ensemble.

With the Redfield theory (see C. Slichter, Principles of nuclear magnetic resonance) one can describe the relaxation rate as a function of the field fluctuations ($< \Delta B_i^2(t) > \neq 0$) (LF and ZF case):

$$\frac{1}{T_1} = \frac{\gamma_\mu^2}{2} \int_{-\infty}^{\infty} (< B_x(t) B_x(t+t') > e^{i\omega_L t'} + < B_y(t) B_y(t+t') > e^{i\omega_L t'}) dt' \qquad [6\text{-}14]$$

in the transverse field case $\vec{B}_{ext} || \hat{z}, \vec{P}(0) || \hat{x}$ one finds:

$$\frac{1}{T_2} = \frac{\gamma_\mu^2}{2} \int_{-\infty}^{\infty} [< B_z(t) B_z(t+t') > + \frac{1}{2}(< B_y(t) B_y(t+t') > + < B_x(t) B_x(t+t') >) e^{i\omega_L t'}] dt' \qquad [6\text{-}15]$$

$< B_q(t) B_q(t+t') >$, q= x,y,z is the autocorrelation function of the local field, which depends only on t'.

Remark:

- No cross-correlation: $< B_q(t) B_k(t+t') >= 0$ for q≠ k .
- The T_1 relaxation depends only on the transverse fluctuations (transverse to $\vec{P}(0)$, observation direction).

Often we can assume a simple exponential correlation function (one single fluctuation time):

$$< B_q(t) B_q(t+t') >=< B_q^2(0) > e^{-\frac{t'}{\tau_c}} \cong$$
$$< S_q(t) S_q(t+t') >=< S_q(0)^2 > e^{-\frac{t'}{\tau_c}} \qquad [6\text{-}16]$$

τ_c is called correlation (or also fluctuation) time. It gives how fast a well defined configuration (of fields or spins) decays, i.e. how fast the correlation disappears. This quantity contains the physics of the dynamical processes producing fluctuating fields or moments. With [6-16], [6-14] and [6-15] become:

$$\frac{1}{T_1} = \gamma_\mu^2 (< B_x^2 > + < B_y^2 >) \frac{\tau_c}{1 + \omega_L^2 \tau_c^2} \qquad [6\text{-}17]$$

$$\frac{1}{T_2} = \gamma_\mu^2 (< B_z^2 > \tau_c + \frac{< B_y^2 > + < B_x^2 >}{2} \frac{\tau_c}{1 + \omega_L^2 \tau_c^2}) \qquad [6\text{-}18]$$

Note the similarity between [6-17] and [5-64], obtained with the strong collision approximation.

$< B_x^2 >, < B_y^2 >, < B_z^2 >$ are obtained from the static field components. In a paramagnet $<B_q>$ = 0, then $< B_q^2 >$ is the second moment of the q-component of $\vec{B}_i$.

T_1 minimum or relaxation rate maximum if $\tau_c(T) = 1/\omega_L$

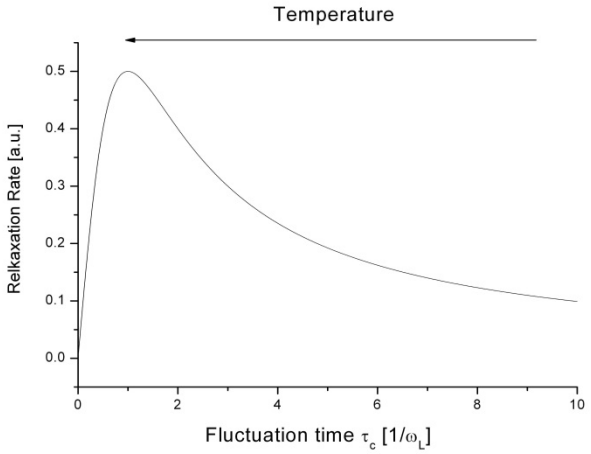

Fig. 6-20: Dependence of relaxation rate on fluctuation time according to Eq. [6-17].

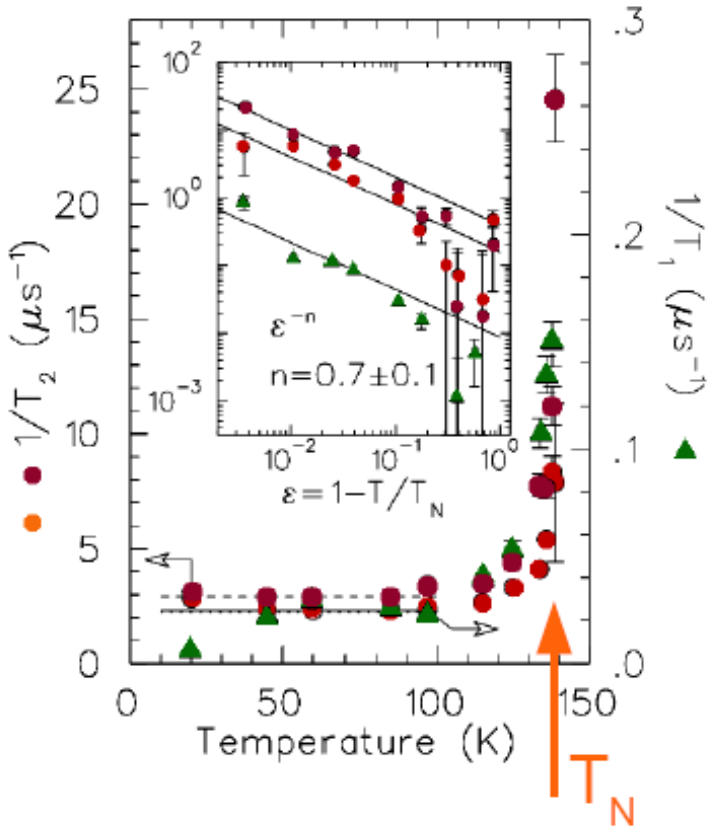

Fig. 6-21: Example of slowing down of spin fluctuations close to the transition temperature T_N of the Ising AF $LaMnO_3$ (from M. Cestelli et al., Phys. Rev. B **64**, 064414 (2001)).

Fit function (after polycrystalline averaging):

$$A(t) = \frac{A_0}{3} \sum_{i=1,2} f_i [e^{-\frac{t}{T_1}} + 2e^{-\frac{t}{T_2}} \cos(\gamma_\mu B_i t)]$$

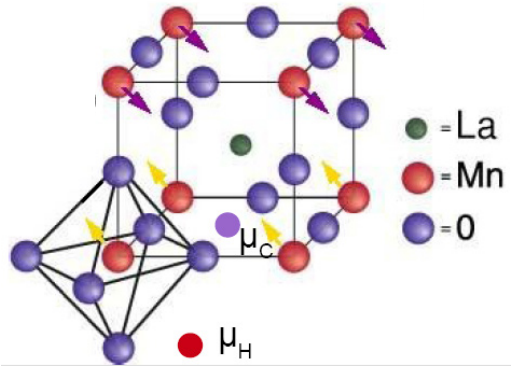

6.6 Relaxation and spectral density

The Fourier transforms J(ω) of correlation (fluctuation) functions are often referred to as spectral density. The relaxation rate gives information about this quantity. In simple cases the field correlation function coincides with the electron spin autocorrelation function, i.e. the response function of the electron system, see [6-16].

Eq. [6-14] shows that the longitudinal relaxation rate is proportional to the Fourier transform of the correlation function of the local field, evaluated at the Larmor frequency.
This can immediately be seen in the case of exponential field correlation:

$$< B_q(0)B_q(t') >=< B_q^2(0) > e^{-\frac{t'}{\tau_c}} \qquad [6\text{-}19]$$

$$J(\omega) =< B_q^2(0) > \int_{-\infty}^{+\infty} e^{-\frac{|t'|}{\tau_c}} e^{-i\omega t'} dt' \propto \frac{\tau_c}{1+\omega^2 {\tau_c}^2} = \frac{\nu_c}{{\nu_c}^2+\omega^2}$$

$$\frac{1}{T_1} = {\gamma_\mu}^2 J(\omega_L) \qquad [6\text{-}20]$$

i.e. the relaxation is induced by fluctuations of the local field with μSR frequency ω_L

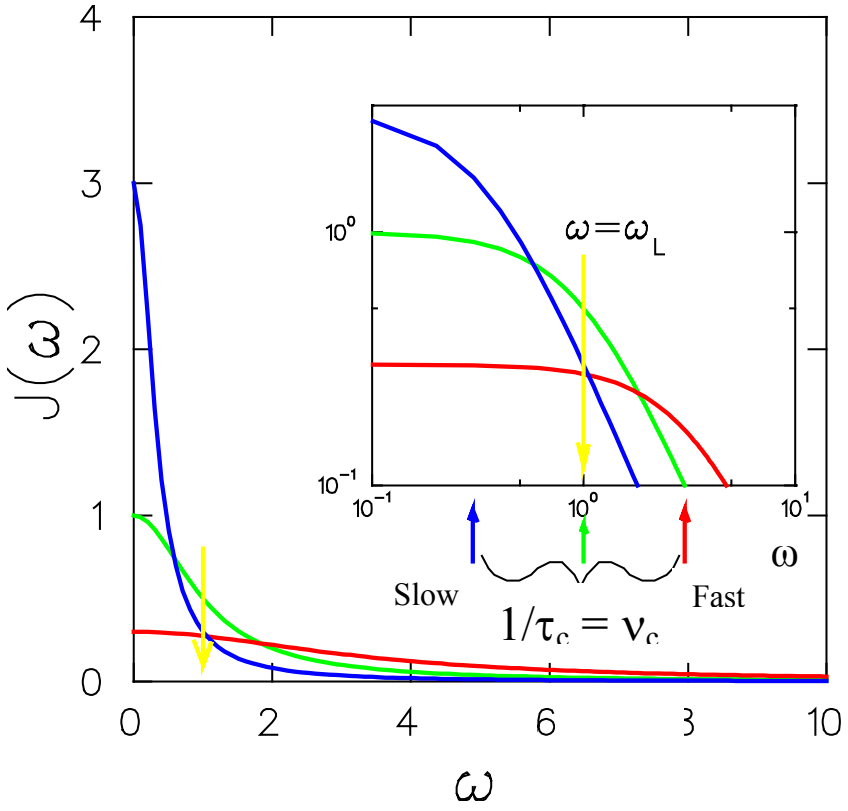

Fig. 6-22: Spectral density at different correlation times τ_c .The muon spin relaxation is an intrinsic resonant phenomenon. The muon picks up only the component at ω_L of the possibly much wider spectrum J(ω) of the fluctuating local fields (see [6-17], [6-18] and [6-20]).

Example: Anisotropic fluctuations

Spin fluctuations slow down (freeze) on approaching a magnetic phase transition.
In an anisotropic antiferromagnet the spin fluctuations are anisotropic, e.g. in Er.

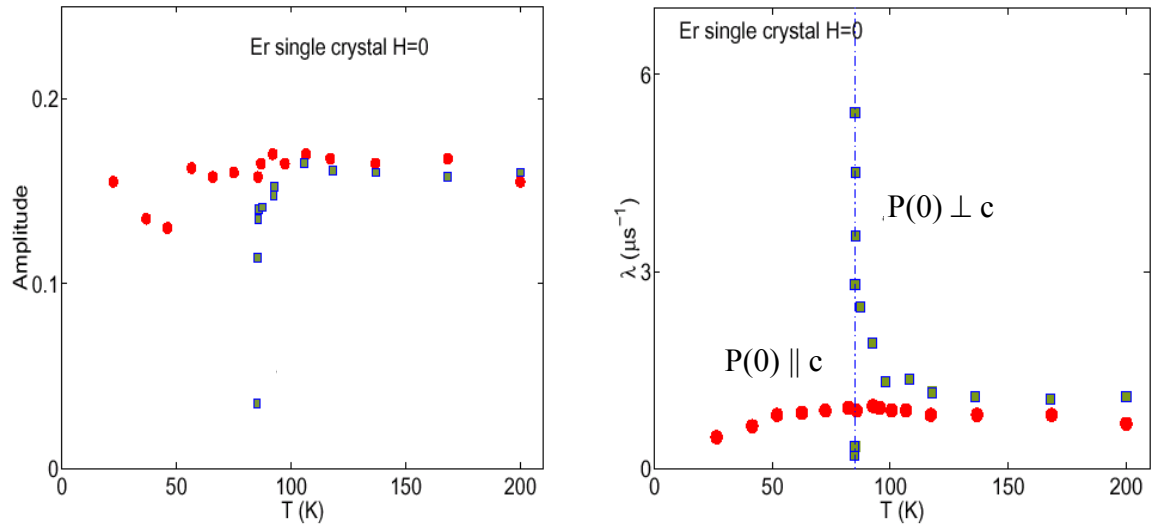

Fig. 6-23: Muon-spin-asymmetry and lattice relaxation rate λ for different orientations of an Er single crystal with respect to $\vec{P}(0)$. The AF transition is at 85K (O. Hartmann et al. Hyp. Int. **64**, 381 (1990)).

The figure shows that the slowing down of fluctuations (increase of λ, decrease of the amplitude) is only observable if $\vec{P}(0)$ is perpendicular to the hexagonal symmetry axis (c –axis). The fluctuating fields at the muon site have only components parallel to the c-axis. Weaker components perpendicular to it do now show any freezing process.

6.7 Distribution of relaxation times and spin glasses: stretched exponential relaxation

Spin glasses are dilute magnetic alloys where the interaction between spins is randomly ferromagnetic or anti-ferromagnetic. They are considered as paradigmatic examples of frozen disorder. The presence of disorder (the random interactions) induces frustration and leads to a greater difficulty for the system to find optimal configurations. As a consequence, these systems exhibit non trivial thermodynamic and dynamic properties, different and richer than those observed in their non-disordered counterpart. Spin glass systems have been extensively studied as a prototype of complex systems, since their magnetic ordering resembles the positional ordering of a conventional glass.
Spin glasses can be modeled using Ising-like Hamiltonians where the bonds between spins can be positive or negative at random. Due to the heterogeneity of the couplings, there are many loops of spin sequences which are frustrated and for which there is no way of choosing the orientations of the spins without frustrating at least one bond.

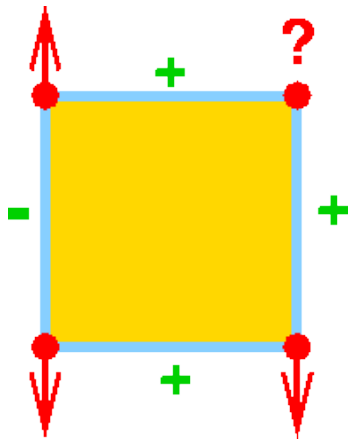

Fig. 6-24: Example of frustrated interaction: + : FM, and – AF.

Since there are many configurations with similar degree of frustration one may expect the existence of many local minima of the free energy.

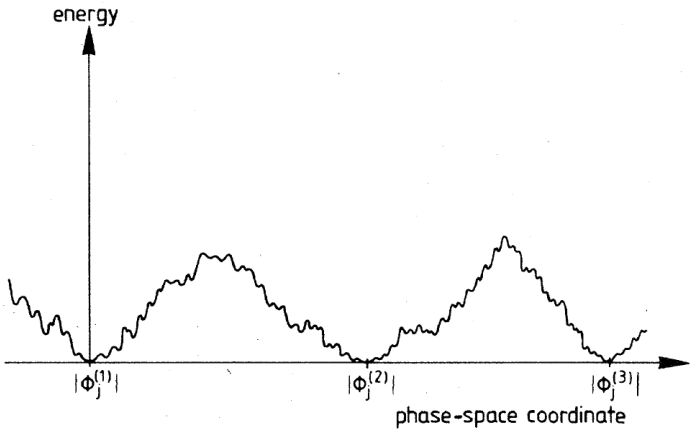

Fig. 6-25: Schematic representation of the free energy of a spin glass vs. a phase space coordinate, which measures a particular ordered state (from K. Binder, A.P. Young, Review of Modern Physics **58**, 801 (1986)).

The most familiar and well-studied spin glass systems are the dilute magnetic alloys such as AuFe, AgMn and CuMn, so-called canonical spin glasses. In diluted magnetic metals the interaction between localized moments is mediated by the metallic electron gas. This type of exchange was first proposed by Ruderman and Kittel and later extended by Kasuya and Yosida (Ruderman–Kittel–Kasuya–Yosida coupling, RKKY interaction). A magnetic ion induces a spin polarization in the conduction electrons in its neighborhood. This spin polarization of the itinerant electrons is felt by the moments of other magnetic ions within range, leading to an indirect coupling.
This indirect exchange couples moments over relatively large distances. It is the dominant exchange interaction in metals where there is little or no direct overlap between neighboring magnetic electrons.

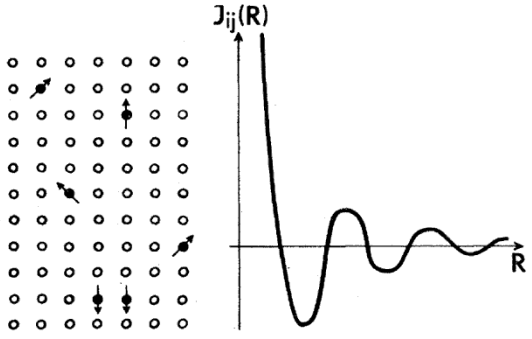

Fig. 6-26: Random distribution of magnetic moments in a metallic matrix and the resulting RKKY exchange interaction plotted as a function of distance.

The interaction is characterized by a coupling coefficient, j , given by

$$j(\vec{r}_i - \vec{r}_j) = 9\pi\left(\frac{j^2}{E_F}\right)F(2k_F\left|\vec{r}_i - \vec{r}_j\right|) \qquad [6\text{-}21]$$

where k_F is the radius of the conduction electron Fermi surface, r_j is the lattice position of the point moment, E_F is the Fermi energy and

$$F(x) = \frac{x\cos x - \sin x}{x^4} \qquad [6\text{-}22]$$

The RKKY exchange coefficient, j, oscillates from positive to negative as the separation of the ions changes and has the damped oscillatory nature shown in Fig. 6-16. Therefore, depending upon the separation between a pair of ions their magnetic coupling can be ferromagnetic or antiferromagnetic.
These spin glasses have Curie-Weiss susceptibilities at high temperature and form strange "antiferromagnetic" low temperature state at low temperatures. There is no sign of any sharp feature in the specific heat: only sometimes a broad bump. However, low field ac susceptibility shows a sharp cusp as a function of temperature, clear evidence for a well defined transition temperature (freezing temperature T_f). There is a consensus that the spin glass transition is a "true" thermodynamic phase transition.

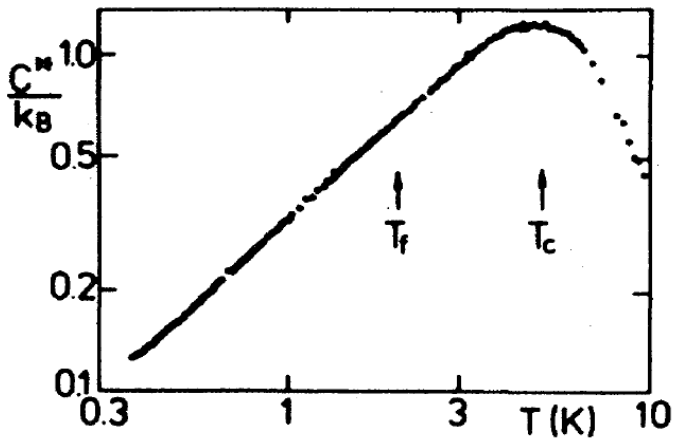

Fig 6-27: Specific heat per Eu atom versus temperature for $Eu_xSr_{1-x}S$ with x=0.54. The spin glass transition temperature T_f and the Curie temperature T_C (transition to a ferromagnetic phase) are indicated by arrows.

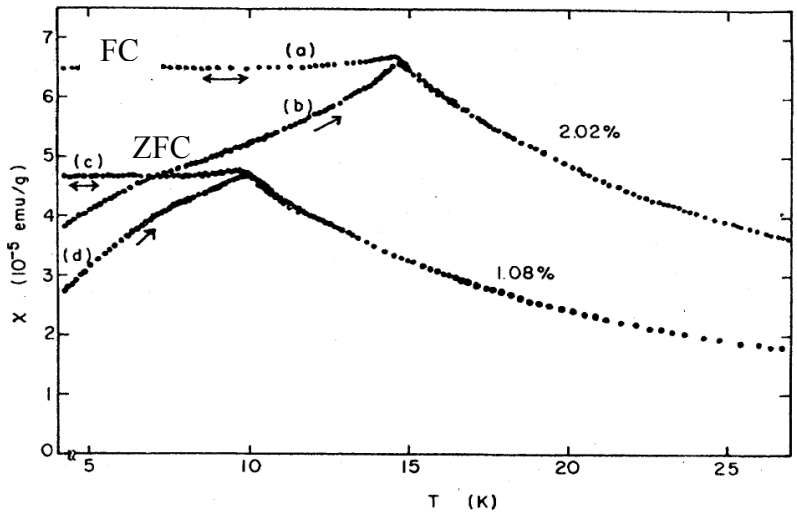

Fig. 6-28: Static susceptibilities of *Cu*Mn vs temperature for 1.08 and 2.02 at. % Mn. After zero-field cooling (H<0.05 Oe) initial susceptibilities (b) and (d) were taken for increasing temperature in a field of 5.9 Oe. The susceptibilities (a) and (c) were obtained in a field of 5.9 Oe, which was applied above T_f before cooling the samples. From S. Nagata et al., Phys. Rev. B **19**, 1633 (1979).

The apparent freezing of the spin dynamics below T_f leads to random but static order of the spin orientation. Above T_f the relaxation of spin glasses is highly anomalous compared to that of standard paramagnets, where one can assume an exponentially damped auto correlation function for the impurity spins, with one single correlation (relaxation) time τ_c:

$$\frac{< S(t)S(0) >}{< S(0)^2 >} = e^{-\frac{t}{\tau_c(T)}} \qquad [6\text{-}23]$$

The experimental data suggest that a single relaxation time is not correct.

μSR can probe slowly relaxing spin systems with a wide relaxation rate spectrum.

In the temperature regime above the freezing temperature the muons initially polarized are gradually depolarized by the fluctuating dipolar fields coming from neighboring local moments. The faster these moments relax the more slowly the muons are depolarized; it is the familiar motional narrowing effect.

Experiments on moderately concentrated spin glasses (5 to 10% magnetic sites) show depolarization functions above T_f, which can be fitted very satisfactorily by stretched exponentials

$$P(t) \propto e^{-(\lambda t)^{\beta}} \qquad [6\text{-}24]$$

λ is a depolarization rate and β is an exponent, both are temperature dependent.

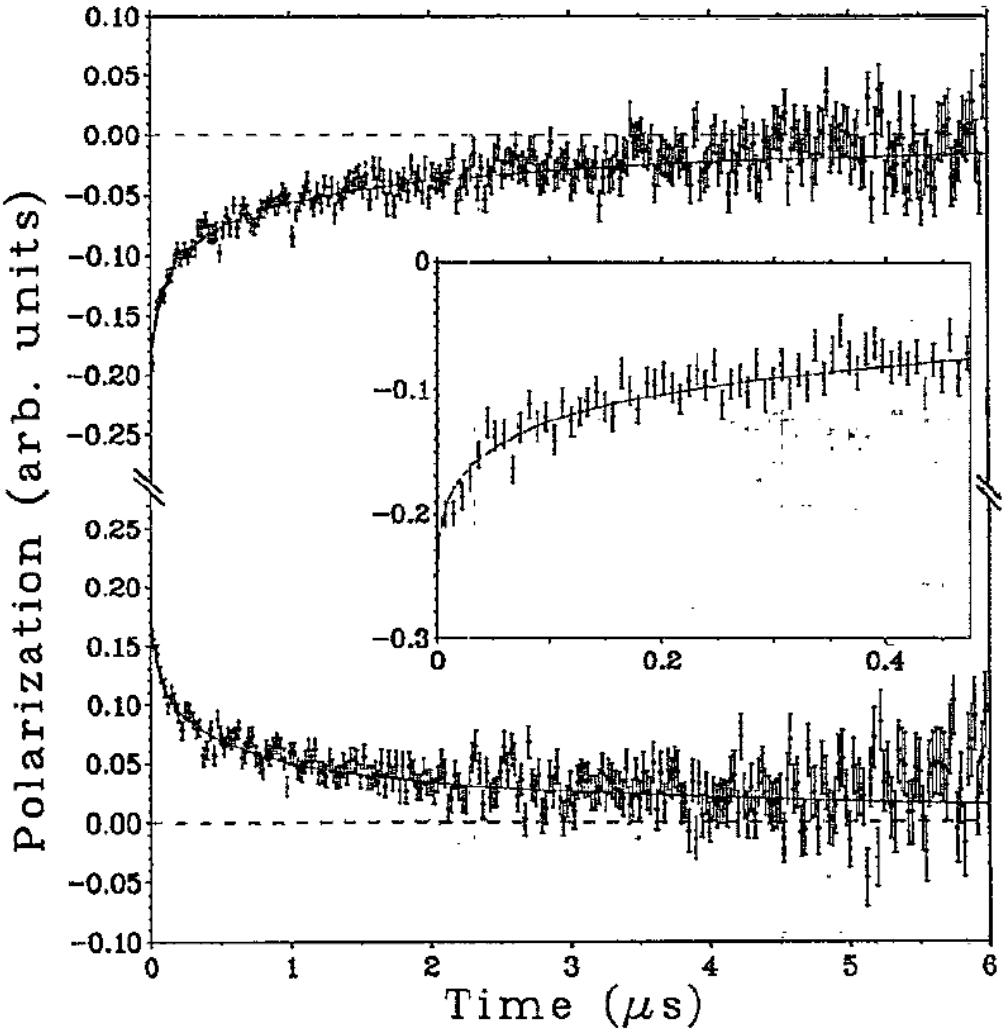

Fig. 6-29: Raw muon depolarization data in *Ag*Mn 7% at T=26K just above T_g=25 K. The upper part/lower part show data from the forward/backward counter. Fit parameter β=0.32(1= and λ=40(6) μs^{-1}. The inset shows a blown up of early times of the forward time spectrum. From I.A. Campbell et al., Phys. Rev. Lett. **72**, 1291 (1994).

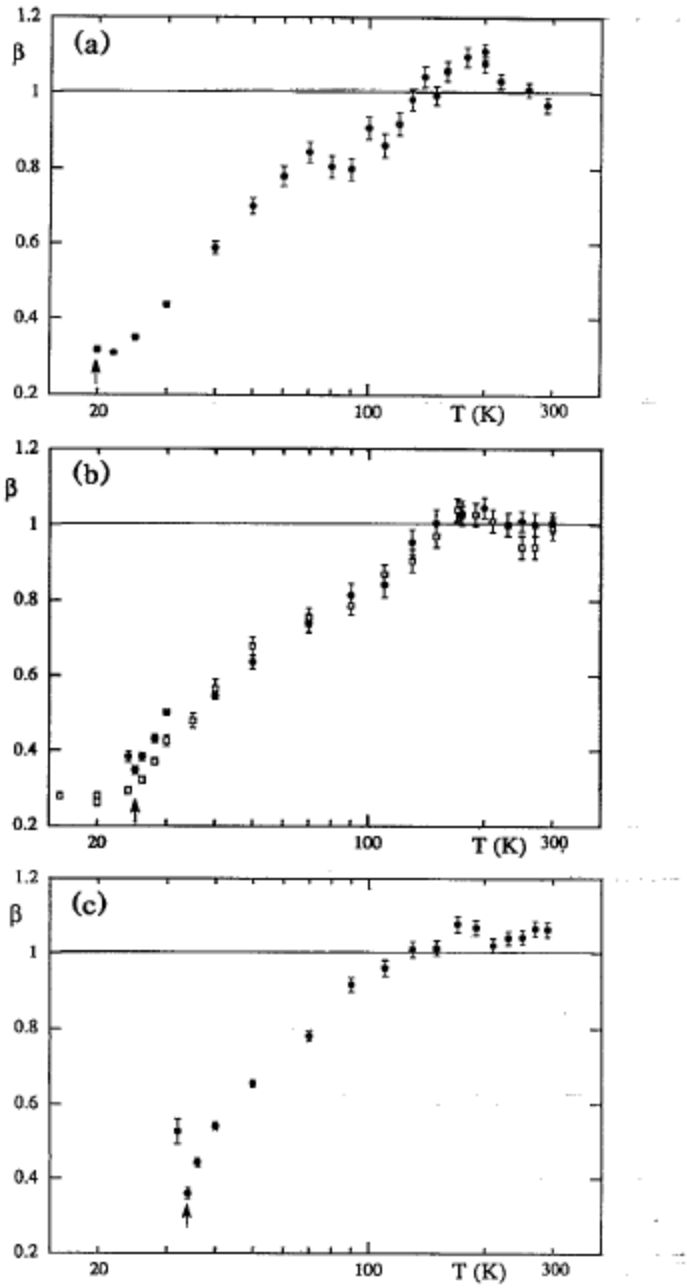

Fig. 6-30: The stretched exponent β as a function of temperature for ZF data (a) *Ag*Mn 5 at. % and (b) *Ag*Mn 7 at. % and (c)) *Ag*Mn 10 at. % (closed symbols). The values indicate the T_f values. Just below T_f the apparent value of β increases sharply; this is an artifact as the stretched exponential is an inappropriate fit function below T_f. Above T_f the longitudinal field data are essentially identical to the ZF data, while below T_f they are quite different and can be fitted with a constant β of about 0.3 (the open squares of (b) are 0.6 T LF data). From I.A. Campbell et al., Phys. Rev. Lett. **72**, 1291 (1994).

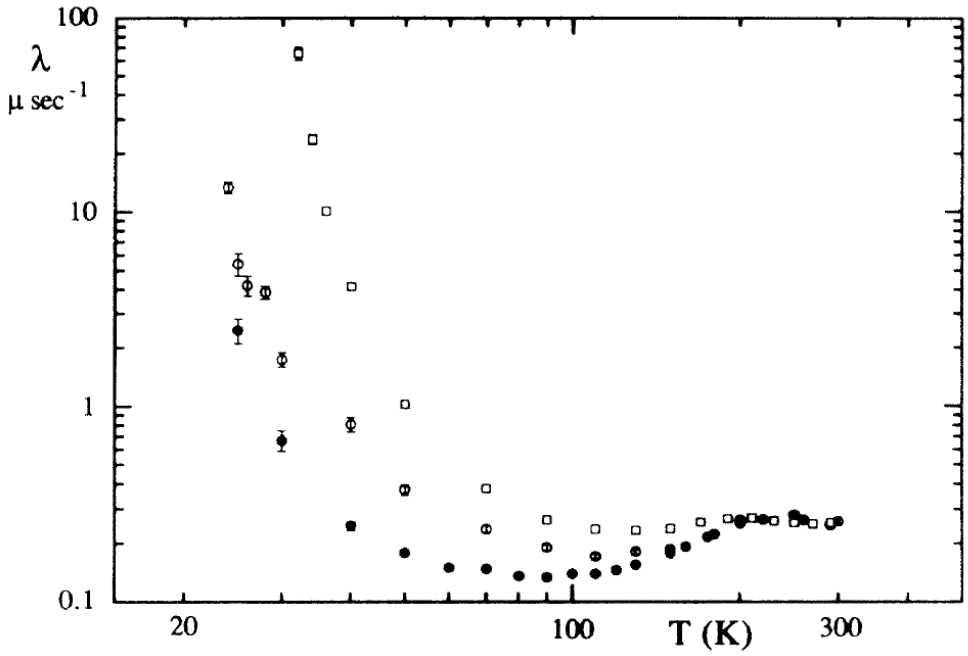

Fig. 6-31: The temperature dependence of the muon depolarization rate λ for ZF data on three *Ag*Mn samples (10% sample: squares; 7% sample: open circles; 5% sample: closed circles). LF values are identical above T_f. From I. A. Campbell et al., Phys. Rev. Lett., **72**, 1291 (1994).

While λ increases when the temperature is lowered towards T_f, β drops from a value near 1 at high temperatures to a limiting value near 1/3 as T_f is approached. This behavior seems to be very general and a number of other spin glasses or glassy systems have been found to follow the same pattern.

At high temperatures β tends to 1; the relaxation becomes "normal": to a good approximation we have a regime with a unique exponential relaxation for all spins.

Lower values of β reflect a widening of the relaxation spectrum specific to spin glasses. Formally we can write a stretched exponential as superposition of independent exponential relaxations λ_i (each proportional to a correlation time τ_i):

$$P(t) = e^{-(\lambda t)^{\beta}} = \int_0^{\infty} G(\lambda_i, \lambda, \beta) e^{-\lambda_i t} d\lambda_i \qquad [6\text{-}25]$$

In the special case β = 1/2

$$G(\lambda_i, \lambda, \beta = \frac{1}{2}) = \frac{\sqrt{\lambda}}{2\sqrt{\pi}\lambda_i^{\frac{3}{2}}} e^{-\frac{\lambda}{4\lambda_i}} \qquad [6\text{-}26]$$

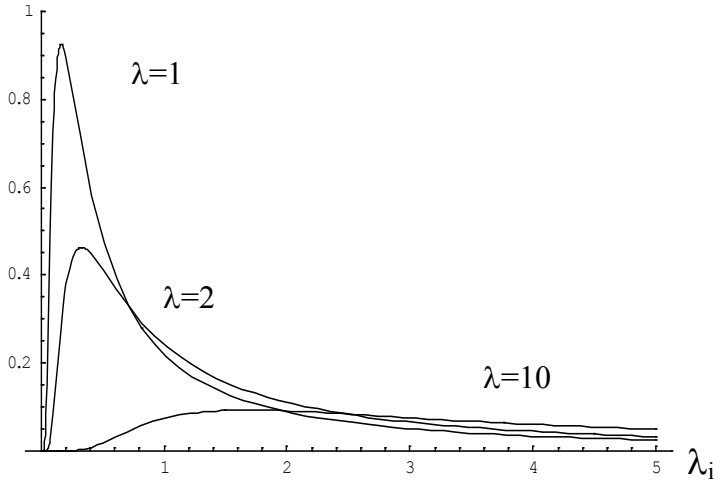

Fig. 6-32: Distribution of relaxation times $G(\lambda_i, \lambda)$ for $\beta=1/2$ and different values of λ. The distribution width is determined by β and λ. Small β gives a broad distribution of relaxation rates. A large λ value further broadens the distribution.

$\beta=1$ corresponds to a single relaxation rate and an exponential muon spin depolarization.

$$G(\lambda_i, \lambda, \beta = 1) = \delta(\lambda - \lambda_i) \quad \text{and} \quad P(t) = e^{-\lambda t}$$

An exponential muon spin relaxation with rate λ reflects an exponential relaxation of the impurity spin autocorrelation with correlation time τ_c ($\lambda \propto \tau_c$)

$$P(t) = e^{-\lambda t} \quad \leftrightarrow \quad q(t) = < S_i(t) S_i(0) > = < S_i(0)^2 > e^{-t/\tau_c} \qquad [6\text{-}27]$$

In the general case with $\lambda_i \propto \tau_i$, i.e. $\tau_i = \alpha \lambda_i$, the autocorrelation function will be given by:

$$q(t) = \int_0^\infty G(\lambda_i, \lambda, \beta) e^{-\frac{t}{\alpha \lambda_i}} d\lambda_i \qquad [6\text{-}28]$$

For $\beta=1/2$ we obtain

$$q(t) = \frac{1}{\sqrt{1 + \frac{4t}{\alpha \lambda^4}}} \qquad [6\text{-}29]$$

This reflects a strongly non-exponential relaxation of the impurity spins.

Remarkable is the degree of universality of the behavior found in canonical spin glasses. It is found in other metallic spin glasses, in insulating and even in particular cases of pyrochlore spin glasses. This implies that there is a universal from of dynamics, with its associated temperature dependent time spectrum, which is a consequence of spin glass ordering.

7. μSR studies of superconductivity

7.1 The vortex state and the corresponding field distribution

Superconductivity characteristics:

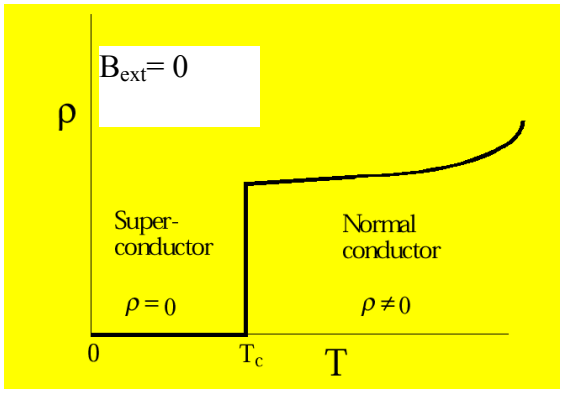

Fig. 7-1: Zero resistance. Resistance versus temperature.

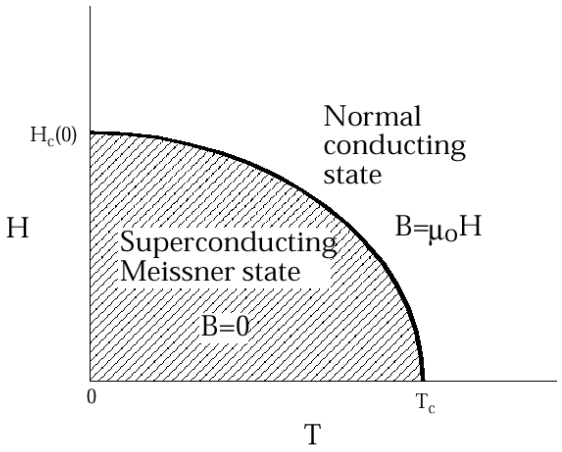

Fig. 7-2: Diamagnetism. Schematic phase diagram of a superconductor of type I, $\kappa \equiv \frac{\lambda}{\xi} < \frac{1}{\sqrt{2}}$.

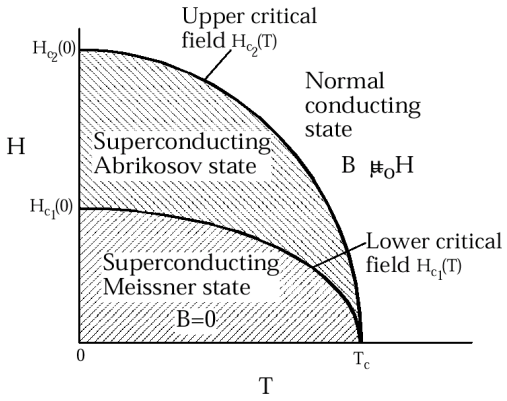

Fig. 7-3: Schematic phase diagram of a superconductor of type II $\kappa \equiv \frac{\lambda}{\xi} > \frac{1}{\sqrt{2}}$.

Superconductors of type II have above H_{c1} a mixed phase, where the magnetic flux can penetrate the sample in the form of fluxoids (vortices). Each vortex contains a flux quantum $\Phi_0 = \frac{h}{2e} = 2.07 \cdot 10^{-15}\ \mathrm{T \cdot m^2}$. The vortices may form a regular lattice, mostly of hexagonal symmetry (flux line lattice, FLL). The FLL is obtained by cooling the superconductor in a field.

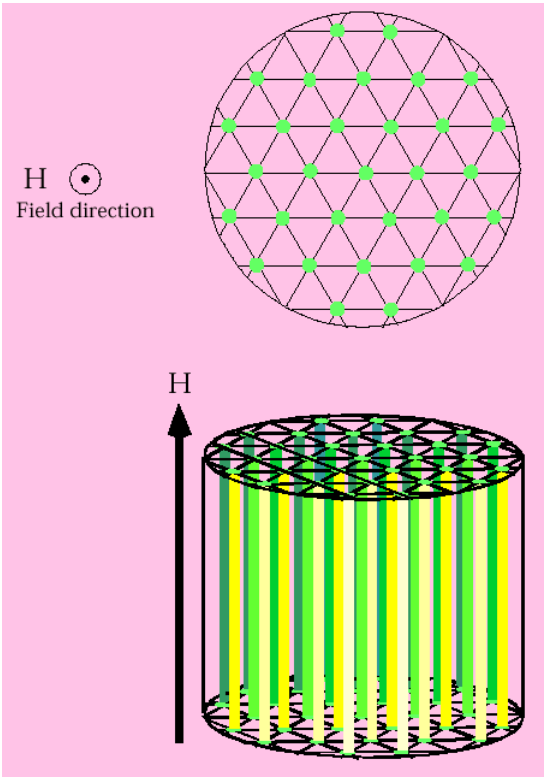

Fig. 7-4: Mixed state (Abrikosov lattice).

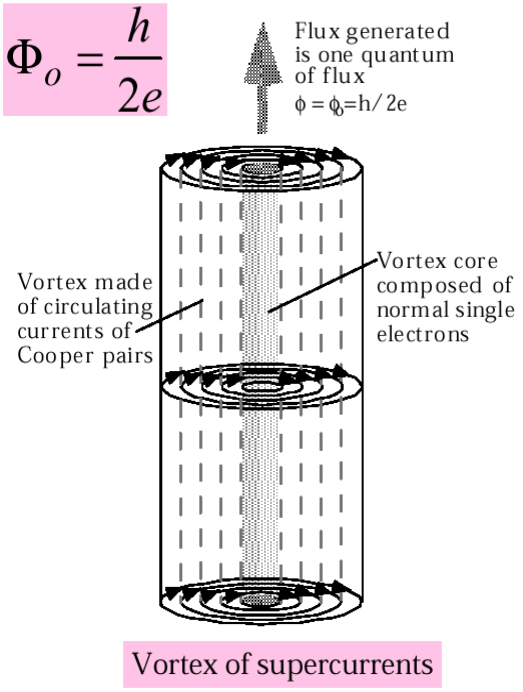

Fig. 7-5: Structure of a vortex

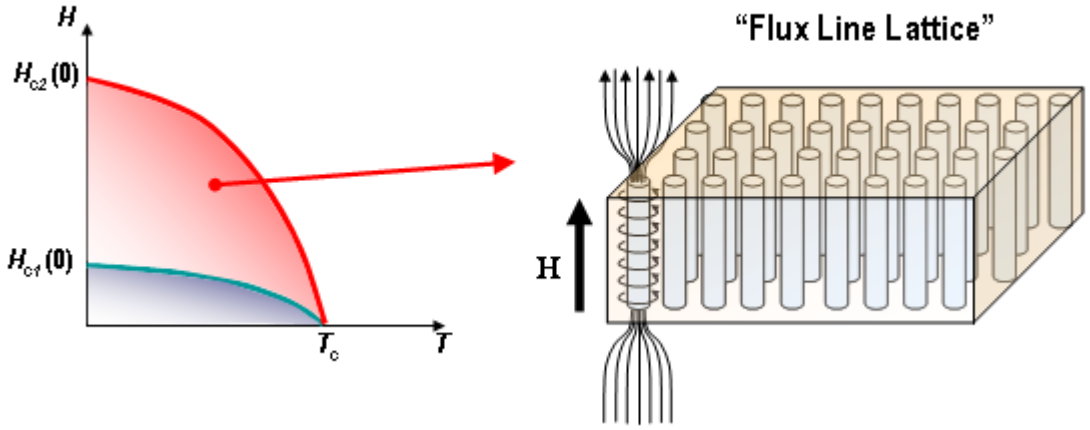

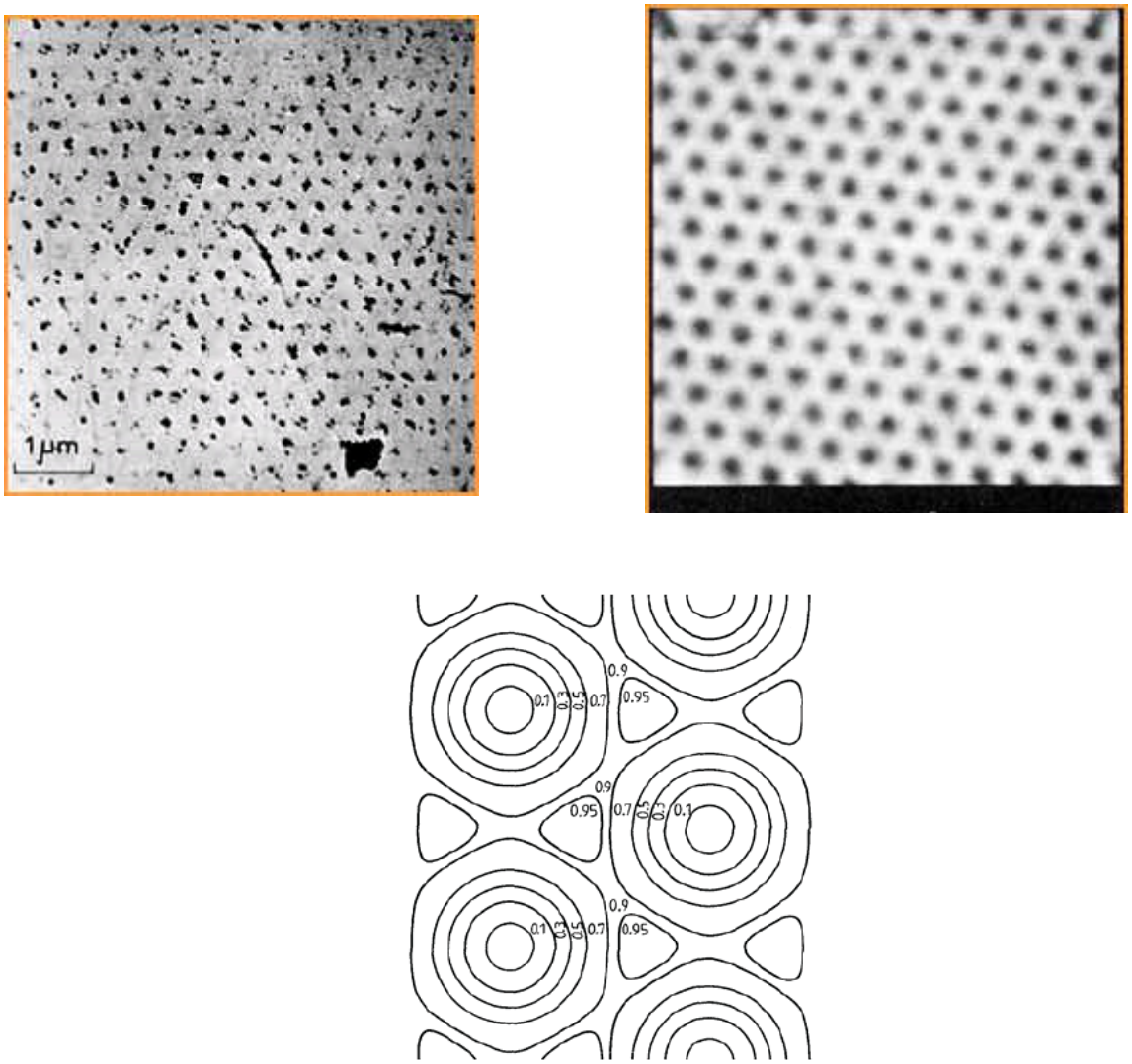

Fig. 7-6: Visualization of a vortex lattice. Top left: Bitter decoration technique. Pb-4at%In, 1.1K, 195 G. (U. Essmann and H. Trauble, Phys. Lett. 24A, 526 (1967)). Top right: Surface image by Scanning Tunnel Microscopy $NbSe_2$, 1T, 1.8K, H. F. Hess et al. Phys. Rev. Lett. **62**; 214 (1989) the vortex spacing is ~ 479 Å. Bottom: The hexagonal Abrikosov lattice showing the contour lines.

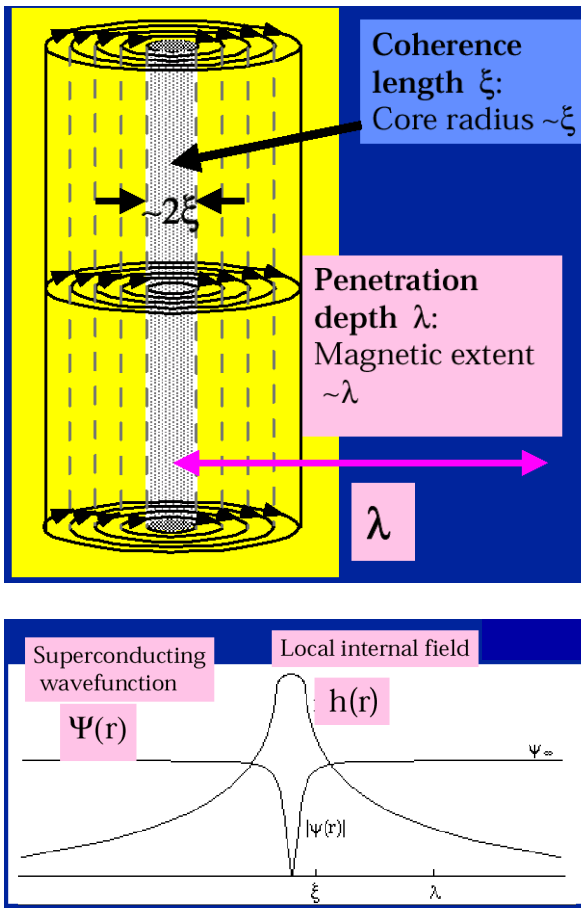

(London) magnetic penetration depth:

Clean limit:

mean free path >> BCS coherence length

$$\ell >> \xi_0 = \frac{\hbar v_F}{\pi \Delta_0}$$

$$\lambda(T) = \sqrt{\frac{m^*}{\mu_0 e^2 n_s(T)}}$$

$\frac{1}{\lambda^2} \propto \frac{n_s}{m^*}$ is called superfluid density

Δ_0 : superconducting gap at T=0

For a clean sc: $n_s(0)=n$

m* : effective mass

n_s : density of the superconducting carriers

n: : carrier density

For a "dirty" superconductor:

$\lambda \to \lambda\sqrt{1+\frac{\xi_0}{\ell}}$ and the superfluid density is reduced by $\approx \frac{\ell}{\xi_0}$

Fig. 7-7: Characteristic length scales in the vortex state. Order parameter ψ(r) and magnetic field h(r) as a function of distance from the center of an isolated vortex (κ≈8). The order parameter squared is proportional to the density of supercarriers n_s.

The field distribution around a single vortex can be obtained from the London equations[13]:

$$B_v(r) = \frac{\Phi_0}{2\pi\lambda^2} K_0\left(\frac{r}{\lambda}\right) \qquad [7\text{-}1]$$

K_0 is the modified Hankel function zeroth order.

[13] London equations: $\frac{d\vec{j}}{dt} = \frac{1}{\mu_0 \lambda_L^2}\vec{E}(t)$ and $\mathrm{rot}\,\vec{j} = -\frac{1}{\mu_0 \lambda_L^2}\vec{B}(t)$ describe perfect conductivity and diamagnetic shielding in a superconductor.

This function can be approximated as follows:

$$B_v(r) \rightarrow \frac{\Phi_0}{2\pi\lambda^2}\ln\left(\frac{\lambda}{r}\right) \qquad \text{for } \xi << r << \lambda \qquad [7\text{–}2]$$

$$B_v(r) \rightarrow \frac{\Phi_0}{2\pi\lambda^2}\sqrt{\frac{\lambda}{r}}e^{-\frac{r}{\lambda}} \qquad \text{for } r >> \lambda \qquad [7\text{–}3]$$

μSR can measure the local magnetic field distribution in the vortex state. Qualitatively, we expect following picture:

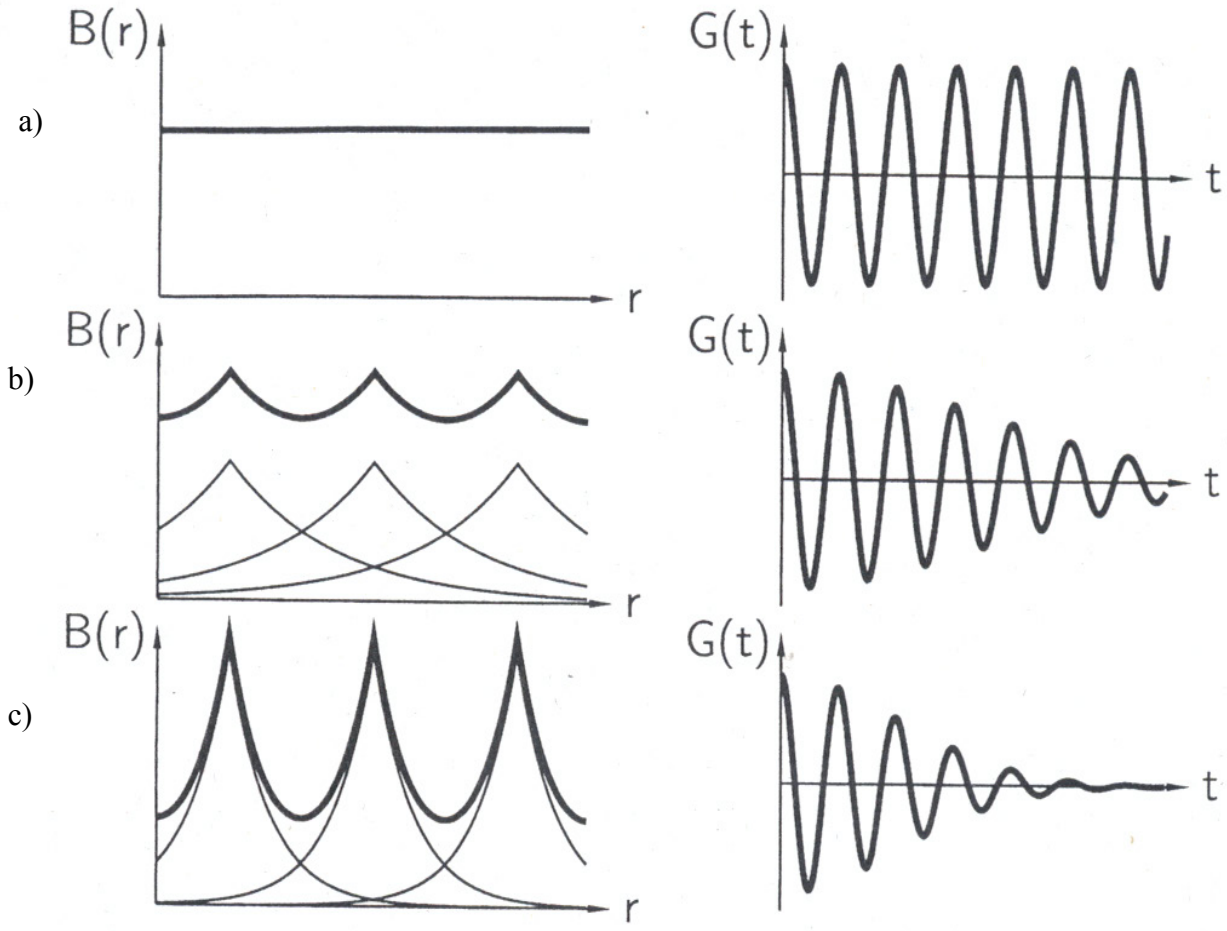

Fig. 7-8: Spatial distribution of fields inside a superconductor (schematically) a) Normal state, b) Vortex state, $T \approx T_c$. c) $T << T_c$. Right: corresponding asymmetry spectra.
From S.J. Blundell, Contemporary Physics **40**, 175-192 (1999).

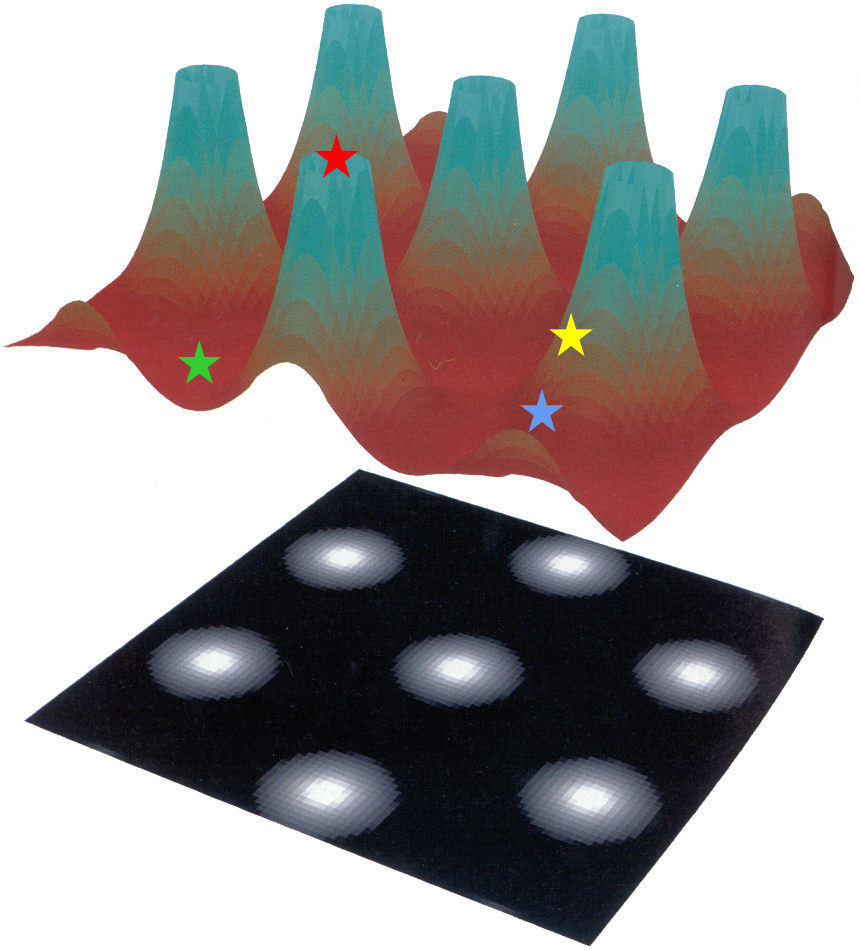

Fig. 7-9: Spatial distribution $B_z(\vec{r})$ of a regular vortex lattice ($\vec{B}_{ext} \parallel \hat{z}$).

The corresponding field distribution $p(B_z)$ is given by

$$p(B_z) = \frac{1}{S}\int_S d^2\vec{r}\ \delta(B_z - B_z(\vec{r}))$$

(S is the surface of the 2D unit cell). The field distribution (and corresponding contour plot in the inset) has the form[14]:

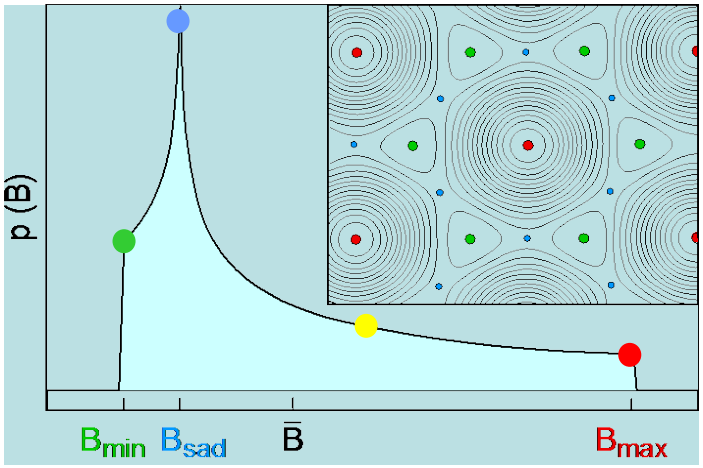

[14] Note that the maximum field (at the center of the vortex) is infinite in the London model. The field profile has been cut here near the flux line center.

The expected μSR signal (TF geometry, $B_{ext} \parallel z$) can be written as (N_μ number of detected muons):

$$P_x(t) = \frac{1}{N_\mu}\sum_{i=1}^{N_\mu}\cos(\gamma_\mu B_i t + \phi)$$

$$P_x(t) = \int p(B)\cos(\gamma_\mu B t + \phi)dB$$

Polarization and p(B) are related via a Fourier transform.

7.2 Second moment of the field distribution of an extreme type II superconductor

The second moment of the field distribution can be calculated explicitely.
Assumptions:
-Ginzburg-Landau parameter $\kappa >> 1$ (we neglect the extension of the vortex core)
-London model valid (up to ~ $B_{c2}/4$)
-Vortex cores are separated and non-interacting
-Linear superposition of the vortex fields

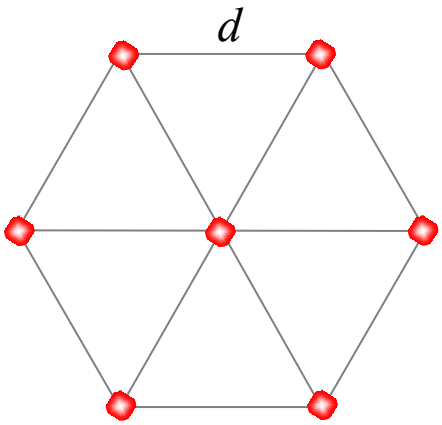

Vortex distance d:

Area of the unit cell containing one vortex:

$$S = d^2\frac{\sqrt{3}}{2}$$

$$\Phi_0 = S < B > \;\rightarrow\; d = \sqrt{\frac{2\Phi_0}{< B > \sqrt{3}}}$$

The special field distribution B(r) can be calculated from a modified London equation taking into account the flux source given by the vortices[15]:

$$\vec{B}(\vec{r}) + \lambda^2(\text{rot rot}\,\vec{B}(\vec{r})) = \Phi_0\sum_n \delta(\vec{r} - \vec{r}_n)\hat{z}$$

$$\vec{B}(\vec{r}) - \lambda^2\Delta\vec{B}(\vec{r}) = \Phi_0\sum_n \delta(\vec{r} - \vec{r}_n)\hat{z} \qquad [7\text{-}4]$$

In an ideal vortex state the vectors $\vec{r}_n$ form a periodic two dimensional lattice. Therefore [7-4] can be solved in Fourier space ($\vec{k}$ space):

[15] The left hand side is obtained by applying the rot operation to the Maxwell equation $\text{rot}\vec{B} = \mu_0\vec{j}$ then using the second London equation and $\text{rot}(\text{rot}\vec{B}) = \text{grad div}\vec{B} - \Delta\vec{B}$.

For an hexagonal lattice:

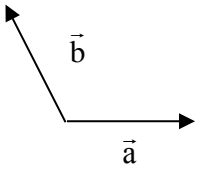

$$|\vec{a}| = |\vec{b}| = d,\ \vec{a}\cdot\vec{b} = \cos 120^\circ$$

Reciprocal vectors:

$$\vec{a}^* = 2\pi\frac{\vec{b}\times\vec{c}}{\vec{a}\cdot(\vec{b}\times\vec{c})}, \qquad \vec{b}^* = 2\pi\frac{\vec{c}\times\vec{a}}{\vec{a}\cdot(\vec{b}\times\vec{c})}$$

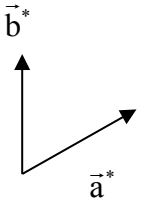

$$|\vec{a}^*| = \frac{4\pi}{\sqrt{3}d} = |\vec{b}^*|$$

$$\vec{k}_{m,n} = m\vec{a}^* + n\vec{b}^*$$

(also hexagonal symmetry)

$$\vec{B}(\vec{r}) = \sum_{\vec{k}} \vec{b}_k e^{i\vec{k}\vec{r}} \qquad [7\text{-}5]$$

With Fourier components:

$$\vec{b}_{\vec{k}} = \frac{1}{S}\int \vec{B}(\vec{r}) e^{-i\vec{k}\vec{r}} d^2\vec{r}$$

London equation becomes (fields parallel to z-direction):

$$\sum_{\vec{k}} (\vec{b}_{\vec{k}} + \lambda^2 k^2 \vec{b}_{\vec{k}}) e^{i\vec{k}\vec{r}} = \frac{1}{S}\Phi_0 \hat{z} \sum_{\vec{k}} e^{i\vec{k}\vec{r}}$$

We find:

$$\vec{b}_k = \frac{<B>}{1+k^2\lambda^2}\hat{z} \qquad [7\text{-}6]$$

Where <B> is the (space) averaged internal field (<B>= $N\Phi_0$, N=1/S: vortex density).

$$B_z(\vec{r}) = \sum_{\vec{k}} \frac{<B>}{1+k^2\lambda^2} e^{i\vec{k}\vec{r}}$$

With $b_0 =< B >$ we obtain for the second moment of the field distribution:

$$<\Delta B_z^2> = \sum_{\vec{k}\neq 0} \left|b_{\vec{k}}\right|^2$$

In a perfect hexagonal lattice:

$$k^2 = k_{m,n}{}^2 = \frac{16\pi^2}{3d^2}(m^2 - mn + n^2) \quad \text{and with } k\lambda >> 1 \ (<B> >> B_{c1})$$

$$< \Delta B_z{}^2 >= \frac{3\Phi_0{}^2}{64\pi^4\lambda^4} \sum_{(m,n)\neq(0,0)} \frac{1}{(m^2 - mn + n^2)^2}$$

$$< \Delta B_z{}^2 >= (\frac{0.003710\ \Phi_0^2}{\lambda^4}) \qquad [7\text{-}7]$$

The quantity $< \Delta B^2 >$ is directly related to the magnetic penetration depth λ.

The measurement of the second moment of the field distribution allows therefore to determine the London penetration depth. Note that [7-7] predicts a field width independent of the external field. The formula is valid for small inductions $b \equiv <B>/B_{c2} << 1$ and large κ, more precisely in the range $0.13/\kappa^2 << b << 1$ (H. Brandt, Phys. Rev. B **68**, 054506 (2003)).

It holds also[16]:

$$B_{min} - < B > \ \propto \frac{1}{\lambda^2}$$

$$B_{max} - < B > \ \propto \frac{1}{\lambda^2}$$

$$B_{sad} - < B > \ \propto \frac{1}{\lambda^2}$$

If we cannot neglect the coherence length ξ (radius of the vortex core), we have to introduce

[16] About demagnetization in vortex state. The quantities H_i, magnetization M, demagnetization factor N $(0 \le N \le 1)$ and mean magnetic flux <B> (which is the mean internal field measured by μSR) are related to each other by: $H_i = \frac{< B >}{\mu_0} - M = H_{ext} - NM$. Since the μ^+ Knight shift is generally negligible (e.g. in high-T_c materials), the muon spin precession shift is given by: $< B > -\mu_0 H_{ext} = (1 - N)\mu_0 M$ (M<0).

in [7-6] a „cutoff“ of the terms with k~1/ξ i.e.[17]:

$$\vec{b}_k = \frac{<B>}{1+k^2\lambda^2}\hat{z} \qquad \rightarrow \qquad \vec{b}_k = \frac{<B>e^{-k^2\xi^2}}{1+k^2\lambda^2}\hat{z}$$

(E.H. Brandt, J. Low Temp. Phys. **73**, 355 (1988)).

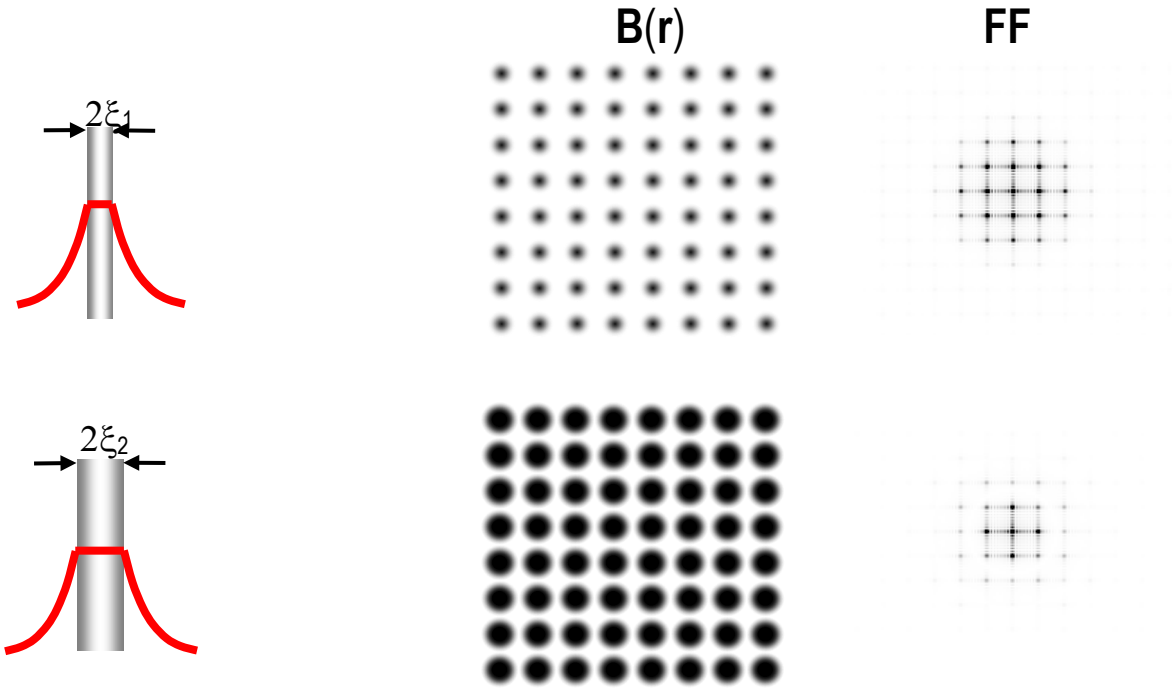

[17] Near b=1 the Abrikosov solution of the linearized Ginzburg-Landau theory yields for all κ values (H. Brandt, Phys. Rev. B **68**, 054506 (2003)):

$$<\Delta B_z^2> = \left(\frac{7.52\cdot 10^{-4}\,\Phi_0^2}{\lambda^4}\right)\frac{\kappa^4(1-b)^2}{(\kappa^2-0.069)^2}$$

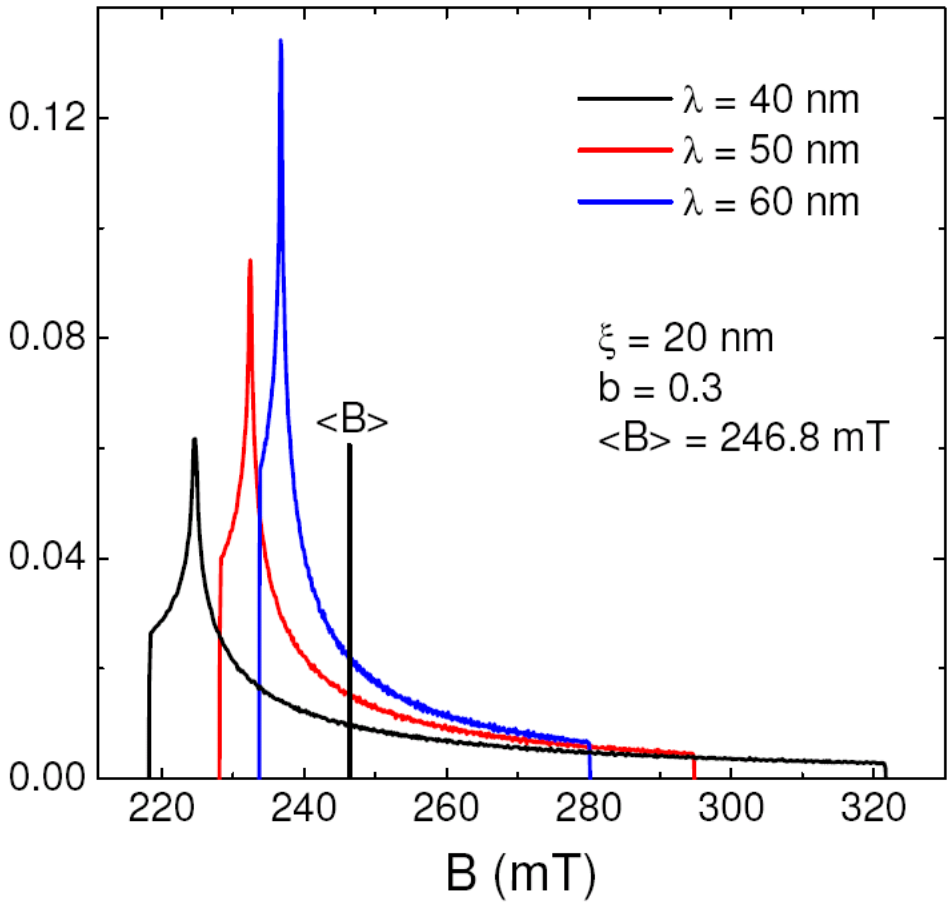

Fig. 7-10: Calculated field distributions. From A. Maisuradze et al., J. Phys.: Condens. Matter **21**, 075701 (2009).

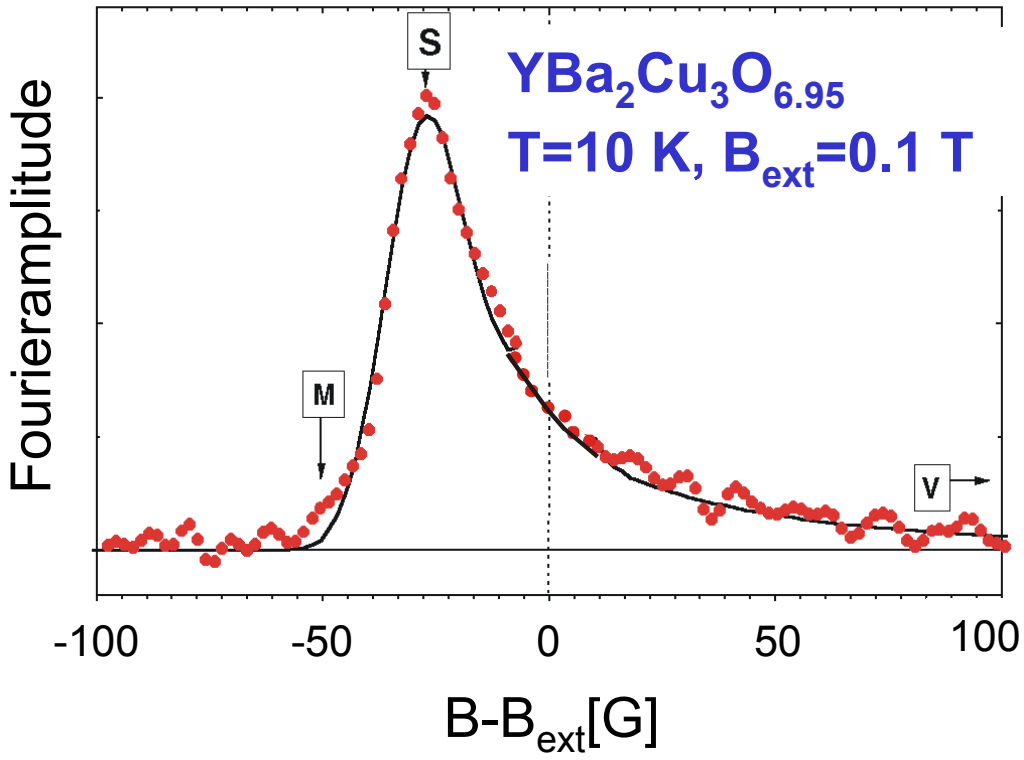

Fig. 7-11: Measured field distribution in YBCO obtained from the Fourier transform of the μSR spectrum.

To determine the magnetic penetration depth the magnetic field is applied above T_c in a TF configuration. Then the temperature is gradually lowered below T_c (field cooling). This way one obtains a regular flux line lattice below T_c ($H_{c1}<H_{ext}<H_{c2}$). In a high-T_c material λ as well as the diamagnetism are anisotropic.
In principle one needs the full field distribution p(B) to determine λ. However, depending on the physical situation the relaxation of the transversal field μSR signal below T_c can be approximated by a Gauss function. In a polycrystalline sample the signal is the integral over all possible orientations of the crystal grains. This leads to a more symmetric p(B), whose Fourier transform (=relaxation function) is closer to a Gaussian function. In this case the second moment of the field distribution can be obtained from the μSR spectrum fitted with a Gaussian relaxation (which implicitly implies that p(B) is Gaussian) and the field width and the magnetic penetration depth are directly related to the Gaussian relaxation rate σ_{sc}:

$$\sigma_{sc}^2 = \gamma_\mu^2 < \Delta B^2 >= \gamma_\mu^2(< B^2 > - < B >^2) \qquad [7\text{-}8]$$

To obtain σ_{sc} one has generally to subtract from the measured σ the temperature independent contribution of the broadening due to the nuclear moments σ_n, which is obtained by a measurement above T_c:

$$\sigma_{sc}(T) = \sqrt{\sigma^2(T) - \sigma_n^2}$$

Assuming Eq. [7-7] and $\frac{\sigma_{sc}}{\gamma_\mu} = \sqrt{<\Delta B^2>}$ there is a simple numerical relationship between the muon depolarisation rate σ_{sc} and the superconducting penetration depth λ namely $\lambda = \frac{327.5}{\sqrt{\sigma_{sc}}}$, σ_{sc} in μs^{-1}, λ in nm. A Gaussian fit is only sensitive to the central part of the field distribution of a non-Gaussian distribution. This is sometimes taken into account empirically by using the expression $\lambda = \frac{270.0}{\sqrt{\sigma_{sc}}}$, σ_{sc} in μs^{-1}, λ in nm.

a)

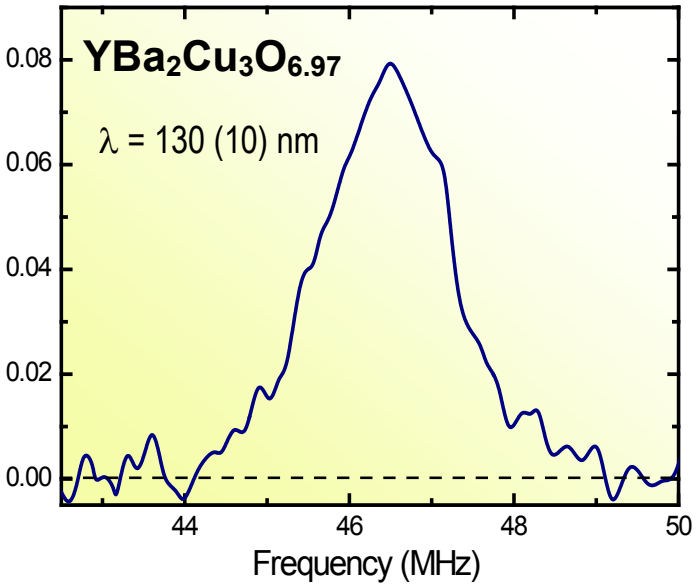

b)

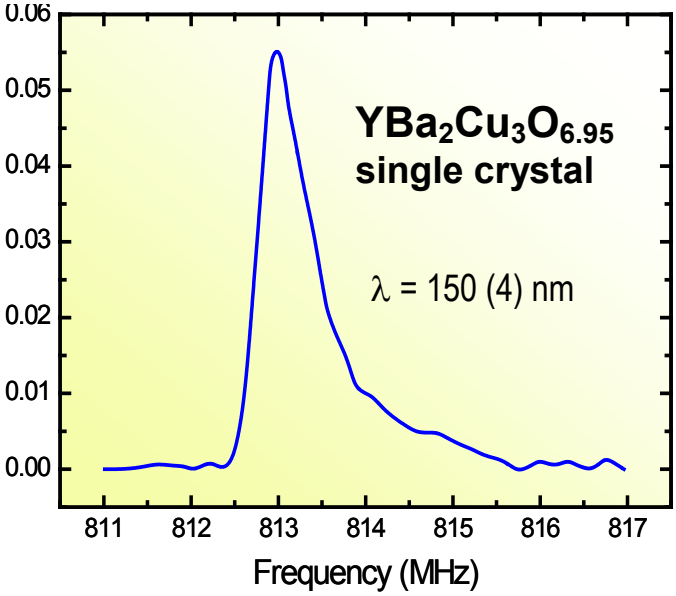

Fig. 7-12: Comparison of p(B) (a) in a polycrystalline YBCO sample (from B. Pümpin et al., Phys. Rev. B **42**, 8019 (1990)) and (b) in a single crystal (from J. Sonier et al., Phys. Rev. Lett. **83**, 4156 (1999)).

7.3 Field dependence of the muon spin relaxation rate

If the applied magnetic field is not small with respect to B_{c2} the decrease of the intervortex distance may lead to a decrease of the width of the internal field distribution. Also the vortex core where the superconducting order parameter is suppressed cannot be neglected any more (remember $B_{c2} = \frac{\Phi_0}{2\pi\xi_{GL}^2}$, Φ_0 flux quantum). In this case, the expected field dependence of the second moment of the field distributions has been calculated within the Ginzburg-Landau model (E. H. Brandt, Phys. Rev. B **68**, 054506 (2003)) and a modified London Model with a Gaussian cut off to take into account the finite size of the vortex core (E. H. Brandt, Phys. Rev. B **37**, 2349 (1988)).The two expressions differ essentially in the higher order corrections to the linear field dependence ($b \equiv \langle B \rangle / B_{c2}$), generally $\langle B \rangle \approx B_{ext}$, see [16]). Calculations based on Ginzburg -Landau can be well approximated by:

$$\sigma_{sc}\ [\mu s^{-1}] = 4.854 \cdot 10^4 (1-b)\left[1+1.21(1-\sqrt{b})^3\right]\frac{1}{\lambda[nm]^2} \qquad [7\text{-}9]$$

whereas the modified London model gives:

$$\sigma_{sc}\ [\mu s^{-1}] = 4.846 \cdot 10^4 (1-b)\sqrt{1+3.9(1-b^2)}\,\frac{1}{\lambda[nm]^2} \qquad [7\text{-}10]$$

An example of such a behavior in the iron pnictide $RbFe_2As_2$ (T_c=2.52 K) is shown below. (Z. (Shermadini et al., Phys. Rev. B **82**, 144527 (2010)).

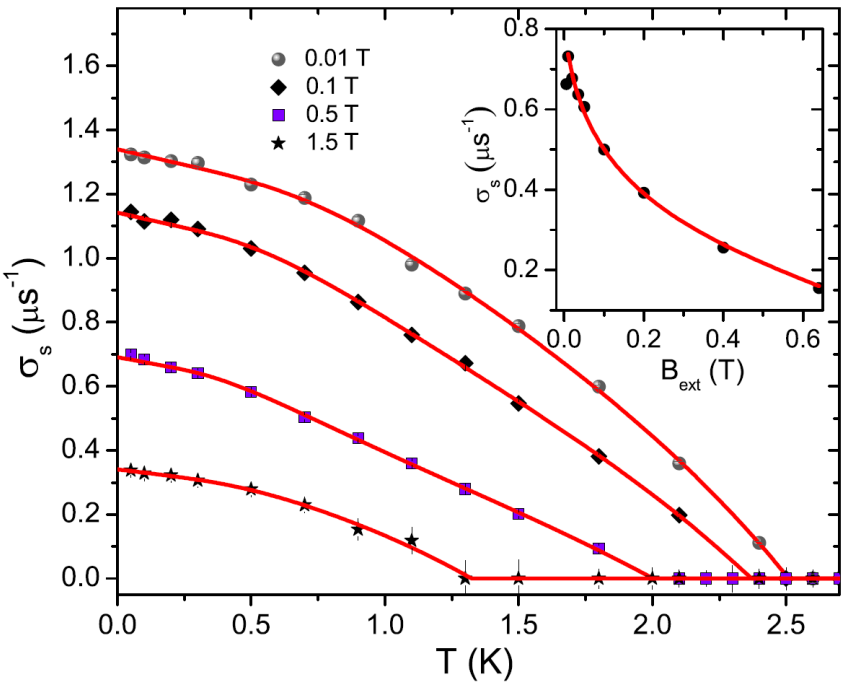

Fig. 7-13: Temperature dependence of the depolarization rate σ_{sc} due to the FLL in $RbFe_2As_2$ and obtained in fields of 1.5, 0.5, 0.1, and 0.01 T (lines are guides to the eyes). Inset: field dependence of σ_{sc} obtained at 1.6 K and analyzed using the Eq. [7-9].

By analyzing at each temperature (not too close to T_c), the field dependence of σ_{sc} with Eq. [7-9] one obtains $\lambda(T)$ and $B_{c2}(T)$. From the temperature dependence of $1/\lambda(T)^2$ we obtain information about the superconducting gap of the material (see section 7.6).

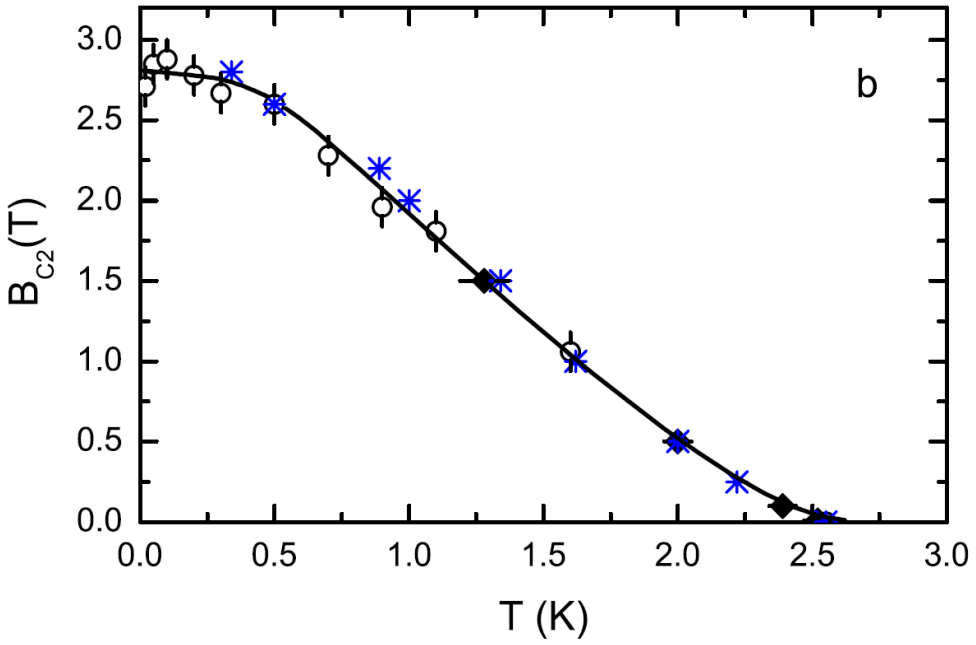

Fig. 7-14: Upper critical field for $RbFe_2As_2$. The open circles are obtained by analyzing the field dependence of σ_{sc} using Eq. [7-9]. The diamonds are the value obtained by analyzing the temperature dependence of σ_{sc}. The stars correspond to the complete disappearance of the resistivity in field. The line is a guide to the eyes.

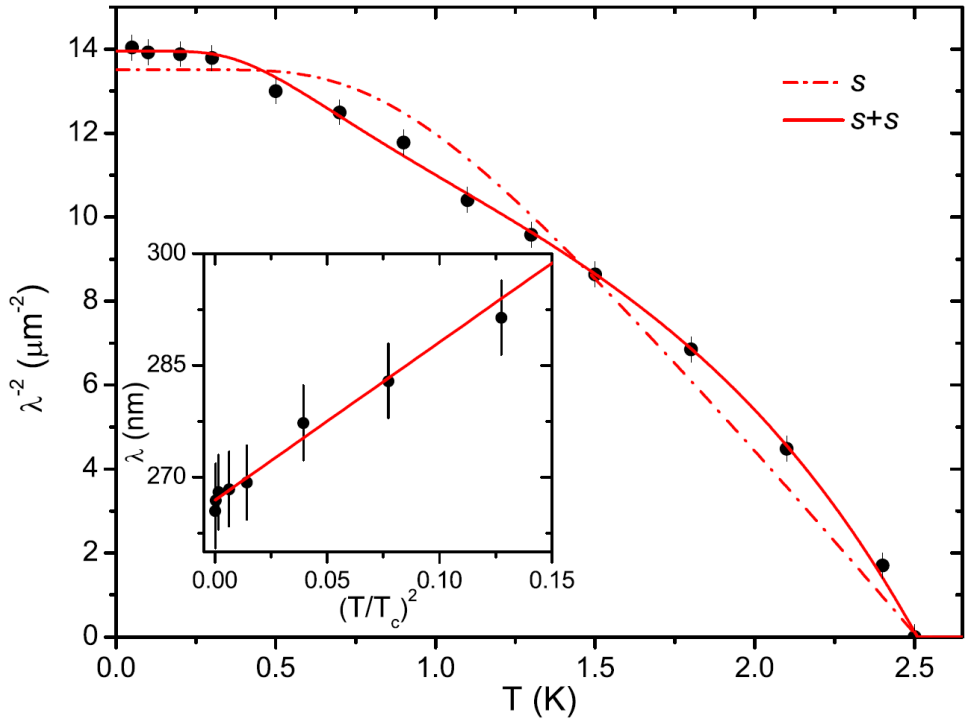

Fig. 7-15: Magnetic penetration depth as a function of temperature obtained with Eq. [7-9]. Above 0.5 K only the values measured in a field of 0.01 T are plotted. The red dashed line corresponds to a BCS *s*-wave gap symmetry whereas the solid one represents a fit using a two-gap *s*+*s* model (see Section 7-6). The inset exhibits the penetration depth as a function of $(T/T_c)^2$.

7.4 Uemura relation: correlation between T_c und σ_{sc}

Since the discovery of superconductivity in the copper oxide materials there has been a considerable effort to find universal trends and correlations amongst physical quantities to find a clue to the origin of the superconductivity. One of the earliest patterns that emerged was the linear scaling of the Gauss relaxation σ_{sc} with the superconducting transition temperature (T_c). This is referred to as the Uemura relation (Phys. Rev. Lett. **66**, 2665 (1991) and works reasonably well for the underdoped materials.
The linear relation between T_c und σ_{sc} (Fig. 7-16) implies a direct correlation between T_c and the superfluid density $\rho_s \equiv \frac{n_s}{m^*}$ since $\sigma_{sc} \propto \frac{1}{\lambda^2} \propto \frac{n_s}{m^*}$. The magnetic penetration depth in cuprates is anisotropic. For polycrystalline samples λ is an average of λ_c and λ_{ab} (ab = CuO_2 planes). For $\lambda_c >> \lambda_{ab}$, σ_{sc} is only sensitive to λ_{ab} (W. Barford and J.M.F. Gunn, Physica C **153-155**, 691 (1988)).

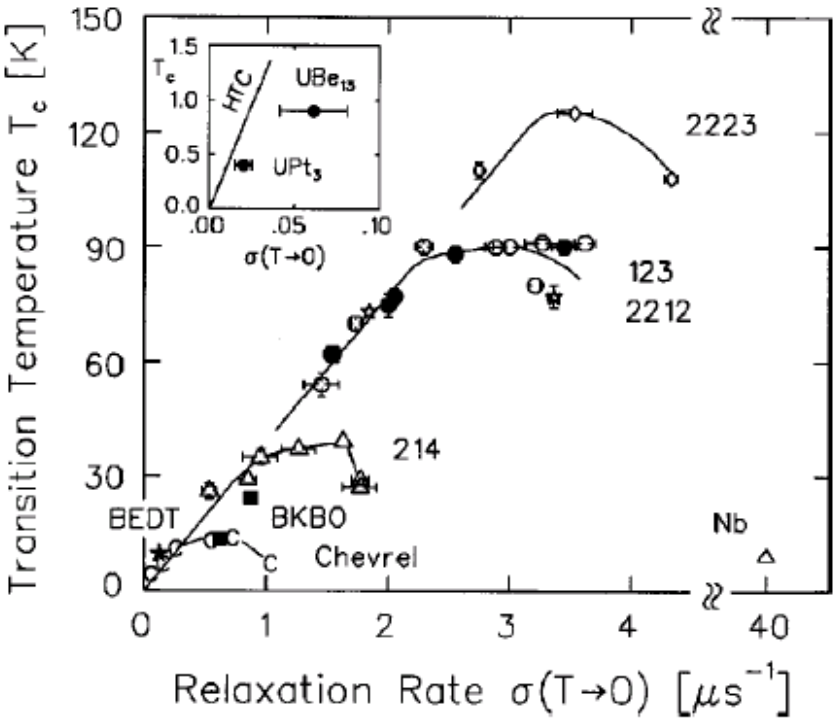

Fig. 7-16: T_c vs muon depolarization rate $\sigma(0)$ in (i) the high-temperature superconductors: $YBa_2Cu_3O_{7-\delta}$ (123), $La_{2-x}Sr_xCuO_4$ (214), $Bi_2Sr_2CaCu_2O_8$, and $Tl_{0.5}Pb_{0.5}Sr_2CaCu_2O_7$ (2212), and $Bi_{2-x}Pb_xSr_2Ca_2Cu_3O_{10}$, $Tl_2Ba_2Ca_2Cu_3O_{10}$, and $Tl_{0.5}Pb_{0.5}Sr_2Ca_2Cu_3O_9$ (2223) [note: hole doping increases with increasing $\sigma(0)$]; (ii) $Ba_{1-x}K_xBiO_3$ (BKBO); (iii) the Chevrel-phase systems $LaMo_6Se_8$, $LaMo_6S_8$, and $PbMo_6S_8$; (iv) the organic superconductor $(BEDT\text{-}TTF)_2Cu(SCN)_2$; (v) the conventional superconductor Nb; and (vi) the heavy-fermion superconductors UPt_3 and UBe_{13}. From Uemura *et al.*, 1991.

Such a correlation is not consistent with conventional weak coupling BCS theory for phonon coupled superconductors, where

$$T_c \cong \frac{2\hbar\omega_D}{k_B} e^{-\frac{2}{VD(E_F)}} \qquad [7\text{-}11]$$

ω_D = Debye frequency (phonon coupling)
$D(E_F)$ = Density of states at Fermi level E_F
V= effective attractive pair potential (→ Cooper pair).

In [7-11] T_c is proportional to ω_D and not simply related to n_s.

Fig. 7-16 indicates that these „unconventional“ superconductors belong to a different class of materials than that of the previously known “conventional” superconductors (such as Nb, Al,..).
If the energy scale of the pairing is of the order of the Fermi energy, one would expect:

$$T_c \propto T_F \qquad [7\text{-}12]$$

For a 2D electron gas the Fermi energy is given by:

$$E_F = k_B T_F = \frac{\hbar^2 \pi n_{s-2d}}{m^*} \qquad [7\text{-}13]$$

High- T_c superconductors are to large extent two dimensional, since the CuO_2 planes contain most of the supercarriers (electrons or holes).

One obtains:

$$T_c \propto \frac{n}{m^*}$$

A linear relationship between critical temperature and superfluid density is also obtained if T_c is primarily determined by long range phase ordering.

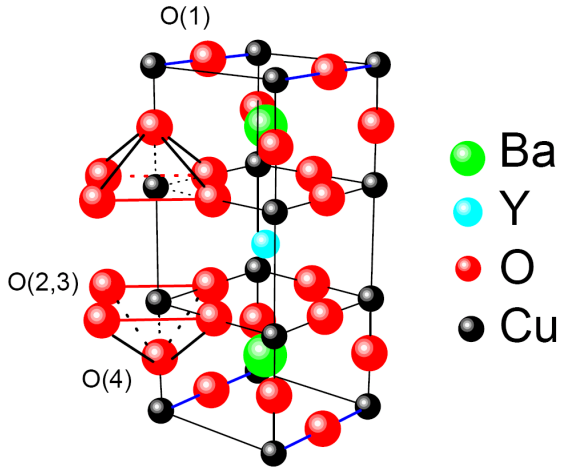

Fig. 7-17: Crystal structure of $YBa_2Cu_3O_{7-\delta}$ with 2 CuO_2 planes and CuO chains as charge reservoir.

μSR measurements of the penetration depth in the vortex state and the Uemura plot are used to classify superconductors (e.g. Fe based superconductors, discovered in 2008, Y. Kamihara, T. Watanabe, M. Hirano, and H. Hosono, J. Am. Chem. Soc., **130** (2008) 3296).

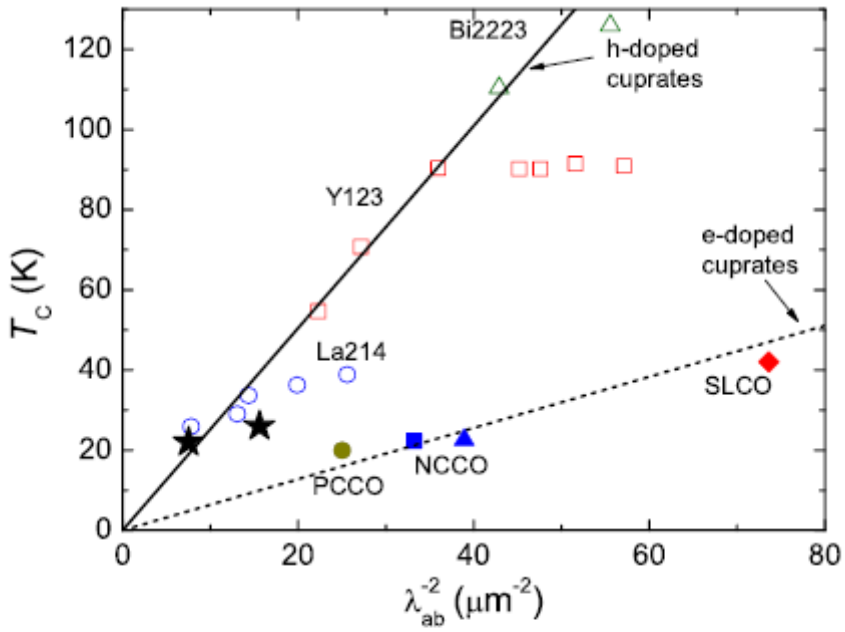

Fig. 7-18: Uemura plot for hole and electron doped high T_c cuprates and for the $LaFeAsO_{1-x}F_x$ pnictide (★) (from H. Luetkens et al., Phys. Rev. Lett. **101**, 097009 (2008)).

7.5 Measurement of the anisotropy of the magnetic penetration depth

Measurement with oriented YBCO single crystals. The theory predicts:

$$\sigma_{sc}(\vartheta) = \frac{const}{\lambda_{ab}\lambda_c}\sqrt{\sin^2\vartheta + \frac{\lambda_c^{\,2}}{\lambda_{ab}^{\,2}}\cos^2\vartheta} \qquad [7\text{-}14]$$

In this equation, λ_{ab} and λ_c are the principal values of the London penetration depth for a superconductor with uniaxial asymmetry: λ_{ab} and λ_c are determined by superconducting screening currents flowing parallel and perpendicular to the CuO_2 planes, respectively.
ϑ is the angle between external field and c-axis.
From the measurement one can determine the anisotropy parameter γ.

$$\gamma^2 = \frac{\lambda_c^2}{\lambda_{ab}^2} = \frac{m_c^*}{m_{ab}^*} \qquad [7\text{-}15]$$

$\vartheta = 0$, $H_{ext} \parallel$ c-axis. Shielding currents flow in (a,b) plane
$\vartheta = 90$, $H_{ext} \perp$ c-axis. Shielding currents flow along c and a (or b) axis

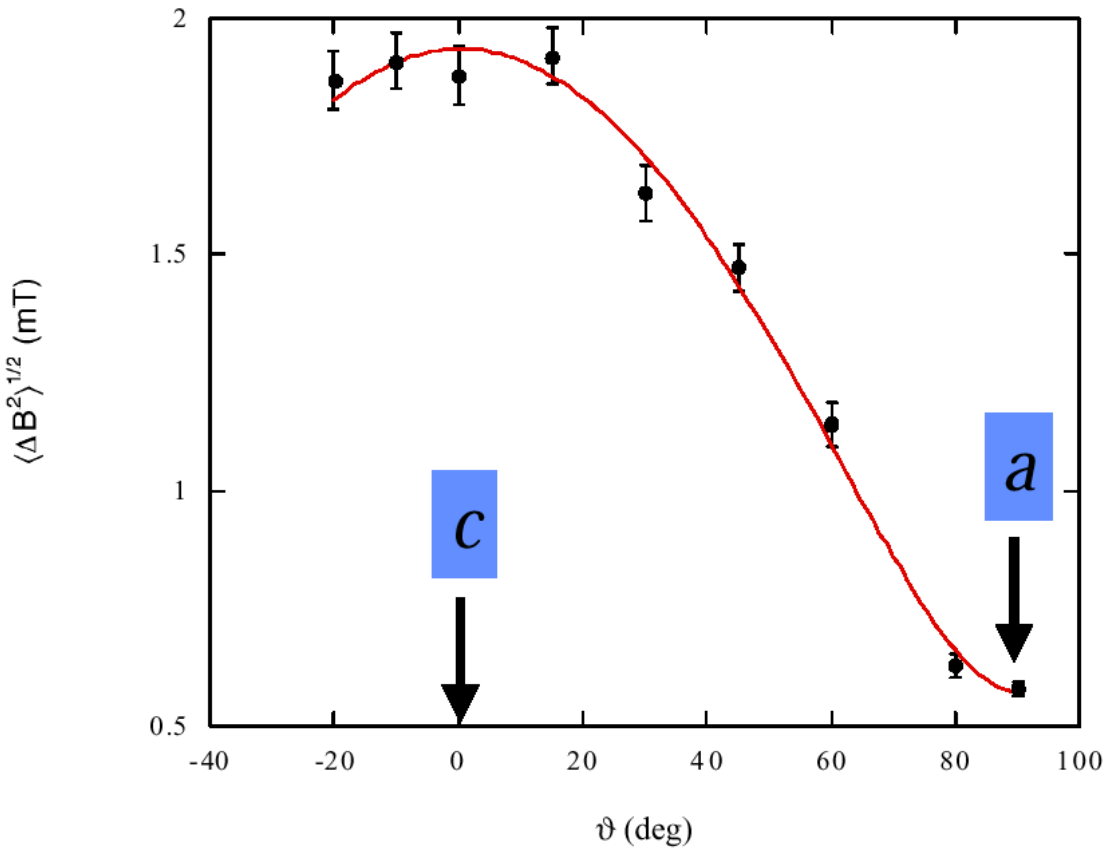

Fig. 7-19: Angular dependence of the second moment of the field distribution in YBCO single crystal. The curve is a fit to [7-14], γ=3.9(6). From E. M. Forgan et al., Hyperfine Interact. **63**, 71 (1990).

7.6 Temperature dependence of λ(T) and of the superconducting carrier density and gap symmetry

From a μSR measurement we obtain $\sigma \propto \frac{1}{\lambda^2} \propto \frac{n_s}{m^*}$. The temperature dependence of n_s contains information on the superconducting gap Δ(T). Therefore, an accurate measurement of the temperature dependence of λ provides information on the superconducting gap such as value at T=0 K and symmetry.

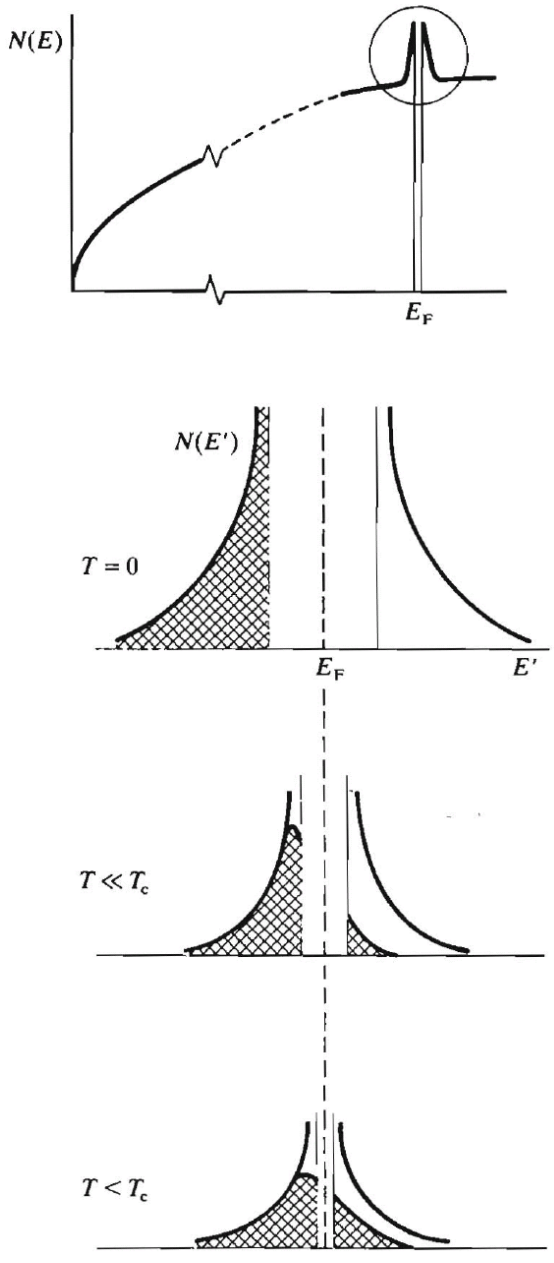

Fig. 7-20: Density of states and state population at different temperatures in an s-wave superconductor, showing the opening of the superconducting gap with temperature.

By taking into account the thermal population of the quasiparticle excitations of the Cooper pairs (Bogoliubov quasiparticles) BCS theory predicts:

$$n_s(T) = n_s(0)\left(1 - \frac{2}{k_B T}\int_0^{\infty} f(\varepsilon,T)\left[1 - f(\varepsilon,T)\right]d\varepsilon\right) \qquad [7\text{-}16]$$

$$f(\varepsilon,T) = \frac{1}{1 + e^{\frac{\sqrt{\varepsilon^2 + \Delta(T)^2}}{k_B T}}} \qquad [7\text{-}17]$$

where ε is the energy of the normal state electrons measured from the Fermi level ($E = \sqrt{\varepsilon^2 + \Delta(T)^2}$ energy of the quasiparticles measured from Fermi level).

For isotropic s-wave pairing (as in the case of conventional BCS superconductor) and $T \ll T_c$:

$$n_s(T) = n_s(0)\left(1 - \sqrt{\frac{2\pi\Delta(0)}{k_B T}}\exp\left[-\Delta(0)/k_B T\right]\right) \qquad [7\text{-}18]$$

and

$$\lambda(T) = \lambda(0)\left(1 + \sqrt{\frac{\pi\Delta(0)}{2k_B T}}\exp\left[-\Delta(0)/k_B T\right]\right) \qquad [7\text{-}19]$$

(B. Mühlschlegel, Z. Phys. **155**, 313 (1959)).

The wave function of the two paired carriers can be written as the product of a space and a spin part: $\Psi(\vec{r}_1, s_1, \vec{r}_2, s_2) = \phi(\vec{r}_1, \vec{r}_2)\chi(s_1, s_2)$.

The wave function must be antisymmetric with respect to particle exchange.
If the spin state is a singlet S=0, $\chi = \frac{1}{\sqrt{2}}(|\uparrow\downarrow\rangle - |\downarrow\uparrow\rangle)$ the space part must be even, e.g.. s-wave (l=0) or d-wave (l=2). Conventional BCS superconductors are so-called s-wave superconductors, whereas high-T_c cuprate superconductors have d-wave symmetry, with a gap which is angular dependent in k-space. This is observable in a measurement of the temperature dependence of the magnetic penetration depth.
Instead of Eq. [7-16] we have for a d-wave superconductor:

$$n_s(T) = n_s(0)\left(1 - \frac{1}{\pi k_B T}\int_0^{2\pi}\int_0^{\infty} f(\varepsilon,T)\left[1 - f(\varepsilon,T)\right]d\varphi d\varepsilon\right) \qquad [7\text{-}20]$$

with:

$$f(\varepsilon,T)=\frac{1}{1+e^{\frac{\sqrt{\varepsilon^2+[\Delta(T)\cos(2\varphi)]^2}}{k_BT}}}$$

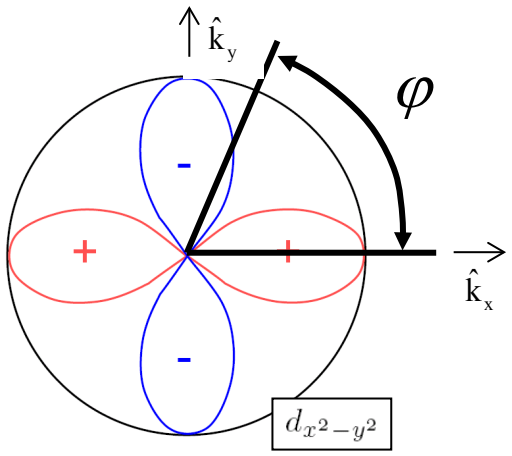

Gap function $\Delta(\mathbf{k})$. It has lower symmetry than the Fermi surface

As the gap disappears along some directions of the Fermi surface ("nodes"), extremely-low-energy quasiparticles excitations (and therefore significant pair-breaking) may occur at very low temperature.

This is reflected in a more pronounced temperature dependence of λ than for s-wave pairing. Remembering that $\lambda=\sqrt{\frac{m^*}{\mu_0 e^2 n_s}}$ one gets for $T\ll T_c$ a linear T-dependence:

$$\lambda(T)=\lambda(0)\left(1+\frac{\ln 2k_BT}{\Delta(0)}\right) \qquad [7\text{-}21]$$

(P. J. Hirschfeld and N. Goldenfeld, Phys. Rev. B **48**, 4219 (1993)).

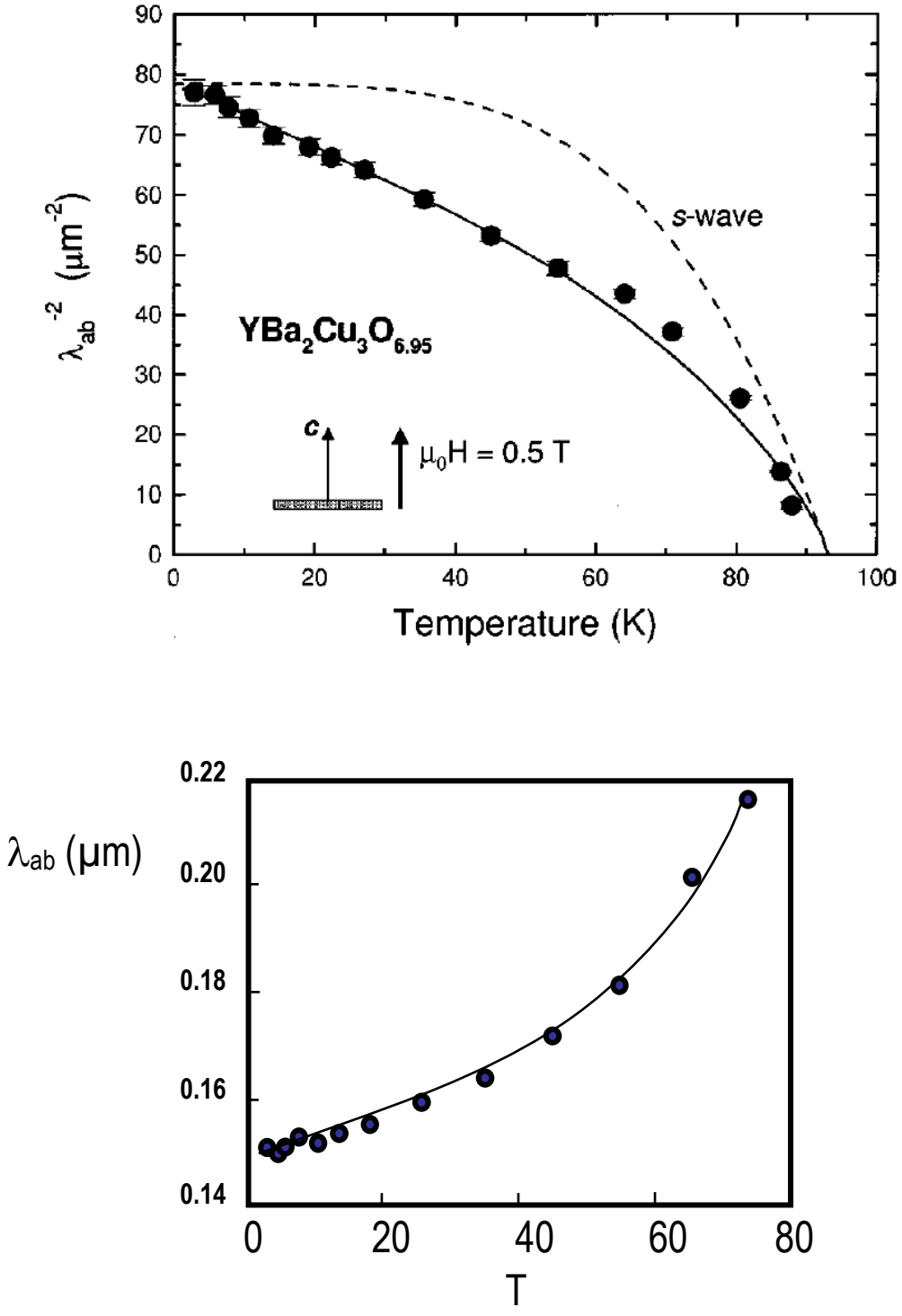

Fig. 7-21: Top: Temperature dependence of λ_{ab}^{-2} in a $YBa_2Cu_3O_{6.95}$ single crystal. Measurement of $\Delta\lambda_{ab}$ with microwave absorption normalized to the μSR measurements. Dashed line: temperature dependence for an s-wave superconductor. (μSR measurement: J. Sonier, Phys. Rev. Lett. **72**, 744 (1994), microwave measurement: W.N. Hardy, Phys. Rev. Lett. **70**, 3999 (1993)). Bottom: $\lambda_{ab}(T)$ showing the linear dependence at low temperatures.

7.7 Melting of the flux line lattice

The vortex state of a High-T_c superconductor represents a unique state of the solid that can be compared with a crystal and its lattice. The "lattice constant" of the vortex state can be changed by the external field and the temperature in a wide range.
Especially in a HT_c superconductor, the combination of extreme anisotropy, thermal fluctuations (important since T_c is large) and material defects lead to a complex behavior, which can be described by a corresponding phase diagram with phase transitions solid-liquid or ordered-disordered.

μSR measurements were the first microscopic investigations that demonstrated the melting of the flux line lattice.

The vortex state is characterized by the moments of the field distribution.

$$\alpha = \frac{<\Delta B^3>^{1/3}}{<\Delta B^2>^{1/2}} \qquad <\Delta B^n> = \int_0^\infty (B - <B>)^n p(B) dB \qquad [7\text{-}22]$$

α represents a measure of the asymmetry of p(B).

In the extreme anisotropic HT_c-superconductor such as $Bi_{2.15}Sr_{1.85}CaCu_2O_{8+d}$ (T_c=84 K) following is observed (S.L. Lee et al. Phys. Rev. Lett. **71**, 3862 (1993)):

a) Until 54K and H_{ext}=45.4 mT the expected distribution is found.
b) Increasing the temperature to 54 K (H_{ext}= 45.4 mT) leads to a dramatic change of p(B). α jumps abruptly to a negative value. This behavior is interpreted as melting of the flux line lattice (Fig. 7-19).
c) Increasing the external field at constant temperature (in a field cooling procedure) one observes above a critical field another phase transition (Fig. 7-22), which is not so drastic as the previous one and which is also characterized by a change of α. This behavior is interpreted as a transition to a less ordered solid state, with a dimensionality change from 3D to 2D (formation of so-called pancakes vortices).

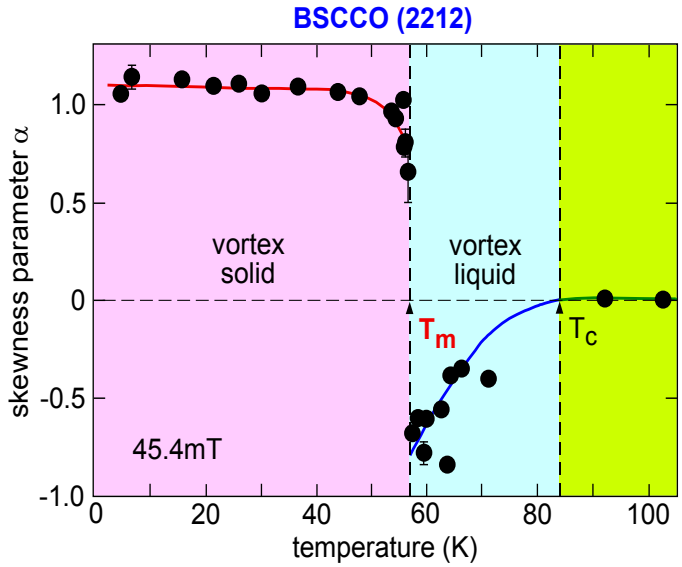

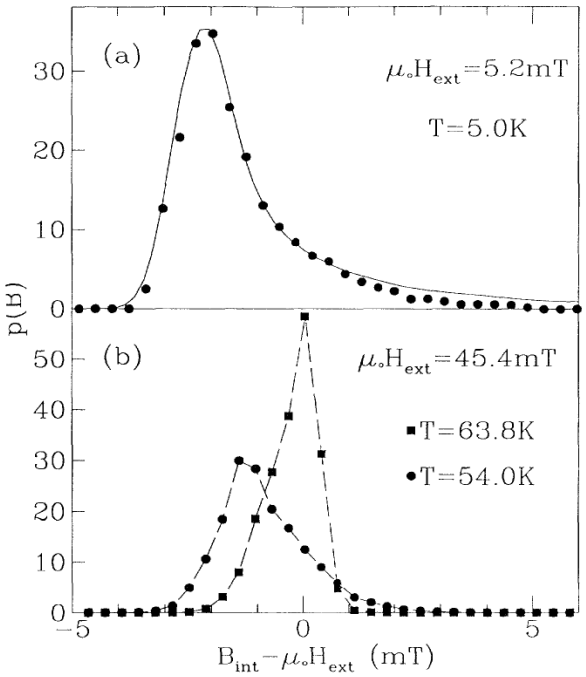

Fig. 7-22: Phase diagram of $Bi_{2.15}Sr_{1.85}CaCu_2O_{8+d}$ and field distribution measured in different states (5 K solid, 63.8 K liquid).

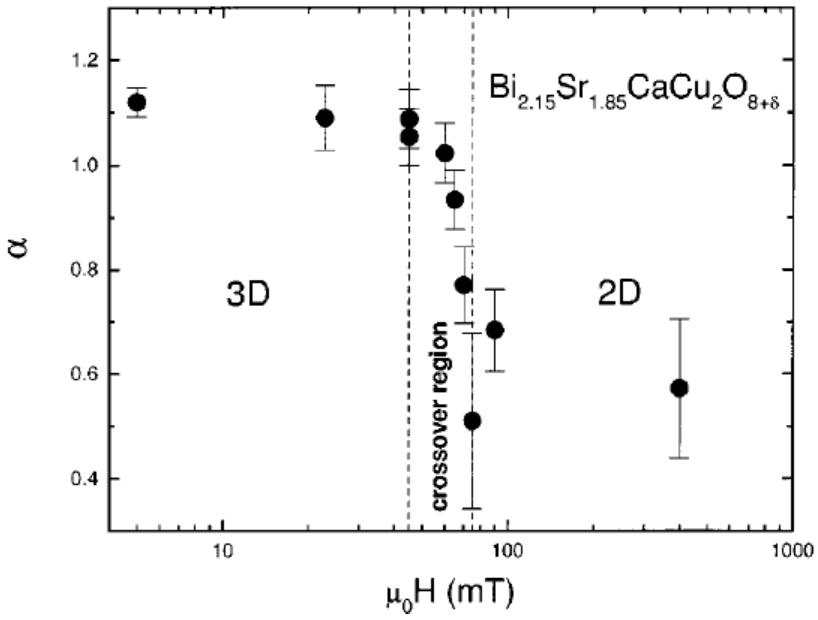

Fig. 7-23:Magnetic-field dependence of the skewness parameter α in single crystal $Bi_{2.15}Sr_{1.85}CaCu_2O_{8+\delta}$ after field cooling at T=5K. The sharp drop in α at $\mu_0 H \sim 50$ mT is attributed to a 3D to 2D crossover in the vortex lattice. From S.L. Lee et al. Phys. Rev. Lett. **71**, 3862 (1993).

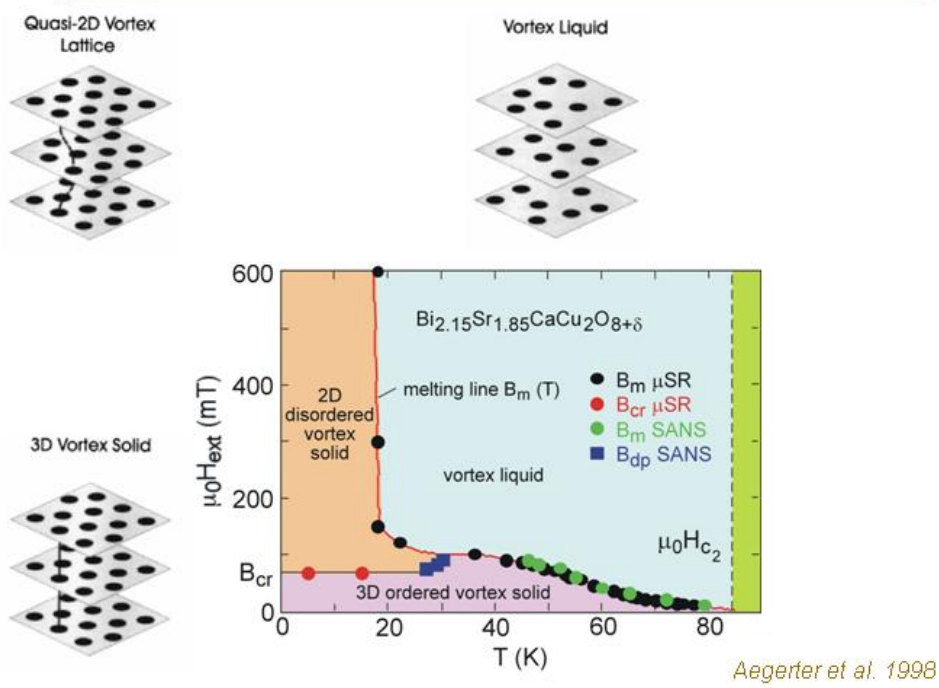

Fig. 7-24: Phase diagram of the vortex state of BSCCO, determined from μSR and small angle neutron scattering experiments (SANS).

7.8 Coexistence of magnetism and superconductivity

Example : $YBa_2Cu_3O_{6+x}$ (ref. S. Sanna et al., Phys. Rev. Lett. **93**, 207001 (2004))
(x Oxygen give h=x/6 holes per Cu planar atom)
Coexistence of magnetic (AF order and correlations) and superconducting phases can be investigated by a combination of ZF and TF (in vortex state) measurements.

ZF:

$$A_z(t) = a_L G_z(t) + a_T G_x(t)\cos(\gamma_\mu \left|\vec{B}_l\right| t)$$

$$a_L + a_T = a_{ZF}$$

$\vec{B}_l$: local field

for a homogeneous magnetic (polycrystalline) sample:

$$\frac{a_L}{a_{ZF}} = \frac{1}{3} \quad \text{and} \quad \frac{a_T}{a_{ZF}} = \frac{2}{3}$$

if only part of the sample is magnetic:

$$\frac{a_L}{a_{ZF}} > \frac{1}{3} \quad \text{and} \quad \frac{a_T}{a_{ZF}} < \frac{2}{3}$$

The volume fraction is given by:

$$f_{AF} = \frac{3}{2}\frac{a_T}{a_{ZF}} = \frac{3}{2}(1 - \frac{a_L}{a_{ZF}})$$

TF in the vortex state:

$$A_x(t) = a_{TF} G_x(t)\cos(\gamma_\mu B_\mu t)$$

$$G_x(t) = e^{-\frac{(\sigma_{sc}^2 + \sigma_n^2)t^2}{2}}$$

$$B_\mu = \mu_0 H(1+\chi) \quad \text{and} \quad \chi<1$$

σ_n is the contribution of the nuclear moments

The volume fraction is given by:

$$f_{SC} = \frac{a_{TF}}{a_0} \quad \text{where } a_0 \text{ is obtained at } T>T_c$$

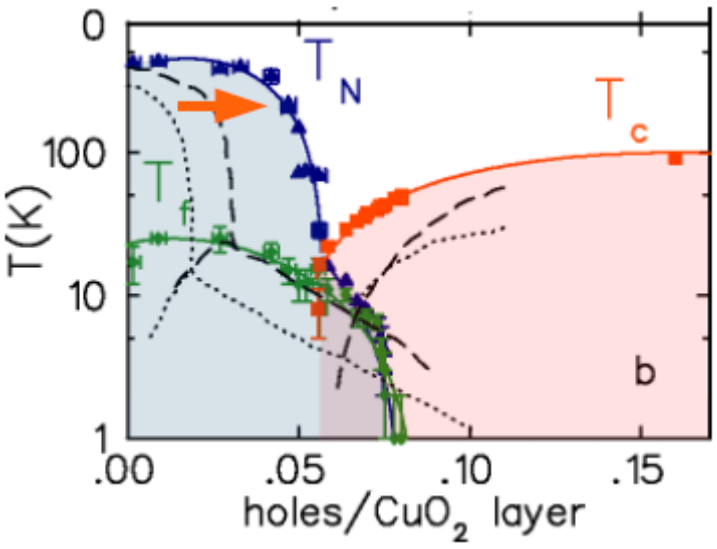

Fig. 7-25: Phase diagram of $YBa_2Cu_3O_{6+x}$. Solid lines are guides to the eye, dashed $Y_{1-y}Ca_yBa_2Cu_3O_{6+x}$) and dotted ($La_{2-x}Sr_xCuO_4$) lines from C. Niedermayer et al., Phys. Rev. Lett. **80**, 3843 (1998).

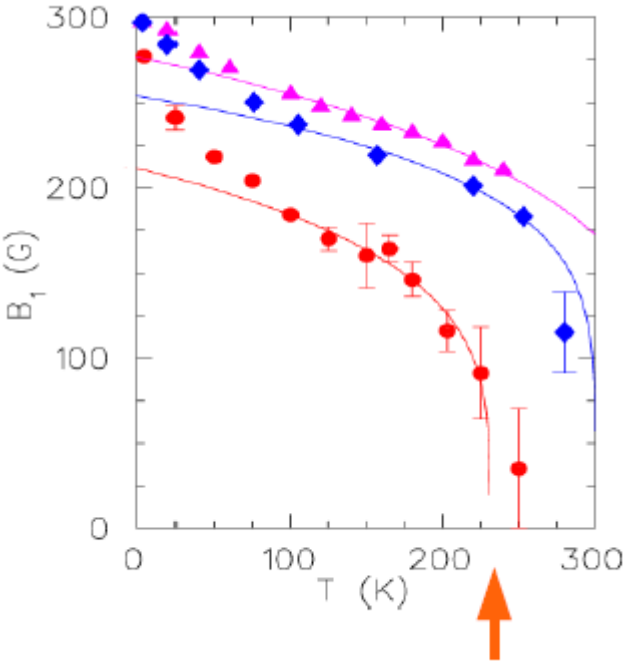

Fig. 7-26: Local field vs T at different doping x.

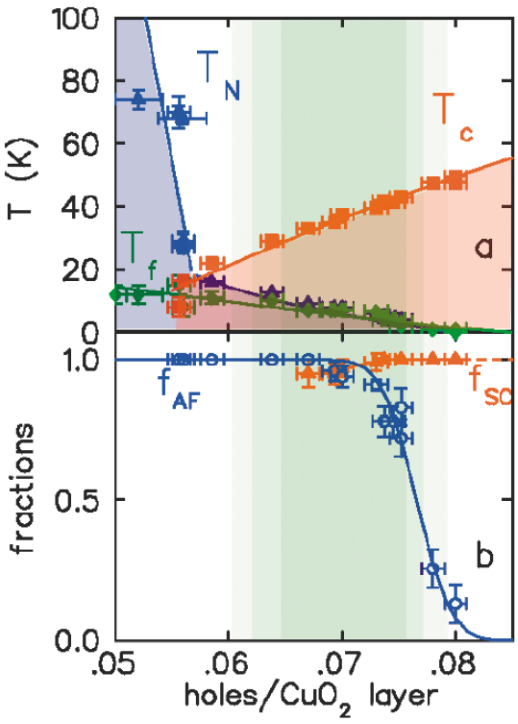

Fig. 7-27: (a) magnetic transition temperatures ▲ from a_L/a_{ZF}, ◆ from $1/T_1$ and sc critical temperature T_c, vs hole concentration *h*; three samples show a distinct $T_N > T_f$.
(b) Muon volume fractions vs *h*: AF (○ at T=0 K) and SC (▲, for $T_f < T < T_c$). Lines in (a), (b) are guides to the eye.

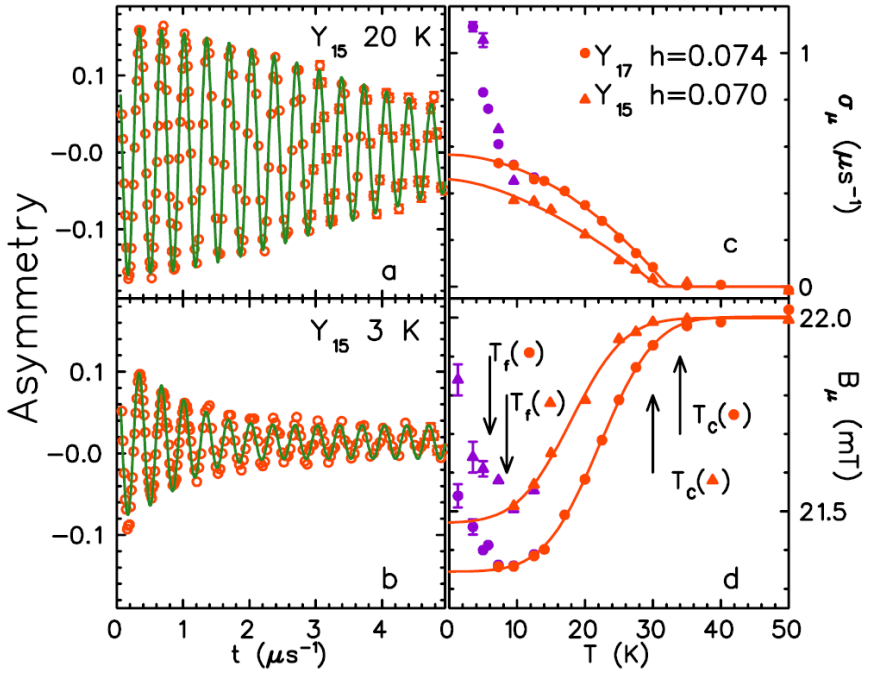

Fig. 7-28: TF μSR data ($\mu_0 H = 22$ mT). Asymmetry (a) for $T_f < T = 20\ K < T_c$ and (b) for $T = 3K < T_f$ in sample Y15; solid curves are best fits to a Gaussian damped precession. (c) Relaxation rate σ_{sc} (here labelled σ_μ) and (d) internal field B_μ from the best fits for samples Y15 and Y17.

Determining the electronic phase diagram of the $LaO_{1-x}F_xFeAs$ superconductor

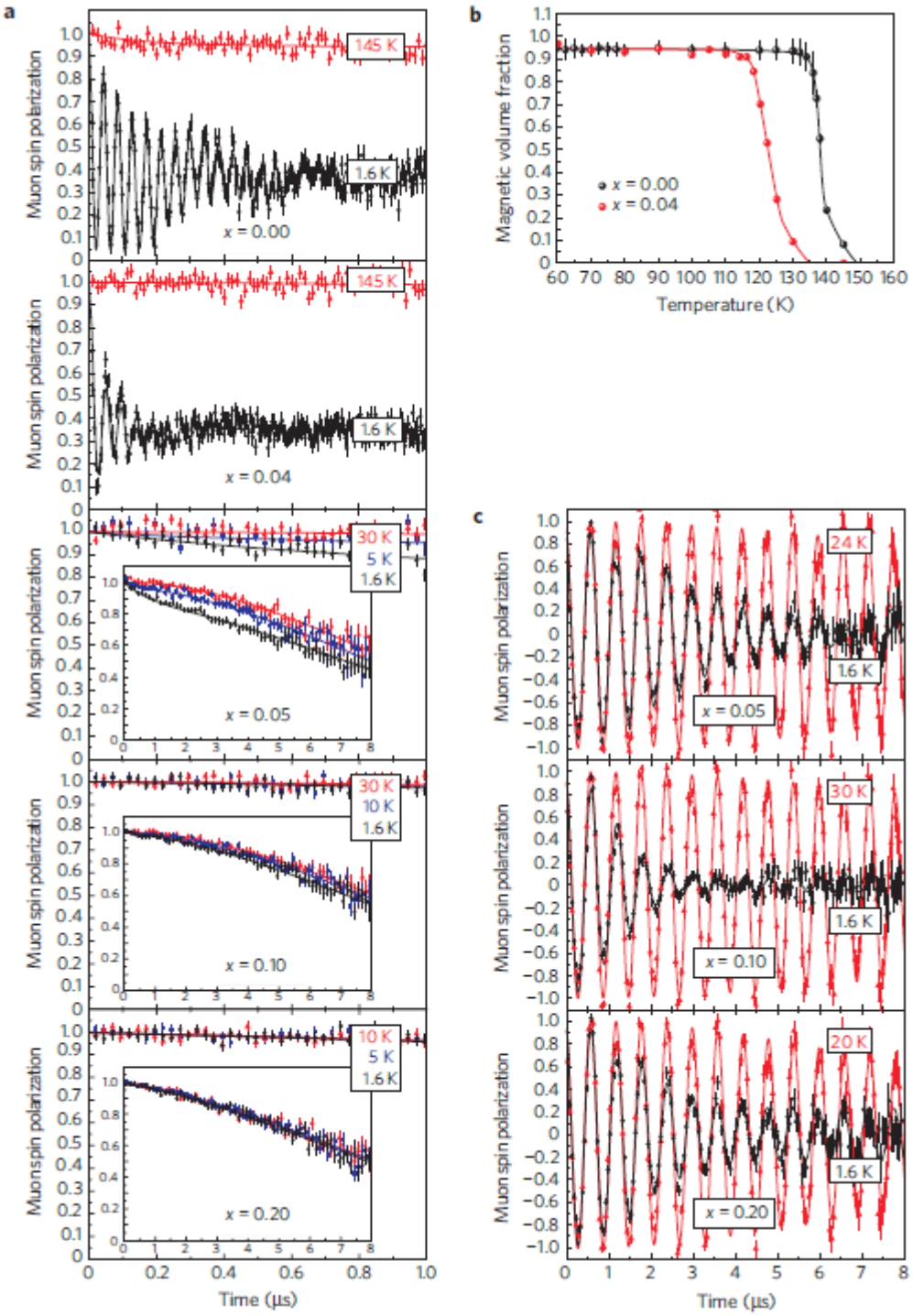

Fig. 7-29: a) Typical zero-field μSR spectra. Only for x≤0.04 a spontaneous muon spin precession indicative of long-range-ordered magnetism is observed. For x≥0.05 a paramagnetic signal is observed down to the lowest temperatures. For *x*=0.05 a weak electronic relaxation typical for diluted static magnetism is detected below 5 K in <30% of the signal (visible on the long timescale in the inset). For x≥0.075 the μSR data prove that no static magnetism is present. b), Temperature dependence of the magnetic volume fraction for *x*=0 and 0.04. Both samples show a transition to a 100% magnetic volume fraction. The ~ 5% non-magnetic signal is attributed to muons stopping in the sample holder. c) Typical

transverse-field μSR spectra measured in an external field of 0.07 T (for clarity shown in a rotating reference frame with frequency 7.8 MHz). The additional Gaussian relaxation due to the formation of the flux-line lattice in the superconducting state is clearly observed below T_C. Note that for x=0.20 a signal fraction of 15% does not show this additional relaxation, indicating the presence of a non-superconducting volume fraction (from H. Luetkens et al., Nature Materials **8**, 305 - 309 (2009)).

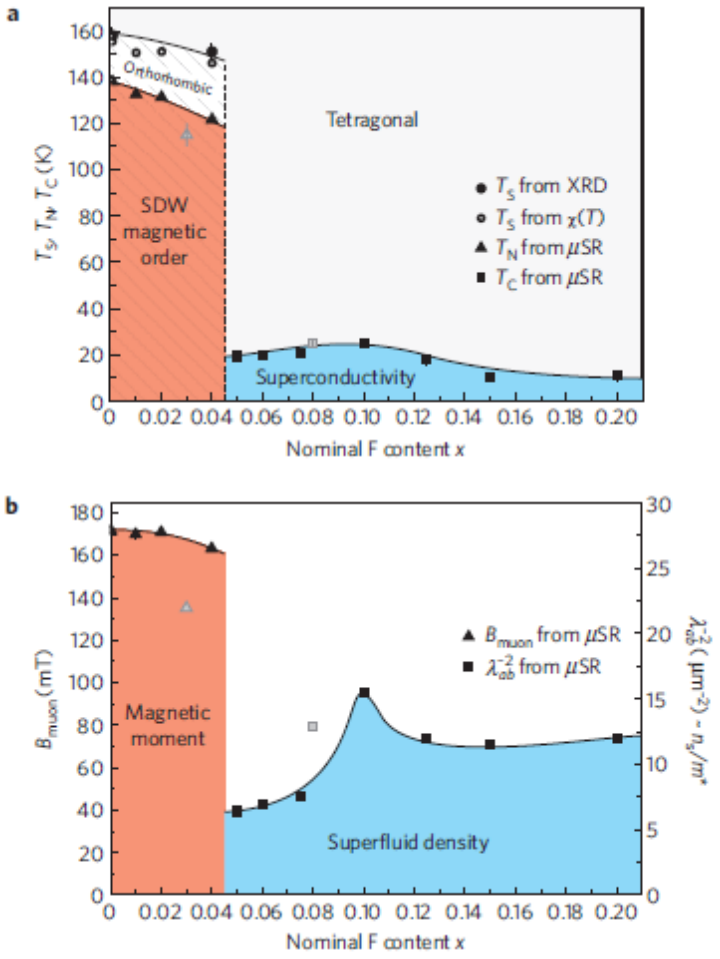

Fig. 7-30: a) The doping dependence of the magnetic and superconducting transition temperatures determined from the μSR experiments. Also shown are the tetragonal-to-orthorhombic structural transition temperatures T_S determined directly from X-ray diffraction and from susceptibility measurements, which show a kink and subsequent strong reduction below T_S. b) The doping dependence of the low-temperature saturation value of the magnetic order parameter $B_{muon}(T\rightarrow 0)$ and of the superfluid density n_s/m^* measured through $1/\lambda_{ab}^2(T\rightarrow 0)$ in transverse-field μSR experiments. The grey data points at x=0.03 and 0.08 are taken from another work. The error bars indicate one standard deviation.

8. Muonium in semiconductors

In semiconductors and insulators the positive muon can capture an electron and form stable muonium. This state corresponds to a non-ionized hydrogen atom in the solid. With muonium spin rotation it is possible to study electronic states and position of an isolated hydrogen atom (impurity) in the solid. Muonium states have been detected in various semiconductors and insulators. Muon spin rotation spectroscopy has played a pioneering role in the discovery and identification of intrinsic hydrogenlike states in semiconductors. Detailed investigations have been performed in SiO_2, in the pure semiconductors Si, Ge, in diamond, in the semiconductors of the group (III-V) and (II-VI) and in various oxides.
Contrary to the muon in magnetic substances or superconductors, the positive muon in a semiconductor is an active probe. With this we mean that we use μSR spectroscopy to investigate a state, which is created by the muon itself.

We consider in the following as examples Si and Ge. One can distinguish different states via the hyperfine interaction. In Si and Ge we find at low temperatures three states:
1) Normal muonium with a strong hyperfine interaction, 2) so called anomalous muonium with a weak anisotropic interaction and 3) to about 10% free or diamagnetic muon. (Ref. B. Patterson, Rev. Mod. Physics **60**, 69 (1988) and S.F.J. Cox, Rep. Prog. Phys. **72**, 116501 (2009)).

8.1 Muon-spin precession in normal muonium in transverse field

Normal muonium has an isotropic hf-interaction. The Hamilton function of the hyperfine interaction in muonium is given by Eq. [3-34] (chapter 3), where we have determined the eigenstates and energy eigenvalues in a magnetic field (Eq. [3-37] to [3-39], Breit-Rabi diagram).

Experimentally, we measure muon spin precession frequencies that correspond to transition frequencies between different muonium levels.

Consider the transverse field experiment. At t=0 the muon spin is parallel to the x-direction: $\vec{B}_{ext} \| z \perp \vec{I}(0) \| x$.
In this case we must calculate the expectation value of $\sigma_x = 2I_x$ ([I_x]=[1]). The Pauli matrix σ_x acts only on the muon part of the wave function.

The captured electrons forming muonium are unpolarized, so their spin is with 50% probability parallel or antiparallel to the muon spin.

This state can be represented by an incoherent superposition of two wave functions:

$$|\Psi_1(0)\rangle = \frac{1}{\sqrt{2}}\left[|M_S = \frac{1}{2}, M_I = -\frac{1}{2}\rangle + |M_S = \frac{1}{2}, M_I = +\frac{1}{2}\rangle\right]$$

$$|\Psi_2(0)\rangle = \frac{1}{\sqrt{2}}\left[|M_S = -\frac{1}{2}, M_I = -\frac{1}{2}\rangle + |M_S = -\frac{1}{2}, M_I = +\frac{1}{2}\rangle\right]$$

The wave functions at any time t are a superposition of eigenstates |i> (given in [3-39]) with their corresponding phase:

$$|\Psi_{1,2}(t)>=\sum_{i=1}^{4} c_i^{1,2}\,|i>\, e^{-i\frac{E_i}{\hbar}t} \qquad [8\text{-}1]$$

The constants have to be determined from the initial conditions and from the normalization.

Initial conditions:

$$<\sigma_x>=1,<\sigma_y>=0,<\sigma_z>=0 \qquad [8\text{-}2]$$

The (observed) polarization in x-direction is then given by following expression:

$$\begin{aligned} P(t) &=<\Psi_1(t)\,|\,\sigma_x\,|\,\Psi_1(t)>+<\Psi_2(t)\,|\,\sigma_x\,|\,\Psi_2(t)> \\ &=\sum_{j,k=1}^{4} c_k^{1*}c_j^{1}e^{-i\frac{(E_j-E_k)}{\hbar}t}<k\,|\,\frac{1}{2}(\sigma_+ +\sigma_-)\,|\,j>+\sum_{j,k=1}^{4} c_k^{2*}c_j^{2}e^{-i\frac{(E_j-E_k)}{\hbar}t}<k\,|\,\frac{1}{2}(\sigma_+ +\sigma_-)\,|\,j> \end{aligned} \qquad [8\text{-}3]$$

This expression can be evaluated using the explicit expression for the eigenstates (see [3-39]). P(t) can be also evaluated within the density matrix formalism, which is useful in case of partial (or zero) polarization (as is the case here for the electrons) (see for instance E. Karlsson, Solid State Phenomena as seen by Muons, Protons and Excited nuclei, Oxford Science Publications 1995).

Some important properties of [8-3]:

- P(t) depends only on transition frequencies.
- Selection rules of the matrix elements: the terms in the sum with j=k are zero since σ_+,σ_- do not possess diagonal elements.
- From the explicit expression for |1>, |2>, |3> and |4> (Eq. [3-39]) we note that the transitions 1→2 and 3→4 do not contribute to P(t).

The result of the calculation gives for [8-3]:

$$P(t)=\frac{1}{2}\left[\cos^2\beta(\cos\omega_{13}t+\cos\omega_{24}t)+\sin^2\beta(\cos\omega_{14}t+\cos\omega_{32}t)\right] \qquad [8\text{-}4]$$

$$\begin{aligned} \cos\beta &= \frac{1}{\sqrt{2}}\left[1+\frac{x}{(1+x^2)^{1/2}}\right]^{1/2} \\ \sin\beta &= \frac{1}{\sqrt{2}}\left[1-\frac{x}{(1+x^2)^{1/2}}\right]^{1/2} \end{aligned} \qquad [8\text{-}5]$$

where $x = \frac{(g_e|\mu_B| + g_\mu \mu_B^\mu)B}{A\hbar^2} \equiv \frac{B}{B_0}$ [8-6]

(for vacuum muonium B_0=0.158 T).

Special cases

A) The transition frequencies ω_{24} and ω_{14} are generally too large, to be resolved with conventional spectrometers with time resolution of about 0.5 ns (rms).

Therefore:

$$< \cos \omega_{24} t >=< \cos \omega_{14} >= 0$$

so that:

$$P(t) = \frac{1}{2}\left[\cos^2 \beta \cos \omega_{13} t + \sin^2 \beta \cos \omega_{32} t) \right] \quad [8\text{-}7]$$

This equation can be written in the following form:

$$P(t) = \frac{1}{2} \cos \omega_+ t \cos \omega\_ t + \frac{1}{2} \frac{x}{\sqrt{1+x^2}} \sin \omega_+ t \sin \omega\_ t$$
$$\omega_\pm = \frac{\omega_{32} \pm \omega_{13}}{2} \quad [8\text{-}8]$$

which gives a beat frequency (see Fig. 8-1).

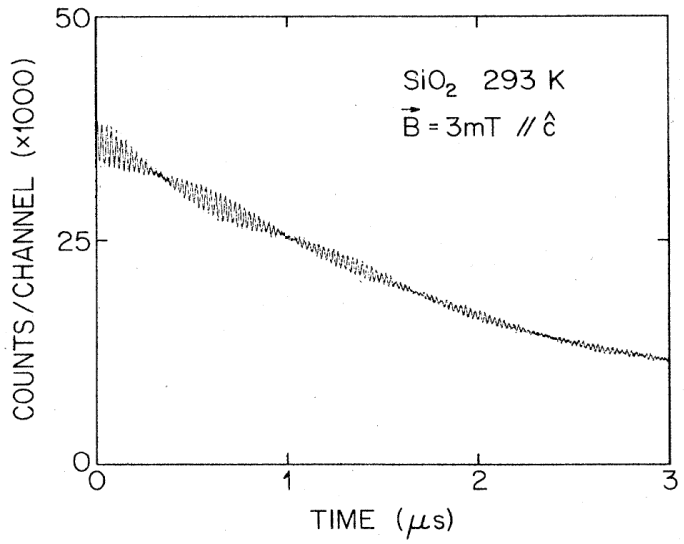

Fig. 8-1: TF-μSR spectrum in quartz at room temperature. Note the beating between frequency ν_{13} and ν_{32}.

The corresponding frequency spectrum is:

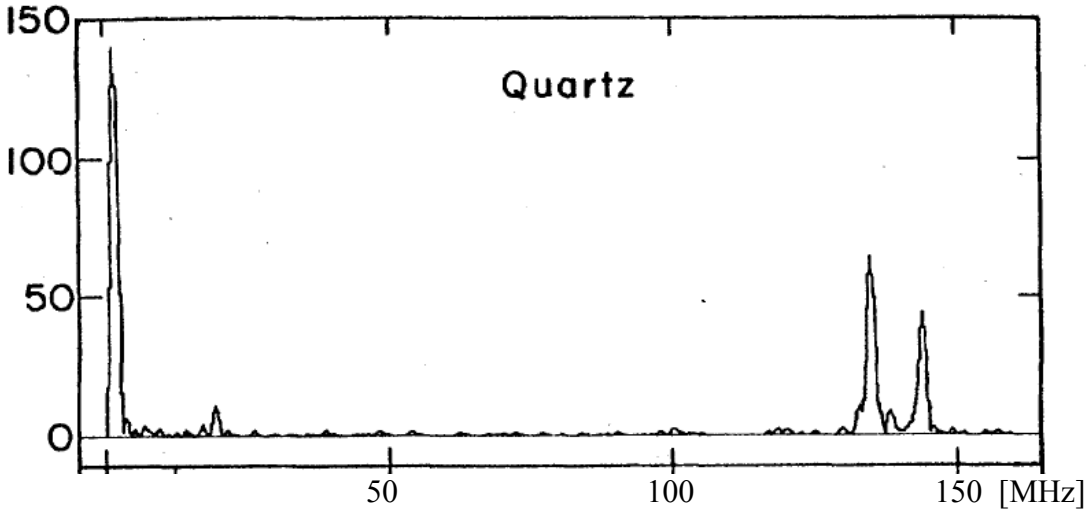

Fig. 8-2: TF frequency spectrum in quartz (10 mT) at room temperature. Visible are the μ^+ precession frequency and that of the isotropic muonium (frequency pair ν_{13} and ν_{32} centered around 140 MHz).

From the frequency splitting we can determine the hyperfine constant A.
With the help of Eq. [3-37] we find an expression for A or the hyperfine frequency ν_{hf}, which depends only on experimental quantities:

$$h\nu_{hf} = \hbar^2 A = \frac{1}{2}\left[\frac{(h\nu_{13} + h\nu_{32} + 2h\nu_\mu)^2}{h\Delta\nu} - h\Delta\nu\right] \qquad [8\text{-}9]$$

$$\Delta\nu = \nu_{32} - \nu_{13}$$

B) If the applied field is very small (x<<1) one can further simplify [8-7] (see also Fig. 8-6a):

$$\cos^2\beta \cong \frac{1}{2}, \sin^2\beta \cong \frac{1}{2}$$

$$\omega_{32} \cong \omega_{13} \equiv \omega_{Mu} = \gamma_{Mu}^T B = \frac{1}{2}(\gamma_e - \gamma_\mu)B$$

$$\omega_- \cong 0$$

[8-7] becomes

$$P(t) = \frac{1}{2}\cos\omega_{Mu} t \qquad [8\text{-}10]$$

This means that in very small TF fields (< 0.5 mT), muonium shows only half of the polarization amplitude (corresponding to the precession of the $M_F = \pm 1$ components in the triplet state). In this case the muon spin polarization precesses with a Larmor frequency $\omega_{Mu} \cong 103\ \omega_\mu$ (with opposite sense of rotation of the precession of a "free" muon). This allows distinguishing the charged (μ^+) from the uncharged state (Mu).

B) No applied field, isotropic hyperfine interaction.

In this case there is only one hyperfine frequency, which in free muonium (corresponding to vacuum muonium) is very high ($\omega_0/2\pi = 4.46$ GHz). Generally it is observable only in systems with very good time resolution.

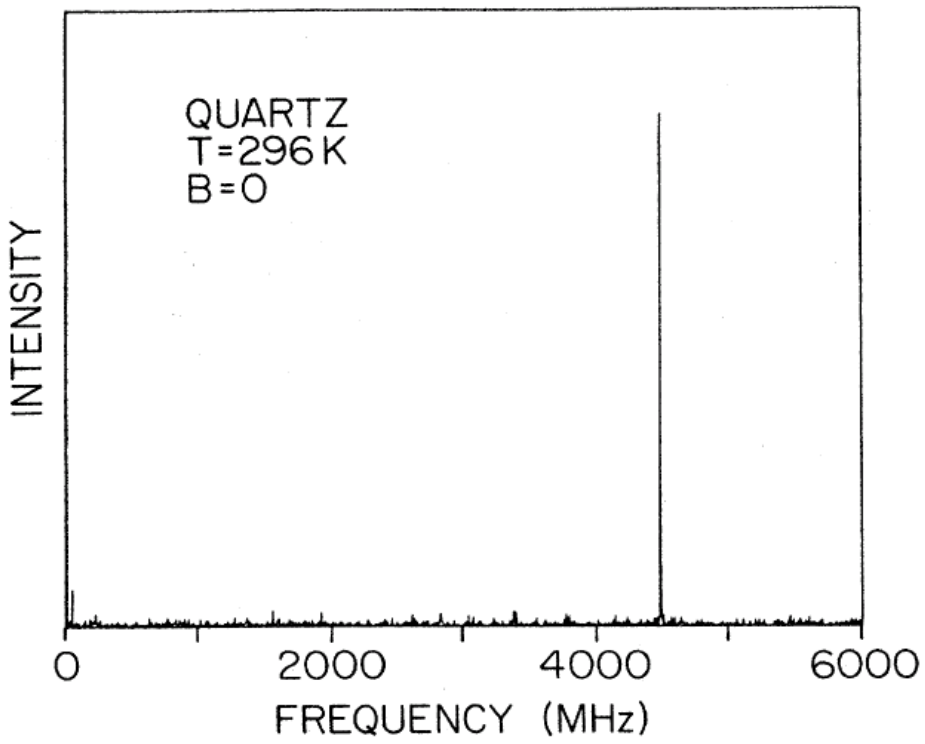

Fig. 8-3: A zero-field μSR spectrum of quartz at room temperature. The Mu hyperfine frequency is close to the vacuum value (4.463 GHz). The FWHM time resolution of this experiment is 110 ps. From E. Holzschuh et al., Helvetica Physica Acta **54**, 552 **(**1981).

Example of muonium spectroscopy of synthetic quartz crystal in 8 T with a high resolution spectrometer. The High Field μSR instrument HAL-9500 at PSI, which uses Avalanche Photo Diodes (APD's) instead of the conventional photomultipliers to transform and amplify the scintillator signal, has a very good time resolution (variance σ=58 or 80 ps, depending on the readout system). This allows spectroscopy of muonium in high fields.

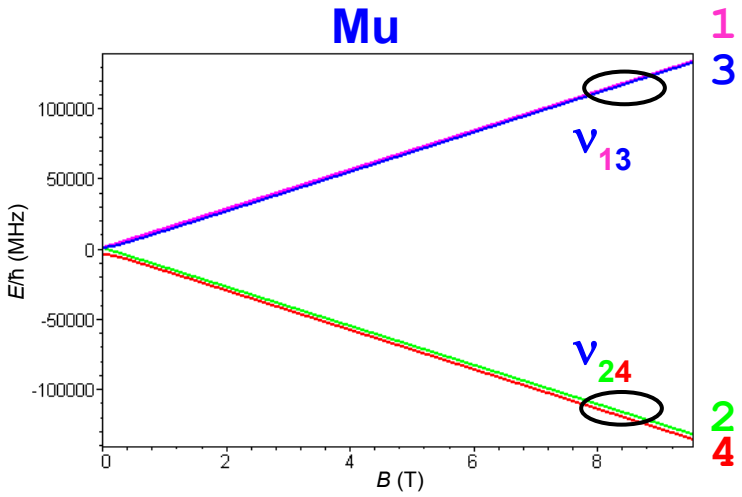

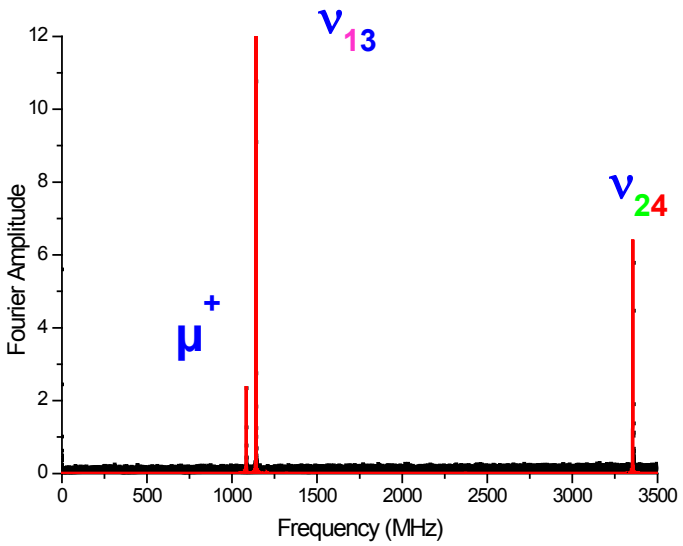

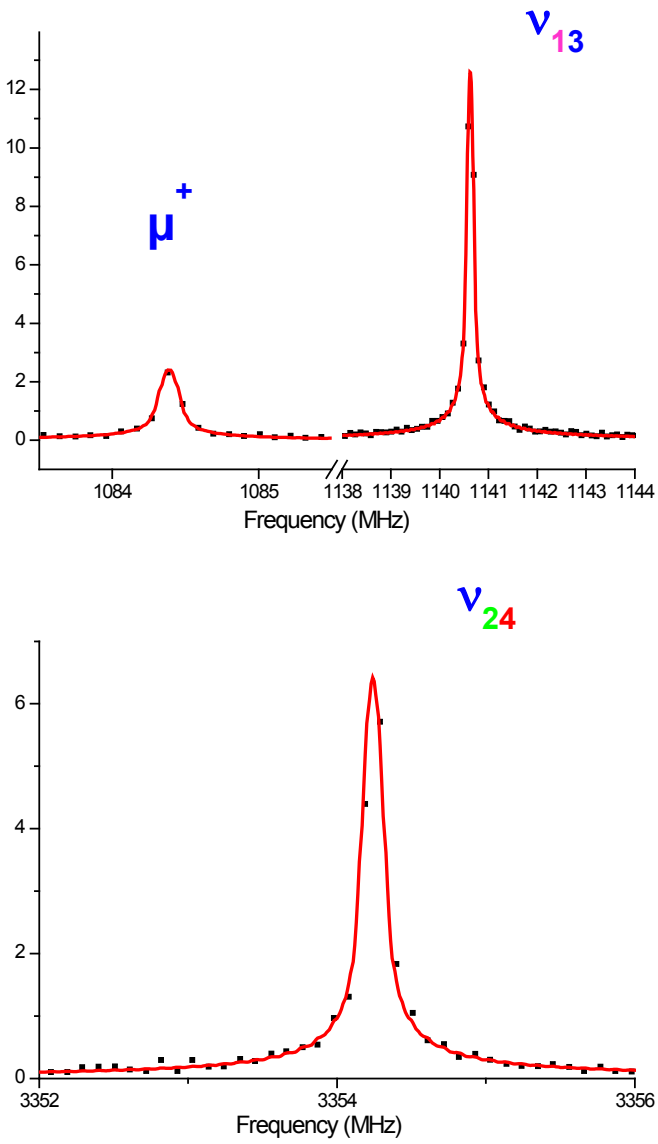

Fig. 8-4: Breit-Rabi diagram and transitions in a synthetic quartz crystal measured with the HAL-9500 high resolution spectrometer at PSI in a 8 T field (R. Scheuermann, private communication).

In inert non conducting substances muonium can exist in a state which is very similar to the atomic state. In this case it is localized in interstitial lattice positions. In alkali fluorides the hyperfine coupling is slightly higher than in vacuum muonium. This corresponds to a slightly compressed wave function with higher spin density at the muon site. Generally the hyperfine coupling is smaller. In some semiconductors it is even much smaller than in the free state. For instance in the elementary semiconductors of the group IV the electron spin density at the muon site is only 50% of the value in the free atom.

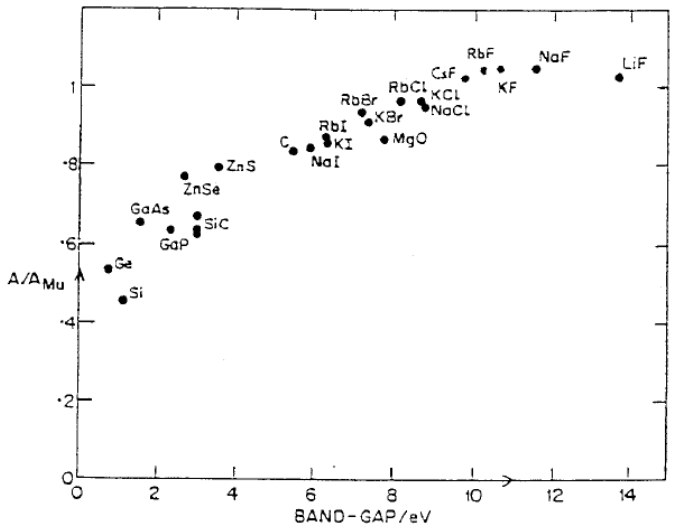

Fig. 8-5: Hyperfine constant for interstitial muonium in semiconductors and dielectrics. The graph shows the correlation between spin density at muon site and band-gap of host material (S.F.J. Cox J. Phys. C: Solid State Phys. **20**, 3187 (1987)).

8.2 Anomalous muonium

In several semiconductors an additional muonium state has been found with a hyperfine constant which is axially symmetric around the [111] crystal axis. This state is called „anomalous muonium“or „anisotropic muonium“ and indicated with Mu^*.

In general we can write the Hamilton function of the hyperfine interaction as follows:

$$H = -\vec{\mu}_e \cdot \vec{B} - \vec{\mu}_\mu \cdot \vec{B} + \vec{I}\vec{A}\vec{S} \qquad [8\text{-}11]$$

(Compare with [3-34] Chapt. 3. Muonium and muonium spectroscopy).

For anomalous muonium the assumption of an axial symmetric hyperfine tensor is justified. [8-11] can be written as:

$$H = -\vec{\mu}_e \cdot \vec{B} - \vec{\mu}_\mu \cdot \vec{B} + A_\perp (I_x S_x + I_y S_y) + A_\parallel I_z S_z \qquad [8\text{-}12]$$

In the special case $\vec{B} \parallel \hat{z} \parallel [111] - \text{axis}$ (<111> symmetry axis)

$$H_{Mu^*} = -\mu_e^z \cdot B_z - \mu_\mu^z \cdot B_z + \frac{A_\perp}{2}(I_+S_- + I_+S_-) + A_\parallel I_z S_z \qquad [8\text{-}13]$$

The eigenvalues of this Hamilton operator can be calculated as in the isotropic case. We obtain:

$$E_1 = \frac{A_\parallel \hbar^2}{4} + \frac{1}{2}(g_e|\mu_B| - g_\mu \mu_B^\mu)B$$

$$E_2 = \frac{A_\parallel \hbar^2}{4} - \frac{1}{2}(g_e|\mu_B| - g_\mu \mu_B^\mu)B$$

$$E_3 = -\frac{A_\parallel \hbar^2}{4} + \frac{A_\perp \hbar^2}{2}\sqrt{1+x^2}$$

$$E_4 = -\frac{A_\parallel \hbar^2}{4} - \frac{A_\perp \hbar^2}{2}\sqrt{1+x^2} \qquad [8\text{-}14]$$

with

$$x_\perp = \frac{(g_e|\mu_B| + g_\mu \mu_B^\mu)B}{A_\perp \hbar^2} \qquad [8\text{-}15]$$

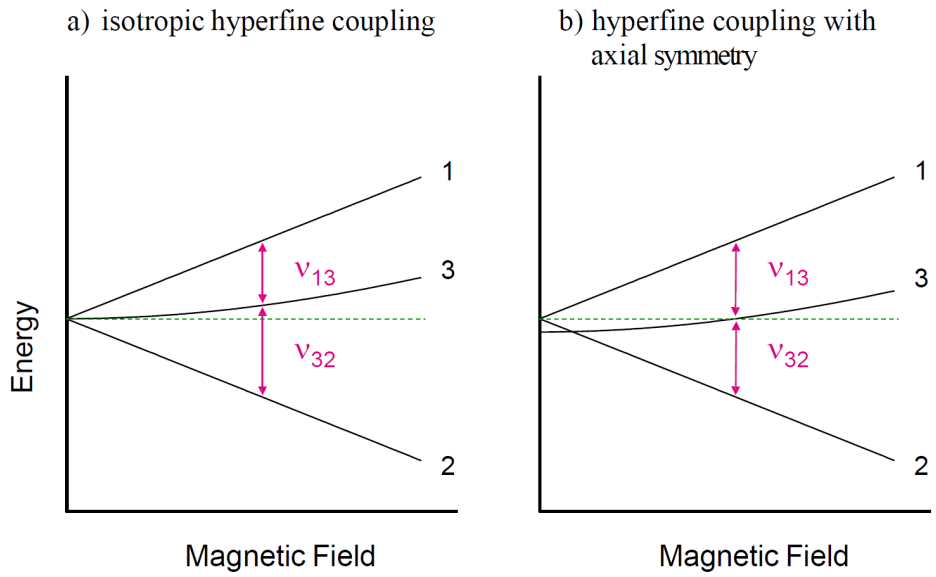

Fig. 8-6: Energy levels of muonium in low magnetic fields. a) Isotropic muonium. b) Anosotropic muonium with axial symmetry.

The hyperfine interaction of Mu^* is generally smaller than that of Mu

$\frac{A_\perp(Mu^*)}{A(Mu)} \cong 0.05$ in Si. Furthermore it is anisotropic $\frac{A_\parallel}{A_\perp} \cong 0.2$ in Si. The precession frequencies depend not only on the B-field strength but also on its direction (see Fig. 8-7, and Fig. 8-8 bottom).

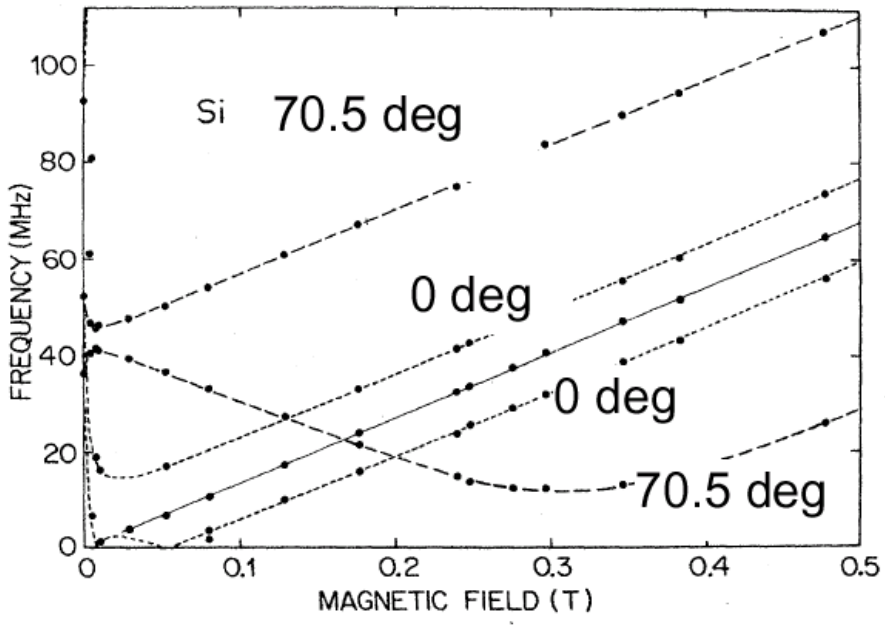

Fig. 8-7: The field-dependent μ^+ and Mu* precession frequencies in Si. The field was directed along the [111] axis. The solid line shows the expected dependence of the diamagnetic μ^+ signal, and the finely and coarsely dashed curves are fits to the axially symmetric spin Hamiltonian [8-13] for angles between the field and Mu* symmetry axis of 0 and 70.5^0, respectively. From B. Patterson et al., Phys. Rev. Lett. **40**, 1347 (1978).

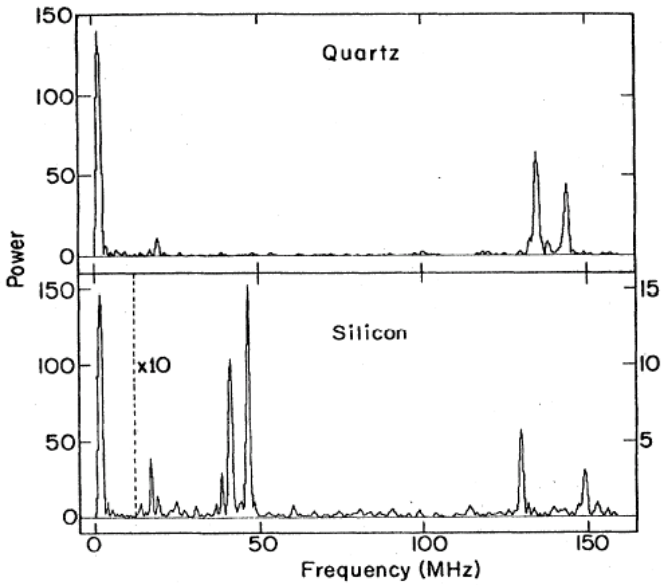

Fig. 8-8: Transverse-field μSR frequency spectra taken at 10 mT in quartz at room temperature and [111] Si at 77 K showing the precession components from diamagnetic μ^+ ($\nu_{\mu+}$=1.36 MHz) and isotropic Mu (the pair ν_{12} and ν_{23} centered on 140 MHz). Note the larger Mu splitting in Si, indicating a weaker hyperfine interaction and the presence in Si but not in quartz of Mu* precession lines (ν_{12} and ν_{34}, $\theta=70.5^0$, at 41 and 46 MHz). From J. Brewer et al., Phys. Rev. Lett., **31** 143 (1973).

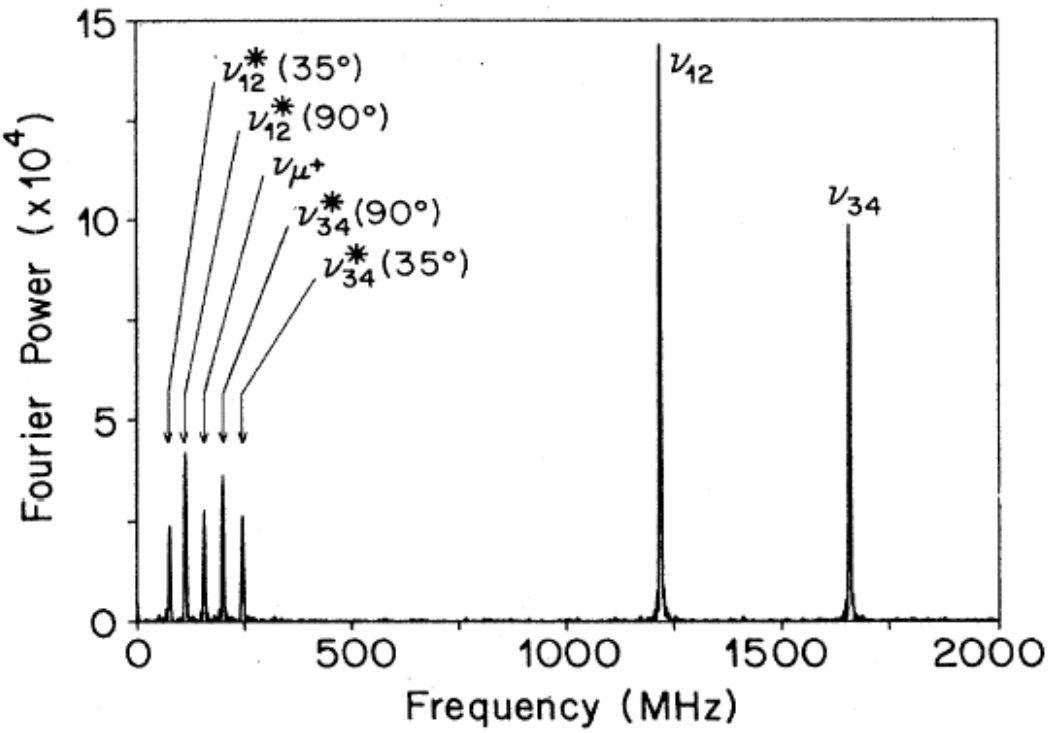

Fig. 8-9:A μSR frequency spectrum taken with a high-time-resolution apparatus in high-resistivity GaAs at 10K with a 1.15 T field applied along the [110] axis. Note the two Mu lines ν_{12} and ν_{34}, the Mu* lines $\nu_{ij}^{*}(\theta)$ (θ is the angle between the [111] Mu* symmetry axis and the applied field), and the diamagnetic muon line $\nu_{\mu+}$. From R. Kiefl et al.Phys. Rev. B **32**, 530 (1985).

Note that in our notation of Eq. [3-37] ν_{12} ,ν_{23} and ν_{34} in Fig 8-8 and 8-9 are designed as ν_{13} ν_{32} und ν_{24}.

TABLE VIII. Fractions of incoming muons forming the various muon states in undoped diamond and zincblende semiconductors at low temperatures.

Sample	f_{μ^+} (%)	f_{Mu^*} (%)	f_{Mu} (%)	$f_{missing}$ (%)
Diamond	8.1 (3.0)	22.7 (8)	68.9 (1.0)	0.3 (3.3)
Si	7.5 (4)	36.8 (1.8)	61.0 (7.6)	−5.3 (7.8)
Ge[a]	10 (2)	8 (4)	72 (10)	10 (11)
β—SiC[b]	65 (12)		30 (5)	5 (19)
α—Sn[c]	~100			
GaP[d]	11 (1)	18 (3)	72 (10)	−1 (11)
GaAs[d]	9 (1)	35 (5)	63 (6)	−7 (8)
GaSb[e]	56 (1)			44 (1)
InP[e]	75 (3)			25 (3)
InAs[e]	106 (2)			−6 (2)
InSb[e]	72 (2)			28 (2)
ZnS	20 (1)		19 (3)	61 (3)
ZnSe	36 (1)		11 (2)	53 (2)
CdS	92 (3)			8 (3)
CdTe	69 (2)			36 (2)
CuCl[f]	16 (4)		66 (3)[I]	
			9.9 (8)[II]	8 (5)
CuBr[f]	23 (4)		66 (5)[I]	
			5.8 (8)[II]	5 (6)
CuI[f]	18 (8)		72 (3)	10 (9)

TABLE IX. Low-temperature hyperfine parameters for anisotropic Mu* ($A_\parallel$, $A_\perp$) and isotropic Mu (A) in diamond and zincblende semiconductors, the maximum temperatures of their observation, and observed transitions among the muon states. The hyperfine parameters for the III-V and II-VI compounds refer to 10 K, and the other values are extrapolations to 0 K. The hyperfine frequency of Mu in vacuum is 4463.302 88 (16) MHz (Mariam *et al.*, 1982).

Sample	$A_\parallel$ (MHz)[a]	$A_\perp$ (MHz)[a]	A (MHz)	$T^{max}_{Mu^*}$ (K)	T^{max}_{Mu} (K)	Transitions
C	+167.983 (57)[b]	−392.586 (55)[b]	3711 (21)[b]	≥1000[b]	405[c]	Mu→Mu*[c]
Si	16.819 (11)[d]	92.59 (5)[d]	2006.3 (2.0)[e]	165	300[f]	Mu*→μ^+[g]
						Mu→μ^+[g]
Ge	27.269 (13)[d]	131.037 (34)[d]	2359.5 (2)[e]	85[d]	120[h]	(Mu,Mu*)→μ^+[i]
β—SiC					≥22[j]	μ^+→Mu?[j]
GaP	219.0 (2)[k]	79.48 (7)[k]	2914 (5)[k]	100	240	
GaAs	217.8 (2)[k]	87.74 (6)[k]	2883.6 (3)[k]	100	300	Mu*→μ^+
ZnS			3547.8 (3)		≥10	
ZnSe			3456.7 (3)		≥13	
CuCl			1334.23 (8)[II]		60[II]	Mu[I]→Mu[II],
			1212.3 (1)[III]		≥300[III]	Mu[II]→μ^+
CuBr			1403.66 (6)[II]		153[II]	Mu[I]→Mu[III]
			1250.9 (2)[III]		≥300[III]	
CuI			1670.9 (2)[l]		102[l]	

From B. Patterson, Rev. Mod. Physics **60**, 69 (1988)

Muonium states in elemental and III-V compound semiconductors have been found and studied to a great extent. Charged states Mu^+ and Mu^- and two forms of the neutral state Mu^0 have been identified and the interplay of site and charge states is understood. Mu^0 can either be isotropic, when in a symmetric interstitial site such as the tetrahedral site in diamond or zincblende structures (Mu^0_T), or anisotropic when situated at the bond-center site (Mu^0_{BC}). In these semiconductors, isolated H and Mu are known to form deep-level centers.

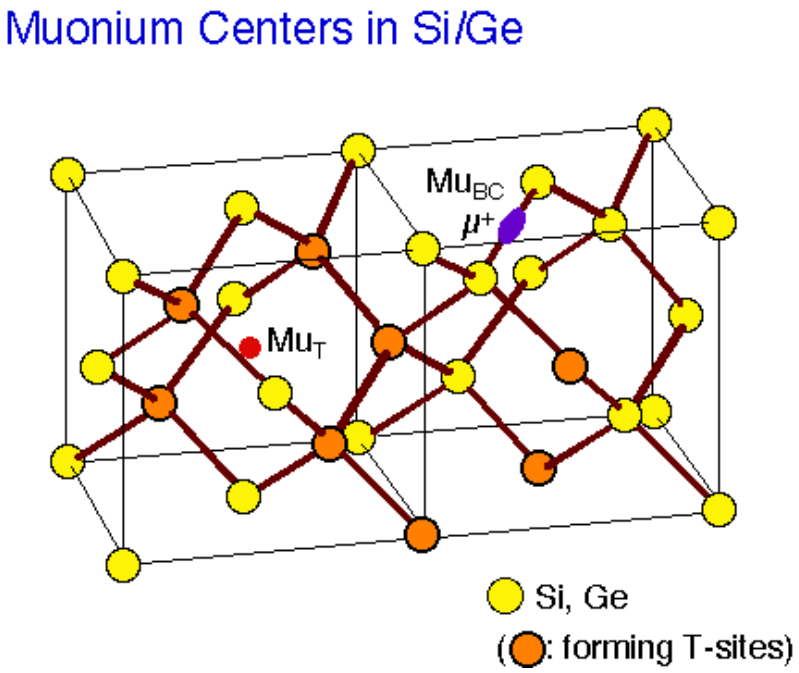

Fig. 8-10: Two different muonium states in Si and Ge.
„Bond Centered muonium" Mu_{BC} (Mu^*) and "tetrahedral muonium" Mu_T .

8.3 Weakly bound muonium (shallow muonium)

More recently, studies of Mu in II-VI semiconductors revealed the existence of a third form of neutral anisotropic Mu^0 in CdS, CdSe, CdTe and ZnO. This state has binding energies characteristic of shallow-level donor centers and is believed to be at the interstitial site anti-bonding to S (Se, Te, or O). Its hyperfine interaction is very weak, amounting to approximately 10^{-4} of the free-atom value. Figure 8-9 shows the μSR signal in CdS, taken over a period of eight muon lifetimes. The Fourier transform of the signal shows five distinct frequencies, indicating an extremely shallow muonium state and providing the first information on this hydrogen-like impurity in the compound (J. M. Gil et al., Phys. Rev. Lett. **83**, 5294 (1999)). In addition to the Larmor precession signal at 1.38 MHz, the Fourier spectrum shows two pairs of lines symmetric around the central line. The outer pair ($\Delta\nu$= 335.7 kHz) and the inner pair ($\Delta\nu$= 214.5 kHz) together with their intensity ratios can be assigned to two orientations of the muonium defect center. The shallow muonium state is described by a hyperfine tensor which can be oriented along definite crystallographically equivalent directions (specific bond directions) which have different orientation with respect to the applied magnetic field.

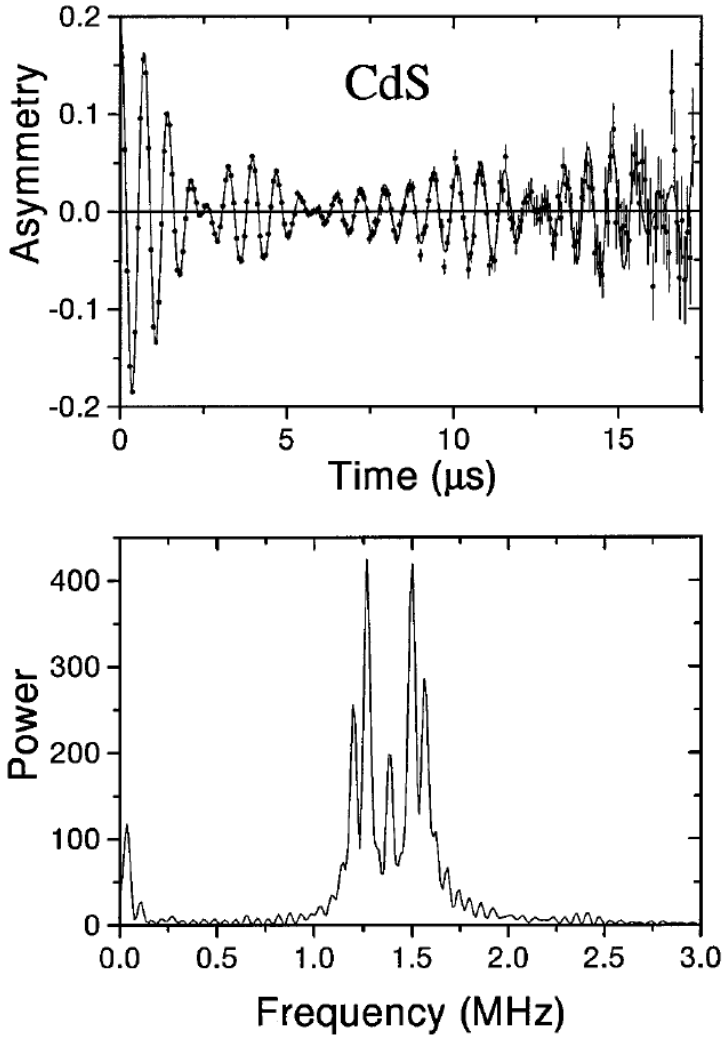

Fig. 8-11: μSR spectrum and its Fourier transform for undoped CdS at 2.1 K (From J.M. Gil et al, Phys. Rev. Lett. **83**, 5294 (1999)). The magnetic field of B =10 mT was parallel to the hexagonal <0001> axis which was also normal to the plane of the disc-like sample. In this geometry, one Cd-S bond direction (suggested to be the symmetry axis of the hyperfine tensor) is at 0^o and three are at 70.6^o to the field direction.

In the high field limit ($A << \gamma_e B/2 = 140$ MHz for B =10 mT) and axial symmetry a simple relation between measured frequencies and hyperfine tensor holds:

$$\Delta\nu = A(\theta) = \left| A_{\parallel} \cos^2\theta + A_{\perp} \sin^2\theta \right| \qquad [8\text{-}16]$$

where $\Delta\nu$ is the separation of two lines symmetrical around the central line, $A(\theta)$ is the hyperfine interaction for a given angle θ (angle between magnetic field and symmetry axis), and $A_{\parallel}$ and $A_{\perp}$ are the hyperfine interaction couplings parallel and perpendicular to the symmetry axis, given by the Cd-S bond direction.
The analysis of the spectrum of Fig. 8-11 yields $A_{\parallel}$ = 335(7) kHz and $A_{\perp}$ =199(6) kHz.

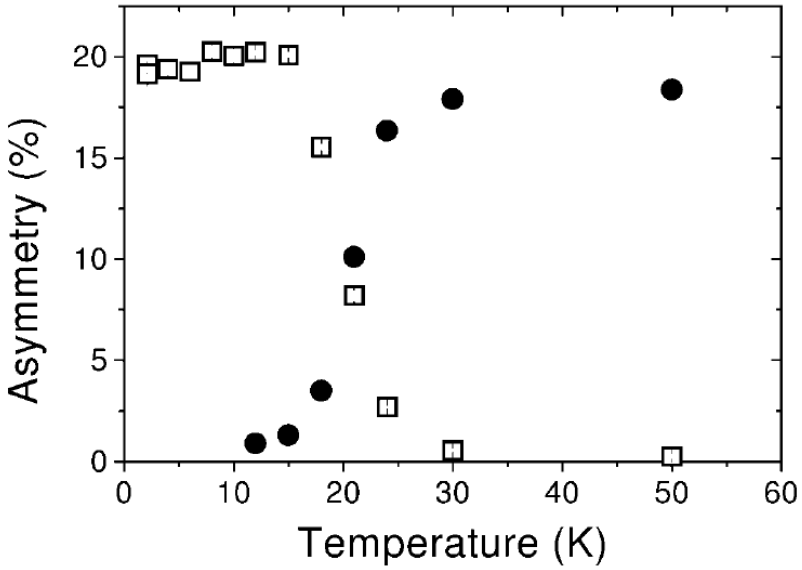

Fig. 8-12: Paramagnetic (Mu) fraction (open squares) and diamagnetic fraction (closed circles) as a function of temperature for CdS at B=10 mT and an angle of 54.7°.

The asymmetry as a function of temperature shows that the diamagnetic line grows at the expense of the paramagnetic lines (Fig. 8-12). This is taken as evidence that the muonium center becomes ionized, i.e., that the electron is no longer bound to the muon. The binding energy of the electron obtained from the activation energy is E_d=18 meV indicating that muonium forms a shallow level with a widely distributed electron wave function as already suggested by the low hyperfine interaction.

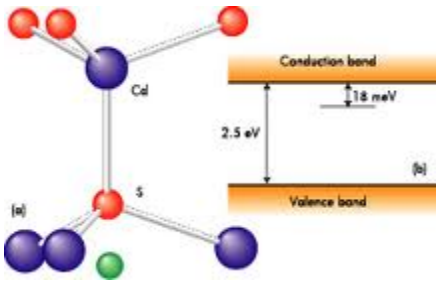

Fig. 8-13: Shallow muonium state in CdS (green circle) and energy level.

9. Thin film and heterostructure studies with low energy muons

Experiments making use of surface muons can't provide depth selective information or study extremely thin samples. With the initial implantation energy of 4.1 MeV, the stopping range of muons in a solid varies from 0.1 mm to 1 mm with a wide distribution of about 20% of the mean value and thus only measurements of the bulk properties can be performed. To extend the scope of the μSR technique to materials, which are of interest in the newly developing technologies of nanomaterials, multilayered thin films, high temperature superconductors etc., spin-polarized muon beams with tunable energies from several eV to several keV and narrow energy distribution are required. These particles can be implanted at well-defined depths ranging from just fractions of a nanometer to a few hundred nanometers (see Fig. 9-1).

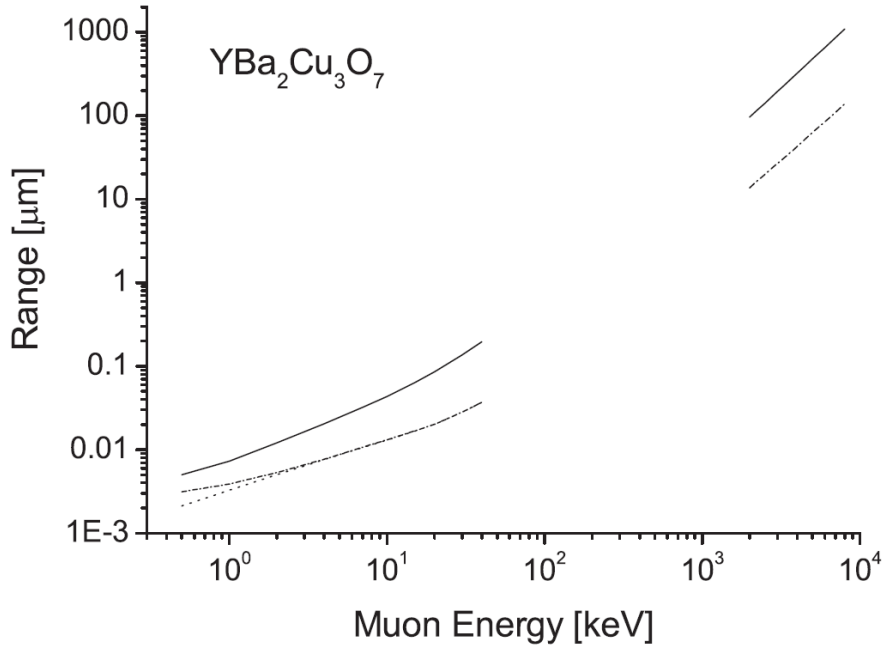

Fig. 9-1: Mean (straight curve) and rms (dash–dotted curve) projected range of positive muons implanted in $YBa_2Cu_3O_{7-\delta}$ as a function of kinetic energy. An absolute energy uncertainty of 400 eV for low energy muons and a relative uncertainty of 6% for the energetic ones has been assumed. The dotted curve at low energies displays the intrinsic resolution for a monoenergetic beam. Whereas the so-called surface muons (~ 4 MeV) are used to investigate bulk properties of matter, low energy muons (LEM) extend the applications of μSR techniques to the study of thin films, multilayers and depth dependent investigation on nanometer scale.

9.1 Generation of slow μ^+ by moderation in thin layers of cryosolids

The most successful method of generating muons with energies of only ~ 15 eV is the muon moderation technique in condensed van der Waals gases, developed at the Paul Scherrer Institute (PSI) in Switzerland, where it is now routinely used for nanoscale investigations. If energetic surface μ^+ are injected into the back of a thin foil (~ 100 μm) covered with a very thin layer (< 1 μm) of a condensed van der Waals gas (such as the Ar, Ne or N_2 cryosolids), very slow μ^+ are emitted from its downstream side (D.R. Harshman et al., Phys. Rev. B **36**, 8850 (1987), E. Morenzoni et al., J. Appl. Phys. **81**, 3340 (1997)). The energy distribution of these particles shows a maximum near 15 eV, with a tail extending to higher energies (see Fig. 9-2). The mechanism is hot emission: the observed very slow μ^+ are particles, which have not completely thermalized in the thin overlayer; therefore they are termed epithermal (i.e. above thermal) μ^+.

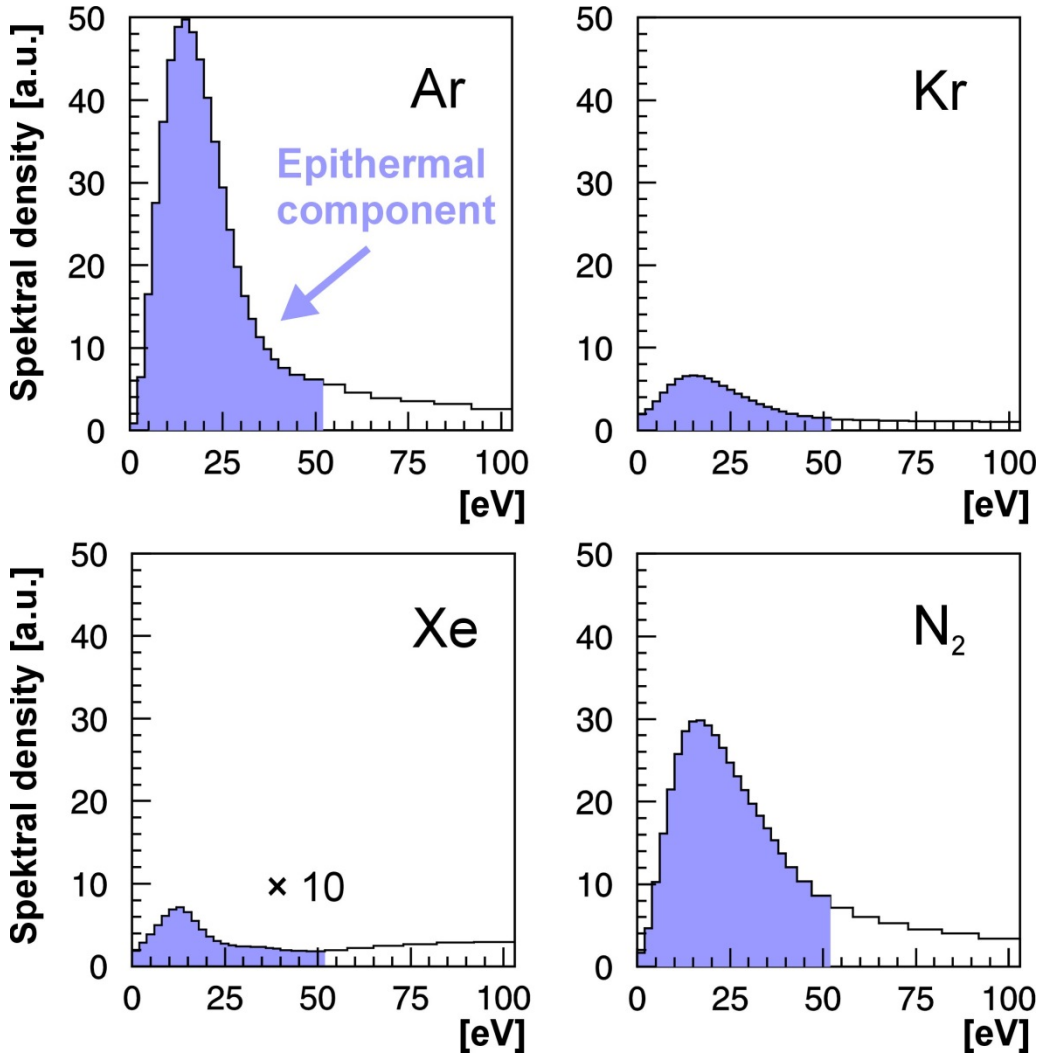

Fig. 9-2: Energy spectrum of the emitted muons after moderation of surface muons in some rare gas solids and solid Nitrogen. The useful energy interval of epithermal muons is shown. From E. Morenzoni, Physics and applications of low energy muons, in *Muon Science*, edited by S. Lee, S. Kilcoyne, R. Cywinski , IOP Publishing, pp. 343-404, (1999).

The moderation steps can be summarized as follows. Initially, the surface μ^+ rapidly loses energy in the thin foil substrate by Coulomb collisions with electrons and by ionizing and exciting the target atoms (electron-hole pair and exciton creation). When a μ^+ has lost most of its energy, at energies below ~ 10 keV, charge exchanging cycles, involving muonium formation in one collision (where the positive muon captures an electron) and muonium break-up in one of the following collisions, also acquire importance as energy dissipating mechanisms (see Chapt. 4. Positive and negative muons in matter). In wide band-gap perfect insulators such as solid Kr, Ar, N_2, and Ne (band-gap energy between 11 and 22 eV) these electronic processes have high threshold energies.
Therefore once the μ^+ has reached a kinetic energy of the order of these levels, the corresponding efficient electronic energy loss mechanisms are strongly suppressed or even become energetically impossible. As a consequence, the energy loss rate becomes considerably lower, since the relatively inefficient elastic scattering and phonon excitation processes remain as the only energy loss mechanisms (see Fig. 4-1).

This results in a large escape depth for epithermal μ^+ (about 100 nm for Ar and 50 nm for Kr), giving rise to a particularly efficient moderation to epithermal energies in these materials. Epithermal μ^+ emission conserves the initial polarization (practically 100%), since depolarization via electron and Coulomb scattering is negligible and the overall time for slowing down to ~10 eV is very short (~ 10 ps). This is an essential feature for the use of these particles as magnetic microprobes on the nanometer scale. Moderation efficiencies range between $1.5 \cdot 10^{-4}$ for solid Ne and ~ $5 \cdot 10^{-5}$ for N_2 and Ar.

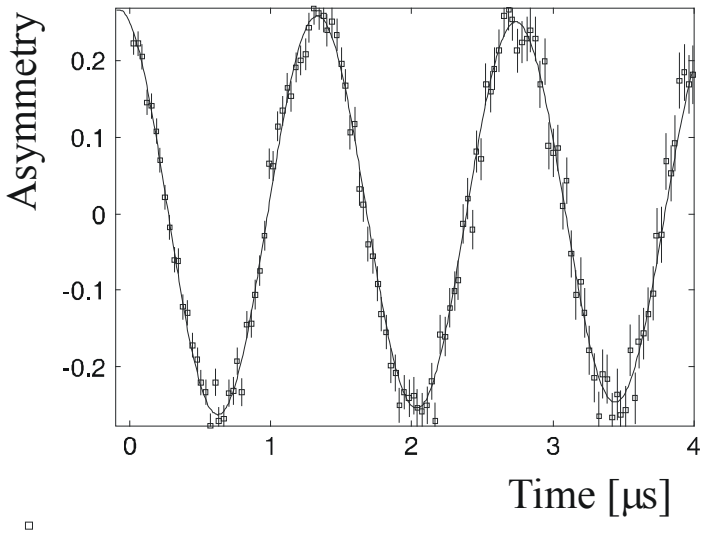

Fig. 9-3: Asymmetry of very slow muons emitted from a solid Argon layer and precessing in a 5 mT transverse magnetic field. The amplitude corresponds to a practically 100% polarization. From E. Morenzoni et al., Phys. Rev. Lett. **72**, 2793 (1994).

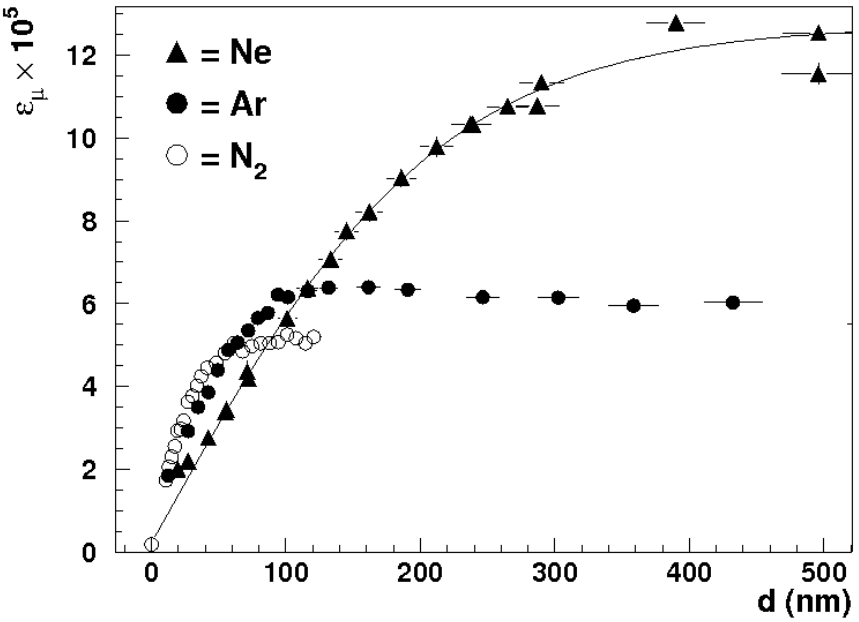

Fig. 9-4: Moderation efficiency ε_μ , defined as the number of epithermal μ^+ divided by the number of incoming surface μ^+, for various moderating materials as a function of the thickness of the solid van der Waals layer condensed onto a patterned Ag substrate, which was held at a temperature of 6 K. From E. Morenzoni et al., J. Phys.: Condens. Matter **16**, S4583 (2004) and T. Prokscha et al., Applied Surface Science **172**, 235 (2001).

9.2 Generation of slow μ^+ by laser resonant ionisation of muonium

An alternative method uses resonant 2-photon ionisation of muonium atoms, which are thermally diffusing out of a hot W foil where surface muons are stopped. Muonium is ionized by the pulsed operation (25 Hz or 50 Hz) of a specially developed laser system (K. Nagamine et al. Phys. Rev. Lett. **74**, 4811 (1995)).
This method is well-suited for pulsed experiments and can potentially produce muons with energies as low as 0.2 eV (2000 K). This method has been tested at the ISIS (UK) pulsed muon source producing about 10-20 slow muons per seconds and is being implemented at the new μSR facility at J-PARC, Japan, where higher intensities are expected (Y. Miyake et al., JPS Conf. Proc. 010101 (2014)).

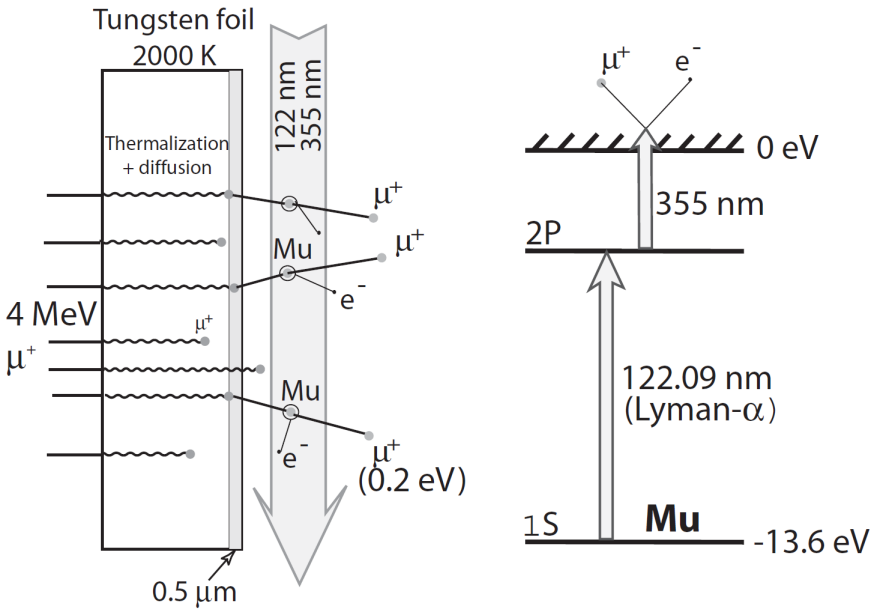

Fig. 9-5: Principle of thermal muonium (Mu) generation from tungsten foil and 2-photon resonant ionization of muonium resulting in the production of low energy positive muons. From P. Bakule and E. Morenzoni, Contemporary Physics **25**, 203 (2004).

9.3 The Low-Energy Muon (LEM) instrument at PSI

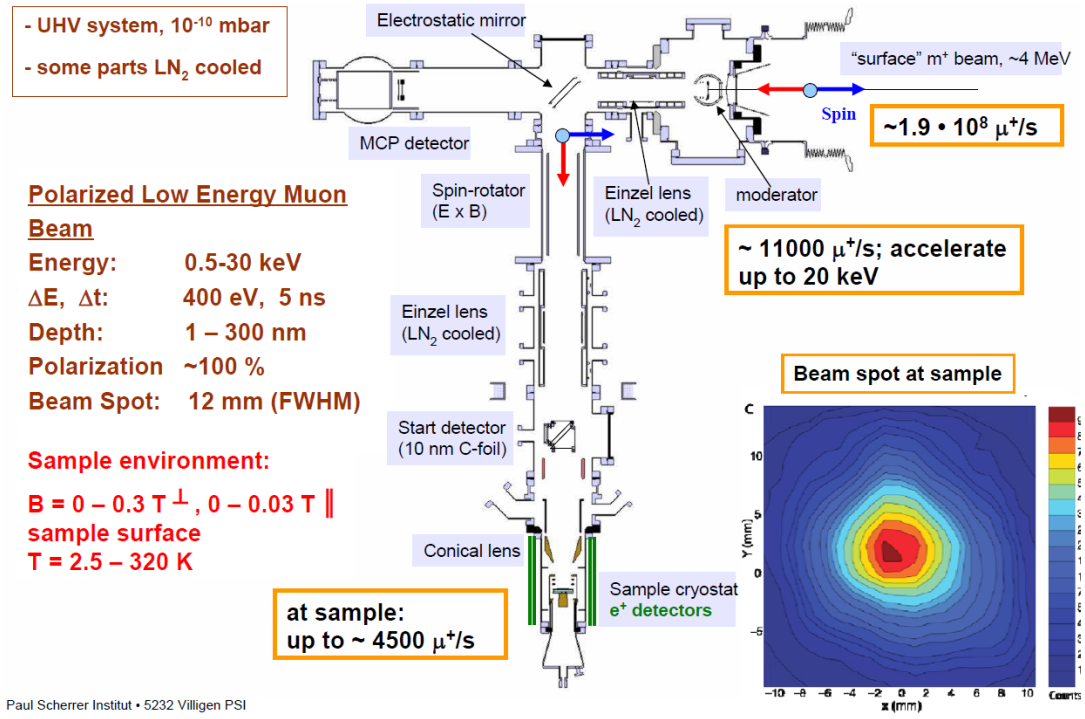

Fig. 9-6: Low energy polarized muon beam generated via moderation and μSR spectrometer for experiments on thin films, multilayers and near surface regions at the Paul Scherrer Institute. Typical intensities and beam characteristics are given.

Epithermal muons emitted from a moderator represent the source of the low energy beam of polarized μ^+ with tunable energy in the desired range. The practical realization of this scheme, developed and in use at PSI, is shown in figure 9-5. This beam is an example of a tertiary beam (the primary being the proton beam generating pions and the secondary the surface muon beam originating from the decay of the pions).

The detailed operation is as follows. "Surface" muons are incident at a continuous rate of presently ~2 10^8/s onto the cryogenic moderator held at a positive potential between 12 and 20 kV. Epithermal muons emerging from the moderator are accelerated in this potential, transported and focused by electrostatic lenses and a mirror to the sample, where they arrive at a rate of ~ 4500/s. The electrostatic mirror is used to separate the low energy muons from any fast muons exiting the moderator. The low energy muons are detected when they pass through a ~ 10 nm thick carbon foil (corresponding to only about 50 atomic layers) placed at an intermediate focus of the beam transport system ("trigger detector" in Fig. 9-6 and 9-7). The μ^+ traversing the foil eject a few electrons, which are directed by a grid system to a micro-channel plate detector where they are detected. This scheme keeps the amount of material interacting with the muons and the consequent effects on the trajectory minimal, while allowing for an efficient (>80%) and fast detection. On passing through the foil, the muons lose about 1 keV and acquire an rms energy spread of ~ 0.4 keV. This detector provides the information about the implantation time of the muon in the sample and starts a time differential measurement (remember: PSI delivers so called continuous beams and only one muon at a time has to be present in the sample, see Chapt. 5. Principles of Muon Spin

Rotation/Relaxation/Resonance). The trigger signal is also used to measure the time-of-flight (TOF) of each low energy muon after it was detected at a scintillator on entering the apparatus. By selecting on TOF, one discards muons coming from the moderator with energies outside the epithermal region, but with low enough energy to be reflected by the mirror. The final kinetic energy of the muons implanted into the sample may be varied over the range 0 to 30 keV by applying an accelerating or decelerating potential of up to 12 kV to the sample, which is mounted in good thermal but electrically insulating contact with a cryostat for low temperature experiments or on other types of sample holder. The 90° deflection at the electrostatic mirror has also the practical effect of transforming the initially longitudinally polarized muon beam into a transversely polarized beam (when the muons arrive at the sample, they are horizontally polarized, transverse to their direction of motion). A small spin rotator can rotate the spin by 90° to have the spin parallel to the momentum (Z. Salman et al., Physics Procedia, **30**, 55, (2012)). The decay positrons from the muons implanted in the sample are detected by a set of scintillator detectors placed left, right, above and below the beam axis.

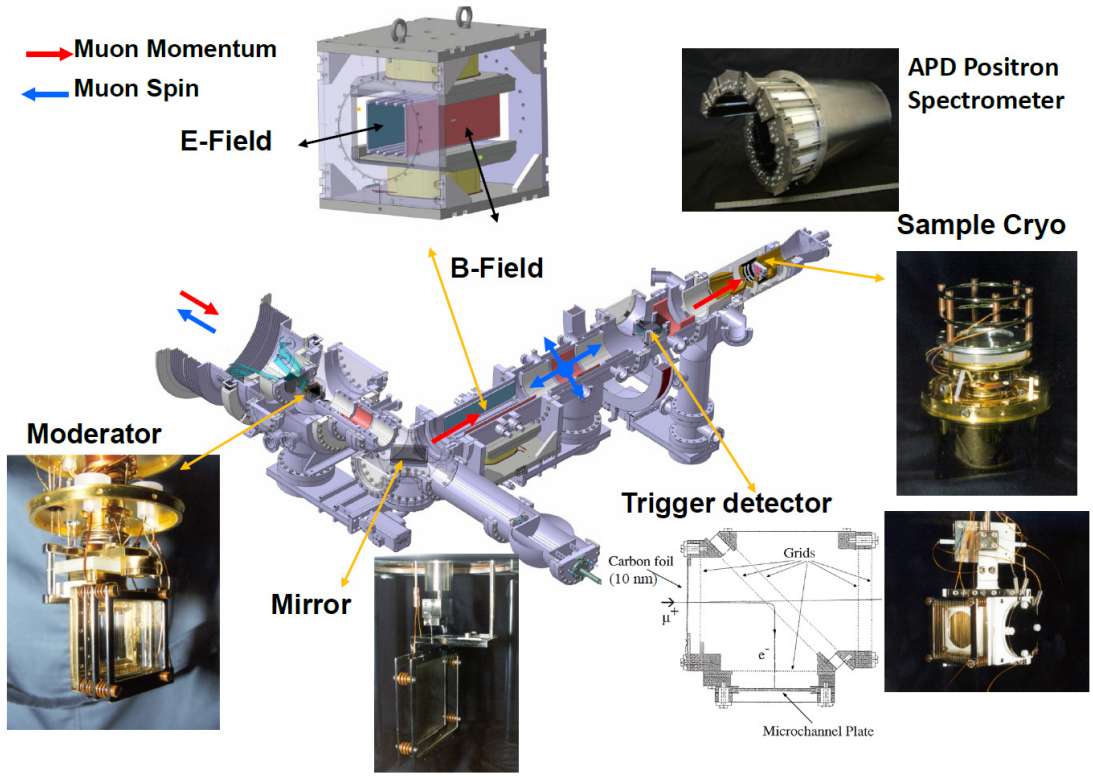

Fig. 9-7: Details of the main components of the LEM setup.

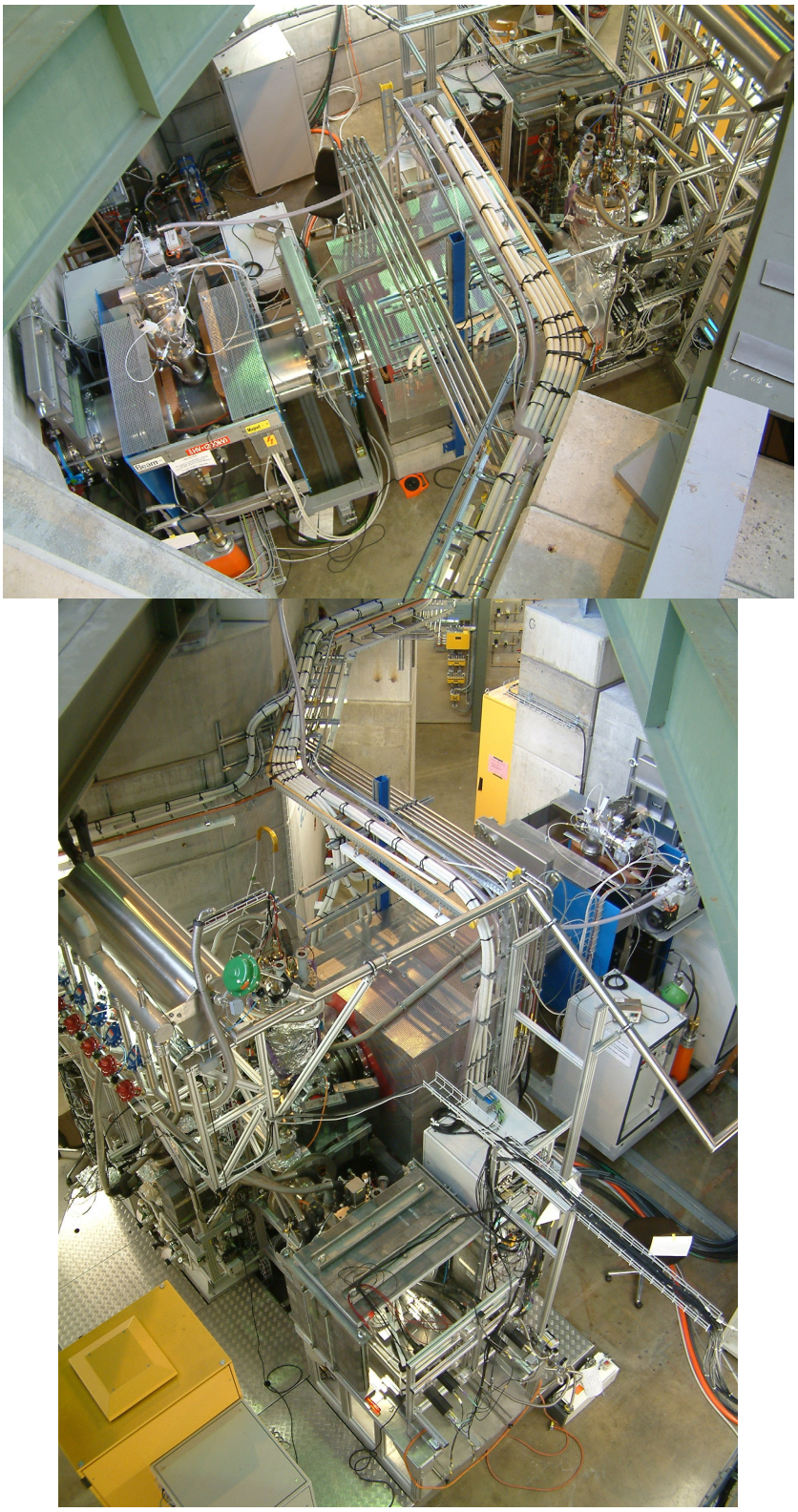

Fig. 9-8: LEM instrument in the μE4 area at PSI. Top: last section of the high intensity surface muon beam feeding the LEM apparatus. Bottom: LEM Apparatus. The surface muons are coming from the right. The moderator cryostat with the 90° deflection as well as the μSR spectrometer and sample chamber in the lower part of the picture are visible (T. Prokscha et al., Nuclear Instruments and Methods in Physics Research A **595**, 317 (2008)).

9.4 Stopping profiles of Low-Energy Muons in thin films

In bulk μSR experiments the exact stopping position is not known and is also irrelevant, as long as the sample is homogenous; in the experiment it is sufficient to ensure that the particles stop inside the sample. In contrast, for unrestricted use of muons on the nm scale, it is important to understand their implantation behavior in detail.

When the muon enters a solid sample the initial kinetic energy, which is much larger than the thermal energy of diffusion, is dissipated within a few ps. It continuously loses energy predominantly by electronic collisions and changes direction mainly by Coulomb scattering with the target nuclei. Due to the random nature of the collisions a stopping profile n(z, E) is obtained as a result of the thermalization process of a muon ensemble of energy E (z depth from the sample surface). First moment and rms of
this distribution are shown in Fig. 9-1 for μ^+ stopping in the high temperature superconductor $YBa_2Cu_3O_{7-\delta}$. The first quantity represents the projection to the beam direction of the total distance travelled (projected range, R_p) and the second the corresponding straggle (ΔR_p). The curves shown in Fig. 9-1 have been obtained from the moments of implantation profiles calculated by using Monte Carlo codes originally developed for protons and heavy ions and taking into account the typical finite energy resolution of the impinging beam. In the simulation the muon is treated as a proton-like projectile of mass $m_\mu \approx 1/9\ m_p = 0.113$ amu. At low energies
the profile width is typically 5–10 nm. Even for perfectly monoenergetic particles there is an inherent limit to the depth resolution due to the statistical broadening of the μ^+ implantation profile. This intrinsic broadening is the dominant effect for μ^+ of energy larger than ≈ 2 keV.

To determine experimentally their stopping site one can rely on the property that polarized muons thermalized in metals behave as a free μ^+, whereas the large majority of muons thermalized in insulators bind an electron and form muonium (Fig. 9-9). Because of the different magnetic moments, the two states (free muon and muonium in the triplet state, $m_F = \pm 1$) and therefore the rest position can be easily distinguished by their different muon spin precession frequency in a low static magnetic field $\vec{B}$ transverse to the initial spin direction (Larmor precession frequency $\omega_\mu = \gamma_\mu B = 0.8516\ \mathrm{Mrad/mT \cdot B\,[mT]}$ and $\omega_{Mu} = 87.617\ \mathrm{Mrad/mT \cdot B\ [mT]}$, see Chapt. 8. Muonium in semiconductors). In a sample composed of a thin (thickness d) metallic layer deposited on an insulator, the amplitude of the corresponding frequency is then directly proportional to the fraction of muons stopped in the corresponding layer. In the experiment one determines partial integrals of the range distribution:

$$N(d,z) = \int_0^d n(z,E)dz \qquad [9\text{-}1]$$

By comparing these fractions with the predictions obtained by Monte Carlo programs, which calculate step-by-step the trajectory of the particle implanted and simulate their slowing down, scattering and thermalization, we are able to test our understanding of these processes.

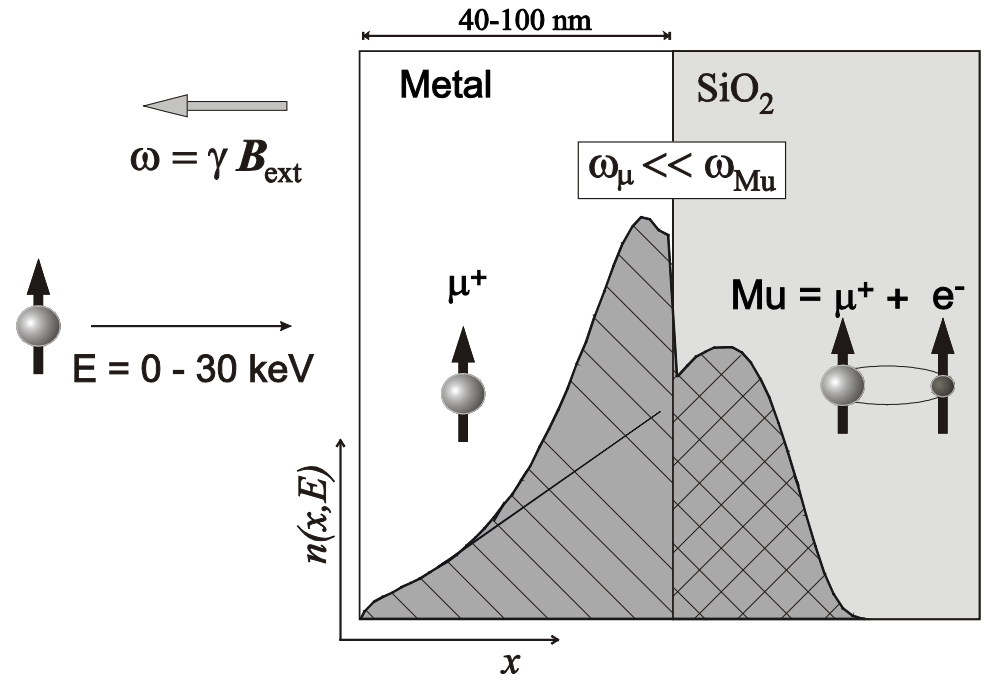

Fig. 9-9: Principle of the muon depth profile studies in metal-insulator films. The fraction of muons stopping in the metal or in the insulator layer can be distinguished by their different Larmor frequency. The results can be compared with Monte Carlo simulations of the muon stopping profile n(x,E).

Figure 9-10 shows as an example the muon fraction measured in a bilayer consisting of Cu deposited on quartz SiO_2.
After an increase at low energies, the fraction of muons stopping in the metal saturates, when essentially all the particles thermalize in the metallic layer. Increasing further the energy the fraction decreases, when the muons penetrate the metallic layer and reach the insulating layer, where they predominantly form muonium. The decrease of the free muon fraction is accompanied by a corresponding increase of the muonium fraction (not shown). The increase with energy at a few keV is a consequence of reflection and simultaneous neutralization of muons scattered at the metallic surface or re-emerging from the bulk. This effect is especially pronounced in samples containing heavy elements. The comparison with simulated integrals of implantation profiles and reflection probabilities shows that we are able to suitably predict the behavior of keV muons.

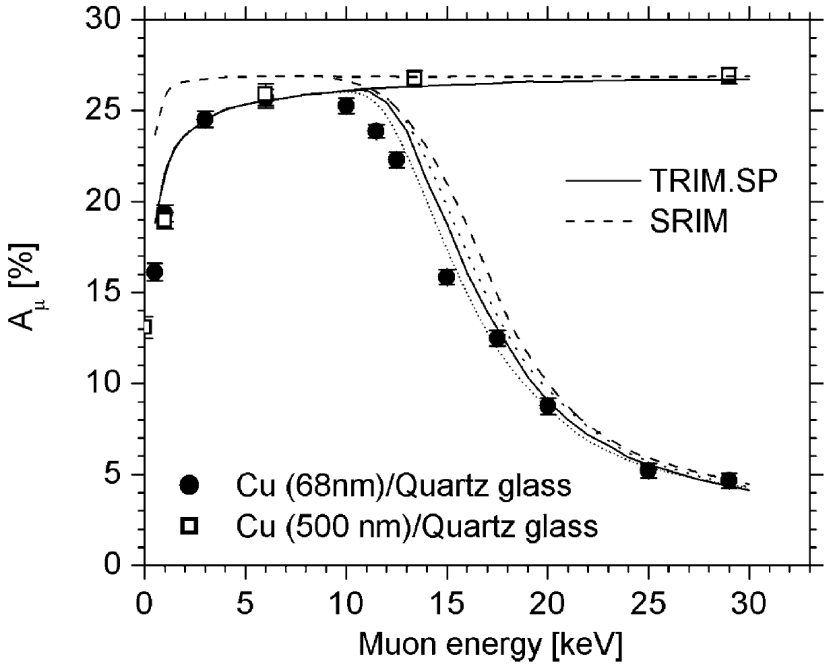

Fig. 9-10: Energy dependence of the diamagnetic asymmetry in Cu deposited on a quartz glass: closed symbols thin (d = 68 nm), open symbols thick (d = 500 nm) sample. The solid lines are the prediction of a simulation based on the TRIM.SP Monte Carlo program (W. Eckstein, Computer Simulation of Ion–Solid Interactions,
Springer, Berlin, Heidelberg, New York, 1991). The dotted line in the intermediate energy region shows upper and lower limits due to the layer thickness uncertainty. The dashed curves are the prediction of the SRIM2000 code (J.F. Ziegler et al., in *The Stopping and Range of Ions in Solids*, Vol. 1, Pergamon, New York, 1985). From E. Morenzoni et al., Nucl. Instrum. Meth. B **192**, 254 (2002).

The full differential implantation profile n(z, E) can be directly imaged in a single implantation and imaging experiment. In analogy with the magnetic resonance imaging technique this quantity can be obtained from the spectrum of the Larmor precession frequencies in an inhomogeneous transverse magnetic field
B(z) of known gradient applied to the sample. The local magnetic field at each stopping site causes a corresponding precession of the muon spin. The temporal evolution of the polarization, P(t), measured at a well-defined energy E is related to the field profile B(z) and the stopping distribution n(z,E):

$$P(t) = \int_0^\infty p(B)\cos(\gamma_\mu Bt + \varphi)dB \qquad [9\text{-}2]$$

p(B) is obtained by Fourier transform.

The field distribution sensed by the muons distributed over a profile n(z, E) is connected to this quantity by the relationship

$$n(z,E)dz = p(B,E)dB \qquad [9\text{-}3]$$

which states that the probability that a muon will experience a field in the interval [B, B +dB]

is given by the probability that it will stop at a depth in the range [z, z + dz].

From [9-3] we have

$$n(z,E) = p(B,E)\frac{dB}{dz}$$

Which shows that the differential stopping distribution can be determined if a sufficiently large and known magnetic field gradient is applied over the range profile

Due to the reduced values of R_p and ΔR_p sizably larger field gradients are necessary. For this we make use of the magnetic field exponentially penetrating the surface of an extreme type-II superconductor in the Meissner state $B(z) = B_{ext} \exp(-z/\lambda)$ (see Sect. 9.5). With typical values of $B_{ext} \approx 10$ mT and $\lambda \approx 100$ nm, field gradients $B_{ext}/\lambda \approx 10^5 \text{T m}^{-1}$ can be generated within the range distribution of LE-μ^+.[18]

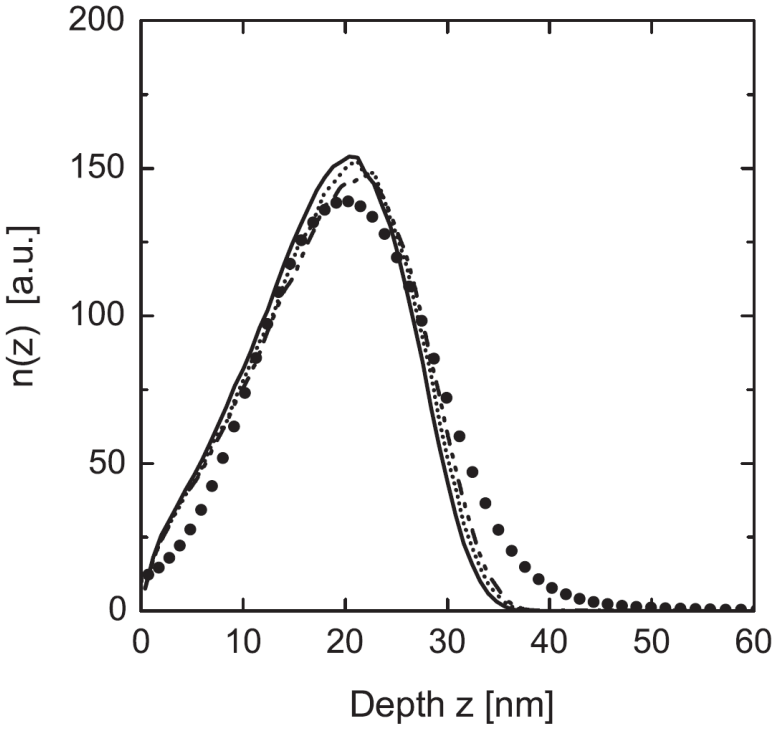

Fig. 9-11: Implantation profile of 3.4 keV muons in a thin film of $YBa_2Cu_3O_{7-\delta}$ obtained by the direct imaging technique (circles). The profile is compared with predictions of Monte Carlo calculations using the code TRIM.SP with different assumptions about the scattering potential. From E. Morenzoni et al., J. Phys.: Condens. Matter **16**, S4583 (2004).
The various tests show that muon implantation profiles in thin films and heterostructures can be reliably simulated with a modified version of the Monte Carlo program TRIM.SP.

[18] Please note that in the next section we will assume the knowledge of the implantation profile to microscopically prove that the field is penetrating exponentially and to make an absolute measurement of the London penetration depth and its temperature dependence. Here, by contrast, we assume an exponentially decaying magnetic profile with known λ_{ab} to measure the depth profile. The argument is non-circular since for the present analysis we determine the value of λ_{ab} by an independent measurement in the vortex state (C. Niedermayer et al., Phys. Rev. Lett. **93**, 3932 (1999)).

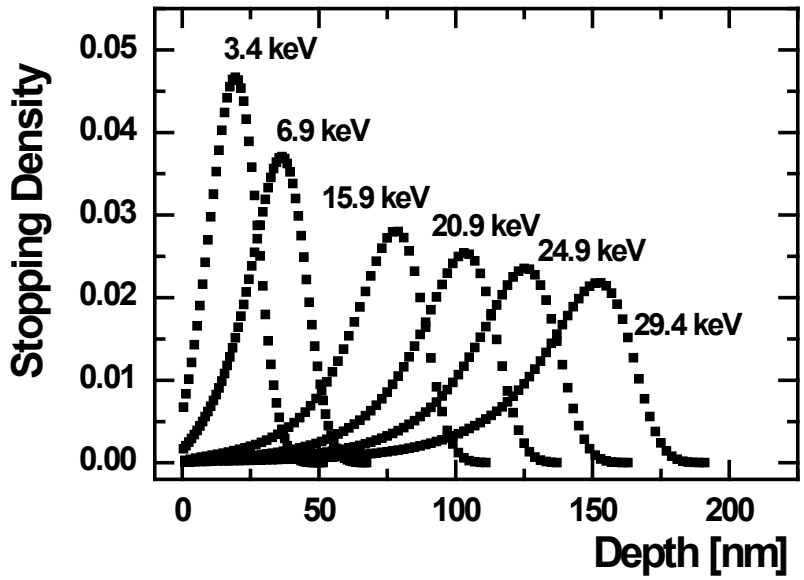

Fig. 9-11: Monte Carlo calculation of stopping profiles of low energy muons in YBCO, as a function of the implantation energy.

9.5 Magnetic field penetration at the surface of superconductors

The depth sensitivity in nm range of LE-μ^+ implanted in the surface region and the local character of the muon probe allow to directly measure single values of magnetic fields as a function of depth, thus to image magnetic field profiles beneath the surface of materials on a nanometer length. At the moment, no other technique is able to provide this information.

To illustrate the near surface sensitivity of LE-μSR we consider here the Meissner effect and a measurement of B(z). This yields a direct determination of otherwise not easily accessible quantities such as magnetic penetration depth and coherence length.
In a superconductor in the Meissner state an applied field is excluded from the bulk and will penetrate only in a near surface region. In the so-called London limit ($\lambda >> \xi$, "clean" superconductor $l >> \xi_0$), for a plane superconducting surface, the functional form of the decaying magnetic field B(z) is predicted to be exponential, with the decay length determined by a single parameter, the London penetration depth λ_L.

This follows from the description of the electrodynamic response of an extreme Type II superconductor, which can be described by the two London equations:

$$\frac{d\vec{j}}{dt} = \frac{1}{\mu_0 \lambda_L^2}\vec{E}$$

$$\mathrm{rot}\vec{j} = -\frac{1}{\mu_0 \lambda_L^2}\vec{B} \qquad (\vec{j} = -\frac{1}{\mu_0 \lambda_L^2}\vec{A})$$

From the second London equation and the Maxwell equation relating field and current (see Chapt. 7. μSR studies of superconductivity) it follows for B_{appl} parallel to the surface:

$$B(z) = B_{appl} e^{-\frac{z}{\lambda_L}} \qquad [9\text{-}4]$$

The magnetic penetration depth λ_L is a fundamental length of a superconductor, since its value reflects the number density n_s and effective mass m^* of the superconducting carriers through the London expression $\lambda_L = \sqrt{m^* / \mu_0 e^2 n_s}$.

As expressed by the name, it is a measure of how deep a magnetic field penetrates at the surface of a superconductor in the Meissner state when a field is applied parallel to its surface. It is a measure of the response of the superconductor to a low frequent electromagnetic field. Besides perfect conductivity, the diamagnetic response to an applied magnetic field is a fundamental property of a superconductor. The superconductor tries to exclude or expel the magnetic flux from its core by shielding the interior with supercurrents flowing in the surface layer. Since an infinite surface current is unphysical the external field is able to penetrate a short distance into the superconductor.
It is interesting to note that Eq. [9-4] was predicted already in 1935 (F. London and H. London Proc. R. Soc. A **149**, 71 (1935)), but never experimentally tested before at microscopic level. LE-μSR provided the first experimental proof of it. Differently from a measurement in the vortex state, the measurement in the Meissner state provides an absolute

and model independent determination of λ. A determination from the vortex state (Chapt.7. μSR studies of superconductivity) is a very reliable and efficient method but it has to rely on a theory describing vortex state (Ginzburg-Landau, London, …) relating measured field distribution p(B) (or its moments) with λ, a regular vortex lattice of known symmetry and eventually take into account effects of field dependence, non-local and non-linear effects, and the influence of disorder.

If the second fundamental length scale in a superconductor, the coherence length ξ, is non-negligible, the electrodynamical response of the superconductor has to be averaged over it (A.B. Pippard Proc. R. Soc. A **216**, 547 (1953) and J. Bardeen, L.N. Cooper and J.R. Schrieffer Phys. Rev. **108,** 117521 (1957)).

Pippard first considered this non-local electrodynamical response

$$\vec{j}(\vec{r}) = -\frac{1}{\mu_0}\frac{3}{4\pi\lambda_L^2(T)\xi}\int \frac{\vec{R}\left[\vec{R}\times\vec{A}(\vec{r}')\right]}{R^4} e^{-\frac{R}{\xi}} d\vec{r}' \qquad [9\text{-}5]$$

$$\vec{R} = \vec{r} - \vec{r}' \quad , \quad \frac{1}{\xi} = \frac{1}{\xi_0} + \frac{1}{\ell}$$

The equivalent BCS expression is:

$$j_\alpha(\vec{r}) = \sum_\beta \int \left\{ \underbrace{P_{\alpha\beta}(\vec{r} - \vec{r}') - \frac{e^2 n_s}{m^*}\delta(\vec{r} - \vec{r}')\delta_{\alpha\beta}}_{K_{\alpha\beta}(\vec{r} - \vec{r}')} \right\} A_\beta(\vec{r}')\, d\vec{r}' \qquad [9\text{-}6]$$

$$\underbrace{\uparrow \qquad \uparrow}_{\text{paramagn.} \quad \text{diamagn.}}$$

If $\lambda >> \xi$ the response becomes local and

$$\vec{j}(\vec{r}) = -\frac{1}{\mu_0\lambda_L^2}\vec{A}(\vec{r}) \qquad [9\text{-}7]$$

From which [9-4] follows.

Fig. 9-12 shows the first measurement of a field profile with LE-muons in a $YBa_2Cu_3O_{7-\delta}$ film providing a direct confirmation of the London formula.

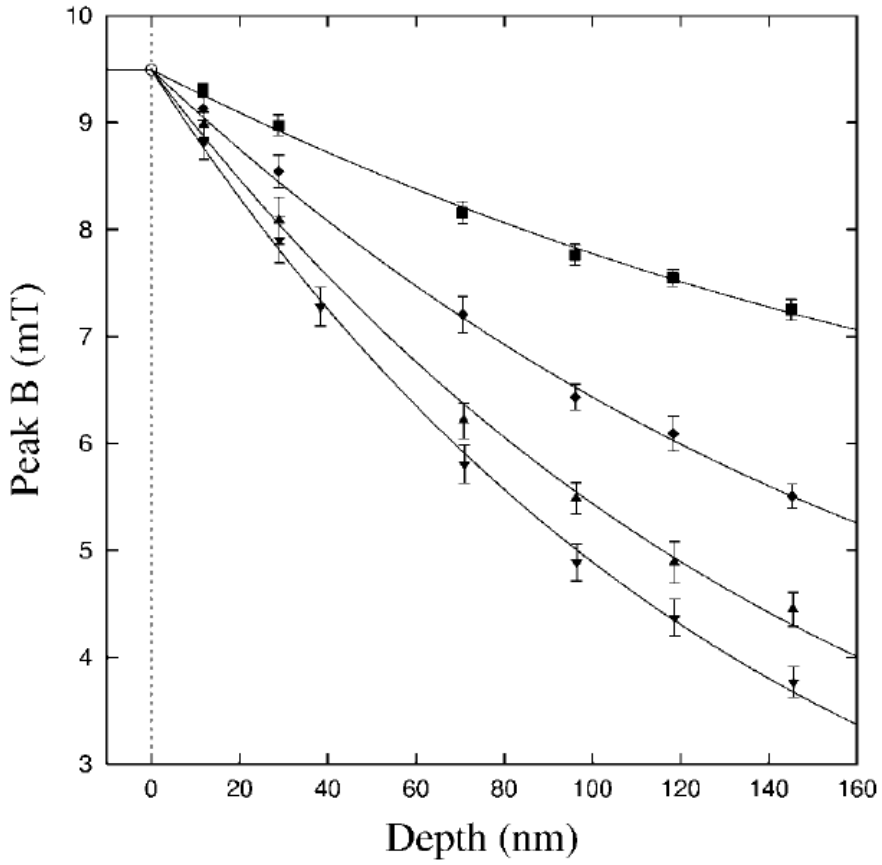

Fig. 9-12: Values of field versus depth for various values of sample temperature 20 K, 50 K, 70 K, and 80 K. The solid lines represent fits of Eq. (5) to the data with λ_L as the free parameter. From T.J. Jackson et al., Phys. Rev. Lett. **84**, 4958 (2000).

The theoretical lines are plots of

$$B(z)=B_{ext}\frac{\cosh(\frac{d-z}{\lambda_L})}{\cosh(\frac{d}{\lambda_L})} \qquad [9\text{-}8]$$

which is the form taken by Eq. [9-4] for a film of thickness 2d, with flux penetrating from both surfaces. The value of z in Eq. [9-8] has been corrected by a small quantity z_0, corresponding to a "dead layer." This may partly be due to a thin layer that is non-superconducting, but arises mainly from the surface roughness of the film, which increases the effective penetration depth in the surface layers.

Fig. 9-13 shows an example of non-local response in a Pb film. From the fit one finds a coherence length ξ_0=59(3) nm and an effective London penetration depth $\lambda_{eff}(0)$=90(5) nm. The effective London penetration depth takes into account corrections due to the scattering of electrons. In the clean limit (i.e. for $l \to \infty$)
$\lambda_{eff} = \lambda_L$.

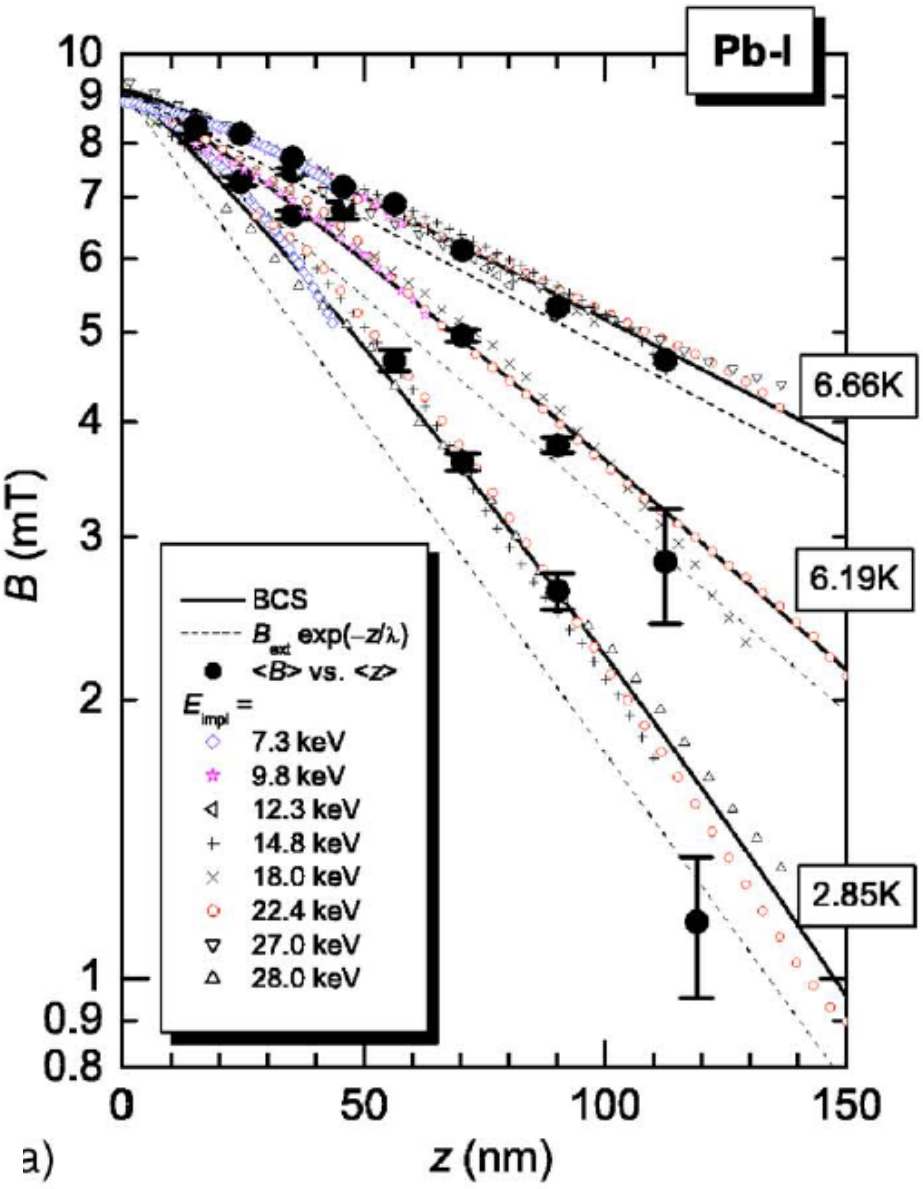

Fig. 9-14: Magnetic penetration profiles for Pb at various temperatures. The solid lines are BCS fits to the data, whereas the dashed line represents $B(z)=B_{ext}\exp(-z/\lambda)$ where the λ from the BCS fit is used. From A. Suter at al. Phys. Rev. B **72**, 024506 (2005).

9.6 In-plane anisotropy of the magnetic penetration depth in ultra clean $YBa_2Cu_3O_{6.92}$

The dependence of λ on T, B_{appl}, orientation, composition, gives information about microscopic properties of superconductor (order parameter, gap symmetry, anisotropy,..). Recently, a direct measurement of the magnetic field profile in an oriented mosaic of high-purity crystals of $YBa_2Cu_3O_{6.92}$ (T_c = 94.1 K, $\Delta T_c \leq 0.1$ K) has been performed, to determine the anisotropy of the magnetic penetration depth. The crystals are detwinned, so that by applying the external field parallel to the a-axis (b-axis), λ_b (λ_a) is measured (see Fig. 9-15).

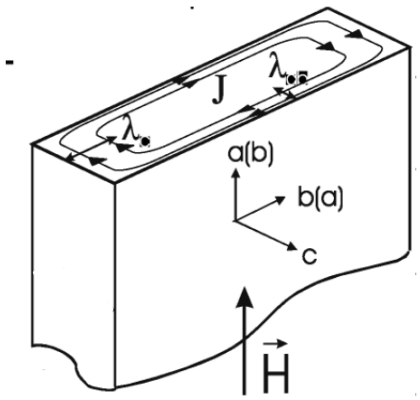

Fig. 9-15: Geometry of the experiment to measure the in-plane anisotropy of the magnetic penetration depth.

In $YBa_2Cu_3O_{6+x}$ the x additional Oxygen goes to the b-axis (so called CuO chains). This additional Oxygen provides holes to the CuO_2 planes leading to superconductivity for $x \gtrsim 0.35$.

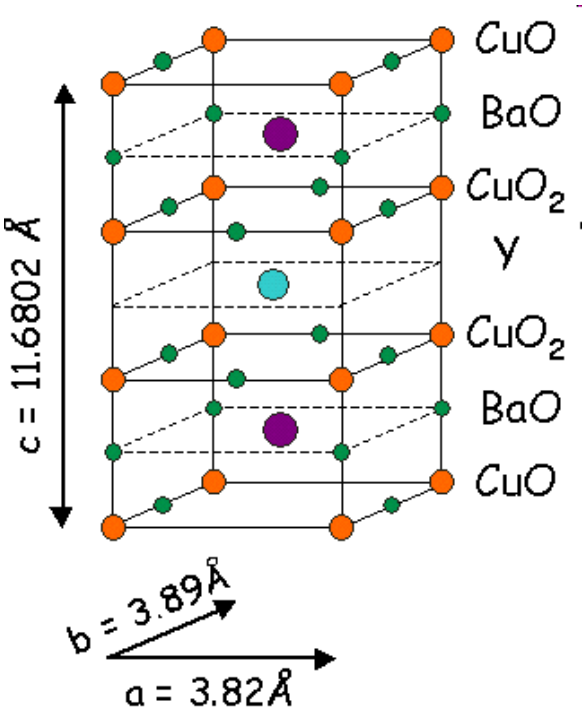

Fig. 9-16: Structure of YBCO, showing the CuO_2 planes and the CuO chains (orange: Cu, green: O).

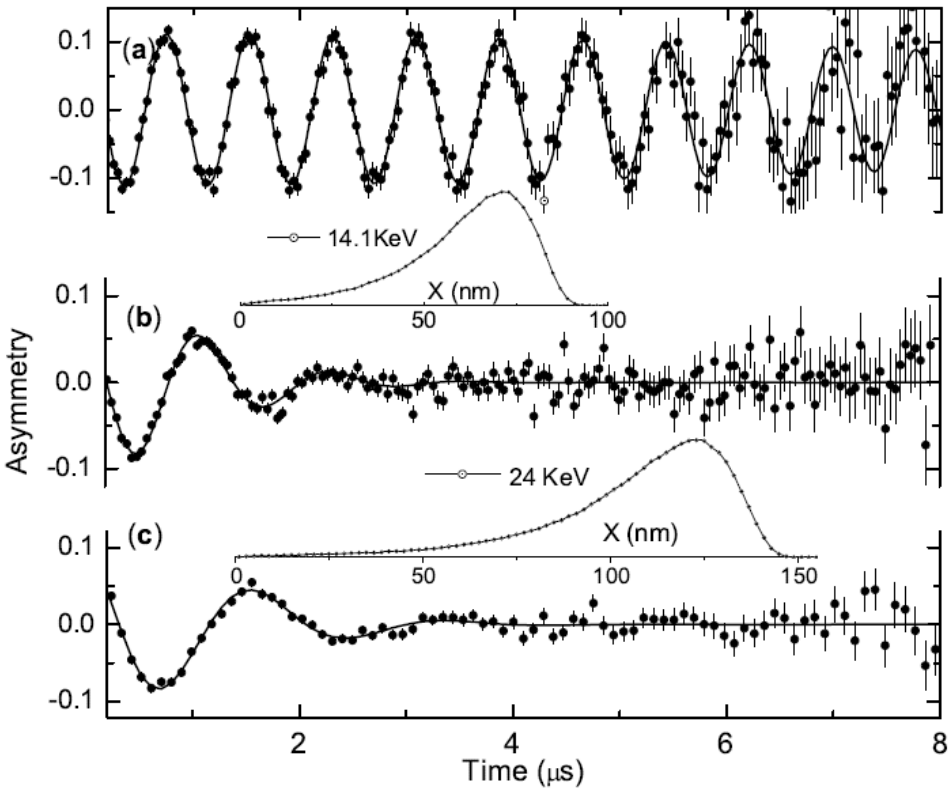

Fig. 9-17: (a) The muon precession signal in the normal state of $YBa_2Cu_3O_{6.92}$ at 110 K in an external field of 9.46 mT applied parallel to the a-direction. The mean implantation energy is E=14.1 keV that corresponds to a mean implantation depth of 62.8nm. The small damping rate is attributed to Cu nuclear dipole moments.
(b) Same conditions as (a) except in the superconducting state at T=8 K. The curve is a fit to a London model profile. The inset shows the calculated stopping distribution. (c) Same conditions as (b) except the energy of implantation is increased to 22 keV. From R. F. Kiefl et al., Phys. Rev. B **81**, 180502(R) (2010).

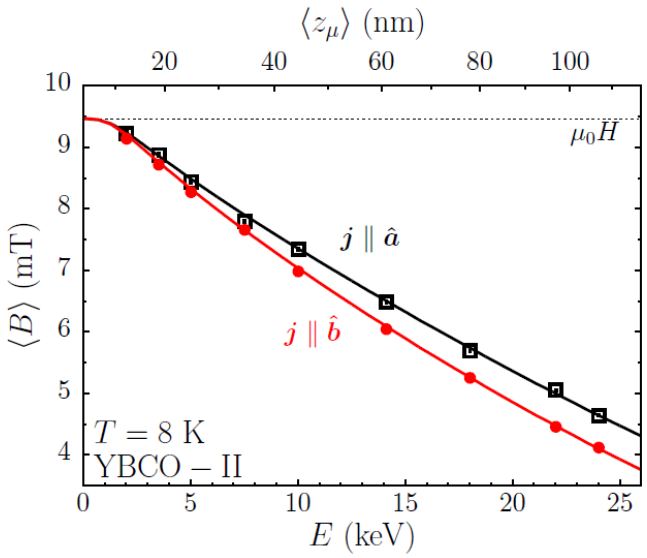

Fig. 9-18: The average magnetic field versus mean stopping depth in an applied field of 9.46 mT such that the shielding currents are flowing in the **a** and **b** direction, respectively. The curves are the average fields generated from a global fit of all the spectra at T = 8 K taken at all energies and for both orientations. From B. M. Wojek, PhD Thesis, University of Zurich, 2011.

Figure 9.18 shows the average local field <B> as a function of beam energy (bottom scale) and the corresponding mean implantation depth (top scale) at T = 8 K.
The filled circles and open squares are from data taken with the shielding currents flowing along the **a** and **b** axes, respectively, or equivalently the magnetic field along the **b** (magnetic penetration depth λ_a) and **a** axes (magnetic penetration depth λ_b), respectively. The profiles clearly reflect the anisotropy of the penetration depth. From the measurements at different temperatures we extrapolate the in-plane anisotropy $\lambda_a/\lambda_b = 1.19 \pm 0.01$ at $T = 0$. This shows that the chain contribute to the superfluid density. Fig. 9-19 (top) shows the temperature dependence of the superfluid density along **a** and **b** direction. The data can be well fitted with a pure $d_{x^2-y^2}$ order parameter. The bottom part of Fig. 9-19 shows the data normalized to $1/\lambda_{a,b}(0)^2$, where for the normalization the absolute values of the magnetic penetration depths obtained from the LE-μSR experiment have been used. No particular difference between the two crystal orientations is observed, at variance with previous surface impedance measurements. In this respect it is important to remark that the slopes of the normalized curves crucially depend on the knowledge of the absolute value of $\lambda_{a,b}(0)$.

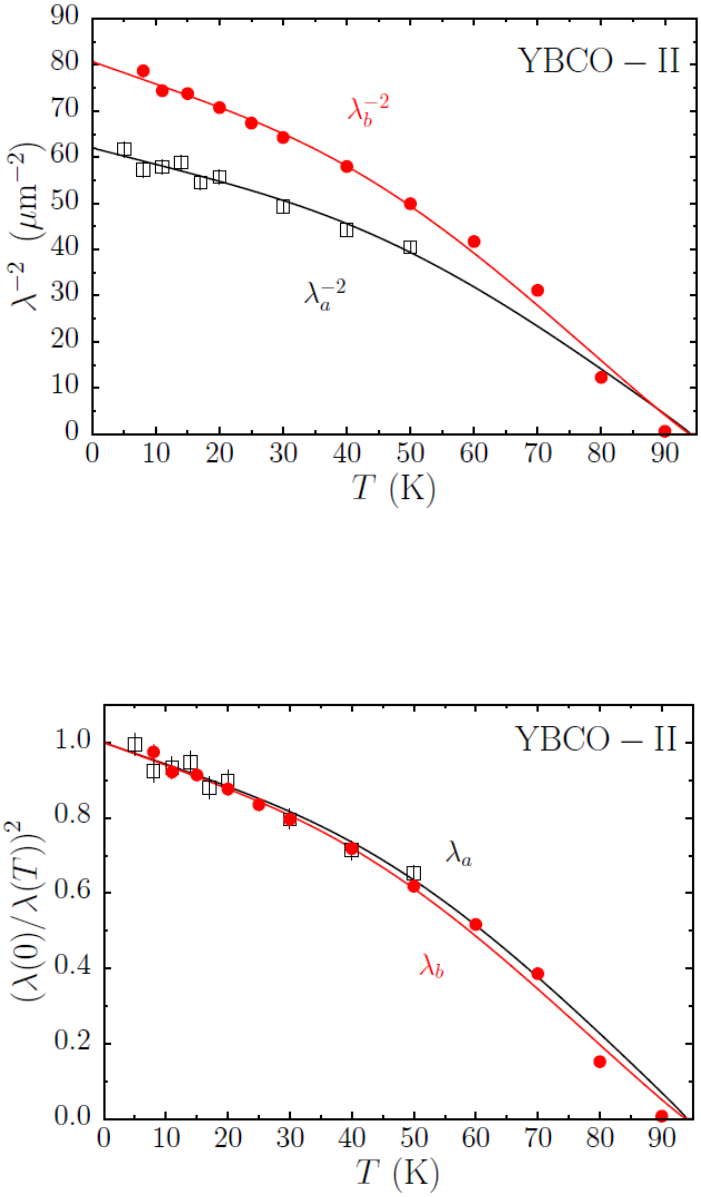

Fig. 9-19: Top: Temperature dependence of the superfluid density along **a** and **b** axis. Bottom: Normalized superfluid density. From B. M. Wojek, PhD Thesis, University of Zurich, 2011.

The very similar shape of the normalized superfluid densities indicate that the presence of the CuO chains along the **b** axis simply adds superfluid density without changing the symmetry of the order parameter. The measured λ_a and λ_b are in surprisingly good agreement with average value of the in-plane magnetic penetration depth $\lambda_{ab} = (\lambda_a \cdot \lambda_b)^{1/2}$ obtained from bulk μSR studies of the vortex state of an earlier generation of crystals. In that case λ_{ab} is obtained from an extrapolation of an effective field-dependent penetration depth to zero field. This suggests that the effective field-dependent penetration depth in the vortex state, at least in the present case, extrapolates to the actual London penetration depth in the Meissner state to within an accuracy of a few percent. The agreement is remarkable considering that there are several phenomenological parameters involved in the fit of the vortex-state data.

9.7 Giant proximity effect in cuprate heterostructures

By directly mapping the magnetic field profile in cuprate heterostructures, it is possible to probe the diamagnetic Meissner response of non-superconducting cuprate barrier layers, when they are brought in close contact with superconducting layers.

Generally the adjacency of materials with different electronic properties gives rise to reciprocal influence. For instance, if a thin normal metal layer is brought in close contact with a superconducting layer, in the interface region Cooper pair can enter the normal layer. The layer may become superconducting and the same time superconductivity is weakened in the superconducting layer (proximity effect).

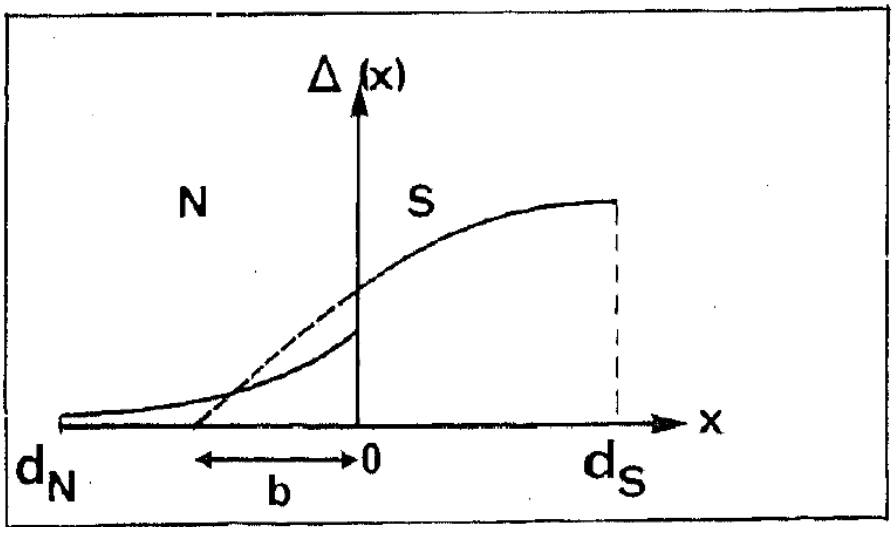

Fig. 9-20: Normal-superconducting bilayer (NS), showing qualitatively the order parameter and the proximity effect.

In cuprates the proximity effect is non-conventional due to the anomalous 'normal' (metallic) state above the critical temperature T_c of high-temperature-superconducting cuprates which features a pseudogap in the density of states and unexpected charge and spin responses. Also unusual diamagnetic signals have been observed, among other an enhanced Nernst effect and unusual supercurrent transport over thick barriers at temperatures well above the T_c' of the barrier.

The results of B(z) are shown for heterostructures consisting of three layers, each 46 nm thick; optimally doped (OP) $La_{1.84}Sr_{0.16}CuO_4$ ($T_c \approx 32$ K) was used for the top and the bottom 'electrodes', whereas underdoped (UD) $La_{1.94}Sr_{0.06}CuO_4$ ($T_c' < 5$ K) served as the 'barrier'. The barrier with a low T_c' offers a broad temperature interval to search for putative long-range proximity effects. Similar results have been obtained with 32 nm thick barriers.

The films were grown on (001)-oriented $LaSrAlO_4$ substrates in a molecular beam epitaxy system designed for atomic-layer engineering of complex oxide materials. The typical surface roughness determined by AFM was 0.5 nm, much less than one unit-cell height (1.3 nm). The UD layer was grown as a single layer (SL) or as a barrier in the trilayer structure (TL). The single phase films were used for control measurements. The comparison of the magnetic behavior in the two cases, which strongly depends on the doping level, confirms the equivalence of the layer and its position in the $La_{2-x}Sr_xCuO_4$ phase diagram.

To map the diamagnetic response of the heterostructure as a function of position along the crystal **c** axis (z coordinate), the samples are cooled in ZF from above T_c to ~ 4.3 K, a magnetic field of 9.5 mT parallel applied to the *ab* planes (x direction) and μSR spectra collected as a function of the muon implantation energy. The depth profile of the mean field $\langle B_x \rangle$ at different temperatures is shown in Fig. 9-21.

It demonstrates the main result: At 10 K, 15 K and 17 K—that is, well above T_c'—the local field is lower than the applied field at all depths, meaning that the entire heterostructure excludes the magnetic flux like a conventional superconductor. The profile has the form of an exponential field decay in the Meissner state with the flux penetrating from both sides and looks like that for two superconductors with different magnetic penetration depths. The observed field profile reflects the shielding supercurrent that runs along the **c** axis as well as in the **ab** planes of the barrier; note that $\langle j_{ab} \rangle = \langle (1/\mu_0)\, dB_x/dz \rangle \neq 0$. This is unexpected when one recalls that in this geometry the supercurrent must pass through the 'barrier' $La_{1.94}Sr_{0.06}CuO_4$ region that is 46 nm thick.

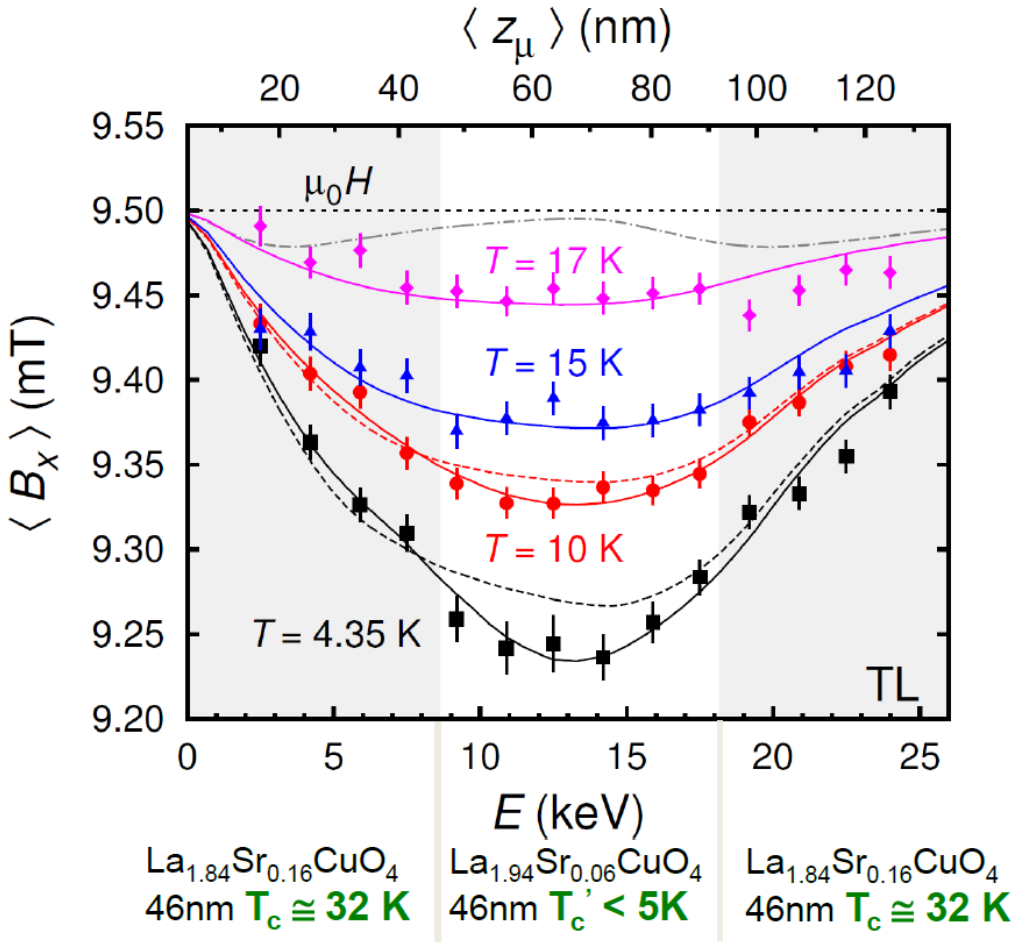

Fig. 9-21: Depth profile of the local field in a cuprate heterostructure at different temperatures. The vertical lines indicate the position of the interfaces of the $La_{1.84}Sr_{0.16}CuO_4$ (46 nm)/$La_{1.94}Sr_{0.06}CuO_4$ (46 nm)/ $La_{1.84}Sr_{0.16}CuO_4$ (46 nm) heterostructure. The horizontal dashed line shows the applied field of 9.5 mT. Points: measured average fields. The entire heterostructure excludes the magnetic flux like a superconductor: it shows the Meissner effect with the UD layer active in the screening. This functional form can only be observed if shielding supercurrents flow across (that is, along the c axis) as well as in the ab planes of the UD barrier. The lines are obtained from fits using a London model. The fit takes into account the energy-dependent muon stopping profiles, which are also used to calculate the average stop depth $\langle z_\mu \rangle$ (upper scale). From E. Morenzoni et al., Nature Communications **2**, 272 (2011).

A comparison of the temperature dependence of the average field in the center of a single-phase film of UD $La_{1.94}Sr_{0.06}CuO_4$ with that in the barrier of the same composition inside a trilayer heterostructure clearly shows that the SL case no shift is observed, whereas in the TL structure a shift up to $T_{eff} \approx 22$ K is observed. What we observe here is a manifestation of a giant proximity effect. This is particularly remarkable if one considers that the Meissner effect is a hallmark of superconductivity.

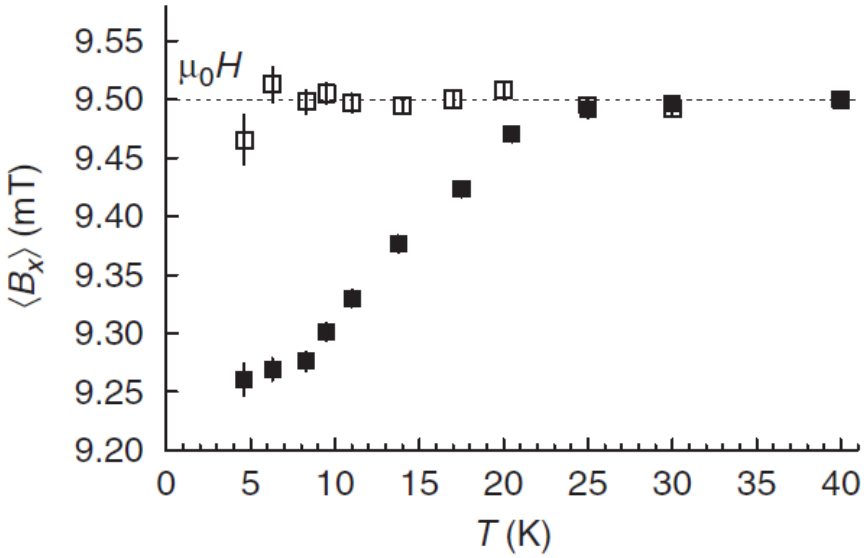

Fig. 9-22: Temperature dependence. Field measured at the centre of the underdoped (UD) layer: as a single layer (open symbols) or as a barrier with thickness of 46 nm in the trilayer (filled symbols). In the latter case the average local field is diamagnetically shifted up to $T_{eff} \cong 22$ K. Above this temperature its value is within the experimental error equal to the applied field. No shift is observed for a single UD layer

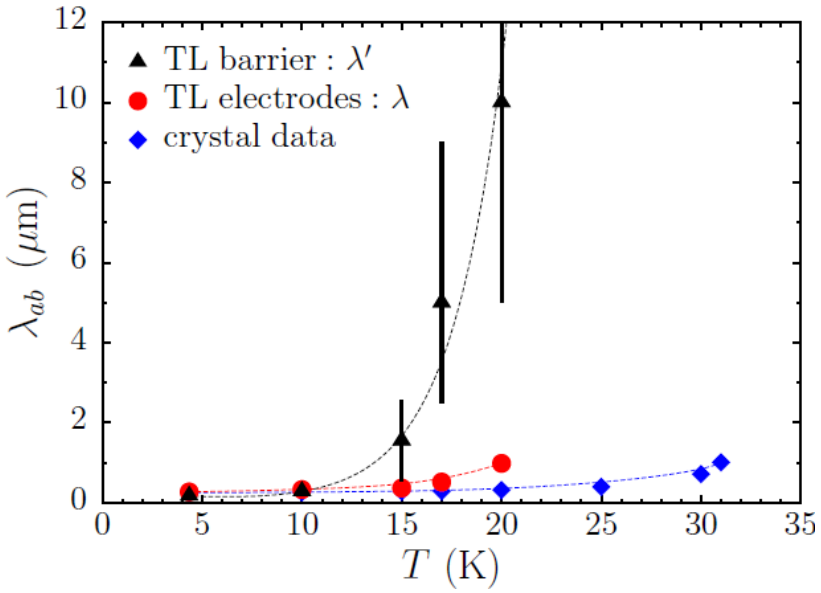

Fig. 9-23: Temperature dependence of the magnetic penetration depths in the barrier (black triangles, λ' and in the electrode layer (red circles, λ) compared with typical behaviour in optimally doped crystals (blue line). Error bars give the fit errors. The dashed lines are guides to the eyes. The divergent behavior of λ' close to 22 K indicates the disappearance of the induced superconductivity in the barrier at that temperature. The temperature dependence indicates that the induced superfluid density in the barrier layer is more sensitive to thermal excitation than in a bulk superconductor.

The conventional proximity theory in which the depth of penetration of Cooper pairs into a normal metal N is given by the induced coherence length ξ_N cannot account for this observation. In the usual situation, where the electron–electron interaction $V_N \rightarrow 0$ and $T_c' = 0$, one has $\xi_N = (\hbar v_F / 2\pi k_B T)$ in the clean limit (v_F is the Fermi velocity). For $T > T_c'$, given that in UD cuprates the transport along **c** axis is semiconducting, it is more appropriate to use the dirty-limit expression $\xi_N = (h v_c l / 2\pi k_B T)^{1/2}$, where l is the mean free path and v_c the velocity along the **c** axis. For T > 8 K, this gives $\xi_N < 2.5$ nm, much smaller than the barrier thickness d = 46 nm.
Several models (existence of local superconducting clusters, quenching of phase fluctuations by the presence of adjacent layers with long-range phase order) have been proposed that are able to provide an enhanced length scale of the proximity effect.

9.8 Probing the spin injection in an organic spin valve

An organic spin valve is an example of heterostructure studied with LE-μSR, which is also a prototype device. Spin valves consist essentially of two ferromagnetic layers which can be magnetized parallel or antiparallel to each other and a barrier level. They show magnetoresistance. The property of giant magnetoresistance in metallic multilayers was discovered in 1988. Already in 1997 this property found its application in sensors (e.g. in read-head of hard disks). In 2007 A. Fert and P. Grünberg won the Nobel prize for the discovery. Using organic materials has great potentially technological relevance because organic materials can be synthetized at low price and can be easily shaped. Magnetoresistance with organic semiconducting spacer has been demonstrated (Fig. 9-24).

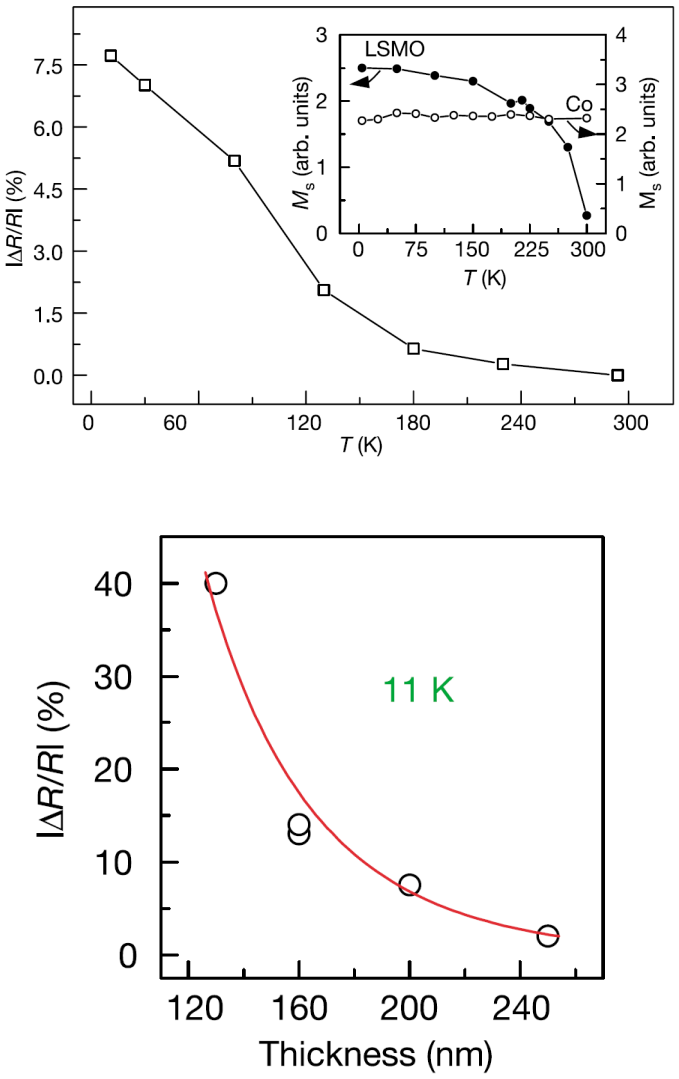

Fig. 9-24: Magnetoresistance $MR = \frac{\Delta R}{R} = \frac{R_{AP} - R_P}{R_{AP}}$ versus temperature and as a function of thickness for an organic spin valve (Z.H. Xiong et al., Nature **427**, 821 (2004)). AP: antiparallel orientation of the magnetization of top and bottom layer. P: parallel orientation (see Fig. 9-25 and 9-27).

The injection of polarized spins in an organic spin valve has microscopically been observed by a depth-dependent change of the mean field and the skewness of the LE-μSR line shape $p(B_\mu)$ (see Fig. 9-25 and 9-26).

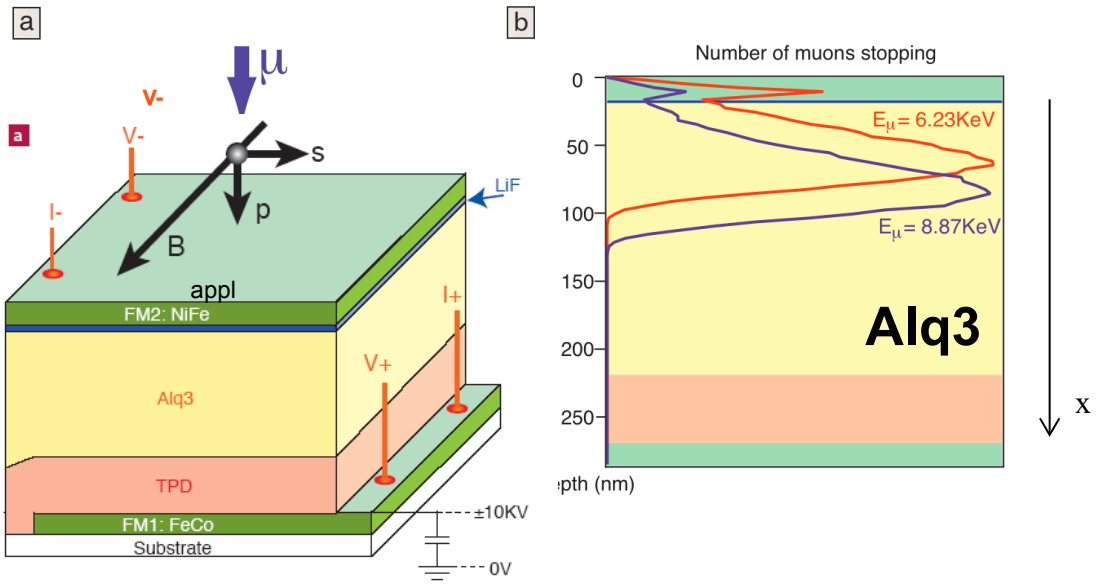

Fig. 9-25: a) Principle of the LE-μSR experiment to probe spin injection in an organic spin valve. (A. Drew et al. Nature Materials **8**, 109 (2009), L. Schultz et al. Nature Materials **10**, 39 (2011)). Muons are stopped in the barrier layer at a depth determined by their energy. There they precess in the local field, which is composed of the applied field and the field produced by the electronic spin polarization. The stopping profile is shown in b).

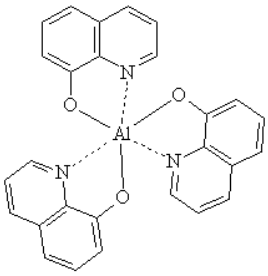

Fig. 9-26: Organic semiconductor Alq3: $C_{27}\,H_{18}\,N_3\,O_3Al$.

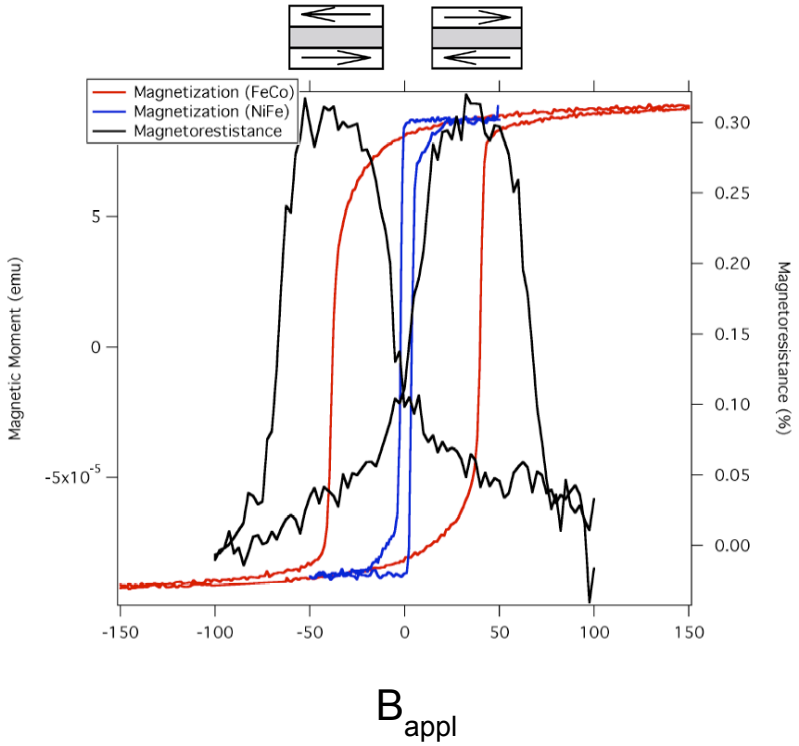

Fig. 9-27: Magnetoresistance and hysteresis of the organic spin valve used in the LE-μSR experiment. The different coercive field of the top and bottom ferromagnetic layers allow to switch the spin valve in one of the 4 states (2 with parallel magnetization, two with antiparallel magnetization).

Principle of the experiment:

-Spins are injected from the top (and bottom) layers into the barrier by applying a small voltage across the structure. These spins have long spin coherence time $>10^{-5}$ s $>> \tau_\mu$, giving rise to a static electronic polarization $<s_z(x)>$.

-In the organic material they produce static field $B_{spin}(x) \propto <s_z(x)>$ that adds (or subtracts) to B_{appl} used to select the spin valve state

- $B_\mu = B_{appl} \pm B_{spin}(x)$ is detected by muons stopped at various depths.

- The field distribution $p(B_\mu)$ is obtained from the Fourier transform of the polarization signal.

-The B_{spin} component can be determined by switching on/off the injection with current (voltage) and by changing its sign with respect to B_{appl} , i.e. by reversing the polarization of the top electrode.

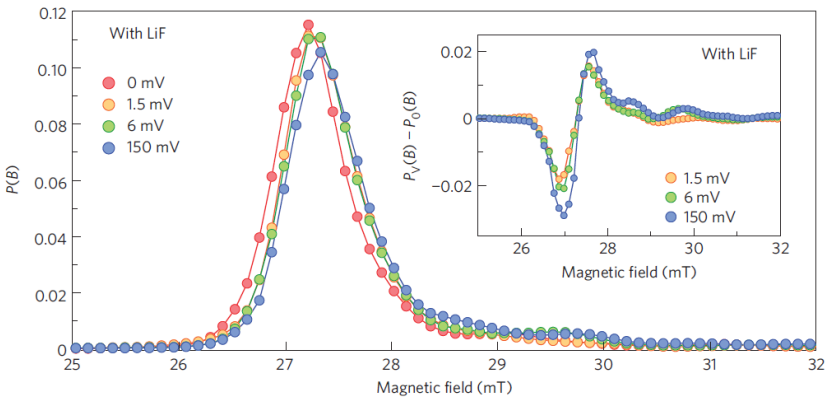

Fig. 9-28: Field distribution measured at various values of the applied voltage.

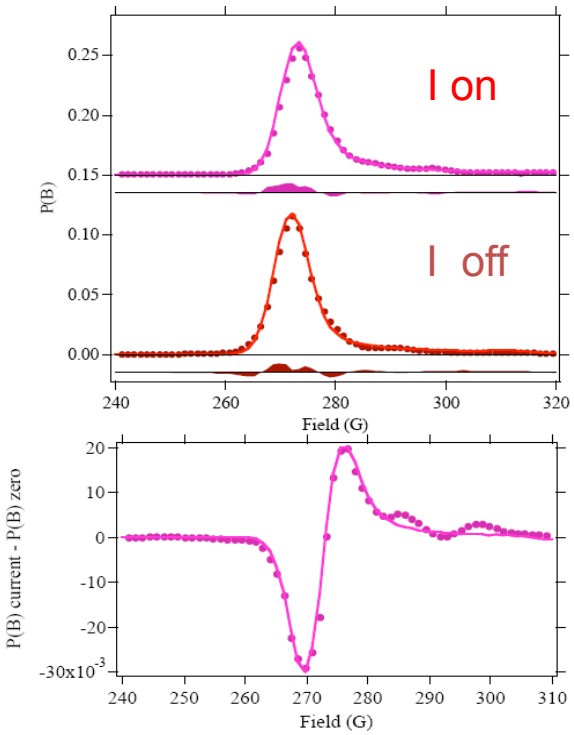

Fig. 9-29: Field distribution measured with and without polarized current and difference of the two spectra.

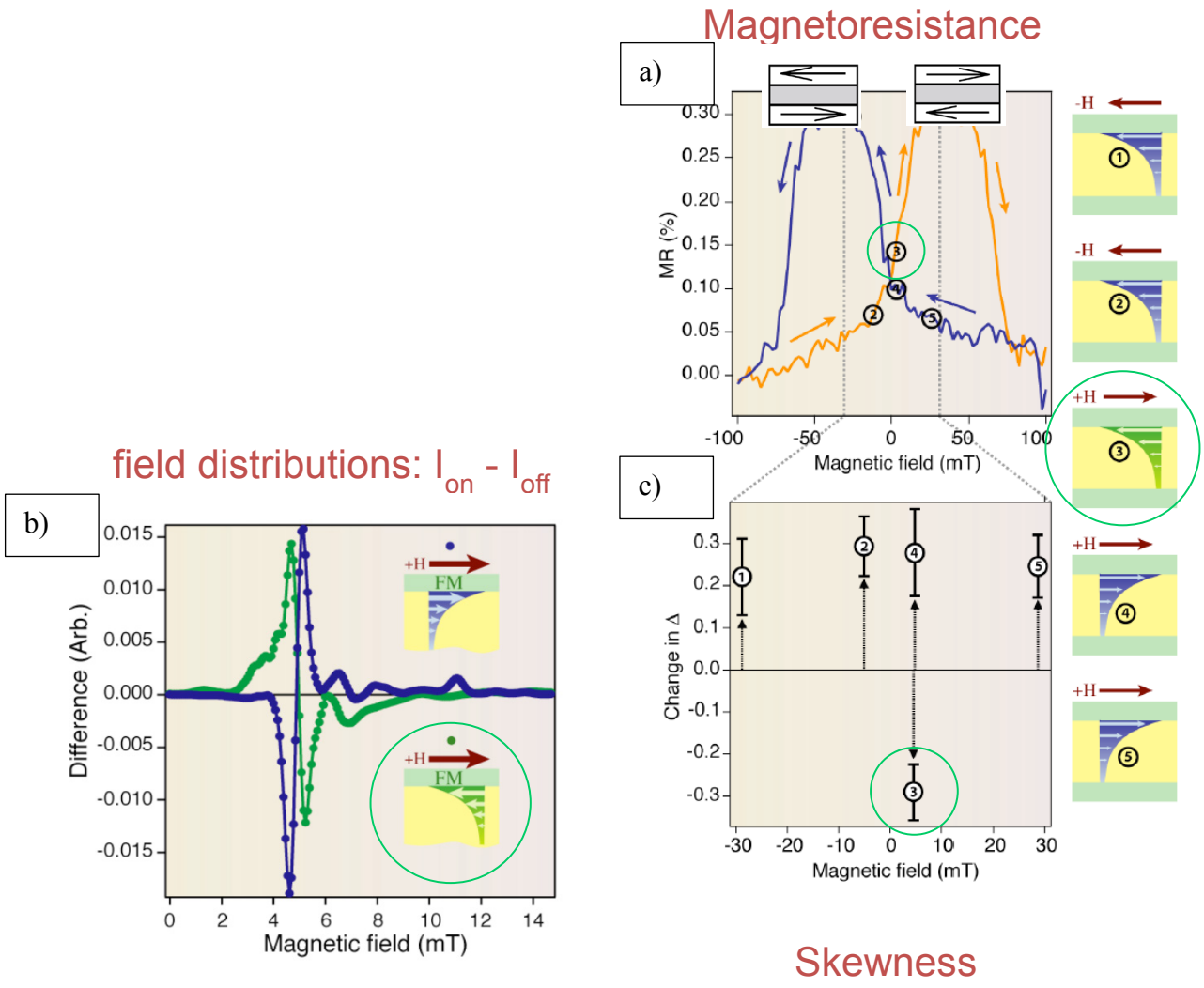

Fig. 9-30: a) Magnetoresistance and measured points with corresponding spin valve state. b) Difference of field distributions (Current on –current off) for two states of the spin valve and c) Skewness of the field distribution determined from the differences.

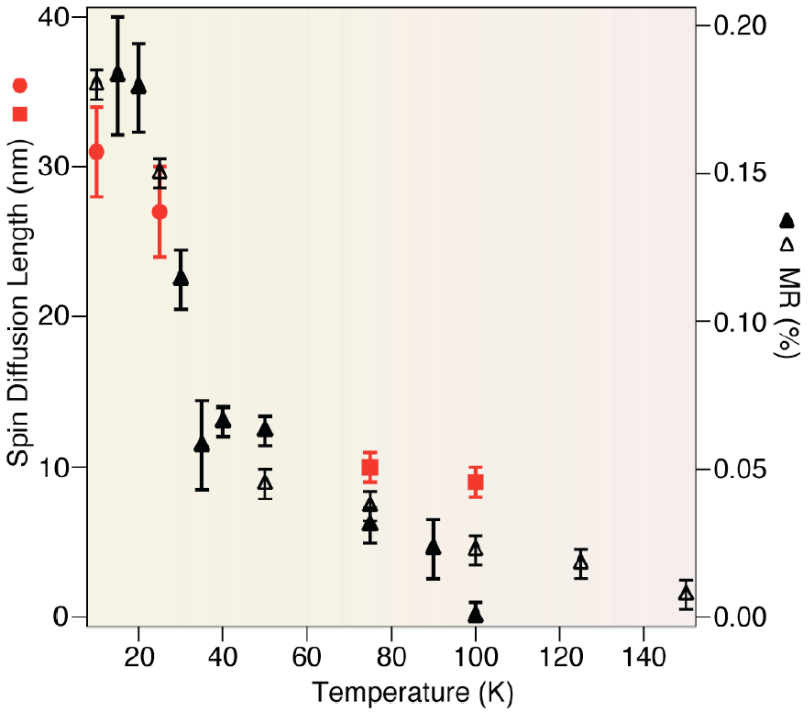

Fig. 9-31: Spin injection detected by shape analysis of local field distribution p(Bμ). The temperature dependence of the spin diffusion length correlates with the magnetoresistance. This experiment is the first direct measurement of spin diffusion length in a working spin valve. From A. Drew et al. Nature Materials **8**, 109 (2009).

From the overall analysis of the field distributions in the different states of the spin valve the spin diffusion length can be determined. It is found that its temperature dependence correlates with the temperature dependence of the magnetoresistance.